University of Oxford

Investigating macrophage-lymphatic vessel interactions in the neonatal mouse model of heart regeneration

Konstantinos Klaourakis

Keble College

Thesis submitted for the degree of Doctor of Philosophy (DPhil) in Chromosome and Developmental Biology

Supervisors: Professor Paul R. Riley & Dr Joaquim M. Vieira

2021

1. Acknowledgements

First and foremost, I would like to thank my supervisors Dr Joaquim Vieira (Joey) and Professor Paul Riley. It is fair to say that I would not have been part of so many publications, developed a side-project or even finished my PhD, without the guidance and (professional/personal) support of Joey. I would also like to thank Paul for trusting me with his project and ideas.

Thank you to everyone in the Riley and Vieira lab, as well as colleagues of other labs that have contributed to my PhD. Specifically, Christophe and Xin deserve a big thank you for the time we spent inside and outside the lab. I wish we could have had more hot pots and watched more football games with Oxford United! Also, a big thank you to Christophe for conducting the cell culture experiments. I am extremely grateful to Carla and Mala for conducting all of the surgeries, this project would not have been possible without them. Thank you very much to Carolyn for performing numerous MRI scans, and to Jacinta for using her expertise in 3D HREM to image my samples. I would like to thank Dany, the Flow Cytometry Facility of the Wellcome Trust Human Genetics and the Oxford Genomics Centre for the great team-work in generating the scRNA-seq dataset. Thank you to Prof David Jackson for his great suggestions during the transfer and confirmation stages of my PhD. A big thank you to my examiners, Dr Oliver Stone and Prof Karina Yaniv, for their time as they correct my thesis and discuss it with me during my viva.

A very special thank you to my partner Lisa who has been by my side through a crazy journey in Oxford, from our first dates at Hotel Chocolat to our endless discussions about our PhD projects, and from living in a 12 m^2 room to getting our first pet-hamster Hippo.

Now, it is time for new adventures and a completely new chapter together with our chocolate Labrador puppy (Koda) in London! I will miss the exciting board game nights with our friends in 41 Stockmore street (Gabi, Antje, and Nicole) and I am looking forward to our next reunion. Finally, I would like to thank my parents, being my support whenever I needed them during this long journey, as well as my grandparents Kostas and Tasia, without them nothing of this would have ever been possible.

Table of Contents

List of Figures

List of Tables

List of Abbreviations

Art EC	Arterial endothelial cells
AV	Aortic valve
BA	Bulbus arteriosus
CM	Cardiomyocytes
CO	Cardiac output
CV	Cardinal vein
DAB	3, 3'-diaminobenzidine
DC	Dendritic cells
dpi	Days post injury
E	Embryonic day
EDL	End diastolic lumen
EDM	End diastolic mass
EF	Ejection fraction
EMPs	Erythromyeloid precursor cells
Endo	Endocardium
Epic	Epicardium
ESL	End systolic lumen
ESM	End systolic mass
FACS	Fluorescence activated cell sorting
Fb	Fibroblast
Gran	Granulocytes
HMVEC-dAD	Human dermal microvascular endothelial cells
hpf	Hours post fertilization
HREM	High-Resolution Episcopic Microscopy
hwt	heart weight
iPSC	Induced pluripotent stem cell
ISVs	Intersomitic vessels
IVS	Interventricular septum
JLS	Jugular lymph sac
JV	Jugular vein
LAD	Left anterior descending
LEC	Lymphatic endothelial cell
LPS	Lipopolysaccharides
LVV	Lympho-venous valve
Mf	Macrophage
MI	Myocardial infarction
MLN	Mediastinal lymph nodes
MRI	Magnetic Resonance Imaging
MV	Mitral valve
P	Postnatal day
PCV	Posterior cardinal vein
Peri	Pericyte
Prol	Proliferating
PV	Pulmonary valve

scRNA-seq	single cell RNA sequencing
SMC	Smooth muscle cells
StV	Stroke volume
sVEGFR3	soluble decoy VEGFR3
SV	Sinus venosus
TV	Tricuspid valve
UMAP	Uniform Manifold Approximation and Projection
VEC	Venous endothelial cell
wpf	weeks post fertilization
X-Gal	5-bromo-4-chloro-3-indolyl-β-D-galactosidase

List of genes and proteins

ARG1	Arginase 1
CCL21	Chemokine (C-C motif) ligand 21
CCR2	C-C chemokine receptor type 2
CCR7	C-C chemokine receptor type 7
COUP-TFII	Chicken Ovalbumin Upstream Promoter Transcription Factor II
CSF1R	Colony Stimulating Factor 1 Receptor
CX3CR1	C-X3-C Motif Chemokine Receptor 1
EMCN	Endomucin
F4/80	Adhesion G Protein-Coupled Receptor E1
FOXC2	Forkhead box protein C2
GATA2	GATA Binding Protein 2
HA	Hyaluronan
HAS	Hyaluronan synthase
IFNγ	Interferon gamma
IL4	Interleukin 4
ISL1	Insulin Gene Enhancer Protein ISL1
ITGB1	Integrin Subunit Beta 1
LY-6C	Lymphocyte antigen 6 complex, locus C1
LYVE1	Lymphatic Vessel Endothelial Hyaluronan Receptor 1
MESP1	Mesoderm Posterior BHLH Transcription Factor 1
MHC-II	Major histocompatibility complex II
MYF5	Myogenic Factor 5
NKX2-5	NK2 Homeobox 5
NRP2	Neuropilin 2
PAX3	Paired Box Gene 3
PDGFRB	Platelet Derived Growth Factor Subunit B
PDPN	Podoplanin
PECAM1	Platelet And Endothelial Cell Adhesion Molecule 1
PROX1	Prospero homeobox protein 1
RELN	Reelin
SOX18	SRY-Box Transcription Factor 18
SPP1	Secreted Phosphoprotein 1
TIE2	Tyrosine-protein kinase 2

VAV1	Vav Guanine Nucleotide Exchange Factor 1
VECADHERIN	Vascular Endothelial cadherin
VEGFC	Vascular Endothelial Growth Factor C
VEGFD	Vascular Endothelial Growth Factor D
VEGFR3	Vascular Endothelial Growth Factor Receptor 3
WNT1	Wnt Family Member 1
WT1	Wilms Tumor 1

2. Abstract

Myocardial infarction (MI) triggers an immune response, whereby phagocytic cells remove dead tissue and assist with the subsequent remodelling and repair of the infarcted heart. In adult mice, MI activates cardiac lymphatics, which function to drain the build-up of interstitial fluid (oedema) and traffic macrophages to mediastinal lymph nodes (MLNs), reducing inflammatory/fibrotic cell content and improving cardiac output. Mice at postnatal day 1 (P1) fully regenerate their heart following MI in a pro-regenerative macrophage-dependent manner, whereas similar injury at P7 leads to scarring driven by pro-fibrotic macrophages. The role of cardiac lymphatics in the regenerative capacity of neonatal mice remains unexplored. Therefore, we hypothesised that lymphatics respond and function differently following MI during this regenerative window (P1 to P7), to clear macrophage specific subtypes depending upon their requirement for regeneration (P1) or fibrotic repair (P7).

To understand the spatiotemporal changes that take place in the cardiac lymphatic vasculature following birth, we initially quantified the expansion of the vascular network along the sub-epicardium. This revealed lymphatic growth and sprouting until P16, and strain-dependent developmental differences. We then investigated the maturation status of lymphatic endothelial cell junctions, which suggested a potential transition from “zipper” (impermeable) to “button”-type (permeable) junctions during the first two weeks of life. In addition, we examined the lymphangiogenic response and the trafficking efficiency of cardiac lymphatics after surgically induced MI. Using 3D light-sheet and confocal imaging; we found that VEGFR3-expressing lymphatics have limited lymphangiogenic response in P1 compared to P7 hearts 7 days after MI. To assess

trafficking of macrophages to MLNs, we performed adoptive transfer of adult splenic *hCD68-eGFP* labelled monocytes into the myocardium of P1 and P7 recipient mice undergoing coronary artery ligation. Imaging of MLNs from these animals indicated a less efficient clearance of GFP-labelled cells from P1 compared to P7 hearts 7 days after MI . To further investigate differences in immune cell trafficking in P1 versus P7 hearts and their association with regeneration/repair, we made use of mice lacking *Lyve1* that exhibit impaired transmigration of interstitial macrophages to lymphatic vessels in adult mice. Unexpectedly, MRI analysis of *Lyve1*$^{-/-}$ mice revealed impaired cardiac regeneration after P1 MI, while no changes were observed in cardiac function after P7 MI compared to the respective intact controls. Lastly, to gain insight into the molecular underpinnings of lymphatic endothelium-macrophage interactions in P1 versus P7, we generated unbiased single cell RNA sequencing datasets from samples collected at different time-points after MI. A summary of the initial computational analyses, as well as future approaches are discussed here.

The results of this project show that cardiac lymphatics continue to grow and mature postnatally and support the hypothesis that cardiac lymphatics respond and function less efficiently after P1 MI, compared to P7, in line with a need to retain pro-regenerative macrophages in the neonatal heart versus clearance of pro-inflammatory/fibrotic macrophages 7-days later. Further analysis is required to uncover the molecular mechanisms that lead to this differential response.

3. Introduction

3.1. The lymphatic vasculature

The circulatory system of vertebrates is composed of two complementary vasculatures, blood and lymphatic[1]. The blood vasculature, is a closed system responsible for transporting gases, nutrients, metabolites and cells to adjacent tissues[2]. The extravasation of fluid and macromolecules results in a continuous accumulation of extracellular fluids and increased interstitial pressure[2]. In addition to regulating interstitial fluid homeostasis, lymphatic vessels have essential roles in the immune response through the uptake and transport of pathogens, antigens and immune cells from tissues to regional lymph nodes, before returning the extravasated fluid and solutes to the blood circulation[3]. In some tissues/organs, lymphatic vessels have specialised functions. For instance, in the intestine lymphatics act as the main route for lipid absorption[4,5], while in the skin close interactions between vessels and stem cells regulate hair follicle proliferation and hair regeneration[6,7]. Structural and/or functional abnormalities in the lymphatic vasculature lead to primary and secondary lymphedema that are characterised by impaired interstitial fluid balance[8,9]. Primary lymphedema, is caused by genetic defects disrupting lymphatic development[9,10]. Secondary lymphedema is usually caused by infections, such as lymphatic filariasis[11], as well as by surgery and radiotherapy leading to lymphatic damage, as a side effect of tumour treatment[8]. Over the last two years several important reviews have been published on:

- the systemic lymphatic network[12,13];
- the role of lymphatic junctions[14];
- the transcriptional, epigenetic, and non-coding RNA regulation of lymphatics[15];
- the lymphatic development in zebrafish[16];
- the leucocyte trafficking through lymphatics[17];

- the immune response to MI[18];
- the cardiac lymphatics in mouse and zebrafish during development and myocardial infarction[19].

3.2. Structure and function of lymphatic vessels

Cardiac lymphatics run alongside the blood vessel network and have many of the functional features of the systemic lymphatic vasculature, specifically the maintenance of homeostasis of interstitial fluid pressure[20,21] and modulation of immune response[17]. Disruption of these processes can lead to severe health problems; for example, a 3.5 % increase in myocardial fluids can lead to 40 % reduction in cardiac output[22,23]. Lymphatic vessels are lined by a monolayer of oak leaf-shaped lymphatic endothelial cells (LECs), and are composed of three compartments: the initial lymphatics, the pre-collectors and the collector lymphatics[1,24]. Interestingly, the localisation of the initial lymphatics and the routes of collector vessels in the heart are not fully conserved between species[25].

3.2.1. *Initial lymphatics*

The initial lymphatics or capillaries are thin, blind-ended, and highly permeable vessels that are ideal for draining cells, fluid, and macromolecules. In most mammals, such as humans, dogs and pigs, the initial lymphatics are located in the area from the sub-epicardium to the sub-endocardium and drain extracellular fluids, cells and macromolecules that make up the lymph[26,27]. However, in rabbit and mouse hearts, lymphatics are absent from the endocardium[28,29]. A primary valve system at the level of the LECs allows the entrance of cells, fluids and macromolecules to the initial lymphatics and prevents their escape back to the interstitial space[4,30–32]. This primary valve system is created by flaps of adjacent LECs

that interconnect and loosely overlap with one another[30,33]. These LECs have specialised cell-cell junctions, called buttons, which are discontinuous, thereby allowing fluid entry to the lymphatic vessels while also securing the structural integrity of the endothelium[33]. Furthermore, the abluminal side of the LECs is overlaid with extracellular-matrix-anchoring filaments that prevent the initial lymphatics from collapsing under increased interstitial pressure[34]. As pressure increases, the lymph is formed inside the initial lymphatics and is transported to pre-collector and collector lymphatic vessels.

3.2.2. *Pre-collector and collector lymphatics*

Lymph travels through the subepicardial pre-collectors and collectors to the mediastinal lymph nodes (MLNs) and then back to the systemic circulation[35]. In the systemic lymphatic vasculature, the LECs have continuous seams of zipper-like cell-cell junctions that make the vessels impermeable to fluids and cells[33]. Despite the structural differences of button and zipper junctions their molecular composition is identical, with both containing adherent and tight junction proteins, such as VE-cadherin (Vascular Endothelial cadherin), ZO-1 (Zonula Occludens-1), Claudin-5 and Occludin[33]. In the systemic lymphatic vasculature, each collecting vessel is arranged in a functional pumping unit called a lymphangion, which is defined as the section between two consecutive secondary intraluminal valves that is overlaid with contracting lymphatic smooth muscle cells (LSMCs)[20,21]. However, cardiac lymphatics do not have a LSMC layer, and lymph flow is solely dependent on passive propulsion powered by the periodic motion of cardiac contraction[36–39]. As the lymph flows towards the MLNs, at each lymphangion the upstream valve closes preventing retrograde flow, while the downstream valve opens resulting in positive flow[20,21].

In human, dog, and pig hearts, collectors composing the left and right lymphatic trunks run along the major coronary arteries[40,41]. The left trunk collects lymph from the anterior and posterior interventricular branches and from the left marginal branch. The left trunk then passes behind the left atrial appendage and ascends onto the posterior surface of the pulmonary trunk and up to the pre-tracheal lymph nodes near the aortic arch. From the pre-tracheal lymph nodes, a single vessel travels behind the aorta to the cardiac lymph node, which lies between the superior vena cava and the right brachiocephalic artery, then several lymphatic vessels lead to the right lymphatic duct, which terminates in the right venous angle. The right trunk collects lymph from the right area of the heart and proceeds on the anterior surface of the aorta. The right trunk then enters the left anterior mediastinal chain and left paratracheal lymph nodes, from where it passes to the thoracic trunk and terminates in the left venous angle.

In contrast to the cardiac collector lymphatics of humans, pigs and dogs, which accompany coronary arteries, in mouse and rat hearts these vessels accompany cardiac veins[25]. Specifically, in the mouse heart the left collector drains the paraconal interventricular sulcus (left and right ventricles) around the left conal vein towards the left side of the pulmonary trunk and upwards to the MLNs[37]. The second collector drains the lymph from the left ventricle running along the left cardiac vein followed by the coronary sinus and then upwards towards the MLNs[37]. The lymph then reaches the draining lymph node *via* afferent collector lymphatics[42]. In the MLNs, cells of the innate and adaptive immune system reside in specific locations, poised to be activated[43,44]. For instance, antigen-presenting cells such as dendritic cells (DC) and macrophage subpopulations are closely integrated in the subcapsular and medullary sinuses to sample antigens and pathogens

transported in the lymph[45]. Macrophages and DCs then present these antigens to follicular B-cells and T-cells initiating a cascade of cytokine production and immune cell recruitment[45]. Following activation of adaptive immunity, lymphocytes enter the lymph and exit the lymph node *via* efferent lymphatic vessels[46,47] until the lymph flow reaches either the right duct or the thoracic duct[46]. From the right duct or thoracic duct, the lymph eventually returns to the venous circulation at the level of the jugular and subclavian veins, where specialised lympho-venous valves ensure the unidirectional drainage of the lymph to the blood[48–51].

3.3. Development of systemic lymphatics

During embryogenesis, the development of lymphatic vessels takes places after the major blood vessels, the dorsal aorta, and the cardinal vein (CV), have been formed. Two distinct mechanisms have been proposed for the development of the lymphatic network: *lymphvasculogenesis*[52–54] and *lymphangiogenesis*[55–58]. These processes require careful molecular regulation, with mutations in essential factors being linked to primary lymphedema in human patients[10].

The origin of the lymphatic vasculature has been the subject of some controversy for many decades. An initial report by Sabin, dating back to the 1900s, suggested that the lymphatic endothelium buds directly from the venous endothelium[59]. By contrast, Huntington and McClure proposed that LECs originate from the mesoderm and subsequently form connections with the venous endothelium[60]. It is now known that the fate of LECs in mice is hard-wired early on during embryogenesis at the level of the mesoderm[61]. Specifically, the *Pax3-Cre* (Paired Box Gene 3) and *Myf5-Cre* (Myogenic Factor 5) labelled paraxial

mesoderm, in addition to lateral plate mesoderm, contributes endothelial cells during embryonic blood vessel development in mice[61]. Around embryonic day (E) 9.5, these paraxial mesoderm- derived endothelial cells selectively differentiate from the dorsolateral part of the anterior CV to form the first precursor LECs, characterised by the expression of the transcription factor prospero homeobox protein 1 (PROX1)[61]. These LECs subsequently give rise to the majority of the lymphatic endothelium, including systemic and organ- based lymphatics (for example, the heart), with only limited contribution to the blood endothelium[61]. Also, preliminary data raise the possibility that *Pax3* and *Myf5* positive dermomyotome may contribute LECs directly and independently of the paraxial mesoderm-derived venous endothelium[61,62]. Nevertheless, *Prox1* expression is necessary and sufficient for LEC specification[63,64] and requires the activity of upstream transcription factors SOX18 (SRY-Box Transcription Factor 18) and COUP-TFII (Chicken Ovalbumin Upstream Promoter Transcription Factor II)[65,66]. Conditional deletion of *Prox1* in embryonic or adult mouse lymphatics leads to transition from LECs to a blood endothelial cell-like phenotype[67]. Both SOX18 and COUP-TFII bind and activate *Prox1* expression directly, whereas COUP-TFII also promotes lymphatic differentiation indirectly by repressing the arterial fate driven by the Notch signalling pathway[65,68]. Mutations in *SOX18* have been reported to cause the rare hypotrichosis-lymphedema-telangiectasia syndrome (OMIM 607823) in humans[69]. In blood vessels FLCN (Folliculin) is responsible for downregulating *Prox1* expression, hence limiting the plasticity in committed venous and lymphatic endothelial cells[70]. When *Prox1* has been expressed, a positive feedback loop between PROX1 and the transmembrane tyrosine kinase receptor VEGFR3 (Vascular Endothelial Growth Factor Receptor 3) maintains the precursor LEC identity[71]. Mitochondrial metabolism of LECs has an important role in the epigenetic regulation of *Prox1* and *Vegfr3*

expression, the maintenance of PROX1-VEGFR3 feedback loop, and subsequently the differentiation and development of embryonic LECs[72–74]. Human patients with mutations in *VEGFR3* suffer from hereditary lymphedema type IA (Milroy lymphedema; OMIM 153100)[75]. Concomitantly, precursor LECs start expressing LYVE1 (Lymphatic Vessel Endothelial Hyaluronan Receptor 1), a protein that is essential for the lymphatic modulation of the immune response during inflammation[76,77], but is redundant during embryogenesis[78,79]. At approximately E10.5, clusters of precursor LECs start aggregating and budding off along the length of the CV to form lymph sacs, which are lymphatic vessel precursors. Lymph sacs form two distinct populations, which migrate from the CV by different mechanisms, called ballooning and sprouting[80]. During ballooning, LYVE1^{high} NRP2^{low} (Neuropilin 2) precursor LECs bud away from the CV and separate through pinching off, forming lymph sacs filled with blood cells[80]. During sprouting, LYVE1^{low} NRP2^{high} precursor LECs migrate directly from the CV without contributing to lymph sac formation[80]. For the budding process to take place, the VEGFR3/VEGFC (Vascular Endothelial Growth Factor C) signalling pathway is essential, although VEGFD (Vascular Endothelial Growth Factor D) also contributes to a lesser extent[56]. VEGFR3 signalling is enhanced by NRP2, which stabilizes the VEGFR3/VEGFC complex[81,82]. At around E12.5, adjacent LECs budding from the CV are connected by continuous, impermeable zipper junctions, providing strong structural integrity to the forming lymphatic vessels[83,84]. Starting at E16.5 and continuing during postnatal development, the junctions of the initial lymphatics transform into permeable buttons while maintaining the same protein composition (Figure 3.1)[33,83,84]. To prevent blood from flowing into the lymph sacs lympho-venous haemostasis is achieved with two different mechanisms[85,86]. First, PROX1 activates the expression and production of the transmembrane glycoprotein PDPN (Podoplanin), which subsequently interacts with

the platelet expressed receptor CLEC-2 (C-type-lectin-like-2)[49], inducing platelet aggregation and thereby lympho-venous haemostasis[49]. Second, blood backflow can be prevented by lympho-venous valves (LVVs) formed by specialised PROX1^{+} LECs residing in the CV, connecting lymphatic vessels with jugular and subclavian veins[48,51]. The development of LVVs, as well as the intraluminal valves found inside the collector lymphatics, is a complex process requiring topological and morphological changes of valvular LECs[51]. The primary event in lymphatic valve formation involves oscillatory shear stress, Wnt/β-catenin signalling and PROX1-induced[48,87] upregulation of GATA2 (GATA Binding Protein 2)[88–90] and FOXC2 (Forkhead box protein C2)[91–95] in a subset of LECs. These transcription factors, together with mechanical force from the lymph flow coordinate to induce gene expression of VE-cadherin[96], integrins[50,97], Connexins 37 and 43[92,98] amongst other genes that mediate lymphatic valve development. *Fat4* (FAT Atypical Cadherin 4) and *Dchs1* (Dachsous Cadherin-Related 1), two GATA2 target genes, are also essential for the LECs polarity in both the vessel and valves morphogenesis[99,100]. Several lymphatic-related diseases have been linked to mutations in *FOXC2*, such as hereditary lymphedema type II (Meige disease; OMIM 153200) and distichiasis-lymphedema syndrome (OMIM 153400)[101]. Also, mutations in *GATA2* have been described in patients with primary lymphedema with myelodysplasia (Emberger syndrome; OMIM 614038)[102], while *FAT4* mutations have been documented in Hennekam lymphangiectasia-lymphedema syndrome 2 (OMIM 616006)[103]. After lymph sacs have formed and separated from the CV, they start expanding into the developing embryonic tissues and organs by lymphangiogenesis, where the lymphatic vasculature continues to mature.

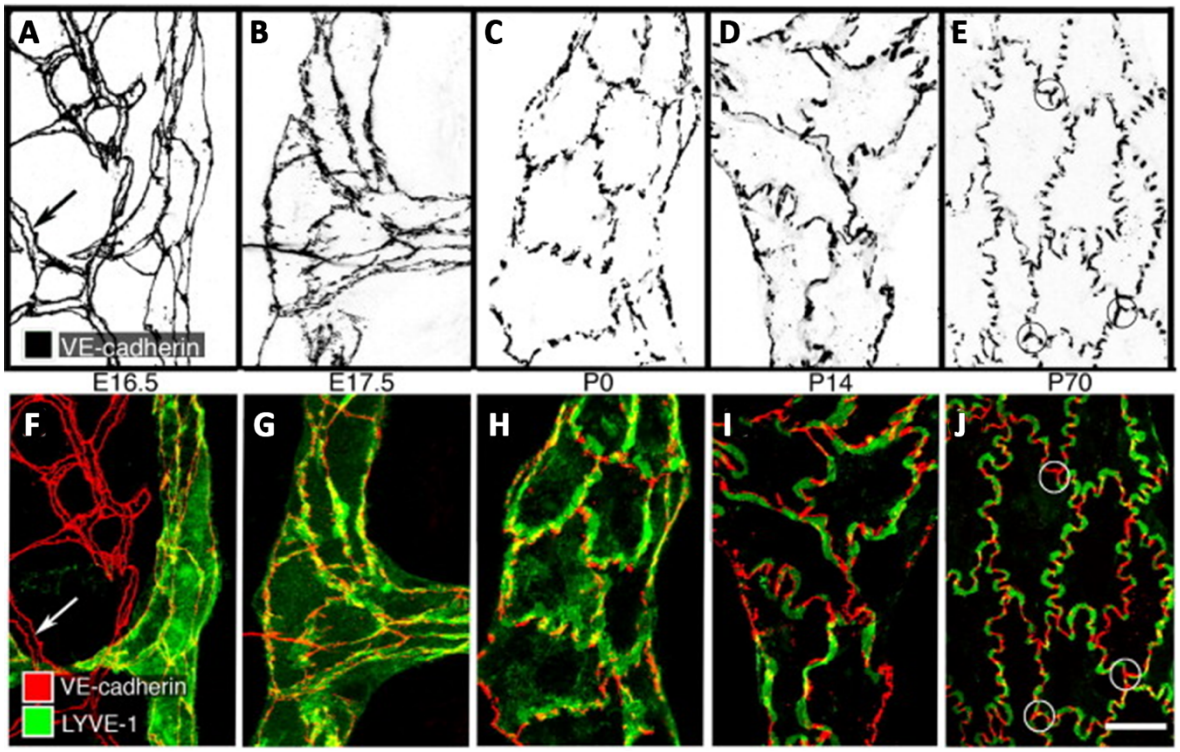

Figure 3.1 Initial lymphatics have specialised cell-cell junctions in the trachea and airways.

Lymphatic endothelial cells have specialised cell-cell junctions in the initial lymphatics of the trachea and airways. During early stages of embryonic development these junctions are a continuous seam called zipper-like junctions, which are mostly impermeable to cells (A-B and F-G). As the lymphatics develop through postnatal life, the junctions of the initial lymphatics transform to discontinous button-like junctions, which have gaps that are permeable to cells (C-E and H-J). Image adapted from Li-Chin Yao et al. Am J Pathol. 2012[84].

Lymphatic vessels are evolutionary conserved across vertebrate species, with the small freshwater fish *Danio rerio* (zebrafish) being one of the most studied non-mammalian models. In zebrafish the development of the lymphatic vessels begins after the formation of the two main axial blood vessels, i.e. dorsal aorta and posterior cardinal vein (PCV), and intersegmental vessels have been completed[104]. Similar to mice, LECs bud off from the PCV at around 32-34 hours post fertilization (hpf) in zebrafish[104,105]. These pre-LECs originate from angioblasts located in the ventral PCV wall, before migrating to the dorsal side of PCV from where they sprout[106]. At about 48hpf, half of these sprouts disconnect from the PCV,

migrate dorsally to the horizontal myoseptum region and form a pool of lymphatic precursor cells, called parachordal lymphangioblasts[107]. These cells then migrate either ventrally to form the main lymphatic vessels at the thoracic duct, or dorsally to form the dorsal longitudinal lymphatic vessel, which will be completed at around 72hpf[105,108]. Interestingly, the molecular regulators involved in zebrafish lymphangiogenesis are not evolutionary conserved and mutant fish display different phenotypes compared to the equivalent in mice. For instance, *coupTFII* and *sox18* morpholino knockdown and mutant zebrafish have grossly normal blood and lymphatic vasculature[109–113]. Zebrafish possess two *Prox1* homologs, *prox1a* and *prox1b*, with the later not being expressed in LECs and being dispensable for development. Interestingly, *prox1a* mutant fish have only a mild decrease in LEC number, suggesting that *prox1a* function, unlike its mammalian orthologue *Prox1*, is not essential for LEC specification[104,110,114]. After the fate of the LECs has been established, they begin sprouting in a Vegfr3-Vegfc-dependent mechanism, similar to mice[104,107,114–116]. Deletion of either *vegfr3* or *vegfc* causes an extensive lymphatic phenotype, due to the inability of endothelial cells to sprout from the CV[104,107,114–116]. Vegfc is produced as a pre-pro-protein which, upon secretion, requires proteolytic cleavage to obtain full biological activity[117]. The extracellular Vegfc-processing machinery comprises Ccbe1 (the collagen and calcium-binding EGF domain 1)[107], as well as Adamts3 and Adamts14 (A disintegrin and metalloprotease with thrombospondin motifs-3 and -14)[118]. Mutation of any of these gene leads to impaired lymphatic development in both zebrafish[119] and mice[120]. In humans mutations of *CCBE1* or *ADAMTS3* causes Hennekam lymphangiectasia-lymphedema syndrome 1 (OMIM 235510) and 3 (OMIM 618154), respectively[121–123]. In zebrafish, Adamts3 is expressed and secreted by motoneurons, as well as by a subpopulation of fibroblasts at the horizontal myoseptum region that co-

expresses *adamts3*, *adamts14*, *ccbe1*, and *vegfc*[119]. This leads to the generation of fully active Vegfc in the direct extracellular space, which is necessary to guide the migration of parachordal lymphangioblasts[119]. In addition to the aforementioned proteins, recent studies have focused on the roles of non-coding RNAs, such as microRNAs (miR) and long non coding RNAs (lncRNA), in lymphatic development[124,125]. Specifically, miR-204[125] and lncRNA LETR1[124] have been identified as a lymphatic-specific in human and zebrafish, and *in vitro*, respectively.

3.4. Development of cardiac lymphatic vessels

3.4.1. *Mouse cardiac lymphatics*

In mice the first cardiac LECs emerge at E12.5 from the extra-cardiac region near the outflow tract on the ventral side of the heart and from the sinus venosus (SV) on the dorsal side of the heart[38]. Between E10.5 and E12.5 a LEC population arises from the CV and migrates towards the SV and outflow tract[38]. By E14.5, cardiac lymphatics extend along the base-to-apex axis on both sides of the heart, with the ventral side being slightly delayed compared to the dorsal side[38]. During embryogenesis, cardiac lymphatics appear only in the sub-epicardial layer[36–38]. From birth to approximately P16, lymphatic vessels continue to grow and branch laterally to adequately cover both dorsal and the ventral surfaces of the mouse heart and also grow deeper into the underlying myocardium, without reaching the endocardium[36,37].

3.4.2. *Cellular origins of mouse cardiac lymphatics*

The majority of cardiac LECs originate from the paraxial mesoderm-derived *Tie2*$^{+}$ (Tyrosine-protein kinase 2) endothelium of the CV[61], although non-venous sources also contribute to the forming vasculature (Figure 3.2)[38,126,127]. Fate mapping using genetic drivers to trace

Mesp1^{+} (Mesoderm Posterior BHLH Transcription Factor 1) mesoderm, *Nkx2-5*$^{+}$ (NK2 Homeobox 5) cardiac mesoderm, *Wt1*$^{+}$ (Wilms Tumor 1) epicardium and *Wnt1*$^{+}$ (Wnt Family Member 1) neural crest cells excluded all these lineages as potential LEC sources. Further genetic lineage-tracing experiments identified the *Vav1*$^{+}$ (Vav Guanine Nucleotide Exchange Factor 1), *Pdgfrb*$^{+}$ (Platelet Derived Growth Factor Subunit B), and *Csf1r*$^{+}$ (Colony Stimulating Factor 1 Receptor) haemogenic endothelium of the yolk sac as a potential contributor of LECs[38,128]. Strikingly, the ventral and dorsal lymphatic endothelium have distinct origins and develop through different mechanisms, with non-venous *Isl1*$^{+}$ (Insulin Gene Enhancer Protein ISL1) second heart field-derived precursors contributing LECs exclusively to the ventral vascular network[126,127]. Similarly in zebrafish, lymphatic progenitors derive from both venous and non-venous angioblast sources (discussed in section 3.4.3)[106,129].

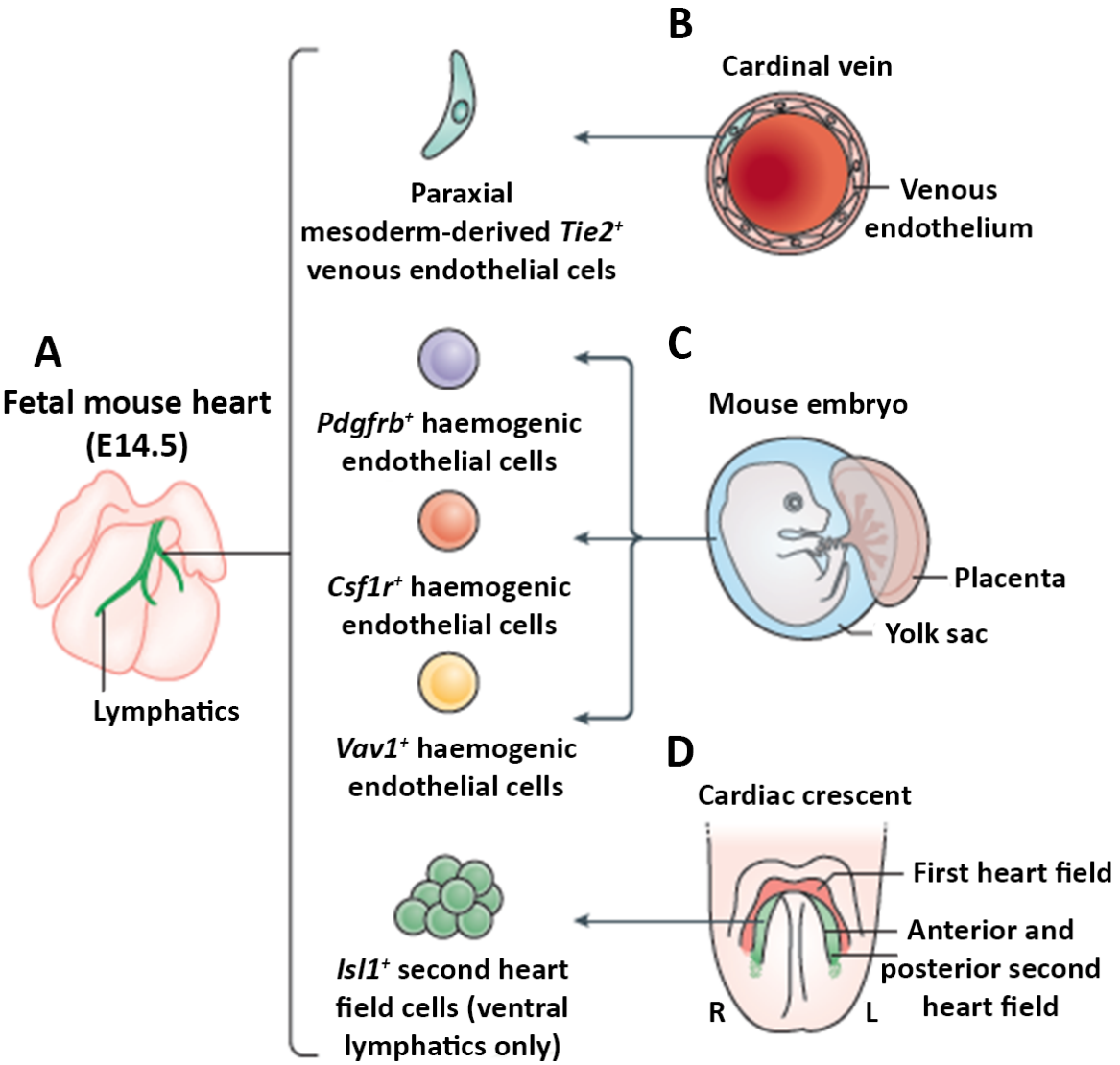

Figure 3.2 Venous and non-venous cell lineages contribute to lymphatic endothelial cells in the mouse heart.

Cardiac lymphatic vessels are present on the dorsal and ventral side of the heart from E14.5 (A). A subpopulation of paraxial mesoderm-derived venous endothelial cells bud from the cardinal vein to give rise to lymphatic endothelium (B). Yolk sac-derived haemogenic endothelium also contribute to the developing lymphatics (C), while a second heart field population is found specifically on ventral cardiac lymphatics (D). Figure adapted from Klaourakis et al. Nat Rev Cardiol. 2021[19].

3.4.3. *Zebrafish cardiac lymphatics*

In zebrafish, cardiac lymphatics are found only in the sub-epicardial layer and drain into large collecting vessels in the outflow tract, which connect to the facial lymphatic vasculature[54]. Similarly to the mouse cardiac lymphatics, zebrafish cardiac lymphatic

vessels derive from both venous and non-venous (angioblast) sources[106,129]. Specifically, the cardiac lymphatic endothelium is first established on the outflow tract, or bulbus arteriosus (BA), from facial lymphatic vessels that originate from sprouts of the CV and primary head sinus (lymphangiogenesis), as well as from a population of lymphangioblasts (lymphvasculogenesis)[54,129,130]. This process takes place relatively late in development, but before the initiation of the coronary vasculature, at about 3-4 weeks post fertilization (wpf)[54,131]. However, the expansion of cardiac lymphatic vessels over the ventricle takes place after the formation of the coronary vasculature in juvenile zebrafish, at approximately 12–16 wpf[54,131]. Over subsequent weeks, the BA lymphatic vessels sprout towards the ventricle in close proximity to the major coronary vessels and continue to grow along the base-to-apex axis in a process analogous to the growth of the cardiac lymphatics in the mouse[54,131]. Interestingly, hearts with an underdeveloped coronary plexus have severe ventricular lymphatic abnormalities, whereas the BA lymphatics are normal[54,131]. Apart from sprouting lymphatics, clusters of isolated LECs of unknown origin have been reported to connect and contribute to the cardiac lymphatic vasculature[54]. Similar to the systemic lymphatic vessels, cardiac lymphatics require Vegfr3-Vegfc signalling to develop, with genetics models such as *vegfr3*$^{-/-}$, *vegfc*$^{+/-}$ or hypomorphic *vegfc*$^{hy/hy}$ zebrafish having a severe lymphangiogenic phenotype[54,131,132].

3.5. Macrophage interaction with lymphatic vessels

3.5.1. *Macrophages in cardiac development*

Macrophages develop during mouse embryogenesis in three waves[133]. First, mesoderm and progenitor cells in the yolk sac differentiate into macrophages at E7.0[134,135]. Second, erythromyeloid precursor cells (EMPs) travel from the yolk sac to the foetal liver, and

subsequently differentiate into monocyte-progenitor cells, which give rise to many tissue resident macrophage populations between E11.0 and E17.5[136]. Third, as the bone marrow develops it produces mature monocytes and becomes the main source of various macrophage lineages from E17.5 until adulthood[137,138]. During normal homeostasis in the adult mouse heart, tissue resident macrophages represent about 7 % of the non-cardiomyocyte population, derived from the yolk sac, as well as from foetal liver and bone marrow monocytes[138,139]. This lineage heterogeneity translates into diversity of molecular markers and responses to injury. To this date, at least four distinct monocyte/macrophage populations in the adult mouse heart have been described depending on expression patterns of the cell surface markers *Ccr2* (C-C chemokine receptor type 2) and *Mhc-II* (major histocompatibility complex II)[138,140,141]. Embryonic derived subpopulations $CCR2^{-}$ MHC-II^{low} and $CCR2^{-}$ MHC-II^{high} are long-lived and maintained through local proliferation, independently of monocyte input[140,142]. With age, however, their self-renewal properties decrease and infiltration of $CCR2^{+}$ MHC-II^{low} circulating monocytes increases[142,143]. The latter predominantly give rise to $CCR2^{+}$ MHC-II^{high} macrophages, leading to a dynamic change of the cardiac macrophage landscape[142,143]. Therefore, it appears that embryonic derived cardiac macrophages are gradually replaced by monocyte-derived ones. In general, embryonic derived macrophages are considered to be anti-inflammatory with regenerative properties, such as stimulating angiogenesis[138,140,143]. In contrast, monocyte-derived macrophages have been shown to be pro-inflammatory with adverse contribution to remodelling upon MI, such as facilitating fibrotic scar formation[138,140,143]. Cardiac resident macrophages have been implicated in important homeostatic functions, such as coronary and cardiac lymphatic vessel development[144–146], and cardiac conduction[147].

3.5.2. *Macrophages in lymphatic vessel development*

The first cardiac macrophages are located predominantly in the subepicardial area at E10.5 and gradually spread, invading the deeper layers of the myocardial wall by the postnatal stage[145,146]. At E12.5, before the development of cardiac lymphatic vessels, cardiac macrophages are positioned in the vicinity of newly formed blood vessels, and from E14.5 cardiac macrophages are in close proximity or in direct contact with lymphatic vessels[145,146]. A subset of the *Csf1r*$^{+}$ lineage EMPs contributes to the developing LECs[145], supporting the hypothesis that haematopoietic cells provide directly to the cardiac lymphatic vasculature[38]. Depletion of cardiac macrophages using mutant mice results to severely disrupted lymphatic network at E16.5 and E19.5, with hyperplastic, shorter and with less lymphatic vessel junctions[145]. Also, *in vitro* experiments suggest that macrophages physically interact with lymphatic vessels using a HA-dependent (hyaluronan) mechanism to promote remodelling of the developing (cardiac) lymphatic plexus[145]. Noteworthy, cardiac macrophages are required for the normal development of coronary vessels too[144,145].

3.6. Cardiac fibrotic repair after adult heart injury

3.6.1. *Myocardial infarction*

Myocardial infarction (MI), also known as heart attack, is a consequence of coronary artery occlusion caused, for example, by the formation of atherosclerotic plaques in the arterial wall[148]. MI results in reduced blood flow to the heart and can lead to prolonged ischaemia and to cardiomyocyte death. Humans and other adult mammals lack the ability to regenerate their heart[149], which after the onset of myocardial ischemia, remodels in an attempt to compensate for the loss of cardiovascular tissue and healing occurs by replacing the dead myocardium with scar tissue[150]. As a result, the function of the heart is impaired

which may result in cardiac rupture or failure followed by sudden death. Following MI, cardiac lymphatics respond according to whether the default wound healing is *via* fibrotic repair, as in adult mammals including humans, or *via* a regenerative response, as occurs in adult zebrafish (Figure 3.3).

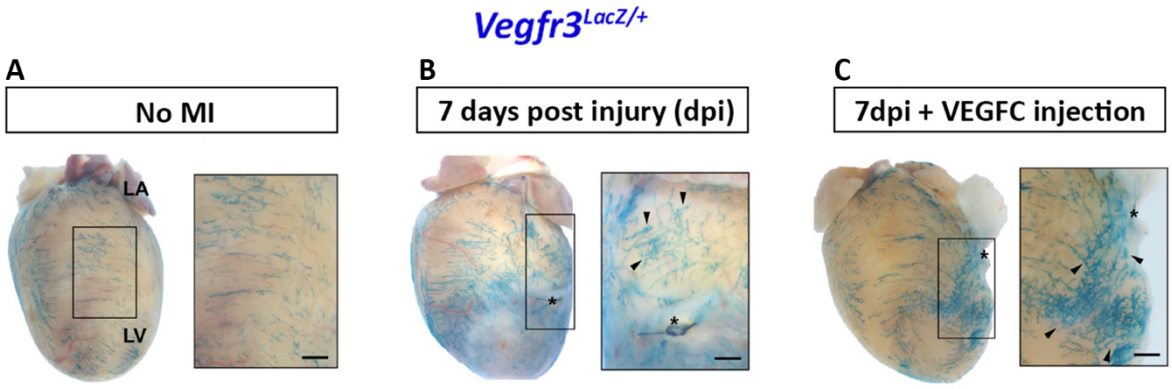

Figure 3.3 Cardiac lymphatics respond to myocardial infarction in adult mice.

In adult mouse hearts, lymphatics respond through lymphangiogenesis at the site of injury after myocardial infarction (A-B). This response can be enhanced by injecting lymphangiogenic factors to the heart, such as VEGFC (C), resulting in reduced oedema and inflammatory immune cells, and consequently better cardiac output. Image adapted from Klotz et al. Nature. 2015[38].

3.6.2. *Oedema after myocardial infarction*

After MI, the endothelium in the ischemic region is also affected, leading to increased vascular permeability and significant loss of lymphatic vessels, causing poor myocardial fluid drainage and persistent oedema[22,151,152]. Myocardial oedema can cause severe effects on cardiac function and healing. The accumulation of fluids can disrupt collagen fibres[153], compromise the structural integrity of the heart and create a greater distance for oxygen diffusion from the blood capillaries to cardiomyocytes, which could result in increased infarct size. Also, cardiac oedema causes myocardial stiffness, impairing contractility and resulting in systolic and diastolic dysfunction[22]. During the remodelling phase, the cardiac

lymphatics undergo lymphangiogenesis by growing and expanding in the infarcted area[76,152,154–156]. However, despite the endogenous lymphatic response, myocardial oedema and inflammation persists[76,152,154–156]. An important contributing factor to the insufficient drainage by the cardiac lymphatics after MI could be the reduced cardiac contractility caused by the death of cardiomyocytes, which acts as the major extrinsic force for lymph propulsion from the heart to the MLNs[157,158]. Interestingly, enhancement of cardiac contractility improves myocardial lymphatic function[157,159]. The increase in interstitial pressure, eventually leads to fibrosis, impaired heart function and ultimately heart failure[22,23,160].

3.6.3. *The immune response to heart injury*

In adult mice, shortly after the induction of MI through surgical ligation of the left anterior descending (LAD) coronary artery[161] circulating pro-inflammatory stimuli, such as damage-associated molecular patterns and cytokines, activate and recruit innate immune cells to the injury site[18]. Neutrophils and monocytes are the first to infiltrate the infarcted myocardium to clear debris and dead cells by phagocytosis and efferocytosis, respectively[162]. In mice, neutrophil numbers peak 3 days after MI, followed by a biphasic response of monocytes and monocyte-derived macrophages up to 5 days post-injury (dpi), with gradual reduction to baseline levels thereafter[163]. During these phases, the embryonic-derived tissue-resident macrophages die and are replaced by monocytes and monocyte-derived macrophages[164]. The first phase (1-4dpi) of the immune response after injury in the adult heart is an inflammatory phase, with an increase in the number of pro-inflammatory monocyte-derived macrophages ($CCR2^+$ $Ly\text{-}6C^+$ [lymphocyte antigen 6 complex, locus C1])[140,156]. These cells secrete inflammatory and proteolytic factors and

have increased phagocytosis and efferocytosis[140,156]. By contrast, the second phase (≥5dpi) is anti-inflammatory phase, with pro-regenerative, tissue resident macrophages ($CCR2^-$, $Ly\text{-}6C^-$) contributing to angiogenesis and scar formation[140,156,165]. Interestingly, macrophages can directly contribute to scar formation in the adult heart after MI by expressing and depositing collagen[166], as well as indirectly by supporting the activation of cardiac fibroblasts into myofibroblasts[156]. Also, in a single-cell RNA sequencing study a subpopulation of cells was discovered that exhibited a hybrid molecular signature of both macrophages and fibroblasts in adult mice[141]. As in the mouse model, hearts from adult patients with heart failure are also populated by tissue-resident $CCR2^-$ and monocyte-derived $CCR2^+$ macrophages[167]. After MI in mice, the epicardium and the pro-inflammatory macrophages secrete VEGFC, which drives lymphangiogenesis and the extensive remodelling of the cardiac lymphatic network[38,76,152]. This endogenous response of cardiac lymphatics attempts to maintain an optimal immune cell load, which is necessary for effective tissue repair[76,152,154–156]. However, the response of the cardiac lymphatics is insufficient to clear the immune cells, which results in chronic inflammation and increased scar formation[39,76]. Apart from neutrophils, monocytes and macrophages, other leukocytes, such as T cells, infiltrate the heart during the first week after MI in adult mice[163]. Although the response of the adaptive immune system to MI has not been well studied, the current view is that regulatory T cells have a beneficial role in cardiac healing[168,169]. By contrast, $CD4^+$ effector T cells produce pro-inflammatory cytokines and $CD8^+$ T cells have direct cytotoxic effects[170,171].

3.6.4. *Augmentation of injury-induced cardiac lymphangiogenesis*

The endogenous lymphangiogenic response is insufficient to clear the myocardial oedema and the infiltrated immune cells after MI. This inefficient endogenous response has prompted attempts to increase lymphangiogenesis and lymphatic function in the injured heart[76,152,154–156]. Augmentation of the lymphangiogenic response with administration of recombinant $VEGFC_{C156S}$, which interacts specifically with VEGFR3, improves cardiac function after MI in animal models, as assessed by echocardiography and cine-MRI[39,76,152]. Injection of micro particles loaded with $VEGFC_{C156S}$ into the left ventricle after induction of MI leads to an increased clearance of myocardial oedema in rats[152]. Intraperitoneal injection of adeno-associated virus-$VEGFC_{C156S}$ at 7-days before MI induces an increased clearance of T cells in female mice and male rats[39]. Lastly, intraperitoneal injection of $VEGFC_{C156S}$ after MI in adult mice increases macrophage clearance *via* a LYVE1-dependent mechanism (Figure 3.3)[76]. LYVE1 is highly expressed at the surface of the initial lymphatics and interacts specifically with HA that coats the surface of leukocytes[172]. Engagement of LYVE1 with HA promotes the docking and transmigration of macrophages to lymphatic vessels *in vitro*[173]. In addition, DCs dock and transmigrate to LECs in a LYVE1-HA-dependent manner in a model of dermal injury[174]. Whereas administration of $VEGFC_{C156S}$ increases lymphangiogenesis and improves cardiac function after MI in animal models, trapping of VEGFC and VEGFD with the use of the soluble decoy VEGFR3 (sVEGFR3) has provided contradicting results. Initially, a study reported significant cardiac lymphatic defects, intramyocardial haemorrhage and higher mortality rate in sVEGFR3 transgenic mice compared to control littermate after MI[175]. However, intraperitoneal injection of adeno-associated virus-sVEGFR3 at 7-days before MI in female mice and male rats[39] did not affect lymphangiogenesis but led to reduced infarct region thinning and T cell infiltration to the

heart at 7dpi, as well as to improved cardiac function at 21dpi[39]. Finally, a study that used different genetic approaches (tamoxifen induced conditionally knock-out *Vegfr3* or *Vegfc/Vegfd*) to block the endogenous lymphangiogenic response seen after MI, reported no significant differences in cardiac function compared to adult wild-type mice that had undergone MI[176]. The authors of that study concluded that external augmentation of lymphangiogenesis fails to improve cardiac function after adult MI and $VEGFC_{C156S}$ injection improves cardiac healing through a non-lymphatic mechanism; however, this hypothesis was not investigated[176]. In contrast, these results reinforce the notion that the endogenous lymphangiogenic response to MI is insufficient to improve cardiac healing and function[39,76,152,176].

Of note, surviving cardiomyocytes at the border zone and infarcted area express high levels of *Vegfr3* and undergo hypertrophy in the first days after MI[177,178]. In the same regions, *Vegfc* and *Vegfd* were upregulated within 3dpi, and *in vitro* studies showed that VEGFC contributes in cardiomyocyte hypertrophy and survival[177,178]. These results collectively point to non-lymphangiogenic roles for VEGFC in the infarcted heart, which must be taken into consideration when interpreting experimental outcomes following interference of the VEGFR3/VEGFC pathway. Furthermore, the cardiac lymphatic vasculature has sex-dependent differences under normal and MI conditions, a variable that was often not factored in the aforementioned studies[179].

Clinical opportunities

MI is currently a major cause of mortality worldwide, and no treatments are currently available to revert the cardiac damage. Current treatments focus on early re-establishment

of the blood flow to prevent further tissue damage and therapy with drugs such as angiotensin-converting enzyme inhibitors and β-blockers to support the surviving myocardium[180]. Restoration of blood flow is initially accomplished by percutaneous coronary intervention and the administration of thrombolytic drugs. In severe cases invasive procedures, such as coronary artery bypass graft surgery or even heart transplantation are required[180]. Therefore, the development of new treatments to repair or regenerate the damaged myocardium continue to be of great interest. Initial studies focused on cell-based therapies involving the injection of cardiac or non-cardiac cells into the infarct area with the aim of replacing the lost cardiomyocytes and improving heart function after MI[181,182]. However, cell-based therapies alone are ineffective with poor survival, engraftment and differentiation potential and require complementary approaches to make the cardiac microenvironment conducive to tissue restoration and regeneration[183–185]. Intracardiac injection of different types of adult stem and progenitor cells, dead cells or a chemical inducer of the innate immune response all improved heart function, attributed to a beneficial acute immune response[186]. Therefore, enabling early inflammation combined with a balanced innate and adaptive immune response seems to be crucial for optimal repair and potential regeneration of the infarcted heart, whereas broad immunosuppression has adverse effects[187,188]. As a result, a time-dependent, drug-mediated manipulation of the lymphatic response could help modulate the inflammatory content in the myocardium and promote both myocardial survival and restoration. Proof of principle is provided by the aforementioned studies targeting recombinant VEGFC-C156S to invoke increased lymphangiogenesis and improved outcome after MI[38,39,152]. However, VEGFC and its isoforms are not optimal drugs, given their very short half-life in serum[55].

Currently, pre-clinical studies are investigating lymphangiogenesis as a potential drug target for immunomodulation after MI[179,189–191]. Most studies are focusing on the VEGFR-3 signalling pathway, because the induction of this pathway has been shown to promote lymphangiogenesis and lead to better outcomes after MI in experimental animal models[38,76,152,175]. A phase I/IIa clinical trial assessing the efficacy and safety of intramyocardial adenovirus vector-mediated VEGF-$D^{\Delta N \Delta C}$ gene therapy in patients with refractory angina showed promising results, with significant improvement of myocardial blood flow compared with placebo[189]. However, this positive finding is compromised by the need for repeat invasive administration of the gene therapy. Therefore, exploring additional pathways that promote a cardiac lymphatic response is important. For instance, the epicardium-specific peptide adrenomedullin (AM encoded by *Adm*) has cardioprotective functions through a beneficial effect on the cardiac lymphatic permeability and lymphangiogenesis. In a pilot clinical study, intravenous injection of AM in patients with acute myocardial infarction resulted in significantly improved cardiac structure and function, as evaluated by MRI, compared with baseline[190]. Additionally, upregulation of *Adm* in mice results in reduced oedema, dilated cardiac lymphatic vessels and improved cardiac function after MI[179]. AM regulates the gap-junction protein Connexin-43 in cardiac LECs, promoting their coupling and potentially increasing the permeability of lymphatics[179]. This highlights that pre-clinical research focusing on inducing cardiac lymphatic growth by lymphangiogenesis, as well as enhancing their functional maturation has therapeutic potential.

3.7. Cardiac regeneration after zebrafish and neonatal mouse heart injury

3.7.1. *Zebrafish cardiac regeneration*

Zebrafish can fully regenerate their heart after apical resection without scar formation[192], or *via* a temporary scar following cryoinjury[193]. During the first week after apical resection, *vegfc* expression increases transiently in the adult zebrafish, with no signs of cardiac lymphangiogenesis[131,132]. By contrast, elevated *vegfc* expression after cryoinjury last for weeks and is accompanied by enlargement and migration of lymphatic vessels into the wound site[54,131,132]. Similar to the mammalian immune response, macrophages and neutrophils migrate to the injured site during the first week after cryoinjury in zebrafish[131]. The immune response and debris are *cleared via* lymphatics from the wound area[131]. Moreover, disruption of the Vegfr3/Vegfc pathway blocks the lymphatic response to cryoinjury, which results in inefficient immune cell clearance and increased scar formation[54,131,132]. Surprisingly, the cardiac regenerative capacity is not completely lost in the absence of lymphatics, as a subset of zebrafish can fully recover after cryoinjury[131,132]. Nevertheless, data from RNA sequencing and immunostaining suggest that lack of lymphatic response shifts the cardiac microenvironment from pro-regenerative to pro-inflammatory after cryoinjury in zebrafish, thereby affecting cardiac healing[131,132].

3.7.2. *Neonatal mouse cardiac regeneration*

In contrast to adult mammalian hearts, which are incapable of functional recovery after heart injury, neonatal mammalian hearts have an evolutionary conserved regenerative capacity[149,194–197]. The widely accepted notion is that in mice, the heart fully regenerates after LAD ligation at P1, whereas the same injury at P7 leads to fibrotic scarring[198–200]. The cardiac regeneration appears to be restricted to P1, since injury at P2 resulted in a permanent scar and subsequent cardiac function impairment[201]. Of note, anecdotal

evidence from clinical case reports suggests that cardiac regeneration occurs in neonatal patients with MI caused by congenital heart disease[202,203]. Observed differences in the degree and time-window of regeneration could be attributed to the intensity injury and/or genetic differences, as in adult mice the healing response varies vastly depending on the genetic background[204].

There are several key physiological differences between neonatal and adult mice that could contribute to cardiac regeneration[205]. During the first postnatal week, cardiomyocytes undergo rapid proliferation[205–207] and a significant portion of the coronary vasculature arises *de novo*[208]. Afterwards, cardiomyocytes become quiescent and remain so throughout adulthood[205–207]. Also, the neonatal immune system is immature, since both the adaptive and innate immune response are quantitatively and qualitatively different compared to adults[209]. At the early postnatal stages macrophages found in normal hearts are primarily tissue resident ($CCR2^-$) that originate from embryonic sources and are maintained through local proliferation[140,142,205]. By contrast, circulating monocytes and monocyte-derived macrophages ($CCR2^+$) contribute little to the cardiac monocyte-macrophage population at these stages[140,142]. In response to cardiac injury in neonatal hearts, the number of tissue resident macrophages expands without additional infiltration of monocytes[140]. Interestingly, general depletion of macrophages with the use of clodronate liposome treatment after MI at P1 inhibits cardiac regeneration and favours fibrotic scar formation with significantly depressed cardiac function[210]. This lack of regeneration is attributed to impaired angiogenesis[210], which is consistent with growing evidence supporting direct and indirect macrophage contributions to angiogenesis[211]. Although clodronate liposomes can target macrophages[212], they also target phagocytic

cells in general, such as dendritic cells, consequently these results need to be interpreted with caution. Moreover, different macrophage deletion strategies can produce contrasting effects[213]. The essential function of macrophages in heart regeneration of neonatal mice[210] together with the immunomodulatory role of lymphatic vessels in the adult mouse hearts[76] highlight an interesting area for further study as to how the cardiac lymphatics respond in a regenerative setting in mammals and to what extent cardiac lymphatics interact with macrophages in neonatal hearts after MI.

3.8. Hypothesis and aims

The major aims of this thesis were to fully investigate the response of cardiac lymphatic vessels and their interaction with macrophages during the regenerative P1 and fibrotic P7 neonatal stages after MI. Based on the knowledge that cardiac macrophages are essential for myocardial regeneration after P1 MI[210], and that cardiac lymphatic vessels clear macrophages from the heart to the mediastinal lymph nodes after adult MI[38,76], the following hypotheses were established:

1) Cardiac lymphatics are not fully mature until late in postnatal life.

2) Cardiac lymphatics respond differently after MI at P1 compared to P7.

3) Cardiac lymphatics function differently after MI at P1 compared to P7.

4) Cardiac macrophages are cleared from the heart to the mediastinal lymph nodes with different efficiency after MI at P1 compared to P7.

To test the above hypotheses, the following aims were established:

1) Characterise the spatiotemporal development and maturation of cardiac lymphatic vessels from birth to adulthood in two genetic backgrounds.

2) Characterise the lymphangiogenic response of cardiac lymphatic vessels after MI at P1 and P7 by using 3D light-sheet and confocal microscopy.

3) Characterise the efficiency of cardiac lymphatic function after MI at P1 and P7 by performing adoptive cell transfer and MRI.

4) Characterise the response of macrophages after MI at P1 and P7, as well as identify potential molecular interaction with LECs, by generating and analysing scRNA-Seq data.

5) Characterise the lineage of *Lyve1*^{Cre} in the heart and assess potential applications of this line for the study of postnatal cardiac lymphatics.

4. Materials and methods

4.1. Mice

4.1.1. *Strains*

The following mouse strains were used for these studies: *Lyve1*$^{-/-}$ [78], *hCd68-GFP* [214], *Prox1*$^{loxP/+}$ [215], *Lyve1*$^{EGFP\text{-}hCre/+}$ [216], *Prox1-tdTomato* [217], *Cx40*$^{EGFP/+}$ [218], *Vegfr3*$^{LacZ/+}$ [219]. Breeding was carried out using only *Cre*$^{+}$ males for all Cre strains. Mice were cared for and housed by Oxford University Biomedical Services. For experiments where wild type mice were required C57BL/6 or CD1 (Charles River Laboratories) when indicated, strains were used. All animal experiments were carried out according to UK Home Office project licences PPL PC013B246 and PDDE89C84 and were compliant with the UK Animals (Scientific Procedures) Act 1986.

4.1.2. *Timed mating*

To generate embryos, females were paired with male studs and were checked for vaginal plugs each morning. The day the vaginal plug was observed was designated as embryonic day 0.5 (E0.5).

4.1.3. *Embryo heart dissection*

Embryos were harvested from pregnant females at the required embryonic stage. The female was euthanised by cervical dislocation and the uterine horns were dissected from the abdominal cavity. Embryos were extracted from the uterine horns, placed in ice cold Phosphate-buffered saline (PBS) (Sigma) and the amniotic sac was removed. Hearts were collected from embryos for subsequent experimental analysis.

4.1.4. *Neonatal heart dissection*

Neonatal mice were sacrificed by schedule 1 cervical dislocation and the heart was removed. Hearts collected for immunostaining were washed in ice cold PBS prior to fixation. Hearts for flow cytometry were washed in ice cold Hank's Balanced Salt Solution (HBSS; Life Technologies) prior to tissue digestion. Hearts for RNA extraction were immediately placed in a cryo-tube (Nunc Thermo Scientific) and the cryo-tube was submerged in liquid nitrogen.

4.2. Neonatal myocardial infarction model

Myocardial infarction surgery was performed by the research technicians Mala Rohling and Carla De Villiers as previously described[220]. At P1 and P7 the litters were removed from the mother and placed in a warm incubator at 35°C. General anaesthesia was induced with 4 % isoflurane inhalation in oxygen (1 L/min) for 15 sec. Once unconscious, cardiorespiratory arrest was induced by immersion in ice for 1-2 min. The incision site was cleaned with Hibiscrub and a sterile field constructed with drapes. The skin was cut using surgical scissors in a horizontal incision across the left mid-thorax. Sharp dissecting forceps were used for thoracotomy, close to the costochondral junction, in approximately the 3rd intercostal space. This space was widened using blunt forceps. The heart was manipulated out of the thoracic cavity by applying gentle pressure on the thorax and diaphragm. LAD artery ligation was induced by passing and tying a 7.0 prolene suture through the anterior wall of the left ventricle. The sham control procedure involved thoracotomy surgery, heart visualisation and suture placement, but no ligature. The ribs and skin were then closed in layers with a 7.0 prolene suture. The pup was then warmed under an infrared lamp, which led to gradual return of circulation and breathing. When respiration returned, oxygen was administered via nose cone until respiration was regular. The pup was returned to the

warmed chamber (35°C) with the other littermates. After surgery was completed on all pups, and before returning the group to the mother, the animals were covered with faeces from their cage homogenized in warmed water to mask surgical smells and reduce cannibalization.

4.3. Molecular methods

4.3.1. *DNA extraction*

Ear biopsies from adult mice and tissue from embryos/neonates were collected for genotyping. The genomic DNA was extracted and amplified using the REDExtract-N-AmpTM Tissue PCR Kit Protocol (Merck). The tissue was incubated in a mix of 100 µL Extraction Solution and 25 µL Tissue Preparation Solution for 10 min at room temperature, followed by a 5 min incubate at 95°C. Immediately, 100 µL Neutralization Solution were added and the mix was vortexed.

4.3.2. *Polymerase chain reaction (PCR)*

Extracted DNA was used for genotyping using PCR. The sequence of the primers used are displayed in Table 4.1. The following reagents were used to set up the PCR reactions: 10 µL REDExtraction-N-Amp PCR Reaction Mix, 0.5 µM of each primer, 4 µL tissue extract and Milli-Q water until total reaction volume of 20 µL. Thermal cycling was carried out in a Veriti™ 96-well thermal cycler (Applied Biosystems) using the programs shown in Table 4.2 and Table 4.3. A positive control sample of known genotype was included for each genotype being tested.

Table 4.1 PCR primers for genotyping

Gene (size)	Primer 1	Primer 2	Primer 3	Primer 4
Vegfr3$^{LacZ/+}$ (500 bp)	TCACTCCCAGCC TAGAGCTGC	CGAGGCAGAGC CACAGGCGC	GACGACAGTAT CGGCCTCAG	
GFP (211 bp)	CAGCCCTCTCTT GGAAAGGAGG	TTCTCGGCTCTG TGAATGACA		
Prox1$^{loxP/+}$ (220 bp)	CAGCCCTTTTGT TCTGTTGGC CAG	GCAGATGCTGTC CCTACCGTCC		
Lyve-1$^{EGFP-hCre/+}$ (210 mutant, 425 control)	TGAGCCACAGA AGGGTTAGG	GAGGATGGGGA CTGAAACTG	TGCCACCTGAAG TCTCTCCT	
Prox1-tdTomato (420 mutant, 324 control)	CTAGGCCACAG AATTGAAAGATC T	GTAGGTGGAAA TTCTAGCATCAT CC	CTTCACGTACGC CTTGGAC	TGTGCCATAAATC CCAGAGC
Lyve1$^{-/-}$ (381 mutant, 310 control)	TCACTCCTATTG AACAGTACC	TCATTCTCAGTA TTGTTTTGCC	CGTGAAAAGGT GAGGTTG	

Table 4.2 PCR thermal cycling program for general genotyping

Stage	Temperature (°C)	Duration (min.sec)	Cycles
1	94	3.00	1
2	94	0.15	35
	63	1.00	
	72	0.20	

3	72	5.00	1
4	4	-	-

Table 4.3 PCR thermal cycling program for Lyve1-KO genotyping

Stage	Temperature (°C)	Duration (min.sec)	Cycles
1	94	3.00	1
2	94	0.30	40
	58	1.50	
	72	0.30	
3	72	7.00	1
4	4	-	-

4.3.3. *Agarose gel electrophoresis*

Following PCR amplification, the DNA was separated on 1.5 % agarose gel. 1.5 g of agarose (Sigma Aldrich, UK) was dissolved in 100 mL of TBE buffer by heating the mix in a microwave. For UV visualisation of DNA 5 µL of GelRed (VWR) were added to the agarose gel before it was poured into moulds and allowed to set. An electric potential of 160 V was passed through the gel for 35 min to allow separation of bands to distinguish between genotypes. Gels were visualised in a UV box.

4.3.4. *RNA extraction from tissue*

RNA was isolated from snap frozen tissue samples using TRIzol reagent (Thermo Fisher Scientific). Tissue was homogenized in 750 µL of TRIzol solution using a manual homogenizer and a 21G sterile needle (Becton Dickinson). After being incubated for 5 min at room temperature, 200 µL of chloroform were added to the samples. Samples were then mixed by hand and incubated for 15 min at room temperature. Following incubation,

samples were centrifuged at 11,000 rpm for 15 min at 4°C, which causes phase separation. The organic phase contains the proteins, the interface contains DNA, and the aqueous phase contains RNA. The top aqueous layer was transferred into a 1.5 mL tube, while the organic layer was discarded. To precipitate RNA, 500 µL isopropanol were added to the samples which were then mixed by hand and incubated at 4°C overnight. Following the incubation, the samples were centrifuged at 11,000 rpm for 10 min, which produced an RNA containing pellet. The pellet was washed with 1 mL of 75 % ethanol (EtOH) before spinning at 9,000 rpm for 5 min at 4°C. The pellet was air-dried for 10 min and resuspended in diethyl pyrocarbonate (DEPC)-treated water. A Nanodrop2000 (Thermo Fisher Scientific) was used to measure RNA quality and concentration.

4.3.5. *Complementary DNA (cDNA) synthesis*

cDNA was synthesized from extracted RNA for use in real-time quantitative PCR (qRT-PCR). Reactions were prepared in RNase free 0.6 mL tubes (Thermo Fisher Scientific) using the following reagents: 1 µg RNA made up to a volume of 8.5 µL with DEPC-water, 0.5µL of random primers (20 µg/mL; Promega), 1 µL dNTPs (from 10 mM, GE Healthcare), 2 µL MgCl2 (25 mM, Thermo Scientific), 2 µL Dithiothreitol (DTT, 0.1 M, Life Technologies), 1 µL RNasin® plus RNase inhibitor (Promega), 4 µL 5X FS Buffer (Life Technologies) and 1 µL of SuperScript® III Reverse Transcriptase (Life Technologies). A Veriti™ 96-well thermal cycler (Applied Biosystems) was used to run the reaction at 25°C for 10 min, 42°C for 50 min and 70°C for 15 min, before cooling to 4°C. Following cDNA synthesis samples were diluted to 4 ng/µL in DEPC treated-water and stored at 4°C prior (short-term) to use in qRT-PCR experiments.

4.3.6. ***Real-time quantitative PCR***

Relative mRNA expression levels from genes of interest were quantified using qRT-PCR. Primer sequences are displayed in Table 4.4. MicroAmp^{TM} Fast Optical 96-well 0.1 mL reaction plates (Thermo Fisher Scientific), were used to set up reactions which were composed of the following reagents: 8 ng cDNA, 13 µL Fast SYBRGreen Master Mix (Thermo Fisher Scientific), 6.5 µL DEPC treated-water, and 0.5 µM of each primer. All samples were run in triplicate and a no-cDNA negative control well was included for each gene analysed. Reactions were run on a ViiA™ 7 Real-Time PCR System (Thermo Fisher Scientific) with thermal cycles of 95°C for 15 min, 40 cycles of 95°C for 15 seconds and 60°C for 1 minute. Melt curves were included to confirm that no unspecific amplification products such as primer-dimers were produced with each primer sets used.

Cycle Threshold (Ct) values were obtained and exported to Microsoft Excel for analysis. The comparative cycle threshold method was used to calculate relative normalised gene expression (2^ΔΔCt)[221]. First, the mean Ct of the technical triplicates for each condition and gene was calculated. Then, the average Ct of all samples in the control group (i.e., sham for LAD surgery or P0 for development) for each gene was determined. The relative difference (ΔCt) between the average Ct for the control group and the mean Ct for individual sample within each target was calculated. The relative quantities (2^ΔCt) were calculated from the ΔCt. For each biological combination, a normalisation factor was determined from the mean of the associated housekeeping genes' 2^ΔCt. The housekeeping genes used here were *Rpl4* and *Eef1e1*[222]. The 2^ΔΔCt for each target gene was then calculated per sample by dividing the 2^ΔCt by the normalization factor. The average 2^ΔΔCt for each biological

group was then calculated using the mean. Statistical analysis and visualisation of qPCR data was done using the ΔΔCt (i.e., Log2(Fold Change)) values.

Table 4.4 Primers for qRT-PCR

Gene	Forward	Reverse
Eef1e1	TCCAGTAAAGAAGACACCCAGA	GACAAAACCAGCGAGACACA
Rpl44	GCCGCTGGTGGTTGAAGATAA	CGTCGGTTTCTCATTTTTGCCC
F4-80	CTTTGGCTATGGGCTTCCAGTCC	GCAAGGAGGACAGAGTTTATCGTG
Cd68	ACTTCGGGCCATGTTTCTCT	GCTGGTAGGTTGATTGTCGT
Cx3cr1	CCATCTGCTCAGGACCTCAC	CACCAGACCGAACGTGAAGA
Ccr2	AAGGAGCCATACCTGTAAATGC	TGTGGTGAATCCAATGCCCT
Ccr7	TCATTGCCGTGGTGGTAGTCTTCA	ATGTTGAGCTGCTTGCTGGTTTCG
Ccl21	TGAGCTATGTGCAAACCCTGAGGA	TGAGGGCTGTGTCTGTTCAGTTCT
Cd206	CAGGTGTGGGCTCAGGTAGT	TGTGGTGAGCTGAAAGGTGA
Cd86	CTTACGGAAGCACCCATGAT	CCCATTGAAATAAGCTTGCG
Cd80	GGCAAGGCAGCAATACCTTA	CTCTTTGTGCTGCTGATTCG
Ccl24	AATTCCAGAAAACCGAGTGG	TCTTATGGCCCTTCTTGGTG
Lyve1	GGCTTTGAGACTTGCAGCTATG	GCAGGAGTTAACCCAGGTG
Vegfr3	CCATCGAGAGTCTGGACAGC	CCGGGATGGTGGTCACATAG
Nrp2	GCAGGTGAGGATTTTAAAGTGGA	TTTGCCAGATGAGGGGTCAC
Prox1	GAAGGGCTATCACCCAATCA	TGAACCACTTGATGAGCTGC
Has1	GAGGCCTGGTACAACCAAAAG	CTCAACCAACGAAGGAAGGAG
Has2	GAGCACCAAGGTTCTGCTTC	CTCTCCATACGGCGAGAGTC
Has3	TGGACCCAGCCTGCACCATTG	CCCGCTCCACGTTGAAAGCCAT
Il10	GGTTGCCAAGCCTTATCGGA	ACCTGCTCCACTGCCTTGCT

Tnf-α	CTGTAGCCCACGTCGTAGC	TTGAGATCCATGCCGTTG
Il6	GGTATTGCTTGGGATCCACACT	CACTCCTTCTGTGACTCCAGCTT
Il1b	AAAGAATCTATACCTGTCCTGTGTAATGAAA	GGTATTGCTTGGGATCCACACT

4.4. Staining

4.4.1. *Whole-mount X-Gal staining*

Following extraction, hearts were washed in ice cold PBS and then fixed in 5-bromo-4-chloro-3-indolyl-β-D-galactosidase (X-Gal) fixation solution (Table 4.5) for 6 hours at room temperature. Then, hearts were washed in X-Gal buffer and incubated in X-Gal staining solution (Table 4.5) overnight at 37°C. The following day fresh X-Gal staining solution was added and left overnight at 37°C. Once staining had developed, hearts were washed in X-Gal buffer and post-fixed in 4 % PFA for 30 min. Finally, hearts were washed in PBS and imaged using a Zeiss stereomicroscope. Analysis of vessels and branching calculations were performed using AngioTool software (Figure 4.1)[223].

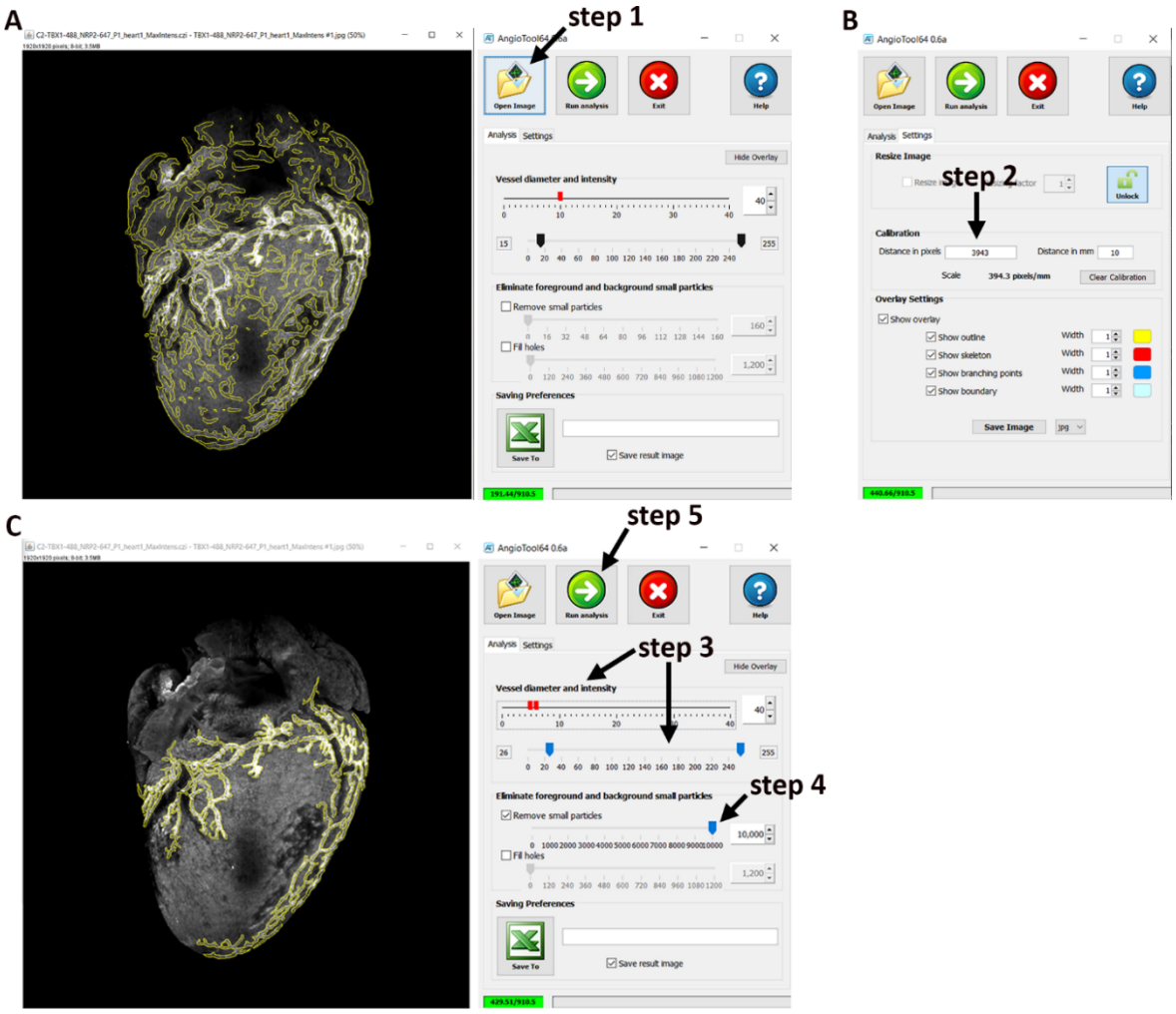

Figure 4.1 Using AngioTool to characterise the cardiac lymphatic vasculature.

The first step requires opening the image (A). In the "Settings" tab, insert the correct scale value in pixels per mm (B). For steps 3 and 4, use the preview window as a guide to define the vessel diameter and intensity, and remove small particles (C). In step 5, hit the "Run analysis" button, which generates an Excel file and a JPEG image of the analysis (C).

Table 4.5 Solutions

Solution	Ingredients
X-gal buffer	5mM EGTA, 0.04 % w/v Cl_2Mg, 0.02 % v/v NP40, 0.01 % w/v Deoxycholate in PBS.
X-gal fixation	1 % v/v Formaldehyde (37 % stock), 0.2 % v/v Glutaraldehyde (25 % stock) in X-gal buffer.

X-gal staining	5mM $K_3Fe(CN)_6$, 5mM $K_4Fe(CN)_6$, 1 mg/mL X-Gal substrate in X-gal buffer.

4.4.2. *Immunostaining of cryosections*

Whole embryo and neonatal hearts were fixed in 4 % PFA overnight at 4°C. Following fixation, samples were washed three times for 10 min in PBS and then transferred to 30 % sucrose and PBS overnight at 4°C. Then, the samples were equilibrated in a 1:1 solution of OCT and 30 % sucrose for 1 hour in 4°C. After equilibration the hearts were embedded in 100 % OCT and frozen at -80°C. 20-25 µm slices were cut using a cryostat and transferred onto Superfrost Plus slides (VMR). Slides were dried on a slide dryer for 15 min before being rinsed with PBS. Then, sections underwent permeabilization with 0.5 % Triton X-100 (Sigma, UK) for 10 min, followed by two rinses in PBS for 5min. Then, sections were blocked in blocking solution, composed of 10 % serum, 4 % bovine serum albumin (BSA) and 0.2 % Triton X-100, for 1 hour. The blocking serum was from the same species in which the secondary antibodies were made from. Blocking was followed by a 4°C overnight incubation in primary antibody, which was diluted in blocking solution. A list of primary antibodies and the dilutions used are included in Table 4.6. For each primary antibody used, one section was incubated without primary antibody as a secondary antibody alone control. Following primary antibody incubation, sections were washed several times with 0.1 % Triton X-100 and incubated with Alexa Fluor-conjugated secondary antibodies for 1 hour at room temperature in the dark. All secondary antibodies were diluted in PBS; a list of the secondary antibodies used is included in Table 4.7. Following incubation in secondary antibody, the slides were washed several times in 0.1 % Triton X-100, with DAPI included in the final 15 min wash. A small amount of 50:50 Glycerol/PBS was then added

to the slides and a 22x50 mm coverslip (Fisherbrand) was placed on top and sealed with nail varnish. Immunofluorescent staining was imaged using a Zeiss LSM780, Zeiss LSM880, Zeiss LSM980 or Leica confocal microscope. Z-stack and tiling functions were used when required. Images were processed using ImageJ software[224,225].

Table 4.6 List of primary antibodies

Primary antibody	**Company/Catalog number**	**Tissue expression/marker**	**Dilution**	**Species raised in**
PROX1	R&D Systems #AF2727	Lymphatic endothelium and cardiomyocytes	1:200	Goat
VEGFR3	R&D systems #AF743	Lymphatic endothelium	1:50	Goat
LYVE1	Angiobio #11-034	Lymphatic endothelium, tissue-resident macrophages, and endocardium	1:400	Rabbit
PODOPLANIN	Fitzgerald #10R-P155A	Lymphatic endothelium and epicardium	1:200	Hamster
NEUROPILIN2	R&D systems #AF567	Lymphatic endothelium and sympathetic axons	1:200	Goat

VE-CADHERIN	R&D systems #AF1002	Adherens junctions	1:400	Goat
ENDOMUCIN	Santa Cruz Biotechnology #SC-53941	Venous endothelium and capillaries	1:200	Rat
PECAM1	BD Pharmingen #553370	Endothelium	1:200	Rat
CD68	Bio-Rad #MCA1957	Macrophages	1:400	Rat
CD206	R&D systems #AF2535	Tissue-resident macrophages	1:200	Goat
TER119	BD Biosciences #550565	Erythrocytes	1:200	Rat

Table 4.7 List of secondary antibodies

Secondary antibody	**Supplier**	**Dilution**
AlexaFluor goat α-rabbit 405	Invitrogen	1 in 500
AlexaFluor donkey α-rabbit 405	Abcam	1 in 500
AlexaFluor donkey α-rat 488	Invitrogen	1 in 500
AlexaFluor donkey α-goat 488	Invitrogen	1 in 500
AlexaFluor donkey α-goat 555	Abcam	1 in 500
AlexaFluor goat α-rat 594	Invitrogen	1 in 500
AlexaFluor donkey α-goat 647	Invitrogen	1 in 500
AlexaFluor goat α-hamster 647	Invitrogen	1 in 500
AlexaFluor donkey α-rabbit 647	Invitrogen	1 in 500

4.4.3. *Immunostaining of embryonic and neonatal hearts*

Whole embryonic and neonatal hearts were permeabilised for 1 hour in 4 % Triton X-100 and subsequently blocked in blocking solution (2 % BSA, 10 % serum, 0.2 % Triton X-100 in PBS) overnight at 4^{o}C. The blocking serum was from the same species in which the secondary antibodies were made from. Samples were incubated with primary antibodies (Table 4.6) diluted in blocking solution for 48 hours at 4°C, then washed ten times for 30 min in PBS. Then, samples were incubated with secondary antibodies (Table 4.7) diluted in PBS overnight at 4°C in the dark. The hearts were washed five times for 15 min in PBS, with DAPI staining included in the last 30 min wash. Immunofluorescent staining was imaged using Zeiss LSM780, Zeiss LSM880, Zeiss LSM980 or Leica confocal microscope, or a Zeiss Z.1 light-sheet microscope. Z-stack and tiling functions were employed to obtain maximum intensity Z-projections of whole hearts. Images were processed using Imaris, Arivis Vision4D and ImageJ software[224,225].

For confocal imaging, samples were mounted on glass slides (VWR) covered in 3-4 layers of electrical tape with windows cut into the tape to create wells. The samples were covered with 50:50 Glycerol/PBS and a coverslip (Fisherbrand) was placed on top of the slides.

For light-sheet imaging, embryonic hearts and neonatal hearts were mounted using 1 mL syringes. A gel solution of 1.5 % low melting point agarose in TBE was prepared and the sample was positioned inside the gel. The tip of the syringe was cut off to create an even cylinder and the gel solution with the sample was pumped in using the plunger. After the gel polymerized, the sample was pushed out and was ready for imaging (Figure 4.2).

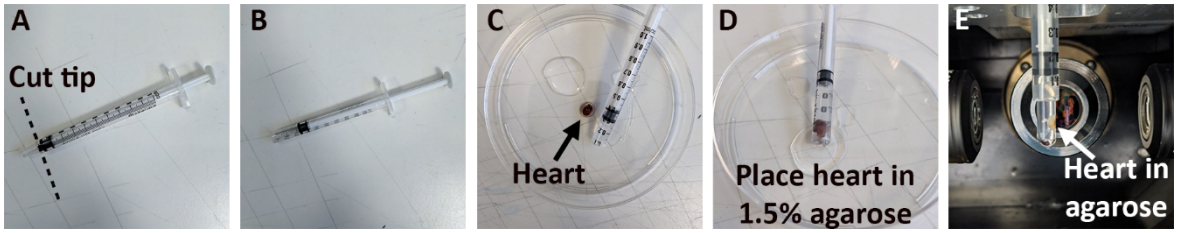

Figure 4.2 Preparing the heart for light-sheet imaging.

The heart is mounted in a 1 mL syringe, with its tip cut off (A-B). A small amount of 1.5 % (w/v) low melting point agarose is placed in the syringe, together with the heart (C-D). After the agarose is fully polymerised, the syringe containing the mounted the heart is placed inside the Z.1 light-sheet chamber and the agarose-containing heart is pushed out (E). The heart is now ready to be imaged.

4.4.4. *3, 3'-diaminobenzidine (DAB) whole-mount staining*

Hearts were fixed in 4 % PFA overnight at 4°C and then washed in PBS. Staining was performed following the VECTASTAIN® ABC HRP Kit (Peroxidase, Goat IgG, and Rat IgG) protocol. Hearts were bleached in 5 % H_2O_2 and PBS (Hydrogen peroxide) for 6 hours until they became pale. This was followed by several washes in PBST (0.1 %Tween-20 (Sigma) in PBS) and two washed in PBTD (0.1 % Tween-20, 1 % DMSO (Sigma) in PBS). Then, the samples were transferred into blocking solution (3 drops of stock blocking serum in 10 mL PBTD) for overnight incubation at 4°C. The preferred blocking serum is from the same species in which the biotinylated secondary antibody is made from. Then, hearts were incubated in primary antibody diluted in blocking solution (Table 4.6) for 48 hours at 4°C. Following this, hearts were washed for 10 times for 30 min in PBTD before overnight incubation at 4°C with the biotinylated secondary antibody (1 drop of biotinylated stock antibody to 10 mL of blocking solution). The following day hearts were washed 7 times for 15 min with PBTD before being placed in Vector ABC Reagent (Avidin:Biotin:Peroxidase complex) for 1 hour. More washes in PBTD were performed before equilibration with DAB developing buffer (from the DAB Peroxidase Substrate Kit, Vector labs) for 15 min. DAB and H_2O_2 were added to the developing buffer to develop the staining. Optimal development

time was determined by for each condition. Once staining had developed hearts were washed in H_2O and were then imaged using a Zeiss stereomicroscope.

4.4.5. *High-Resolution Episcopic Microscopy (HREM)*

HREM was performed in collaboration with Dr Jacinta Kalisch-Smith (DPAG, University of Oxford). E15.5 embryos were fixed overnight in 4 % paraformaldehyde at 4°C and were dissected for heart-lung complexes. The heart-lung complexes were fixed in 4 % PFA and dehydrated by performing serial washes, each for 1 hours, in the following dilutions of methanol: 10 %, 20 %, 30 %, 40 %, 50 %, 60 %, 70 %, 80 %, 90 %, 95 % and 100 %. The samples were incubated in 50:50 mixtures of methanol/JB4 resin (Polysciences, 00226-1, GMBH, Germany) overnight. The samples were incubated in JB4 resin for 1 hour and transferred to fresh resin for 3 days' incubation. The samples were embedded individually in JB4 according to manufacturer's instructions and were cut at 3 µm sections on an optical HREM (OHREM) microscope (Indigo scientific) with images taken using a Jenoptik Gryphax camera. Image stacks were processed into cubic data and reduced to either 10 % or 50 % for 3D modelling using the Amira software package 2019.4 (Thermo Fisher Scientific). Greyscale images were imported into MD DICOM viewer version 9.0.2 (Pixmeo), or Horos 3.3.6 (https://horosproject.org) in a 50 % stack, inverted to black-white, and rendered into 3D.

4.5. Flow cytometry

4.5.1. *Neonatal cardiac cells isolation*

The digestion of hearts was based on a previously published protocol[226]. From the isolated hearts the atria were removed, and the ventricles were cut in half. Blood was removed from the ventricular chambers. The ventricles were minced using a sterile scalpel (Swann-

Morton) before being added to a 15 mL tube containing 5 mL of Hank's Balanced Salt Solution (Life Technologies) and 500 units/mL of Collagenase II (Worthington). The tubes were placed in an orbital incubator at 37°C, moving at 190 RPM. Plastic transfer pipettes were used to break-up the tissue suspension every 10 min during the 30 min digestion within the orbital incubator. Once digested, the tissue suspension was passed through a 40 µm cell strainer attached to a 50 mL tube. The tubes were then centrifuged at 350 *g* for 10 min at 4°C and the supernatant was discarded, leaving a pellet. The pellet was resuspended in 5 mL 1X red blood cell (RBC) lysis buffer (BioLegend) and was left on room temperature for 10 min. The tubes were then centrifuged again at 350 *g* for 5 min at 4°C and the supernatant was discarded, leaving a pellet. The cell pellet was resuspended in 5 mL 2 % FBS/PBS. The tubes were centrifuged again at 350 *g* for 5 min at 4°C and the supernatant was discarded, leaving a pellet. The pellet containing the cardiac cells was resuspended in 200 µL 2 % FBS/PBS.

For single cell RNA sequencing (scRNA-seq), the pellet containing the cardiac cells was resuspended in 200 µL 2 % FBS/PBS and transferred to Falcon® 5 mL Round Bottom Polystyrene Test Tube, with a 35 µm nylon mesh Cell Strainer Snap Cap prior to Fluorescence activated cell sorting (FACS) of live cells using 7AAD.

4.5.2. *Neonatal splenocytes isolation*

Isolated spleens were placed on a 70 µm cell strainer attached to a 15 mL tube with 1X RBC lysis buffer (BioLegend) and were homogenized with a 1 mL syringe plunge. After homogenized, the cells were incubated for 10 min at room temperature in the lysis buffer. The tubes were centrifuged at 350 *g* for 5 min at 4°C and the supernatant was discarded

leaving a pellet. The pellet containing the splenocytes was then resuspended in 200 µL 2 % FBS/PBS and transferred to Falcon® 5 mL Round Bottom Polystyrene Test Tube, with a 35 µm nylon mesh Cell Strainer Snap Cap prior to FACS of live cells for Single-Cell RNA sequencing.

4.5.3. *Neonatal blood isolation*

The neonates were decapitated, and the blood was collected through a glass capillary that had previously been embedded in EDTA to prevent blood forming clots. The blood (approximately 100 µL/mouse) was added in 1 mL of 1X RBC lysis buffer and incubated for 10 min at room temperature. Then, the samples were centrifuged at 350 *g* for 5 min at 4°C and the supernatant was discarded, leaving a pellet. A second incubation with 1 mL of 1X RBC lysis buffer for 10 min at room temperature was needed for complete haemolysis. Then the samples were centrifuged at 350 *g* for 5 min at 4°C and the supernatant was discarded, leaving a pellet. The pellet containing the haematopoietic cells was resuspended in 200 µL 2 % FBS/PBS and transferred to Falcon® 5 mL Round Bottom Polystyrene Test Tube, with a 35 µm nylon mesh Cell Strainer Snap Cap prior to FACS of live cells for Single-Cell RNA sequencing.

4.5.4. *Neonatal bone marrow isolation*

The bone marrow was extracted as previously described[227]. Both hind legs were cut off above the pelvic-hip joint with sharp sterile scissors. The tibia was then cut off from the hind leg below the knee joint with sharp sterile scissors. The muscles and resident tissues surrounding the femur were removed and both ends of the femurs were cut. An insulin syringe was used to flush the bone marrow with HBSS out onto a sterile 1.5 mL Eppendorf until the flow through turned white. The tubes were then centrifuged at 350 *g* for 10 min

at 4°C and the supernatant was discarded, leaving a pellet. The pellet was resuspended in 1 mL 1X RBC lysis buffer and was left on room temperature for 10 min. The tubes were then centrifuged again at 350 *g* for 5 min at 4°C and the supernatant was discarded, leaving a pellet. The cell pellet was resuspended in 1 mL 2 % FBS/PBS. The tubes were centrifuged again at 350 *g* for 5 min at 4°C and the supernatant was discarded, leaving a pellet. The pellet containing the bone marrow cells was then resuspended in 200 µL 2 % FBS/PBS and transferred to Falcon® 5 mL Round Bottom Polystyrene Test Tube, with a 35 µm nylon mesh Cell Strainer Snap Cap prior to FACS of live cells for Single-Cell RNA sequencing.

4.5.5. ***Antibody staining***

150 µL of the cell suspension were taken for antibody staining, while 25 µL were kept for full negative control and 25 µL for 7AAD only staining. To each cell suspension 2 % FBS/PBS were added to a final volume of 200 µL. For the antibody staining, 2.5 µL Fc receptor blocking reagent (Miltenyi Biotech) were added to the suspension and the cell suspension was left on ice for 5 min. Antibodies were then added at the dilutions shown in Table 4.6 and the tubes were incubated at room temperature in the dark for 30 min. 1 mL 2 % FBS/PBS was added to each tube and the samples were centrifuged at 350 *g* for 5 min at 4°C to give a cell pellet. The pellet containing the stained cells was then resuspended in 500 µL 2 % FBS/PBS and transferred to Falcon® 5 mL Round Bottom Polystyrene Test Tube, with a 35µm nylon mesh Cell Strainer Snap Cap. Just before flow cytometry, 5 µL 7AAD (1 % final concentration) viability staining solution (eBioscience) were added to allow exclusion of dead cells. Flow cytometry quantification and FACS were performed on a FACSAria III cell sorter or a LSRFortessa X20 Analyzer (BD Biosciences). An appropriate gating strategy had previously been set up in pilot studies. Each experiment included

negative and 7AAD only controls. Fluorescence compensation controls were used to correct for spectral overlap. All FACS for Single-Cell RNA sequencing experiments took place at the Oxford Wellcome Centre for Human Genetics Flow Cytometry Facility.

4.5.6. *Sample analysis*

Flow cytometry data obtained from the FACSAria III cell sorter and LSRFortessa X20 Analyzer were exported to FlowJo software for further analysis.

4.6. Adoptive transfer studies

Monocytes were isolated from the spleen of *hCd68-GFP*$^{+}$ adult mice. Following schedule 1 cervical dislocation, the spleen was dissected and disrupted with the blunt end of a sterile syringe. The disrupted spleen was washed through a 70 µm cell filter into RBC lysis buffer and incubated at room temperature for 10 min. Cells were then spun down (400 *g* for 5 min) and RBC lysis buffer removed by aspiration. Monocytes were purified from the cell pellet using the EasySep^{TM} Mouse Monocyte Enrichment Kit according to the manufacturer's instructions. Prior to surgery, cells were counted and resuspended in PBS to give a final concentration of 50 x 10^3 per 5 µL for injection. Each recipient received 1 x 5 µL injection of cells by intracardiac injection (using a 30G insulin syringe) at the time of MI surgery.

4.7. Magnetic resonance imaging (MRI)

4.7.1. *Cardiac cine-MRI scanning*

Neonatal MRI scanning and analysis was performed in collaboration with Assistant Professor Carolyn Carr (DPAG, University of Oxford). Cardiac cine-MRI was performed post-MI at day 28 as previously described[199]. Mice were anesthetised with 4 % isoflurane in O_2

in an induction chamber before being transferred into a purpose-built cradle and placed in the supine position. A nose cone connected to the cradle supplied 2 % isoflurane in O_2 to maintain anaesthesia. Warm air was supplied to the cradle to maintain the temperature of the animals under anaesthesia. ECG electrodes were inserted into the forepaws and a respiration loop was taped across the chest. The cradle was lowered into a vertical-bore of an 11.7 T MR system (Magnex Scientific, Oxon, United Kingdom) with a 40 mm birdcage coil (Rapid Biomedical, Würzburg, Germany). The system was connected to a Bruker console running Paravision 2.1.1 (Bruker Medical, Ettlingen, Germany). The Paravision 2.1.1 software was set up to obtain a stack of contiguous 1 mm thick true short-axis ECG-gated cine-FLASH images. Images were acquired to cover the whole of the left ventricle (TE/TR 1.43/4.6 ms; 17.5° pulse; field of view 25.6 × 25.6 mm; matrix size 128 × 128 zero filled to 256 x 256 giving a voxel size of 100 × 100 × 1000 µm; 20 to 30 frames per cardiac cycle). Long-axis two-chamber and four-chamber cine images were also obtained.

4.7.2. ***MRI data analysis***

MRI data were processed manually by image analysis with ImageJ. All analysis was performed blind so as the intact/surgery and wild-type/mutant groups were unknown at the time of image processing. Measurements were calculated as previously described[228]. End-diastolic and end systolic volumes were measured for each slice and summed over the whole heart. Stroke volume was calculated by subtracting the end-systolic volume from the end-diastolic volume. Ejection fraction was calculated by dividing the end-diastolic volume by the stroke volume. End diastolic mass was calculated as the left-ventricular end-diastolic volume multiplied by the myocardial specific gravity (1.05 g/cm^3), end systolic mass was also calculated in this way using the left-ventricular end-systolic volume. Cardiac output was calculated as stroke volume multiplied by heart rate. The relative infarct size

was calculated from the average of the endocardial and epicardial circumferential lengths of the thinned, akinetic region of all slices, measured at diastole, and expressed as a percentage of the total myocardial surface.

4.8. Single cell RNA sequencing and analysis

The experimental planning and sample preparation for the scRNA-seq were performed in collaboration with Dr Daniela Pezzolla (DPAG, University of Oxford).

4.8.1. *10x Sequencing*

All the 10x scRNA library preparation and sequencing took place at the Oxford Genomics Centre part of the Wellcome Trust Centre for Human Genetics.

4.8.2. *Bioinformatics analysis*

The raw scRNA-seq data were demultiplexed by Dr Adam Braithwaite (Radcliffe Department of Medicine) using cellranger mkfastq from the Cell Ranger software suite to generate fastq files. Demultiplexed fastq files were aligned to the mouse mm10/GRCm38 reference transcriptome and gene expression matrix was counted using cellranger count program. Downstream bioinformatics analysis was performed in R using the package Seurat (v4)[229,230]. A cut-off was applied to filter out low-quality cells based on the number of genes detected (<500), the number of UMI detected (<250), and the mitochondrial gene content (>30 %) per each cell. Data from all samples were combined, scaled by regressing out S and G2 cell cycle phases, and integrated using the Seurat package. Dimensional reduction of the data was performed by RunUMAP function implemented in the Seurat package. Unsupervised cluster identification was performed *via* the FindClusters function, and cell clusters were further annotated based on expression of known marker genes[231]. Identification of enriched genes in cell clusters and single cell differential expression analysis were performed using Seurat functions FindMarkers and FindAllMarkers, using

gene expression detected in > 25 % of cells for at least one of the populations being compared, with an absolute Log2(Fold change) > 0.25 as cut-off threshold.

4.9. Cell culture

All in vitro assays were performed by Christophe Ravaud (DPAG, University of Oxford).

4.9.1. *Cell lines*

Primary human dermal microvascular endothelial cells (HMVEC-dAD), derived from an adult donor (Lonza) were cultured in the presence of endothelial cell growth medium (ECGM)-MV2 (PromoCell), according to the manufacturer instructions. Human wild-type (WT) macrophages were derived from the human induced pluripotent stem cell (iPSC) line SFC856-03-04 and obtained from the James Martin Stem Cell Facility (Sir William Dunn School of Pathology, University of Oxford, UK). iPSC-derived macrophages were cultured in macrophage medium composed of X-VIVO 15 (Lonza), GlutaMax (Invitrogen) and M-CSF (Invitrogen). Cell lines were maintained in a humidified atmosphere of 5 % CO_2 at 37°C.

4.9.2. *iPS-derived macrophage transfection*

Macrophages were transfected in a 24-well plate as previously described (Troegeler et al., 2014). Macrophages were washed twice with warm complete XVIVO in order to remove floating cells. Fresh complete XVIVO was added (250 µl per well), and the cells were kept at 37°C with 5 % CO_2. siRNA (3.75 µl of 20 µM; Thermo Fisher Scientific), 110.25 µl XVIVO depleted (without MCSF) and 11 µl HiPerfect (Qiagen) were gently mixed in a tube and incubated at room temperature for 15-20 min. 125 µl of the mix was then added in each well drop by drop. The plate was gently rocked to ensure even distribution of the mix. After 6 h, 0.5 ml of Complete XVIVO was added and the cells were harvested 3 days later for RNA extraction and/or experimental procedures.

4.9.3. *Spheroids sprouting assay*

Spheroids of 400 HMVEC-dAD were generated using a 24-well plate Aggrewell 400 (Stemcells Technologies) using EGM2 (Promocell) depleted of VEGF, FGF and EGF (EGM2-Incomplete). The following day, spheroids were collected and embedded in 25 µL of Type I collagen hydrogel (1 mg/ml) and cultured in black clear-bottom 384-well plates (Perkin-Elmer) in the presence or absence of 2500 human iPSC-derived macrophages per well. After 60 min of incubation, a 1:1 mix containing EGM2-Incomplete (Lonza) and macrophage media (v/v) was added, and the spheroids incubated for 24 hours at 37°C. The spheroids were then fixed with 2 % PFA for 30 min, washed twice with PBS and stained with Alexa Fluor 488 phalloidin (Invitrogen). Each well was imaged with an automated cell imaging system (Pico microscope, Molecular Devices) and the number of sprouts per spheroids calculated.

4.10. Statistical analysis

All statistical analyses were performed using GraphPad Prism 8 software. Comparisons between two groups were made using an unpaired two-tailed T test, this included an F test to confirm the two groups had equal variances. A one-way ANOVA was used to make comparisons between three or more experimental groups that had one independent variable. A two-way ANOVA was used to make comparisons between three or more groups that had been split in two independent variables. In all cases a *p-value* of less than or equal to 0.05 was deemed significant.

5. Results I: Characterisation of the cardiac lymphatic vasculature during postnatal development

5.1. Background

The cardiac lymphatic vessels in mammals were first documented by Rudbeck in 1653[232]. Since then the cardiac lymphatic vasculature has received a lot of attention leading to the identification of its cellular origin and the description of its development from embryonic stages to adulthood[19].

In mice, cardiac LECs originate from the paraxial mesoderm-derived *Tie2*$^+$ endothelium of the CV[61,64,233], as well as from non-venous sources, including the haemogenic endothelium of the yolk sac (*Vav1*$^+$, *Pdgfrb*$^+$, and *Csf1r*$^+$)[38] and second heart field (*Isl1*$^+$) exclusively in the ventral aspect of the heart[126,127]. At E12.5, the first cardiac LECs emerge both from the extra-cardiac region near the outflow tract on the ventral side of the heart, and from the SV on the dorsal side of the heart[38]. By E14.5, cardiac lymphatics grow on both sides of the heart from base-to-apex, with the vessels on the ventral side being delayed compared to vessels on the dorsal side[38]. During embryogenesis, lymphatic vessels appear primarily in the sub-epicardial layer, sprouting laterally to cover both the dorsal and the ventral areas of the heart until approximately P15[36–38,234]. Later in development (postnatal stages), cardiac lymphatics start extending deeper into the underlying myocardium, without ever reaching the endocardium[37]. Initial lymphatic vessels have permeable cell-cell junctions at their blind ends, called buttons, that allow the entrance of cells. In contrast, larger collecting vessels have junctions that are impermeable, called zippers[30,33,235]. In the trachea and lungs, the junctions of the initial lymphatics start as zippers during early embryogenesis

and transform to buttons during postnatal development, while maintaining the same protein composition[84].

While the development of cardiac lymphatics has been described in a qualitative way[36–38], there has not been a detailed quantitative analysis of their postnatal development to date. Moreover, the type of initial lymphatic junctions in the neonatal heart has not been studied. Understanding postnatal growth and functional maturation of cardiac lymphatics would allow for the assessment of potential differences during the so-called regenerative window (P1 to P7), as well as the detailed study of different lymphatic responses and functions after cardiac injury.

5.2. Aims

The aims of this chapter were to identify a reliable method to visualise and quantify cardiac lymphatic vessel development to subsequently document in detail the cellular, molecular, and structural changes taking place from birth to adulthood.

5.3. Results

5.3.1. *Assessing the specificity of lymphatic markers in the postnatal heart*

The heart grows substantially in size during postnatal development from an average area of 2.5 ± 0.5 mm^2 at P1 to 10 ± 1.7 mm^2 at P16, and subsequently maintains its size (Figure 5.1). During these stages the heart increases in size through cardiomyocyte proliferation from P2 to P5 and cardiomyocyte hypertrophy from P12[207,236–238]. To identify staining and imaging methods that would allow qualitative and quantitative analysis of the postnatal cardiac lymphatic vasculature, different experimental strategies were tested. Here, imaging of the transgenic reporter mouse line *Prox1-tdTomato*[217] (Figure 5.2), as well as

knock-in lines *Lyve1*$^{+/Cre}$ [216] (Figure 5.3) and *Vegfr3*$^{+/LacZ}$ [219](Figure 5.4) was conducted. Also, immunostaining against lymphatic markers such as PDPN, NRP2, VEGFR3 and LYVE1 using fluorescent-conjugated antibodies (Figure 5.5), and DAB based immunostaining against VEGFR3 (Figure 5.6) were performed.

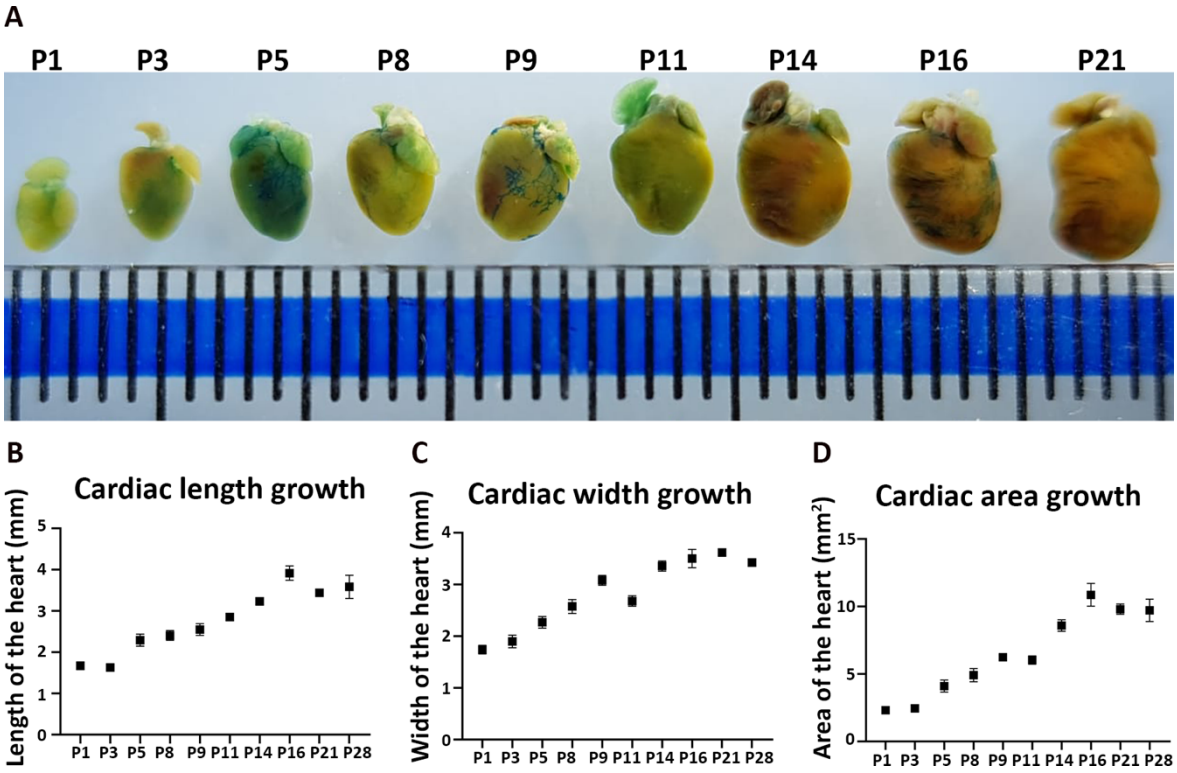

Figure 5.1 The area of the heart expands fourfold during postnatal development.

Hearts were harvested to quantify the length and width size of the ventral side at different time points postnatally (A). The heart was found to grow lengthwise in proportion to the increase in width (B-C). Four weeks after birth, the area of the heart had increased four-fold on the ventral side. Data are presented as mean ± SEM; n = 3-10 for each time point. Significant differences were calculated using 1-way ANOVA followed by Tukey's multiple comparisons test. Scale bar: 1 mm.

Two transgenic lines, *Prox1-tdTomato*[217] and *Cx40-GFP*[218], were inter-crossed with the intention of visualising the cardiac lymphatic and coronary arterial network (Figure 5.2). While the *Prox1-tdTomato* line allows for visualisation of lymphatic endothelium and cardiomyocytes, the *Cx40-GFP* line enables visualisation of the arterial endothelium and cardiac conduction system. However, this breeding strategy was unsuccessful due to

several challenges. Specifically, the *Prox1-tdTomato* litter size was very small with less than 4 pups per litter. Additionally, only hemizygous females could be used for breeding, as hemizygous males were non-productive, which made this line overall unsuitable for large scale experiments. Having said that, two samples were obtained and imaged successfully (Figure 5.2). Here, the lymphatic vasculature, coronary arteries, and low levels of cardiomyocytes were visible (Figure 5.2). It is important to note that the tdTomato signal is cytoplasmic, in contrast to the nuclear signal of PROX1 protein immunostaining. This allowed imaging of the lymphatics as continuous vessels, rather than individual nuclei, and made it easier to distinguish lymphatics from *Prox1* positive cardiomyocytes. Overall, this mouse line could be useful for future studies if the litter size is improved, potentially by breeding it with a better genetic background (e.g., outbred mouse strains).

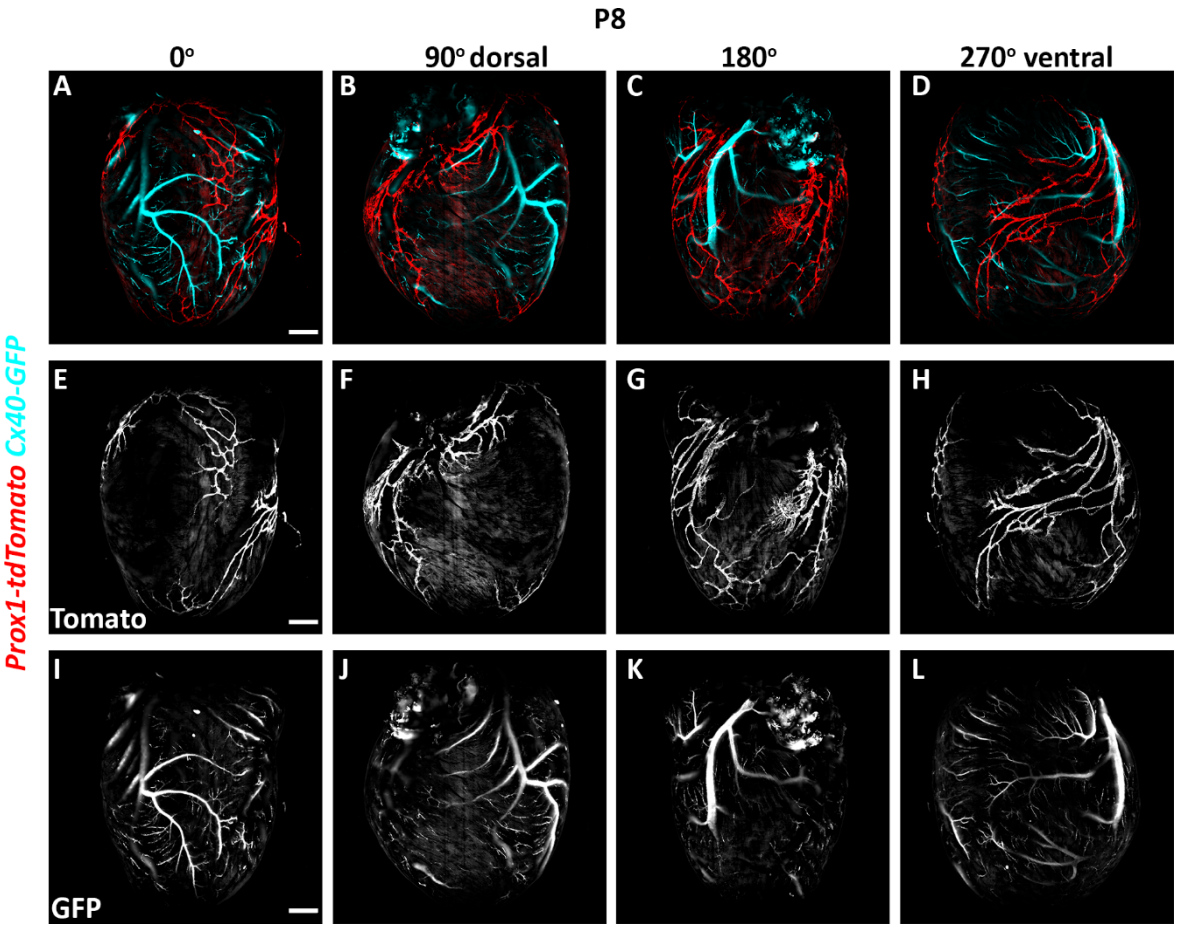

Figure 5.2 *Prox1-tdTomato* allows visualisation of lymphatic vessels with low background from cardiomyocytes.

Crossing the transgenic mouse lines *Prox1-tdTomato* and *Cx40-GFP* enabled simultaneous visualisation of the lymphatic and arterial vasculature of whole-hearts (A-D). Also, imaging with 3D light-sheet microscopy produced a multi-angled view of the heart, allowing appreciation of the vasculatures from a 3D perspective (A-D). The cytoplasmic signal from tdTomato was strong enough to be distinct from PROX1-expressing cardiomyocytes (E-H), while GFP was highly produced in sub-epicardial arterial vessels. The conduction system that expresses *Cx40* could not be identified as it locates deeper in the myocardium. n = 2. Scale bar: 500 µm.

In a second attempt to use a genetic mouse line to study the cardiac lymphatic vasculature, male knock-in *Lyve1*$^{+/Cre}$ mice were crossed with female *R26R-tdTomato* mice (Figure 5.3). *Lyve1* is expressed by lymphatic endothelial cells and macrophages, as well as by blood endothelial and endocardial cells during the early stages of embryogenesis[239]. Consistent with previous studies[240], tdTomato expression promoted by the *Lyve1-Cre* driver was identified in both endomucin (EMCN) positive blood capillaries and LYVE1 positive

lymphatic vessels, not allowing for their distinction, and hence quantification of lymphatics was not possible (Figure 5.3).

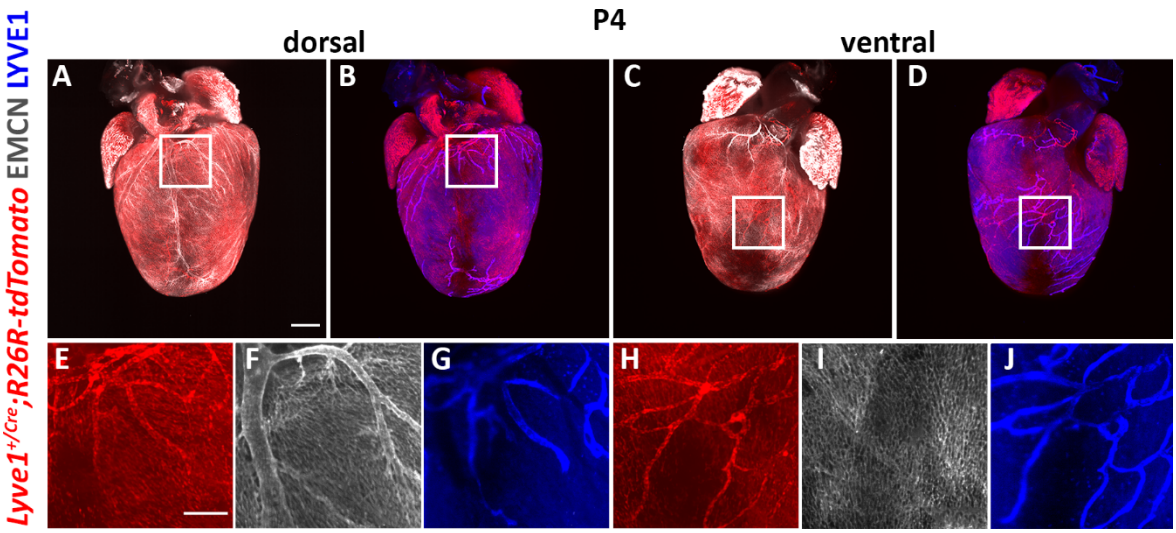

Figure 5.3 *Lyve1* is expressed in the blood and lymphatic vasculature of the heart during mouse embryonic development.

Crossing *Lyve1*$^{+/Cre}$ knock-in male with *R26R-tdTomato* female mice allowed for tracing the gene expression history of *Lyve1* in whole-hearts (A-D). Higher magnification revealed that *Lyve1* is expressed by blood capillaries, stained with EMCN antibody (E-F and H-I). Also, LYVE1 antibody stained only for lymphatics and macrophages, but not blood capillaries at P4 (G and J). n= 2. Scale bars: A-D 500 µm, E-J 200 µm.

Next, Xgal staining was used to assess the knock-in mouse line *Vegfr3*$^{+/LacZ}$, which has been successfully used to study cardiac lymphatic vessels in the past[38]. The Xgal staining allowed for specific detection of lymphatic vessels and produced a clear signal that was distinguishable from the background (Figure 5.4), an essential requirement for the downstream quantification analysis. Consequently, Xgal staining of *Vegfr3*$^{+/LacZ}$ hearts was selected as one of the methods for detailed quantification of the developing postnatal lymphatic vessels.

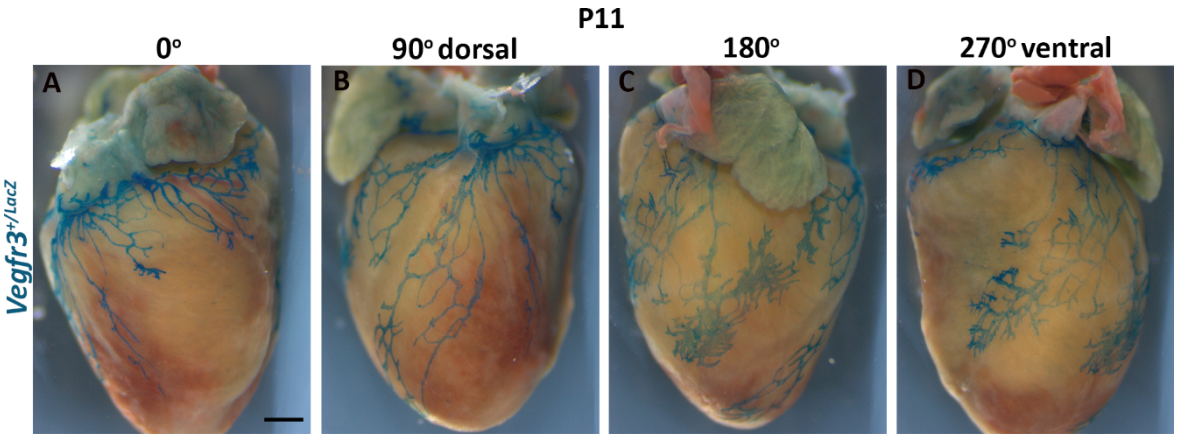

Figure 5.4 *Vegfr3* is expressed specifically by LECs at postnatal stages.

Whole-mount *Vegfr3*$^{+/LacZ}$ mouse hearts stained with Xgal produced a strong lymphatic-specific signal (A-D). The samples were imaged from all sides using low magnification bright-field imaging which, together with the specificity of the signal, enabled further downstream quantification of the lymphatic vasculature. n = 4. Scale bar: 0.5 mm.

Next, whole-mount staining using antibodies against known lymphatic markers PDPN, NRP2, LYVE1 and VEGFR3 was performed (Figure 5.5). Although all of these markers have key roles in the function or development of lymphatics, not all of them are specific for LECs. Specifically, PDPN is expressed in the epicardium[241], making it challenging to identify lymphatics expanding into the sub-epicardial compartment (Figure 5.5 A-E). Moreover, NRP2 localises in lymphatics[242] and axon tracts of the cardiac autonomic nervous system[243] (Figure 5.5 F-J), and LYVE1 is co-expressed in lymphatics and tissue-resident macrophages[145] (Figure 5.5 P-T). Antibody staining against VEGFR3 confirmed that it is specifically expressed in lymphatics during postnatal development (Figure 5.5 K-O). This is in agreement with previous reports suggesting that *Vegfr3*, whilst initially expressed in blood endothelium, becomes progressively restricted to LECs during embryogenesis[38,244].

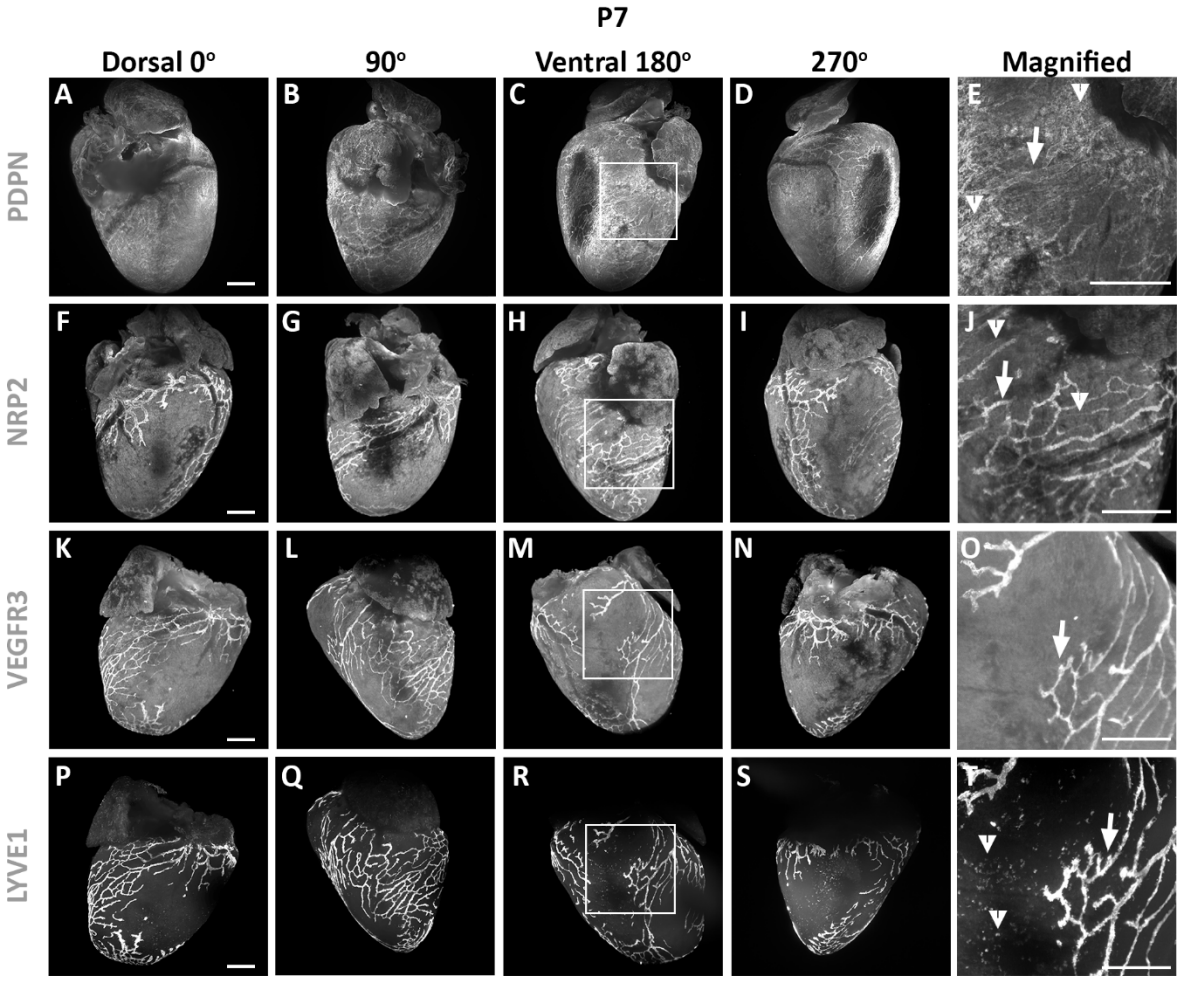

Figure 5.5 VEGFR3 is the most specific lymphatic marker at postnatal stages.

Whole-mount antibody staining for different lymphatic markers established VEGFR3 as the most specific cardiac lymphatic marker at postnatal stages (A-T). PDPN labelled the epicardium (white arrowheads at E), making challenging to distinguish the sub-epicardial lymphatic vessels even with high magnification (white arrow at E). NRP2 was produced in lymphatics (white arrow at J) and in axons that could be detected with high magnification (white arrowheads at J). VEGFR3 was specific for cardiac lymphatics (white arrow at O), as no other cell populations appeared to be expressing it. LYVE1 was expressed in tissue-resident macrophages (white arrowheads at T), as well as cardiac lymphatics (white arrow at T). n = 2-3 for each time point. Scale bar: 0.5 mm.

Finally, whole-mount DAB staining was done for VEGFR3 (Figure 5.6), which produced similar results to the Xgal and antibody staining approaches. However, DAB stainining was fainter and less distinct from the background compared to Xgal and immunofluorescence. Moreover, DAB staining was associated with frequent occurance of large bleeched areas on the heart surface, making it unsuitable for downstream quantification analysis.

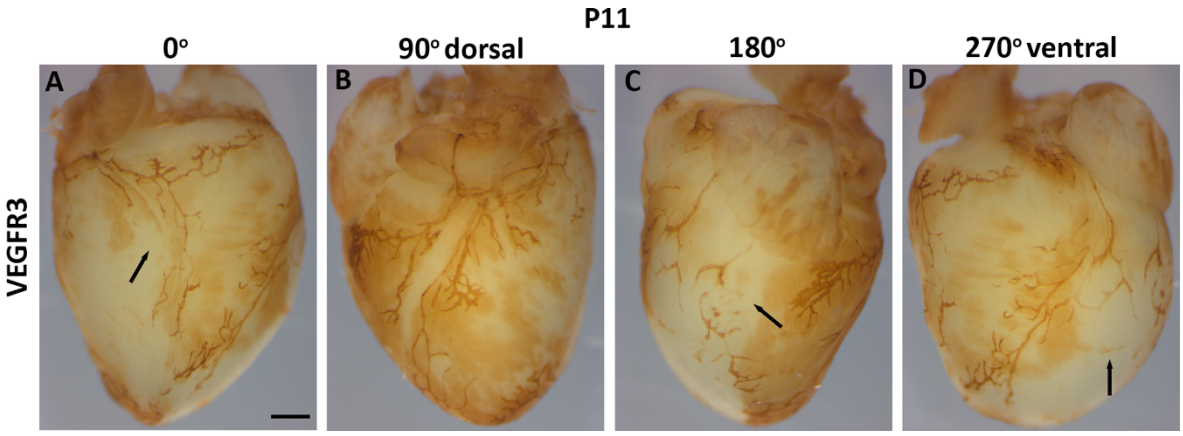

Figure 5.6 DAB staining for VEGFR3 is suboptimal compared to Xgal and immunostaining.

The use of whole-mount 3,3'-diaminobenzidine staining for VEGFR3 was specific for cardiac lymphatics but produced low contrast and bleached areas (arrows in A, C and D). n = 2. Scale bar: 0.5 mm.

5.3.2. *Cardiac lymphatic vessels continue growing and sprouting postnatally*

Having established that Xgal staining of *Vegfr3*$^{+/LacZ}$ hearts and immunostaining for VEGFR3 give the most specific signals for cardiac lymphatics, both staining strategies were used to quantify the spatiotemporal changes of the developing postnatal cardiac lymphatic network from P1 to P28 (Figure 5.7 to Figure 5.9). For quantification, the software ImageJ and AngioTool were used, as described in Materials & Methods.

At P1, lymphatics were located near the base of the heart on the ventral side (Figure 5.7 A), while on the dorsal side lymphatics were found extending towards the apex, running near major coronary veins (Figure 5.7 B). During the first week of postnatal development (from P1 to P9) no sprouting of new lymphatic vessels was observed on either the ventral or dorsal side of the heart (Figure 5.7 A-J). During this period, cardiac lymphatic length increased, following the cardiac growth, and maintaining full coverage of the base-to-apex axis on the dorsal side and incomplete coverage on the ventral side (Figure 5.7 A-J). The

reduced length of vessels on the ventral side is in line with a previous observation of delayed lymphatic development during embryonic stages, when compared to the vasculature on the dorsal side[38]. Also, a small number of isolated VEGFR3 positive cells were noticeable on the dorsal side of the heart, which were not connected to the already established lymphatic vasculature at P1 and P3 (Figure 5.7 B and D). These isolated cells could resemble the isolated LECs that have been recently described to contribute to the cardiac lymphatic network in zebrafish and mammals through lymphvasculogenesis [54]. From P11, the first sprouts of vessels were visible on both the ventral and dorsal side (Figure 5.7 K-L). These sprouts continued expanding until they formed a complex network of vessels that appeared fully developed by P21 (Figure 5.7 M-T). Notwithstanding some minor differences, there were constant features in lymphatic vessel morphology across the various samples. For instance, lymphatics formed a very dense network of vessels on the dorsal side near the apex, which started developing at P14 and was fully shaped by P21 (Figure 5.7 M-T). Also, there were areas on both the ventral and the dorsal side that were depleted of lymphatics, such as the apex on the ventral side and the right ventricle on the dorsal side (Figure 5.7 S-T).

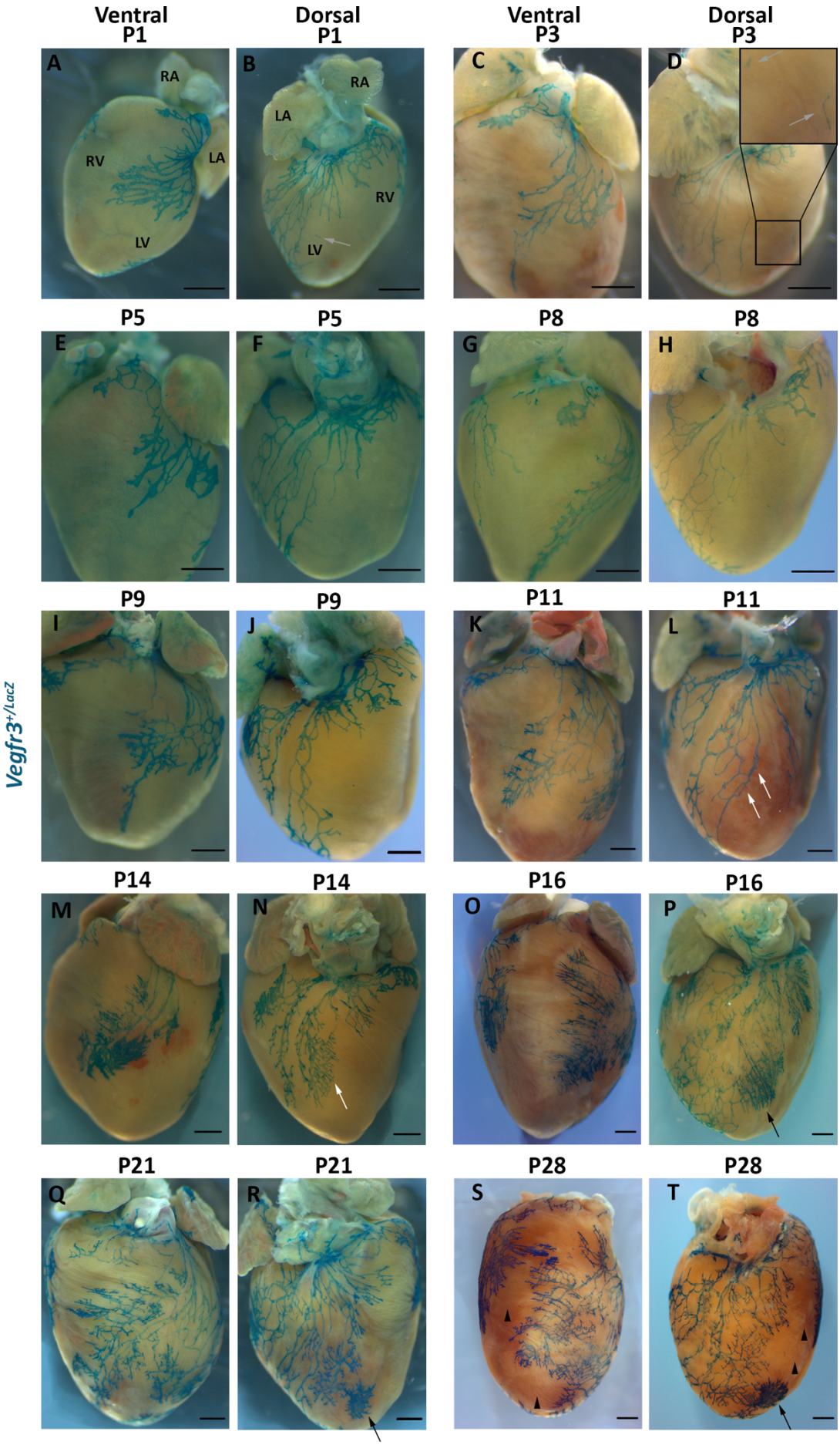
Ventral
P1
Dorsal
P1
Ventral
P3
Dorsal
P3
A
RA
RV
LA
LV
B
RA
LA
RV
LV
C
D
P5
P5
P8
P8
E
F
G
H
P9
P9
P11
P11
I
J
K
L
P14
P14
P16
P16
M
N
O
P
P21
P21
P28
P28
Q
R
S
T
Vegfr3+/LacZ

Figure 5.7 The cardiac lymphatic network continues expanding until late in postnatal development.

Whole-mount imaging of *Vegfr3*$^{+/LacZ}$ hearts showed extensive growth and sprouting of the cardiac lymphatic vasculature on both the dorsal and ventral side of the heart during postnatal life (A-T). Isolated LECs were present on the dorsal side of the heart during early postnatal stages (grey arrows in B and D). At P11 and P14 sprouts were detected arising from a large lymphatic vessel on the dorsal side of the heart (white arrows in L and N). These sprouts produced a dense plexus of vessels on the dorsal side near the apex at P16 (black arrow in P, R and T). Also, areas depleted of lymphatics were present in stereotypical locations of the heart, such as the apex on the ventral side (black arrowheads in S) and the right ventricle on the dorsal side (black arrowheads in T). n = 3-5 for each time point. Scale bars: 0.5 mm.

These observations were confirmed upon quantification of the images, in particular the parameters of total vessel length (Figure 5.8 A) and total number of vessel end points (Figure 5.8 B). This approach revealed that length and number of individual vessels, increased marginally from P1 (Dorsal mean ± SEM : 21 ± 2 mm and 83 ± 8 vessels; Ventral mean ± SEM : 13 ± 1 mm and 52 ± 6 vessels) to P11 (Dorsal mean ± SEM: 33 ± 9 mm and 98 ± 36 vessels; Ventral mean ± SEM: 25 ± 18 mm and 98 ± 77 vessels), suggesting limited growth and sprouting. Consistent with the visualisation of lymphatic sprouting after P11, there was significant increase in total vessel length on the dorsal side from 33 ± 9 mm at P11 to 66 ± 15 mm at P14 ($p < 0.001$) and from 66 ± 15 mm at P14 to 91 ± 11 mm at P16 (mean ± SEM; $p = 0.01$). On the ventral side, vessel length increased from 25 ± 18 mm at P11 to 52 ± 7 mm at P14 (mean ± SEM; $p < 0.011$) and from 66 ± 11 mm at P16 to 96 ± 14 mm at P21 (mean ± SEM; $p = 0.005$). Also, the total number of end points increased significantly on the dorsal side from 98 ± 36 vessels at P11 to 273 ± 133 vessels at P14 (mean ± SEM; $p < 0.001$). Comparing lymphatic vessels from the ventral side of the heart against dorsal lymphatics, the number of end points was never significantly different. A trend towards smaller total vessel length on the ventral side was observed throughout postnatal development. However, this was statistically significant only at P16 with 91 ± 11

mm vessel length on the dorsal compared to 66 ± 11 mm on the ventral side (mean ± SEM; p = 0.009). Taken together, these results highlight the different spatiotemporal behaviour of lymphatic vessels on dorsal versus ventral side of the heart during postnatal development.

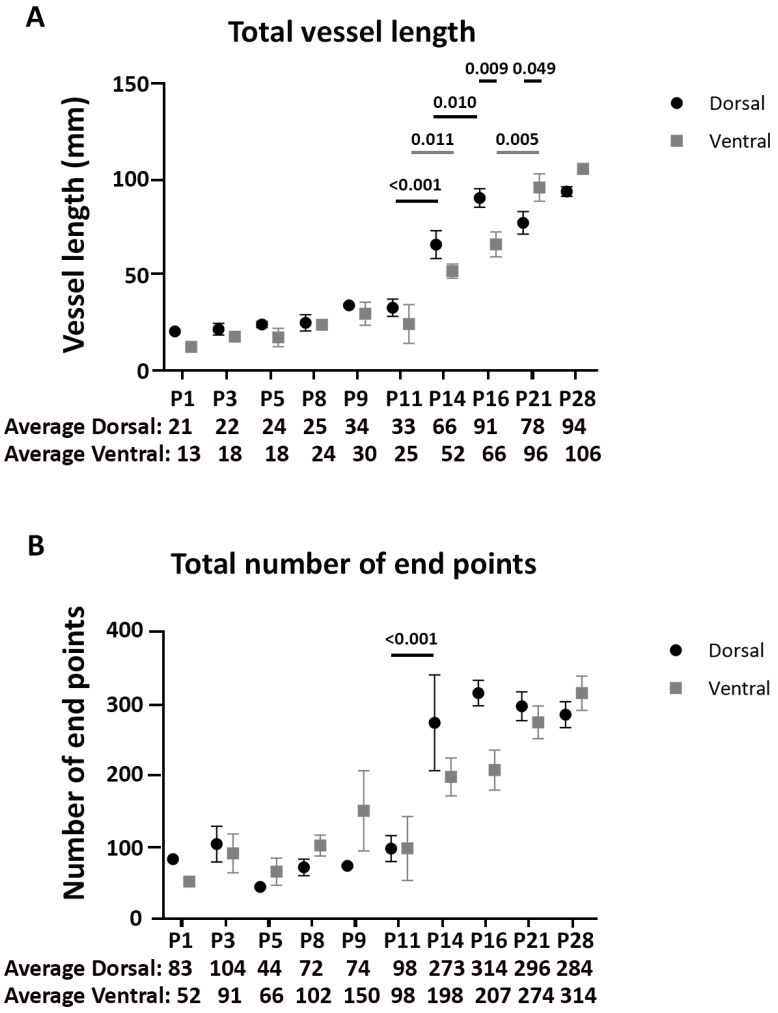

Figure 5.8 The cardiac lymphatic vasculature has different dynamics on the dorsal and ventral side of the heart during postnatal developmental.

Quantification of the cardiac lymphatic vasculature identified its developmental progress on the dorsal and ventral side of the heart during postnatal development. The total vessel length and number of end points remained stable until P14 when they start increasing on both sides of the heart, reflecting lymphangiogenesis. By P16 the lymphatics were completely grown on the dorsal side, while ventral lymphatics reached full length by P21. Data are presented as mean ± SEM; n = 3-5 for each time point. Significant differences were calculated using 2-way ANOVA.

5.3.3. ***Different spatiotemporal development of cardiac lymphatics in CD1 versus C57BL/6 mouse genetic backgrounds***

Immunostaining against VEGFR3 was carried out to validate the results from the Xgal staining of *Vegfr3*$^{+/LacZ}$ hearts using hearts from CD1 wild-type mice at different postnatal stages (Figure 5.9). VEGFR3^{+} lymphatics on the dorsal side of the heart appeared morphologically identical between CD1 and C57BL/6 hearts (*Vegfr3*$^{+/LacZ}$) at P1 and P7 stages (compare Figure 5.7 B to Figure 5.9 A and Figure 5.7 H to Figure 5.9 B). However, from P14 the gross morphology of the lymphatic network was different in the two genetic backgrounds (compare Figure 5.7 N to Figure 5.9 C and Figure 5.7 R to Figure 5.9 D). Contrasting the observations in C57BL/6 *Vegfr3*$^{+/LacZ}$ hearts at P14, the dorsal side of CD1 hearts was fully covered with lymphatics, indicating that sprouting occurred at an earlier time point and with greater efficiency. Moreover, lymphatics on the dorsal side of CD1 hearts continued expanding concurrently with cardiac growth at least until P21.

Quantification of lymphatics from the dorsal side of CD1 hearts showed that the total number of end points increased from 50 vessels at P1 to 500 vessels at P14 (Figure 5.9 F). After P14, the number of end points remained stable, suggesting no further sprouting. However, there was an increase in the total vessel length in CD1 hearts from 15 mm at P1 to 175 mm at P21 (Figure 5.9 E) in line with continuous growth. While the developmental pattern of cardiac lymphatics in CD1 and C57BL/6 genetic background mice was similar, there were substantial differences in the rate and degree of development. For instance, at P21 the average total vessel length and the average number of end points on the dorsal side of the heart was 78 mm and 296 vessels in C57BL/6 mice compared to 166 mm and 546 vessels in CD1 mice (compare Figure 5.8 A-B with Figure 5.9 E-F). Overall, these data suggest that cardiac lymphatics in mice with different genetic background could have

different developmental dynamics, which could have implications on the endogenous capacity to respond to injury.

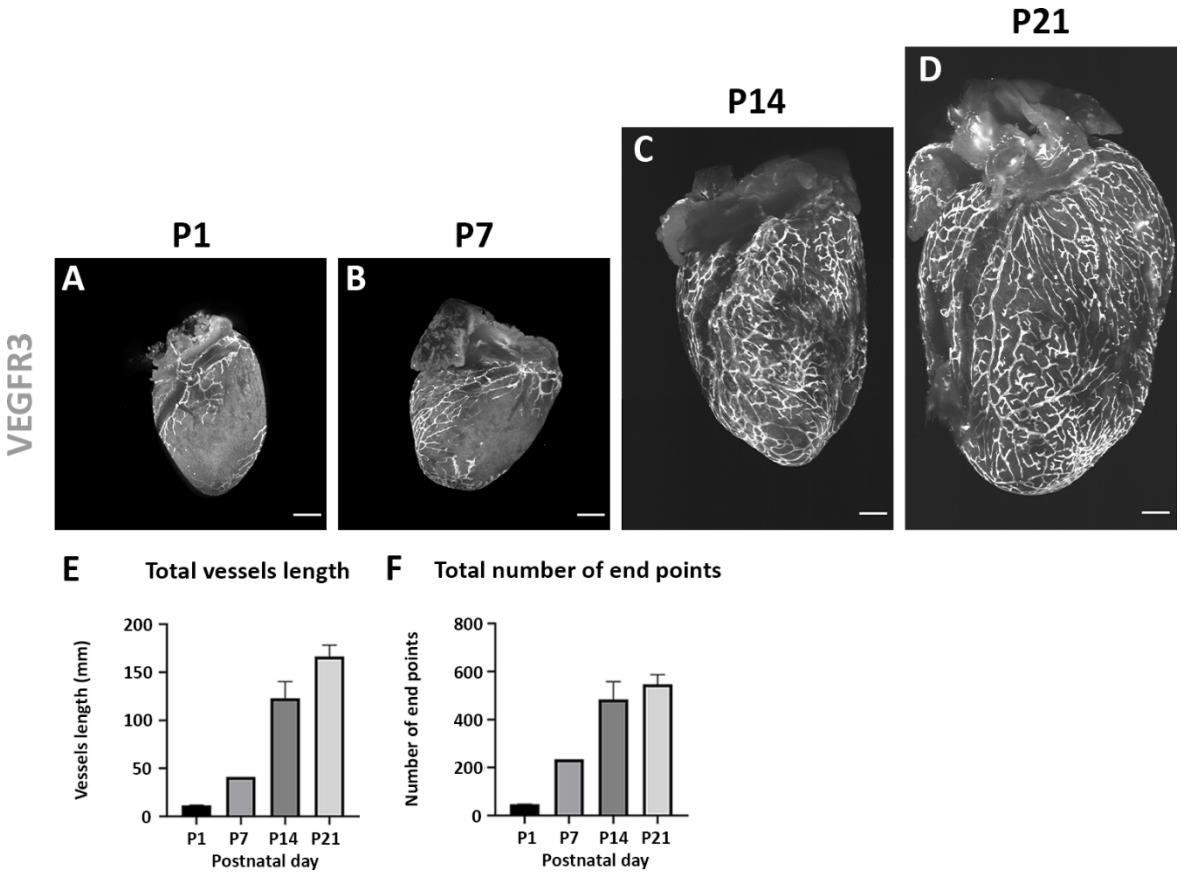

Figure 5.9 The cardiac lymphatic vasculature of CD1 mice during postnatal development.

Whole-mount antibody staining for VEGFR3 using CD1 mice confirmed that cardiac lymphatics grow and sprout extensively during postnatal development. While little growth or sprouting was observed in the first week of postnatal life (A-B), by P14 a dense network of lymphatic vessels had formed covering the entire dorsal side of the heart (C). This network continued growing in proportion to the heart expansion (D). Quantification of cardiac lymphatics on the dorsal side confirmed that there is a significant increase in total vessel length and total number of end points during the second week of life (E-F). Data are presented as mean ± SEM; n = 2-5 for each time point. Scale bar: 500 µm.

5.3.4. *Gene expression of key lymphatic markers fluctuates during postnatal cardiac development*

Imaging the lymphatic vasculature allowed for the observation of morphological changes that take place during postnatal development. To uncover potential molecular changes that occur during these stages' qPCR using a panel of known lymphatic markers and whole-

heart samples was conducted (Figure 5.10). The gene expression levels for most lymphangiogenic markers reached two peaks during postnatal development, one at P2-P3 and one at P7-P9 (Figure 5.10 A-E). At P2-P3 the expression levels of *Prox1*, *Nrp2*, and the ligands *Vegfc and Vegfd* doubled compared to P0. Subsequently, expression levels dropped for *Prox1*, *Vegfc* and *Vegfd* and remained stable for *Nrp2* until P6. Then, the expression levels of *Vegfc* (LogFC ± SEM: -0.26 ± 0.13 vs 0.99 ± 0.23; $p = 0.007$) and *Nrp2* (LogFC ± SEM: -1.13 ± 0.18 vs 0.82 ± 0.26; $p = 0.036$) increased significantly from P6 to P7. Meanwhile the expression levels for *Vegfr3*, *Vegfd* and *Prox1* doubled at P8-P9 compared to P0. After P11, the expression levels of all genes decreased, except for *Nrp2*, which retained high levels. Specifically, expression of *Vegfc* (LogFC ± SEM: 1.78 ± 0.05 vs 0.66 ± 0.17; $p = 0.014$) and *Vegfd* (LogFC ± SEM: 1.53 ± 0.12 vs 0.21 ± 0.19; $p = 0.04$) declined significantly from P11 to P14, and expression of *Vegfr3* and *Prox1* returned to nearly P0 levels. Expression of *Pdpn* remained relatively stable during postnatal development (Figure 5.10 F), with a significant increase (LogFC ± SEM: 1.75 ± 0.23 vs -0.33 ± 0.14; $p < 0.001$) at P9 compared to P8, and a subsequent significant decrease (LogFC ± SEM: 0.03 ± 0.21 vs 1.33 ± 0.12; $p = 0.016$) to baseline levels at P14 compared to P11. Considering the findings arising from the imaging studies, it is likely that the increased expression of lymphatic markers at P2-P3 is related to the expansion of cardiac lymphatics that associates with neonatal heart growth. Furthermore, the increased expression levels at P8-P11 might be associated with the lymphangiogenic sprouting observed after P11.

The analysis of the expression of genes involved in lymphatic function rather than development showed a different pattern (Figure 5.10 G-H). Such pattern is seen for instance in the expression levels of *Ccl21* (Figure 5.10 G), the gene encoding for the LEC-

secreted chemokine CCL21 (Chemokine [C-C motif] ligand 21) that is responsible for recruitment of leukocytes and subsequent trans-migration into the lymph[245–247]. Here, expression levels were found to be 2-fold increased at P2 compared to P0 and returned to baseline levels by P6. At P7, there was a significant increase (LogFC ± SEM: 1.52 ± 0.31 vs -0.38 ± 0.13; $p < 0.001$) in the expression levels compared to P6. The expression remained stable until P14, after which there was a second significant increase (LogFC ± SEM: 1.25 ± 0.09 vs 3.06 ± 0.22; $p < 0.001$) at P21. From P21 until adulthood the expression levels of *Ccl21* remained stable with an 8-fold increase compared to the baseline. Similarly, expression of *Lyve1* increased significantly (LogFC ± SEM: 1.37 ± 0.36 vs -0.82 ± 0.39; $p < 0.001$) at P21 compared to P14 and remained stable into adulthood with a 2-fold increase compared to P0 (Figure 5.10 H). Also, *Lyve1* was the only gene to have a 2-fold decrease in expression levels compared to P0, which occurred between P3 and P7. These data suggest that cardiac lymphatics become functionally mature late in postnatal development. The functional maturation at P21 is in line with the imaging data, as well as the gene expression of lymphangiogenic markers.

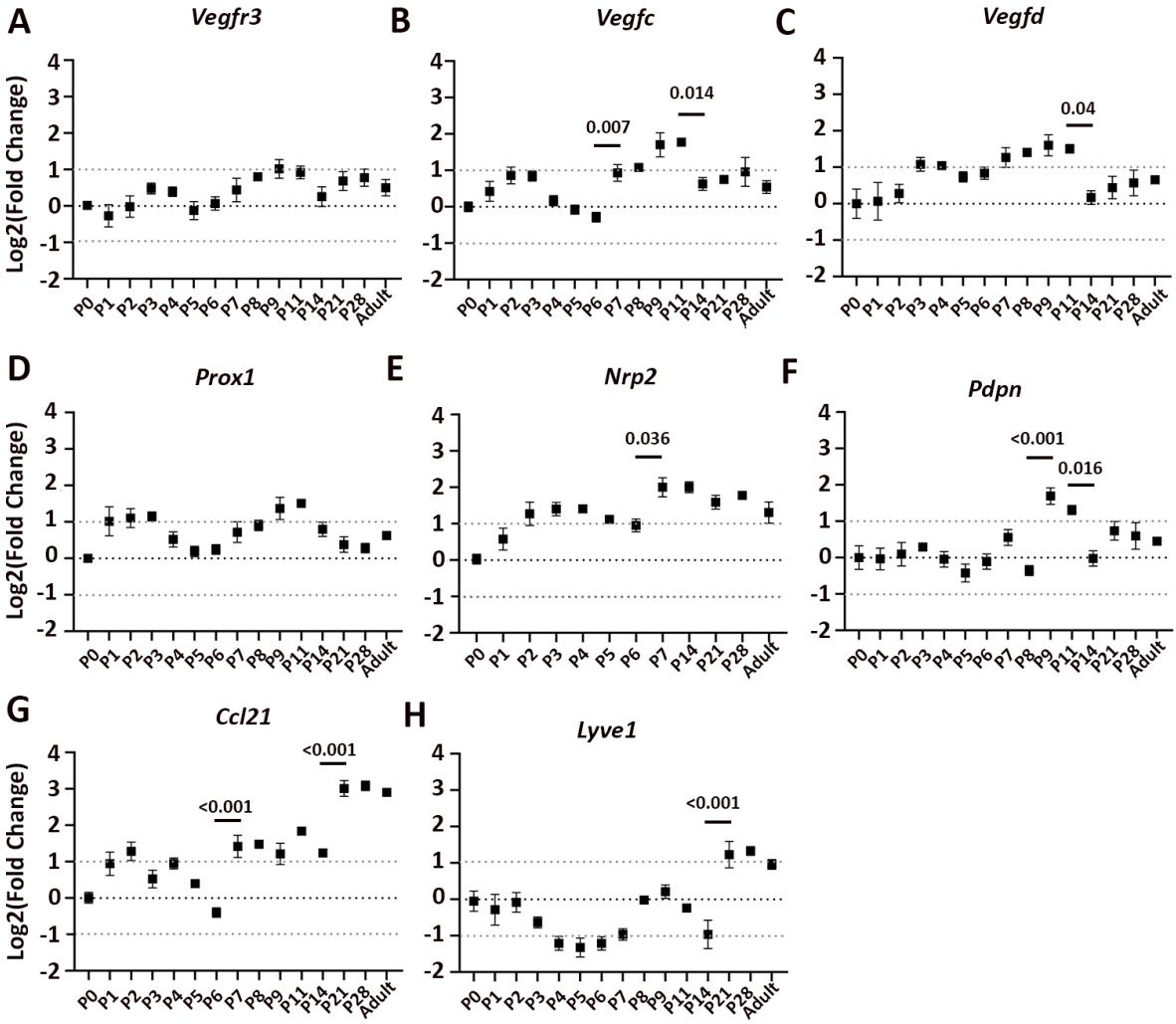

Figure 5.10 Gene expression of lymphatic markers indicate morphological and functional postnatal changes.

Whole-heart samples were used to perform qPCR of lymphatic markers during several time-point of postnatal development. Expression levels of genes important for lymphangiogenesis, such as *Vegfr3* (A), *Vegfc* (B), *Vegfd* (C), *Prox1* (D) and *Nrp2* (E) displayed two waves of increase, one between P2 and P3 and a second around P9. *Pdpn* increased only between P9 and P11 (F). Genes important for lymphatic function, such as *Ccl21* (G) and *Lyve1* (H) displayed an expression pattern where levels fluctuated during the first week, before increasing significantly at P21 and remained stable thereafter. Data are presented as mean ± SEM; n = 4-5 for each time point. Significant differences were calculated using 1-way ANOVA followed by Tukey's multiple comparisons test.

It is important to consider that whole-heart extracts were used for qPCR studies and most of the genes analysed are not specific for cardiac LECs. Thus, some of the changes in gene expression that were observed could be affected by other cell populations. For instance, the decrease in *Lyve1* levels between P3 and P7 could be due to a reduction in the number

of *Lyve1*-expressing macrophages during this developmental period. Also, cardiomyocytes which proliferate during early postnatal development and express *Prox1*, could have contributed to the increased levels of expression. Finally, *Pdpn* is expressed by the epicardium and, hence, changes in epicardial mRNA levels during postnatal development could have affected the data. Despite these caveats, the overall gene expression patterns suggest that key lymphangiogenic markers have two transient increases at P2-P3 and P7-P9, while factors for lymphatic function rise once at P21 and subsequently remain stable, which agrees with our findings arising from immunostaining approaches.

5.3.5. ***Transformation from zipper- to button-like cardiac LEC junctions during the postnatal period***

LECs have specialised intercellular junctions with different degrees of cell permeability, known as permeable button-like and impermeable zipper-like junctions[30,33,235]. In the lungs and trachea, the junctions of initial lymphatics undergo transformation during postnatal development replacing zipper-like with button-like junctions, while maintaining the same junctional proteins[84]. To study the type of junctions in initial lymphatics of the neonatal heart, high-magnification confocal microscopy (63x) was used after staining for VE-Cadherin and LYVE1 (Figure 5.11).

At both P1 (Figure 5.11 A-C) and P7 (Figure 5.11 D-F) the junctions of initial lymphatics resembled zipper-like junctions with a continuous seam of VE-Cadherin and no gaps between each LEC. This suggests that lymphatics might not be permeable to cells on these postnatal stages. However, by P14 (Figure 5.11 G-I) LEC junctions near the end of lymphatics resembled button-like structures with discontinuous VE-Cadherin and gaps between LECs observed. While the transformation from zippers to buttons was not

complete at P14, as both type of junctions were still detected, there was a clear dynamic change in the junctional morphology that could potentially continue in later stages of postnatal development.

Of note, tissue resident *Lyve1*$^{+}$ macrophages were identified in close proximity or direct physical contact with initial lymphatics during the first two weeks of postnatal developmental (Figure 5.11). These macrophages underwent morphological changes during this period. At P1, macrophages were spherical in shape with no particular orientation in relation to lymphatics (Figure 5.11 B). Interestingly, they had an elongated shape with an orientation parallel to the lymphatic vessel by P14 (Figure 5.11 I). These changes could potentially be the result of the interaction between macrophages and endothelial cells[144,145] or due to changes in epicardial cues[248].

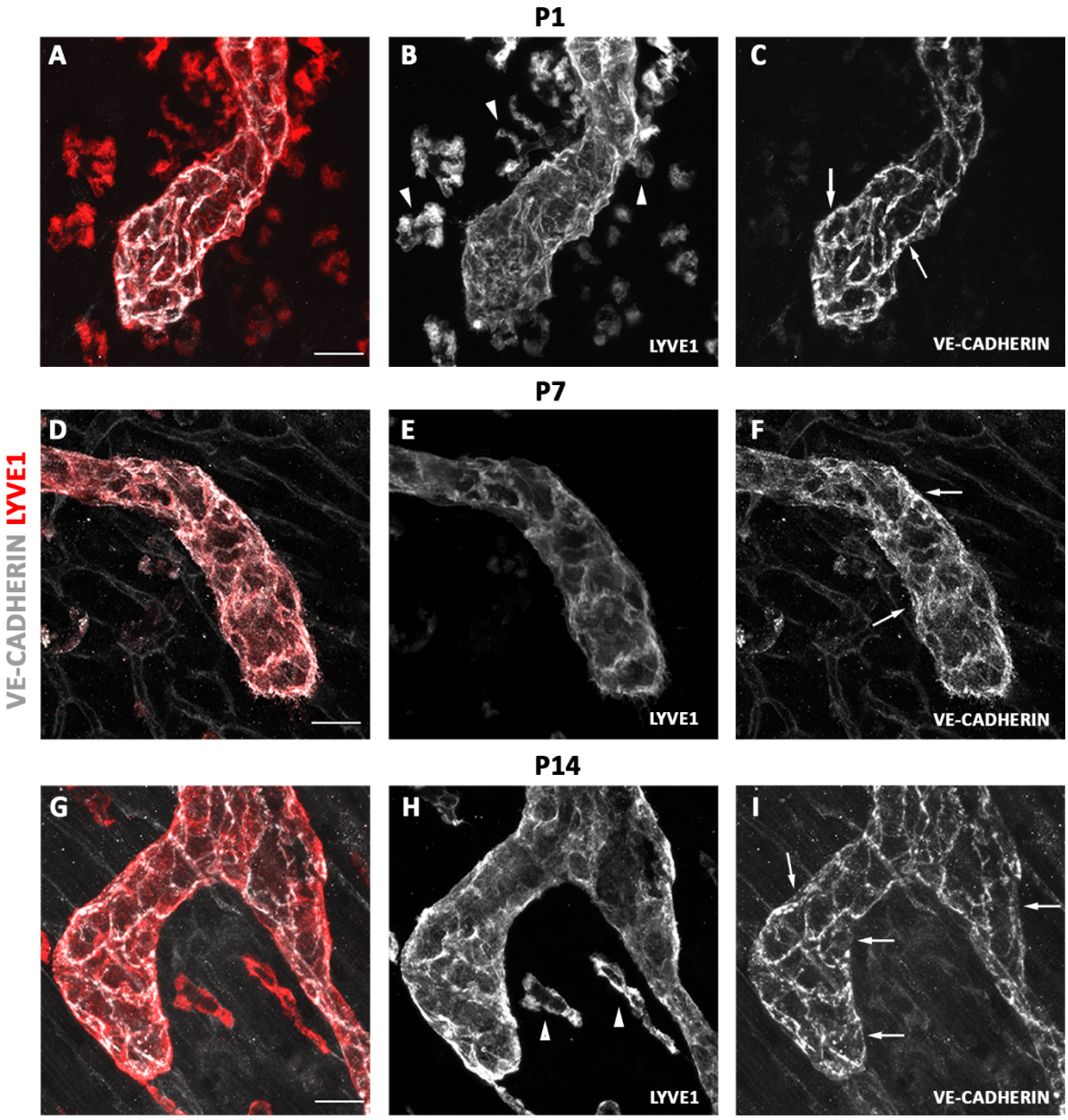

Figure 5.11 Cell-cell junctions of cardiac LECs undergo transformation during postnatal developmental.

High magnification confocal imaging of LEC staining against VE-Cadherin and LYVE1 allowed visualisation of their cell-cell junctions at different postnatal stages (A-I). The morphology of the junctions appeared to be continuous, resembling that of zippers (arrows in C and F). No button-like junctions were identified at these stages. The morphology of the junctions appeared to transform to discontinuous button-like junctions at P14 (arrows in I). Both zipper- and button-like junctions were identified at P14. Also, macrophage morphology changed during these two weeks period. At P1, $LYVE^{+}$ macrophages were spherical in shape (arrowheads in B). At P14, the shape of macrophages was elongated, and macrophages positioned parallel to lymphatic vessels (arrowheads in H). n = 3-4 for each time point. Scale bars: 20 µm.

5.4. Discussion

In this chapter the specificity of known lymphatic markers was tested in the mouse heart and the spatiotemporal development of the lymphatic vasculature was characterised from birth until adulthood. Whole-mount immunostaining data showed that VEGFR3 is the most specific marker to study cardiac lymphatics in the postnatal heart. This is in agreement with previous reports suggesting that, whilst initially expressed in blood endothelium, *Vegfr3* becomes progressively restricted to LECs during embryogenesis[38,244]. Other markers, such as PDPN, LYVE1, and NRP2 are suboptimal, as they are co-expressed in the epicardium, macrophages and sympathetic axons, respectively.

Previous developmental studies have used India ink injections[37], immunohistochemistry[36,234], and whole-mount immunofluorescence[38] to describe the growth of the postnatal cardiac lymphatics in a qualitative way. In this project, a quantitative analysis of the sub-epicardial lymphatic network was performed using two genetic backgrounds, CD1 and C57BL/6, and multiple time points from P1 to P28. On the ventral side of C57BL/6 hearts, lymphatics appeared to be slightly delayed compared to the dorsal side during postnatal development. This is in line with previous observations in embryonic hearts[38]. Thus, while the lymphatic network had fully expanded by P16 on the dorsal side, it continued growing until P21 on the ventral side. It is possible that the discrepancy in the developmental dynamics between ventral and dorsal side of the heart is caused by the different origins of LECs. For example, LECs on the ventral side of the heart can originate from the second heart field, while on both the ventral and dorsal side of the heart there is equal contribution of venous-derived and haemogenic endothelium-derived LECs[38,126,127]. Apart from growing and sprouting lymphatics from pre-existing vessels, short

isolated lymphatic vessels were also detected on the ventricular surface, predominantly at the early postnatal stages. Similar isolated LECs have been previously described in zebrafish and mouse hearts, suggesting potential growth through lymphvasculogenesis[249]. However, the isolated lymphatics were only detected distant from the main lymphatic network and remained relatively short in length. As a result, the contribution of these isolated LECs to the main cardiac lymphatic network could not be confirmed.

Gene expression levels of several key lymphangiogenic markers showed two waves of significant increase, one between P2 and P3, and a second between P9 and P11. Also, expression of genes important for the function of lymphatics, such as *Lyve1* and *Ccl21*, increased after P21 and maintained high levels of expression, thereafter, suggesting that functional maturation may take place later in postnatal life. While these results were obtained by qPCR of extracts from whole-hearts and not LECs only, the two observed peaks in expression levels are highly consistent with observations made by whole-heart imaging of lymphatics. Specifically, the increase at P2 could be required for cardiac lymphatic growth and the increase at P9 could be a prerequisite for the lymphatic sprouting evident by P11.

Previous studies in the trachea and lungs have shown that LECs have two types of specialised cell-cell junctions: permeable junctions near the initial lymphatics (buttons) that act as the preferential draining point, and impermeable junctions at the larger collecting vessels (zippers) that are responsible for the unidirectional transport of the lymph[30,33,235]. When lymphatics first form during embryogenesis they only have zipper-type junctions, which transform into button-type junctions during postnatal development[84]. In

this study data suggest that a similar transformation process takes place in the junctions of cardiac LECs. High magnification confocal imaging showed that the junctions are predominantly continuous zipper-like during the first week of postnatal life, while there is a morphological change towards discontinuous button-like junctions in the second week of postnatal life. The transformation of cardiac lymphatic cell-cell junctions during postnatal development could have functional significance in immune cell clearance after MI, with cardiac lymphatics being potentially less permeable to cells at P1 compared to P7.

5.5. Summary

The work presented in this chapter characterises the spatiotemporal changes of cardiac lymphatic vessels during postnatal development. The data demonstrate that cardiac lymphatics grow and sprout significantly from P11 until P16 on the dorsal side and from P11 until P21 on the ventral side. This postnatal lymphatic growth occurs through a process of lymphangiogenesis and potential lymphvasculogenesis. During the same period, cell-cell junctions connecting cardiac LECs shift from cell-impermeable zippers to cell-permeable buttons. Overall, the lymphatic vasculature appears to undergo significant changes during the first three weeks of postnatal life, supporting the hypotheses that lymphatics may respond or function differently in the regenerative P1 stage compared to the fibrotic P7 stage after heart injury.

6. Results II: Characterisation of the cardiac lymphatics response to myocardial infarction in regenerative P1 and fibrotic P7 neonatal stages

6.1. Background

Heart attack, or MI, is caused by coronary artery occlusion and leads to the death of cardiomyocytes as a result of prolonged ischemia[1]. Adult mammals lack the ability to regenerate their heart, and healing occurs by replacing the damaged myocardium with scar tissue[3]. This process eventually leads to impaired heart structure and function, including heart failure. In adult mice after MI, the lymphatic vasculature gets compromised near the infarction site leading to increased oedema and reduced ability to clear immune cells[4–7]. In response to injury, lymphatic vessels grow and sprout through lymphangiogenesis to reduce the adverse effects[5,7–9]. However, this endogenous response is insufficient to clear the infiltrated immune cells and oedema[5,7,9]. Enhancing lymphatic growth using lymphangiogenic factors, such as VEGFC, leads to better clearance of interstitial fluids and macrophages, consequently improving the cardiac function in adult mice[5,7,9].

In contrast to humans and other adult mammals, it is now proven that some urodele amphibians, such as newts[250,251], a number of fish, such as the zebrafish[10,11] and the surface-dwelling Mexican tetra[12], as well as neonatal mammals have cardiac regeneration capacity[13–17]. Similar to the lymphangiogenic response seen in adult mice after MI, cryoinjury stimulates cardiac lymphatic growth to the site of injury in zebrafish[18–20]. This lymphangiogenic response is necessary for complete regeneration of the damaged tissue, as zebrafish with impaired cardiac lymphatics cannot clear the infiltrating immune cells, thus leading to prolonged inflammation and reduced regeneration[18,20]. Interestingly, there

is limited lymphangiogenesis after ventricular resection in adult zebrafish, potentially due to the reduced inflammatory response and lack of scarring that follows ventricular resection[131]. Although the immune response appears to be promoting scar formation in the cryo-injured zebrafish (transient scar) and infarcted adult mouse heart (permanent scar), it is essential for the regeneration of neonatal mice hearts injured at P1[21]. Depletion of macrophages leads to impaired regeneration and reduced cardiac function after MI in P1 mice[21]. Given that macrophages are required for heart regeneration in P1 hearts, it is unclear how the cardiac lymphatic vessels respond and function to clear immune cells after MI at this regenerative setting. To date, the cardiac lymphatic response and their function after MI at neonatal stages have not been investigated.

6.2. Aims

The aims of this chapter were to characterise the response of cardiac lymphatics to MI, as well as their ability to clear macrophages from the site of injury to the MLN in regenerative P1 versus non-regenerative (fibrotic) P7 mice.

6.3. Results

6.3.1. *The lymphangiogenic response of cardiac lymphatics to myocardial infarction differs between P1 and P7 stages*

To examine the response of neonatal cardiac lymphatics after MI, the LAD coronary artery was surgically ligated in *Cd68-GFP* mice at P1 and P7 stages. Initially, hearts were harvested within 30 to 60 minutes after LAD ligation, termed 0 days post injury (dpi). Immunostaining for VEGFR3 allowed for visualisation of the lymphatic vasculature, while the endogenous CD68-GFP signal allowed for imaging of macrophages. The lymphatic vessels appeared to be expanding from the base of the heart to the site of injury at 0 dpi in both P1 and P7

stages (Figure 6.1). As described in chapter 5, the developing lymphatic network had more vessels and was morphologically more complex at P7 than at P1 (compare Figures 6.1 E-H to Figures 6.1 M-P). At 0 dpi, the macrophage response had not initiated yet, as there was no obvious increase in *Cd68-GFP*$^{+}$ macrophage representation near the injury site (Figure 6.1 A-D and Figure 6.1 I-L). The response of macrophages in P1 and P7 MI will be discussed in more detail in chapter 7.

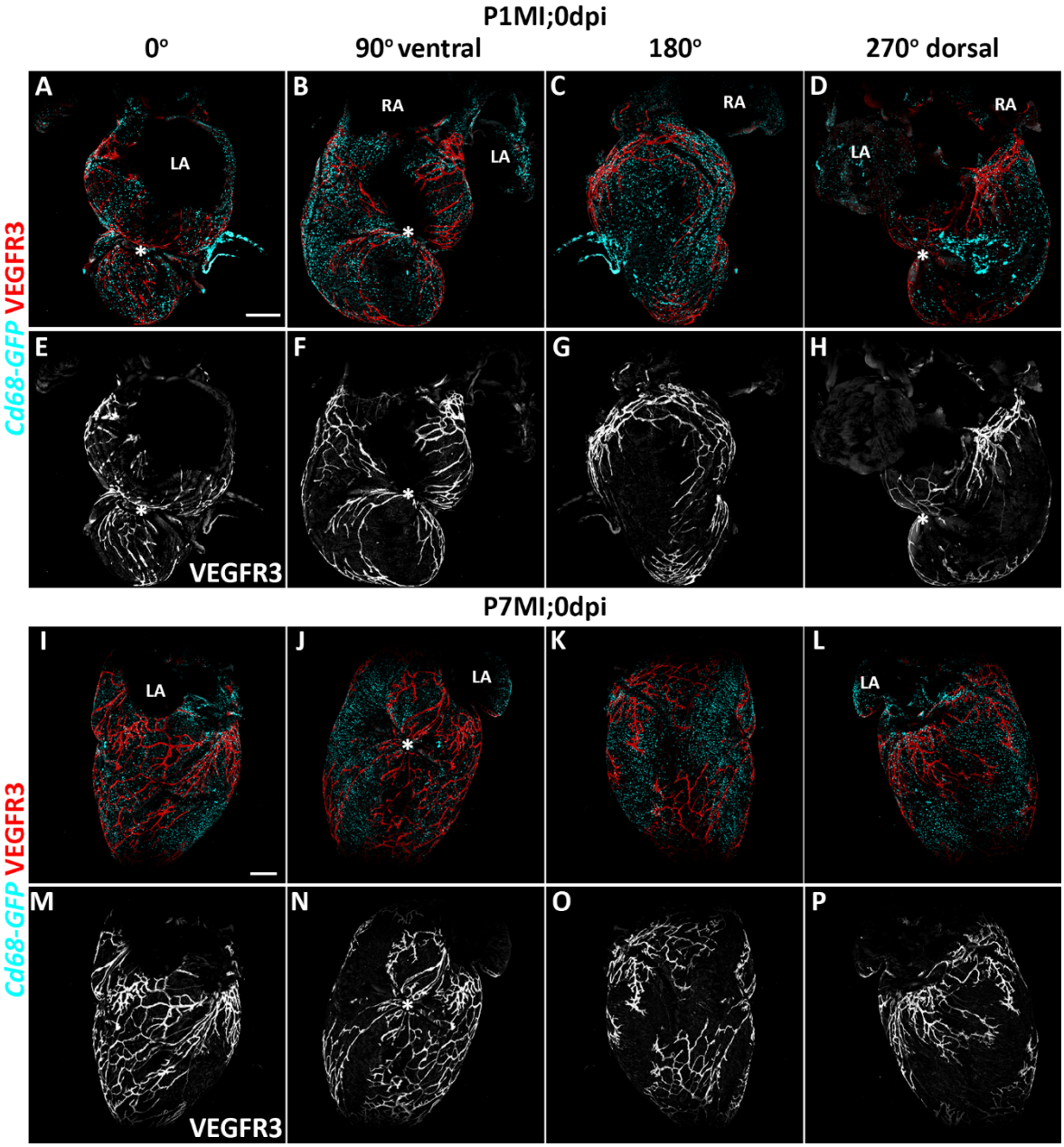

Figure 6.1 Postnatal cardiac lymphatics immediately after MI.

To assess the response of postnatal cardiac lymphatics and macrophages after MI, the LAD artery was surgically ligated at P1 and P7 stages. Immediately after surgery hearts were harvested to visualise lymphatic vessels and macrophages (A-D and I-L) at the onset of injury response. Macrophages covered equally all areas of the heart as the immune response had not initiated yet (A-D and I-L). Lymphatics extended from base to apex in both P1 (E-H) and P7 hearts (M-P). During ligation, the suture captured lymphatics that were located in the area of injury (asterisk in N and F). Asterisk – suture site; LA - left atria, RA - right atria. n = 2 for each time point. Scale bar: 0.5 mm.

In adult mice, cardiac lymphatics respond to the site of injury by 7 dpi[7,8]. Thus, the P1 and P7 mice were allowed to heal for 7 days before their heart was harvested. Whole-mount

light-sheet imaging of hearts stained for VEGFR3, showed limited lymphangiogenic response at the site of injury after P1 MI compared to intact age-matched control P8 hearts (compare Figure 6.2 B to D). Higher magnification revealed a limited presence of lymphatics proximal to the suture site (Figure 6.2 E). Also, a large vessel expanding from below the left atria to the injury site was consistently present in P1 MI hearts (Figure 6.2 E). Notably, lymphatics were also present in the same area in control P8 hearts, suggesting that these large vessels are a result of normal lymphatic development, rather than a response to infarction. On the dorsal side of the heart, the lymphatic network appeared unaffected by MI at P1 (compare Figure 6.2 A to C). In contrast to the limited lymphangiogenic response observed in P1 MI hearts, there was a clear response at the location of the suture in P7 MI hearts 7 dpi (Figure 6.2 J-K). Here, higher magnification revealed lymphatics surrounding the suture area (Figure 6.2 K). Apart from this, the rest of the lymphatic network on both dorsal and ventral sides of the heart appeared underdeveloped in P7 MI hearts 7dpi compared to P14 controls (compare Figure 6.2 G to I and H to J). These results suggest that there is a localised lymphangiogenic response at the site of injury, while the normal developmental program is delayed in the other areas of the heart 7 days after MI at P7, perhaps reflecting the whole-heart impact of myocardial ischemia. Notably, the size of hearts was significantly larger 7 days after MI in both P1 and P7 mice compared to the intact age-matched control P8 and P14 mice compare (Figure 6.2 F and L). This is potentially due to myocardial hypertrophy and/or increased oedema as a result of the cardiac injury, as previously reported in the adult mouse heart[152,252–255].

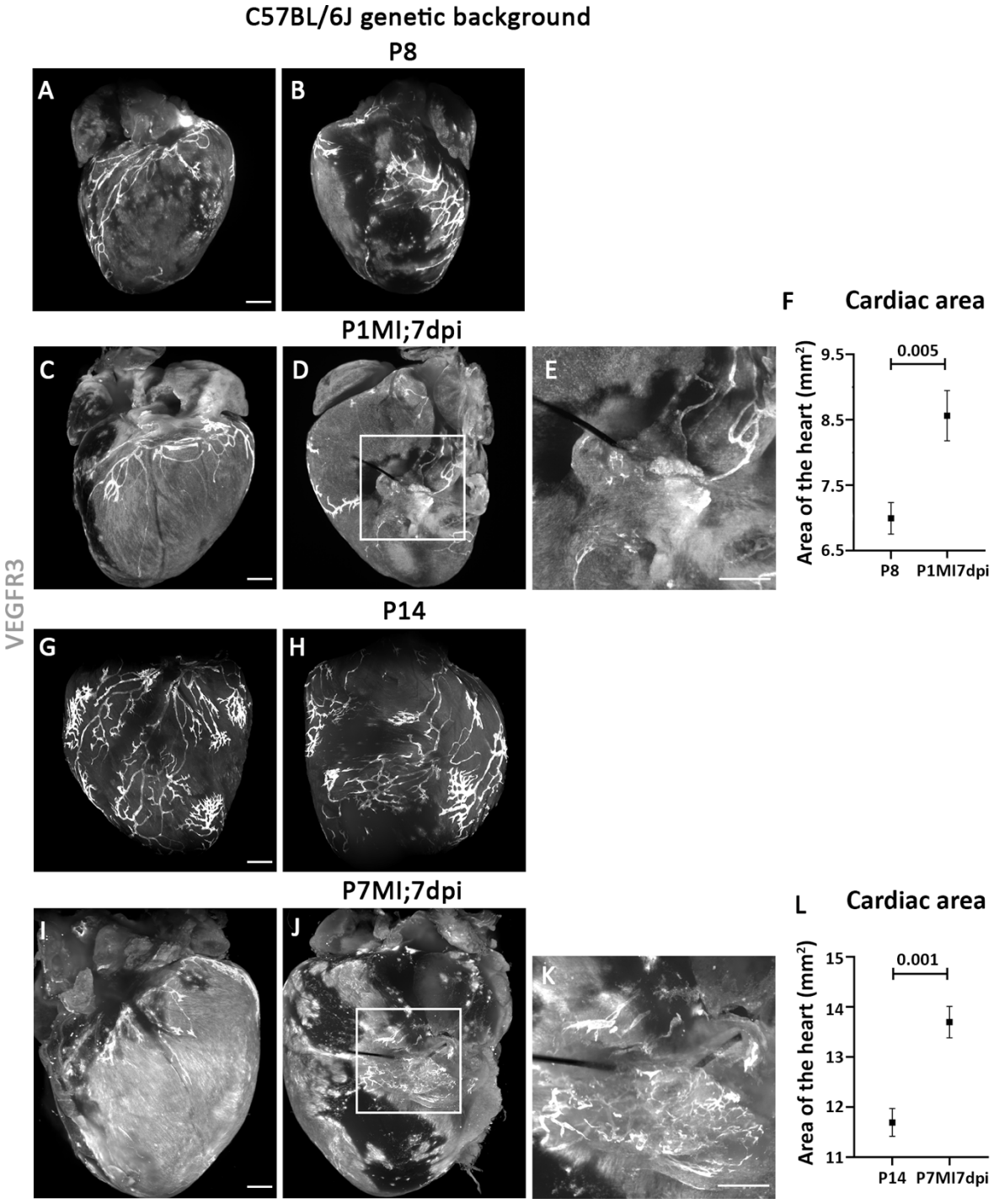

Figure 6.2 Limited lymphangiogenic response 7 days after MI at P1 in C57BL/6J mice.

Whole-mount immunostaining for VEGFR3 combined with light-sheet imaging showed a limited lymphangiogenic response after MI at P1 (D-E). Lymphatic vessels covered the injury site after MI at P7 (J-K). On the dorsal site of the heart, lymphatics appeared underdeveloped after MI at P7 compared to the P14 control (compare G with I), while no difference was observed between MI at P1 and the P8 control (compare A with C). There was a significant increase in the heart size after MI at both P1 and P7 compared to the respective control stage (F and L). E – magnified view of D box; K – magnified view of J box. Data are presented as mean ± SEM; n = 4-8 for each time point. Significant differences were calculated using an unpaired, 2-tailed Student's t test. Scale bar: 0.5 mm.

To confirm the results observed by whole-mount staining, transverse serial-sections of MI and intact hearts were stained against lymphatic markers PDPN and LYVE1 and imaged using confocal microscopy (Figure 6.3). In both P8 and P14 intact hearts, lymphatics were found scattered throughout the sub-epicardial space of the heart. Also, the lumen of the lymphatics appeared collapsed, with *Cd68-GFP*$^{+}$ macrophages not co-localising with the vessels (Figure 6.3 A-E and Figure 6.3 K-O). However, a lymphangiogenic response was seen 7 days after MI at P7 (Figure 6.3 P-T), and to a lesser extent after MI at P1 (Figure 6.3 F-J). Specifically, lymphatics were found concentrated in the area of injury indicated by the increased number of macrophages after MI at P7 (Figure 6.3 P-T). Compared to the controls, the vessels of the P7 MI hearts infiltrated deeper into the myocardium, were enlarged and surrounded by *Cd68-GFP*$^{+}$ macrophages (compare Figure 6.3 P-T to K-O). After MI at P1, the lymphatic response was detectable, albeit in a smaller scale compared to P7MI hearts (compare Figure 6.3 F-J to P-T). Lymphatic vessels were found near the suture after MI at P1, however, they showed a significantly reduced lumen size compared to the lymphatics after MI at P7 (Figure 6.3 U and compare Figure 6.3 F-J to P-T). Finally, after MI at P1 an increased concentration of macrophages was detected around the area of injury as compared to P8 controls (compare Figure 6.3 H to C).

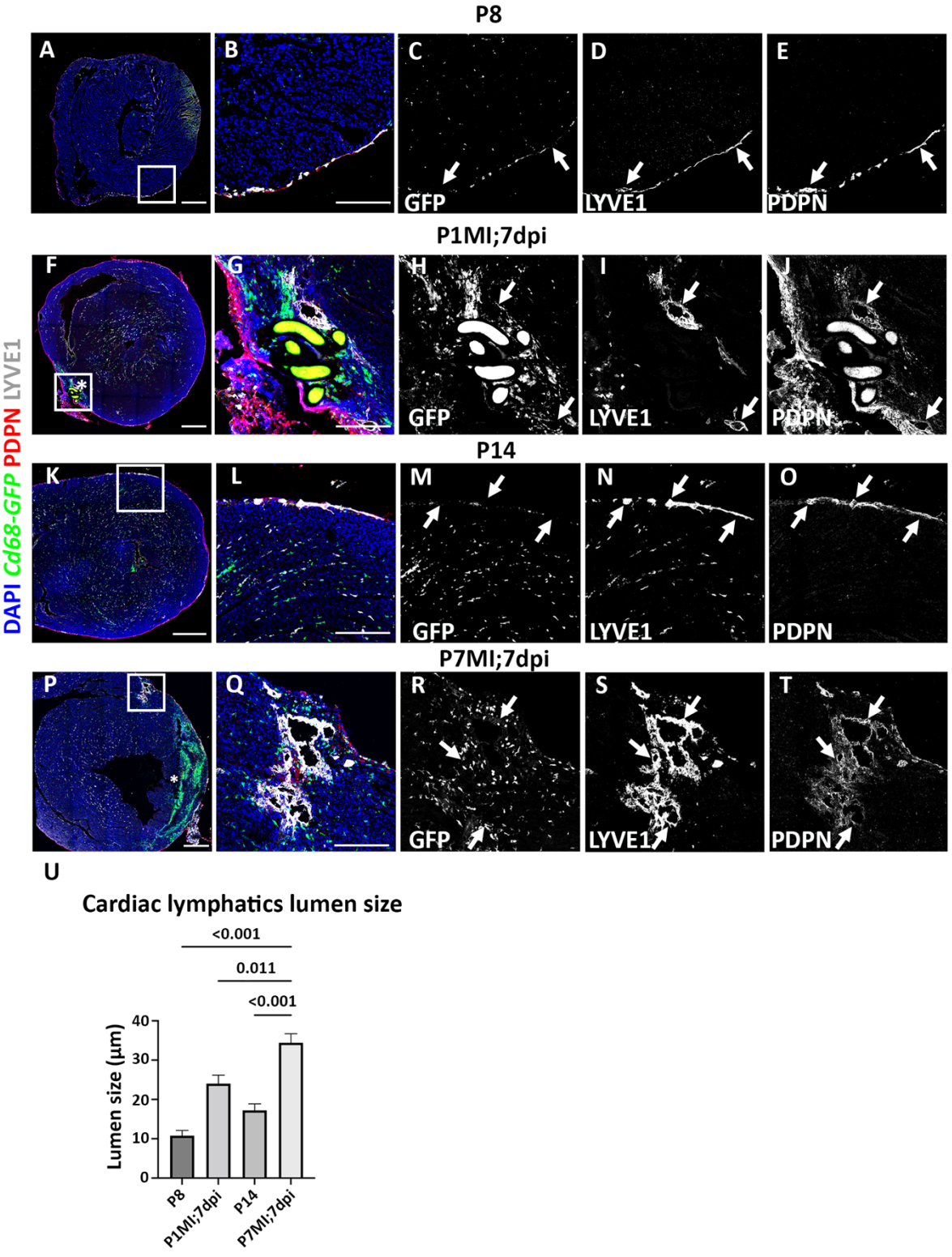

Figure 6.3 Lymphatic vessels are enlarged 7 days after MI at P1 and P7 in C57BL/6J mice.

Serial section staining for PDPN and LYVE1 combined with confocal imaging confirmed the limited lymphangiogenic response after MI at P1 compared to MI at P7 (compare G-J with Q-T). After MI there was increased number of lymphatic vessels with dilated lumen, more pronounced in P7MI samples, compared to the respective intact control (compare B with G and L with Q). *Cd68-GFP*$^{+}$

macrophages were enriched in the site of injury after MI at P1 and P7 (H and R). Suture visible through autofluorescence in panels F-H and J. Quantification of cardiac lymphatic lumen (U). B-E – magnified view of A box; G-J – magnified view of F box; L-O – magnified view of K box; Q-T – magnified view of P box. Data are presented as mean ± SEM; n = 3-4 for each time point. Significant differences were calculated using 1-way ANOVA followed by Tukey's multiple comparisons test. Scale bar: 0.5 mm for A, F, K and P; 0.2 mm for magnified views.

6.3.2. *The response of cardiac lymphatics to myocardial infarction is different depending on genetic background.*

In chapter 5 it was shown that the cardiac lymphatic network develops faster and to a greater extent during post-natal stages in CD1 mice compared to C57BL/6J mice. Thus, whole-mount immunostaining was used to investigate potential differences in the cardiac lymphatic response after MI at P1 in the different genetic backgrounds (Figure 6.4). Strikingly, a clear response of cardiac lymphatics to the area of injury was observed in CD1 mice after MI at P1 (compare Figure 6.4 B to D-E). This contrasts with the limited response that was observed in C57BL/6J mice (Figure 6.2 D-E). However, the hearts showed extensive growth after MI independent of the genetic background, suggesting that the lymphangiogenic response in CD1 hearts is not the driver for changes in the heart's size (Figure 6.4 F). Also, the lymphatics on the dorsal side of the heart appeared unaffected by the injury at P1 in both CD1 and C57BL/6J mice (compare Figure 6.4 A to C).

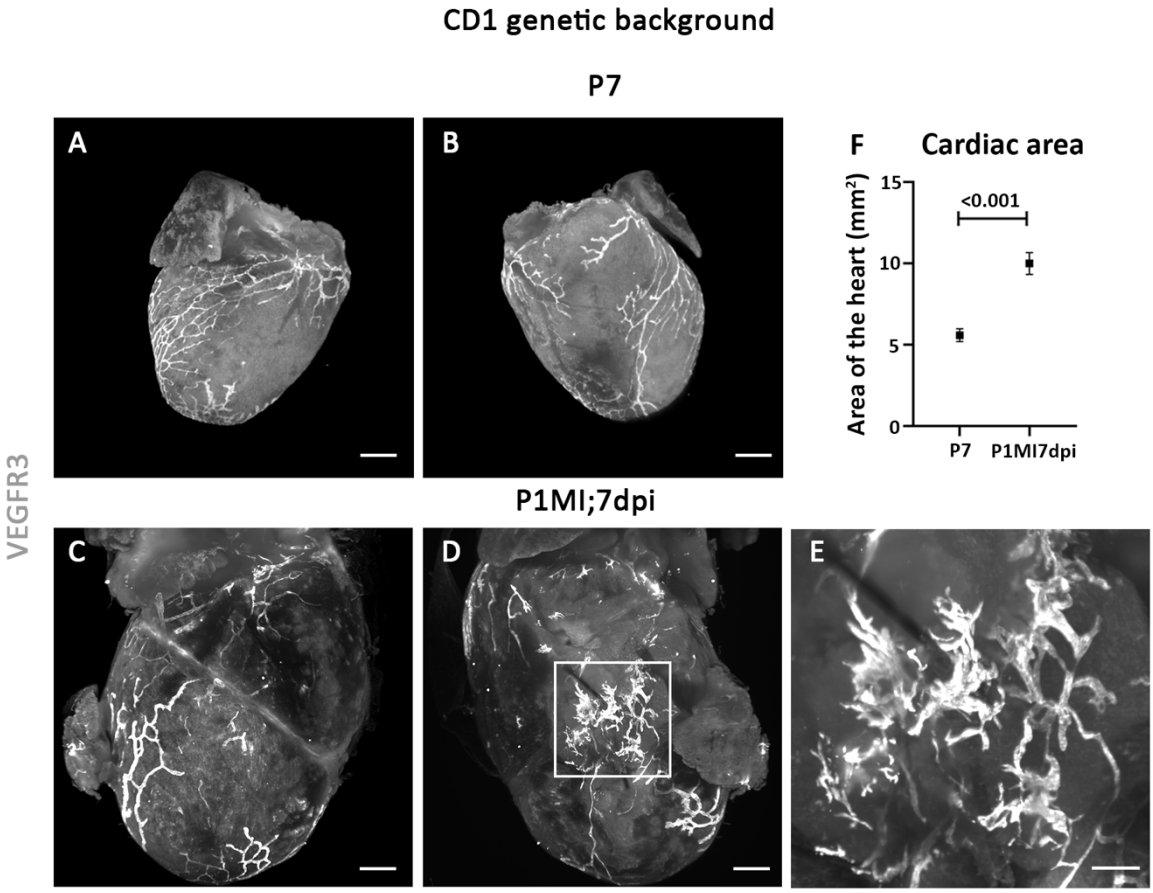

Figure 6.4 Increased lymphangiogenic response 7 days after MI at P1 in CD1 mice.

Whole-mount immunostaining for VEGFR3 combined with light-sheet imaging showed increased lymphangiogenic response after MI at P1 in CD1 mice compared to the P7 intact control (compare D-E with B. There was a significant increase in the heart size after MI at P1 compared to the control (F). E – magnified view of D box. Data are presented as mean ± SEM; n = 4-5 for each time point. Significant differences were calculated using an unpaired, 2-tailed Student's t test. Scale bar: 0.5 mm.

6.3.3. *Cardiac lymphatics clear macrophages from the heart to the mediastinal lymph nodes with different efficiency after myocardial infarction at P1 and P7*

After having shown that cardiac lymphatic response 7 days after P1 injury differs depending on genetic background, the lymphatics' function to clear macrophages from the heart to MLNs 7 days after MI at P1/P7 was assessed. First, adoptive cell transfer of *hCD68-eGFP* monocytes was performed as described in detail in the Material and Methods section. Briefly, splenic *hCD68-eGFP* monocytes were isolated from adult mice and approximately

$30x10^3$ cells were injected into the myocardium of CD1 P1 and P7 recipient mice at the time of MI surgery (Figure 6.5 A). The number of cells injected was based on a previous study that performed adoptive transfer by intramyocardial injection of $100x10^3$ cells in adult recipient mice[76], and it was adjusted to the smaller size of neonatal hearts compared to adult hearts. The hearts and MLNs were harvested at 7 dpi and imaged to identify GFP^+ macrophages engrafted in the heart, as well as cleared GFP^+ macrophages in the MLNs (Figure 6.5 A).

The identification of lymph nodes in early postnatal mice was challenging, as they are very small and embedded in surrounding thoracic tissue at these stages, thus staining for PDPN was used to confirm their identity. PDPN had a distinct expression pattern and was found in the periphery, as well as occasionally in the central area of MLNs (Figure 6.5 B and F). MLNs were also stained with antibody against the pan-macrophage marker CD68, to confirm that the GFP^+ cells were indeed macrophages (Figure 6.5 C-D and G-H). Interestingly, only a small number of individual GFP^+ macrophages was identified in the MLNs of mice that underwent MI at P1 (Figure 6.5 E). However, large clusters of GFP^+ macrophages were present in the MLNs of mice that underwent MI at P7 (Figure 6.5 I). Quantification of cleared GFP^+ macrophages in the MLNs was not performed due to technical limitations of the adoptive transfer experiment. Specifically, the number of GFP^+ that were injected in the heart could not be exact and consistent for each sample, as macrophages died during the injection process and/or did not enter the myocardium. As a result, the adoptive transfer data suggest that cardiac lymphatics may clear macrophages from the heart to the MLNs with less efficiency after MI at P1 than after MI at P7; however, more experiments need to be performed to verify this.

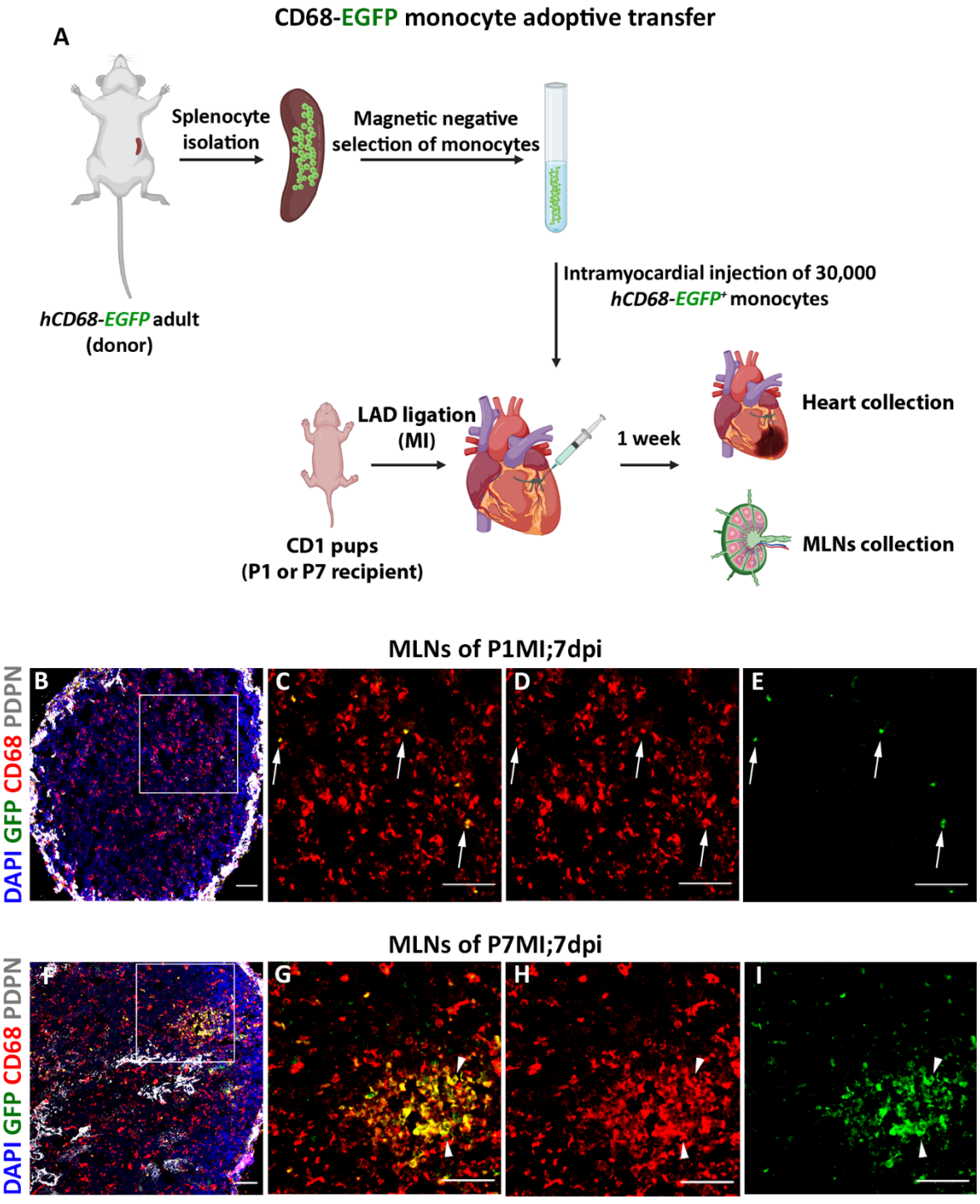

Figure 6.5 Adoptive transfer of splenic GFP+ monocytes indicates different efficiency in immune cell clearance to MLNs after MI at P1 and P7.

Schematic of the adoptive cell transfer approach using adult *hCD68-EGFP* transgenic mice as splenic GFP$^+$ monocyte donor and recipient neonatal CD1 mice receiving intramyocardial delivery of labelled monocytes at the time of LAD artery ligation, to assess immune cell trafficking to MLNs (A). Immunostaining for GFP (green) and CD68 (red) of tissue sections derived from MLNs of P1 and P7 mice that underwent MI indicated the presence of cleared CD68$^+$GFP$^+$ macrophages (C white

arrows and G white arrowheads). However, $CD68^{+}GFP^{+}$ macrophages presence was reduced after MI at P1 compared to after MI at P7 (compare E with I). C-E - magnified views of B box; G-I – magnified views of F box. n = 4. Scale bars: 50 µm.

Immunostaining of CD68 and GFP was performed in hearts from the recipient CD1 mice to confirm that the adoptive transfer was successful. As expected, GFP^{+} macrophages were present in all hearts and were located predominately at the site of injury in both P1 (Figure 6.6 A-B) and P7 mice (Figure 6.6 C-D). This confirms that GFP^{+} macrophages were successfully transferred to the heart of recipient mice, as well as that macrophages had not been fully cleared from either the P1 or the P7 heart a week after the MI.

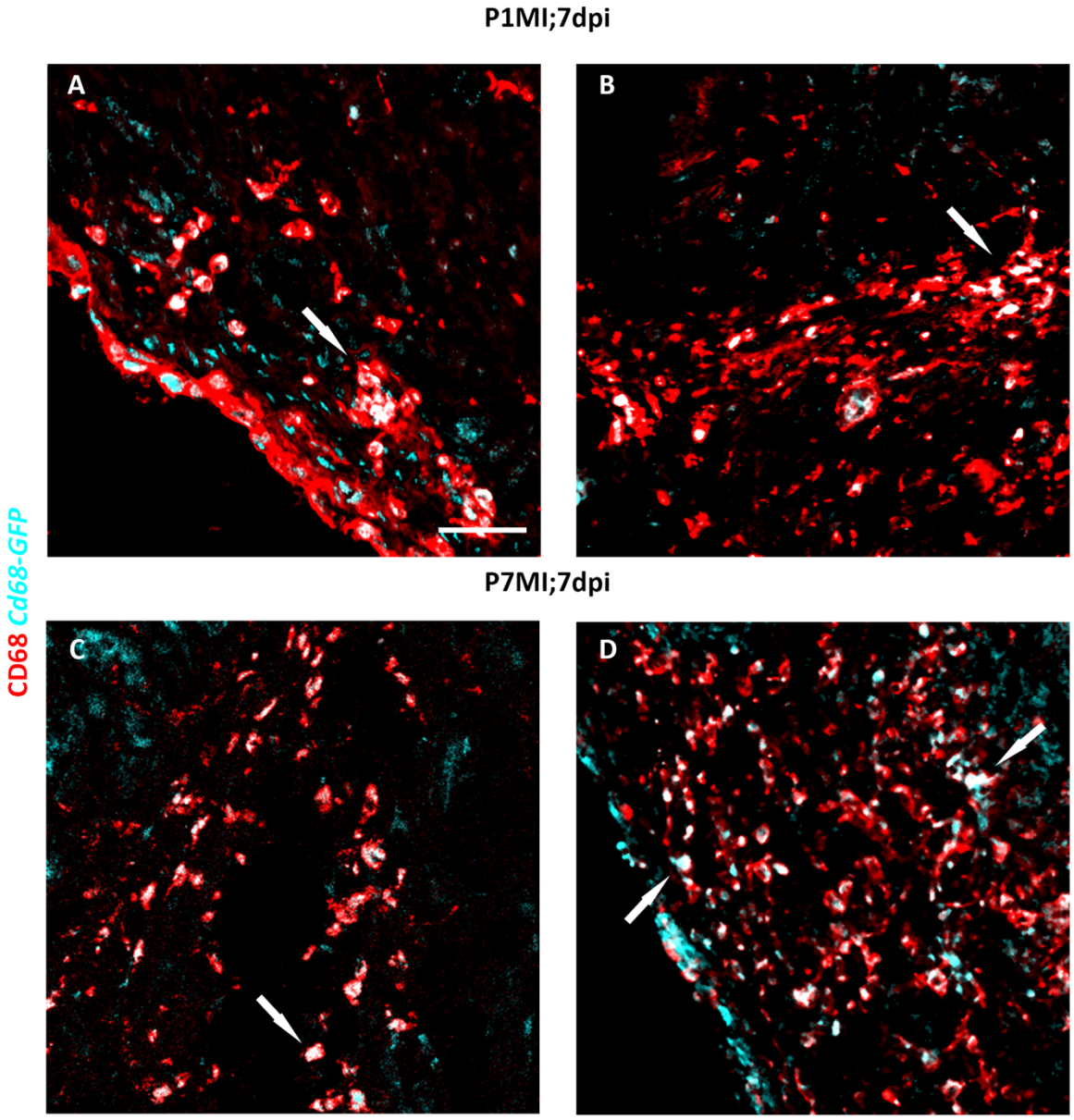

Figure 6.6 Successful engraftment of CD68+GFP+ monocytes in the heart after adoptive cell transfer.

GFP (cyan) and CD68 (red) immunostaining of cardiac tissue sections documenting engraftment of CD68+GFP+ monocytes within the injury area 7 days after adoptive transfer at P1 and P7 (white arrows). Images are from two representative hearts for each condition. n = 4. Scale bar: 50µm.

To further validate the data from the adoptive transfer experiment, MLNs were isolated from *Cd68-GFP* injured and control mice. The MLNs were sectioned, and images were acquired for quantification of the $CD68^{+}$ macrophage numbers in relation to the lymph node size (Figure 6.7). The quantification of $CD68^{+}$ macrophages was calculated as the

percentage of total $CD68^+$ stained area to the total DAPI-labelled tissue area. Interestingly, the presence of $CD68^+$ macrophages in MLNs 7 days after MI at P1 (mean ± SEM: 5.6 ± 1.7 %) was found to be increased compared to intact P8 hearts (mean ± SEM: 2.9 ± 0.8 %) (Figure 6.7 I and compare Figure 6.7 A-B to C-D). Similarly, macrophage concentration was elevated after MI at P7 (mean ± SEM: 20.1 ± 4.1 %) compared to P14 intact hearts (11.8 ± 6.8 %) (Figure 6.7 I and compare Figure 6.7 E-F to G-H). While there was increased macrophage clearance from the heart to the MLNs in both P1 and P7 stages after MI, the concentration of macrophages after MI at P1 (mean ± SEM: 5.6 ± 1.7 %) was significantly lower compared to the MI at P7 (mean ± SEM: 20.1 ± 4.1 %; $p < 0.009$) (Figure 6.7 I and compare Figure 6.7 C-D to G-H).

Taken together, the results of the adoptive transfer and macrophage quantification experiments suggest that cardiac lymphatics in both CD1 and C57BL/6J mice may clear macrophages from the heart to the regional lymph nodes less efficiently after P1MI than P7MI. In the future, more experiments need to be conducted to provide further evidence of the cardiac lymphatic clearing ability after P1 and P7MI, as the adoptive transfer contained multiple variables (discussed in chapters 9 and 11).

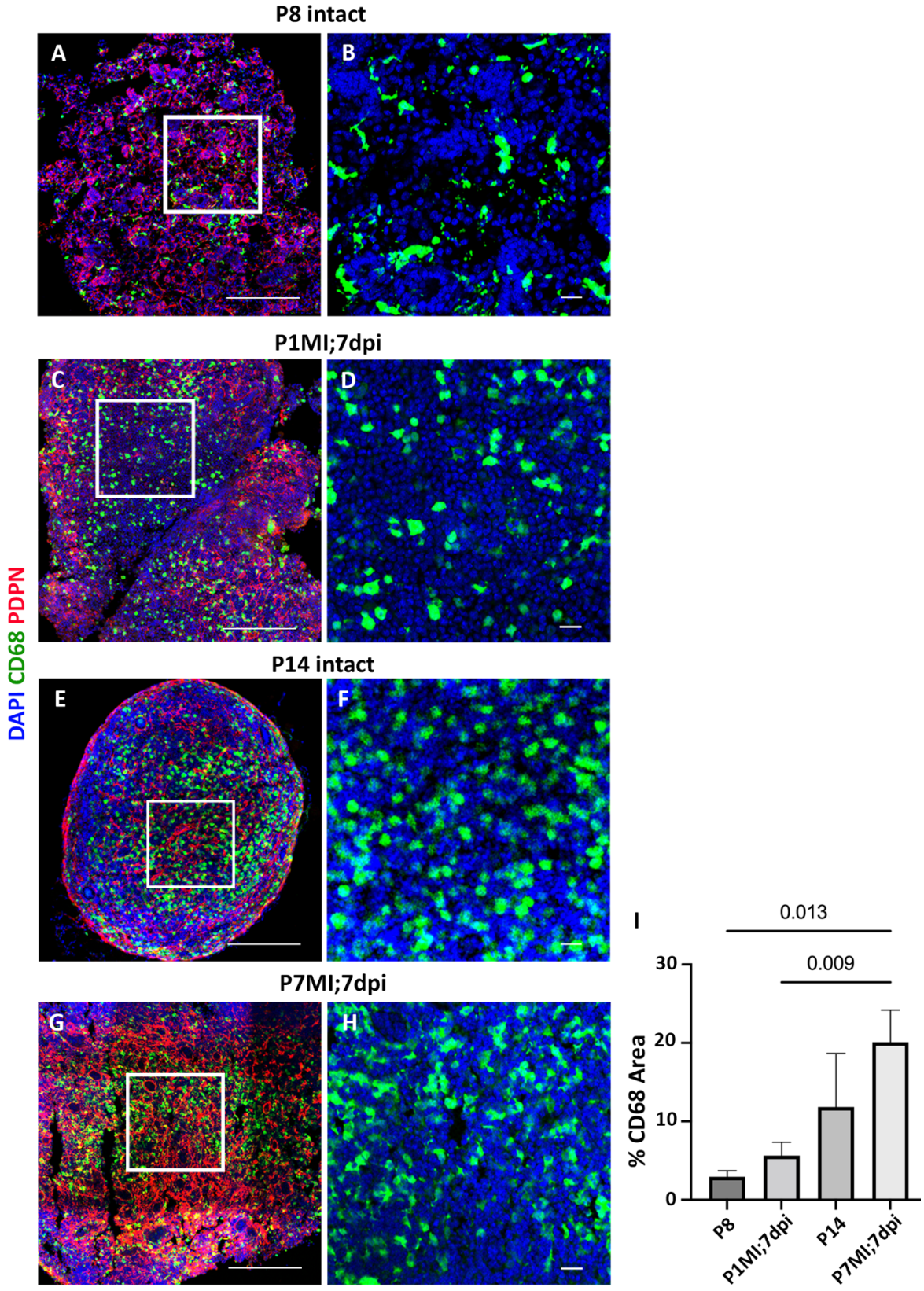

Figure 6.7 Imaging MLNs from CD68-GFP+ mice confirms different efficiency of macrophage clearance after MI at P1 compared to MI at P7.

Visualisation of endogenous CD68-GFP from MLNs confirmed the increased macrophage clearance after MI at both P1 and P7 compared to the respective controls (compare B to D and F to H). The number of GFP^+ macrophages appeared smaller after MI at P1 compared to after MI at P7 (compare D to H). Quantification of macrophage concentration in the MLNs further validated these observations (I). B – magnified view of A box; D – magnified view of C box; F – magnified view of E box; H – magnified view of G box. Data are presented as mean ± SEM; n = 3-5 for each time point. Significant differences were calculated using 1-way ANOVA followed by Tukey's multiple comparisons test. Scale bars: 0.5 mm for A, C, E and G; 20 µm for B, D, F and H.

6.3.4. *Gene expression of lymphatic markers is reduced after myocardial infarction at P1*

To understand whether the differences observed in response and function of cardiac lymphatics after MI at P1 and P7 are a result of different expression profiles of genes related to lymphangiogenesis and cell clearance, qPCR was performed using whole-heart extracts (Figure 6.8 and Figure 6.9). The expression level of the lymphangiogenic factor *Vegfr3* decreased significantly 7 days after MI at P1 compared to the P8 control (LogFC ± SEM: -1.44 ± 0.06 vs 0.01 ± 0.08; $p < 0.001$) (Figure 6.8 A). Expression of the VEGFR3 ligand *Vegfd* also decreased, but this was found not to be statistically significant (LogFC ± SEM: -0.45 ± 0.17 vs 0.02 ± 0.11; $p = 0.054$) (Figure 6.8 C). Meanwhile, *Vegfc* and the master regulator of LECs, *Prox1*, showed similar expression levels in P1 hearts 7 days after MI and the P8 control (LogFC ± SEM: -0.13 ± 0.11 vs 0.01 ± 0.09; $p = 0.374$ and -0.04 ± 0.23 vs 0.03 ± 0.14; $p = 0.783$, respectively) (Figure 6.8 B and D). In contrast, expression levels of both *Vegfc* and *Vegfd* increased significantly 7 days after MI at P7 (LogFC ± SEM: 0.56 ± 0.04 vs 0.03 ± 0.17; $p = 0.01$ and 0.99 ± 0.08 vs 0.03 ± 0.19; $p = 0.003$, respectively), almost to double the levels of the P14 control (Figure 6.9 B-C). However, expression levels of *Vegfr3* and *Prox1* were the same in hearts after MI at P7 and the P14 control (LogFC ± SEM: -0.51 ± 0.14 vs 0.07 ± 0.27; $p = 0.626$ and 0.65 ± 0.04 vs 0.03 ± 0.19; $p = 0.119$, respectively) (Figure 6.9 A and D). Interestingly, expression of genes responsible for the clearance of immune cells by lymphatics, *Ccl21* and *Lyve1*, were found to be significantly decreased 7

days after MI at P1 to less than half of the expression levels seen in the P8 control (LogFC ± SEM: -1.63 ± 0.2 vs 0.01 ± 0.1 and -1.34 ± 0.14 vs 0.01 ± 0.08, respectively; $p < 0.001$) (Figure 6.8 E-F). However, the expression of both *Ccl21* and *Lyve1* was the same 7 days after MI at P7 as compared to the P14 control (LogFC ± SEM: -0.33 ± 0.04 vs 0 ± 0.09; $p = 0.503$ and 0.58 ± 0.19 vs 0.13 ± 0.39; $p = 0.184$, respectively) (Figure 6.9 E-F).

Generally, expression levels of genes associated with lymphangiogenesis and immune cell clearance were found to be either stable or decreased after MI at P1 compared to the P8 control. Whereas, gene expression levels were either stable or increased after MI at P7 compared to the P14 control. Notably, these data were generated from whole-heart extracts and are therefore not LEC-specific.

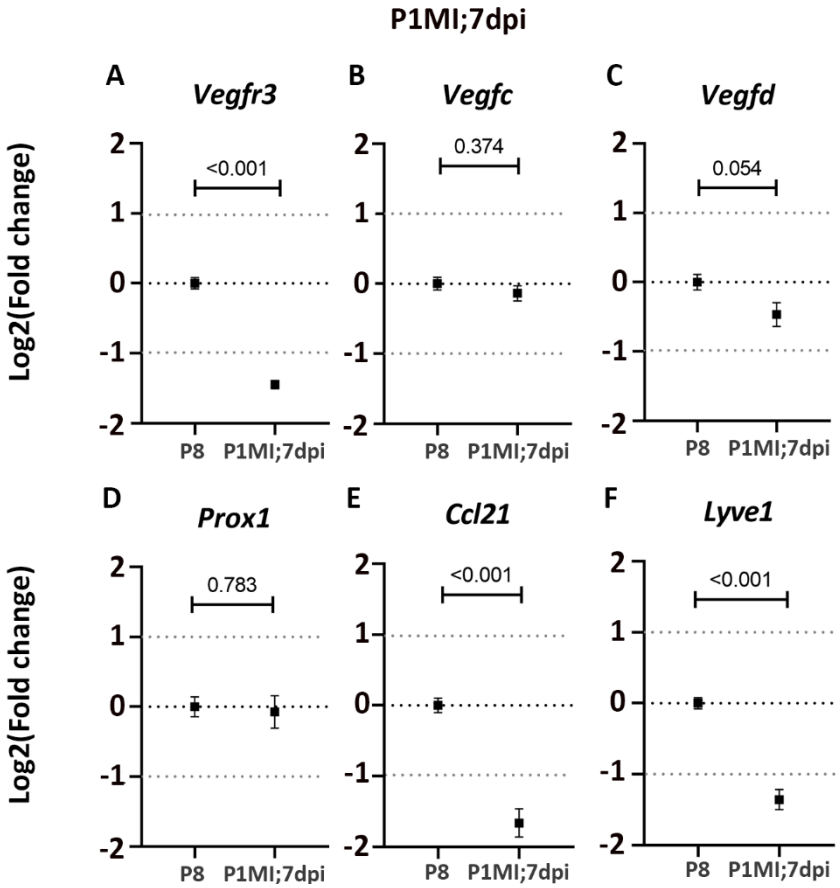

Figure 6.8 Gene expression of lymphatic markers is reduced 7 days after MI at P1 compared to P8 intact.

Whole-heart qPCR data showed that gene expression of lymphangiogenic markers either reduces significantly (A) or is at the same level (C-D) after MI at P1 compared to the P8 control. Gene expression of *Ccl21* and *Lyve1*, which are associated with lymphatic function, was found significantly reduced after MI at P1 compared to control. Data are presented as mean ± SEM; n = 3-4 for each time point. Significant differences were calculated using an unpaired, 2-tailed Student's t test.

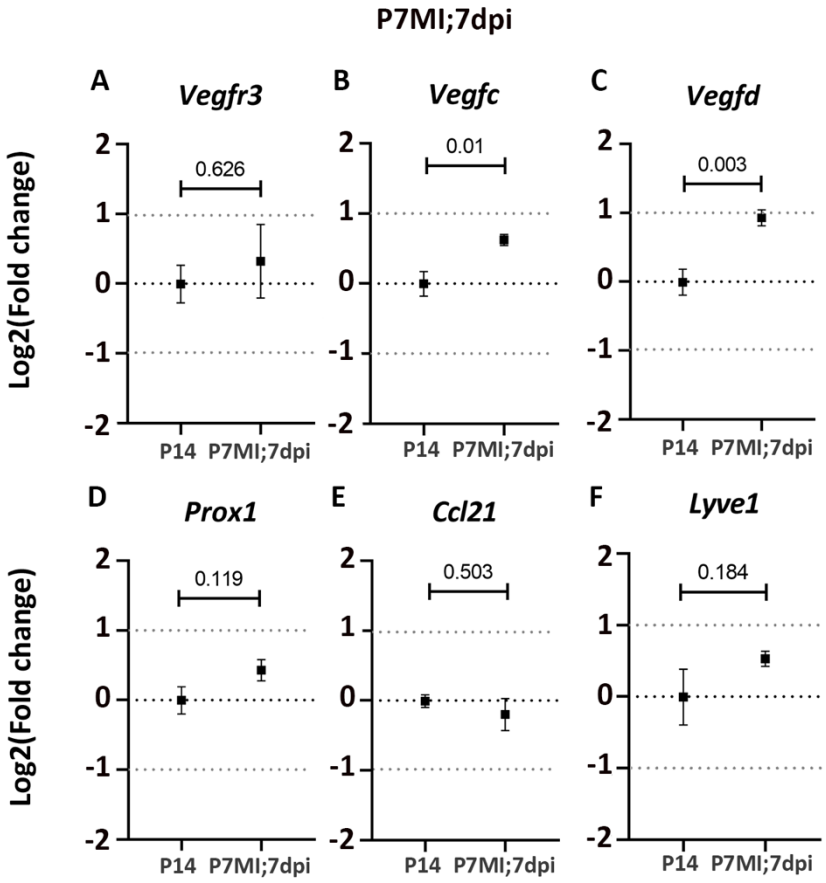

Figure 6.9 Gene expression of lymphatic markers is increased 7 days after MI at P7 compared to P14 intact.

Whole-heart qPCR data showed that gene expression of lymphangiogenic markers either increases significantly (B-C) or is at the same level (A and D) after MI at P7 compared to the P14 control. Gene expression of *Ccl21* and *Lyve1*, which are associated with lymphatic function, was found the same at P14 control and after MI at P7. Data are presented as mean ± SEM; n = 4-5 for each time point. Significant differences were calculated using an unpaired, 2-tailed Student's t test.

6.3.5. *Vascular endothelial cells proliferate after myocardial infarction at P1*

To gain a deeper insight into the cellular heterogeneity of P1 and P7 hearts after MI with respect to molecular differences in response to injury, scRNA-seq was performed at different time points using the 10X Genomics Chromium platform (Figure 6.10). The heart, spleen, bone morrow and blood were isolated from CD1 mice. Intact P1 and P7 mice served as controls, while MI was performed either at P1 or P7 and subsequently mice were culled 1 day or 7 days after injury to capture the cell populations that respond to the early and later stages of injury, respectively. Although cDNA libraries were prepared from all four

organs, for the purpose of this thesis only the hearts were sequenced. Also, the cells from each condition were pooled together and sequenced as individual samples, thus no statistical tests could be performed. After sequencing, the data were analysed in R using the previously published Seurat pipelines[230].

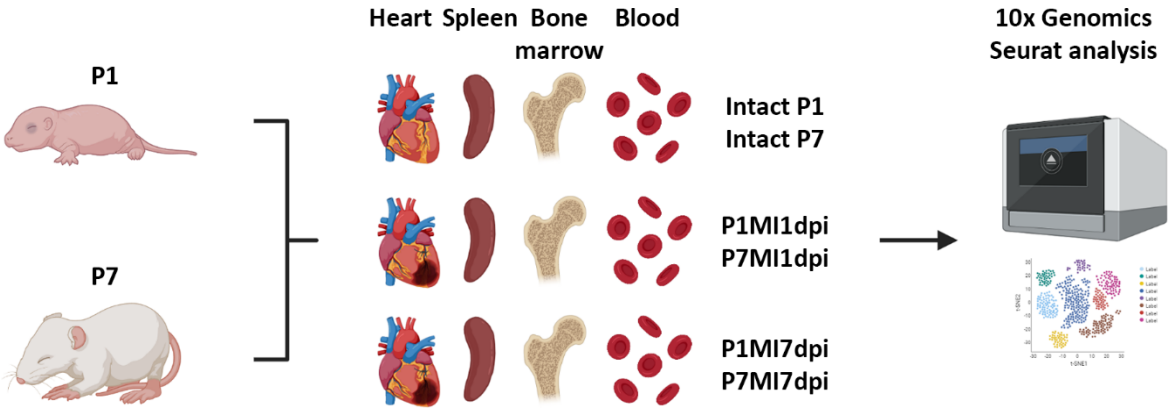

Figure 6.10 Experimental design for scRNA-seq.

Schematic of the approach that was used to perform scRNA-seq for the heart, spleen, bone marrow and blood of control and injured CD1 mice. For the injured conditions, the LAD artery was surgically ligated either at P1 or at P7. Next the organs were harvested at 1dpi (P1MI1dpi and P7MI1dpi) or 7dpi (P1MI7dpi and P7MI7dpi). For the intact conditions, the samples were collected at either P1 or P7 without any prior surgery (Intact P1 and Intact P7). The samples were FACS-isolated using the 7AAD marker to isolate the live cells and libraries were prepared for sequencing using the 10x Genomics platform. After scRNA-seq the data were processed in R environment using the previously published Seurat pipelines. n = 3 animals were used for tissue collection. n = 1 sequencing library was generated for each time point and condition.

Using both automated cluster annotation and manual consolidation of published gene markers[231,256] for individual cell types, 21 clusters of cells with defined gene expression signatures were identified (Figure 6.11 A-B). The following clusters with respective signature genes markers were determined: cardiomyocytes (CM; *Myh6* [Myosin Heavy Chain 6]), six clusters of ECs (Art EC, VEC 1, VEC 2, Endo, Prol VEC and LEC; *Cdh5* [Cadherin 5]), four clusters of fibroblasts (Fb 1, Fb 2, Fb 3 and Prol Fb; *Pdgfra*), epicardial cells (Epic; *Msln*), smooth muscle cells (SMC; *Myh11*), pericytes (Peri; *Kcnj8*), macrophages and

monocytes (Mf; *Adgre1*), dendritic cell-like cells (DC-like, *Naaa*), granulocytes (Gran, *S100a9*), T-cells (*Cd3g* [CD3g), B-cells (*Ms4a1*), glial cells (*Plp1*), and platelets (*Itga2b*) (Figure 6.11). For LECs the top five differentially expressed genes were *Ccl21a*, *Mmrn1* (Multimerin 1), *Lyve1*, *Prox1*, and *Reln* (Reelin) (Figure 6.11 A). Two-dimensional visualisation using Uniform Manifold Approximation and Projection (UMAP) revealed four major clusters: endothelial cells, fibroblasts, immune cells, as well as mural pericytes and smooth muscle cells (Figure 6.11 C). This suggests comparable gene expression features within the four individual cell populations.

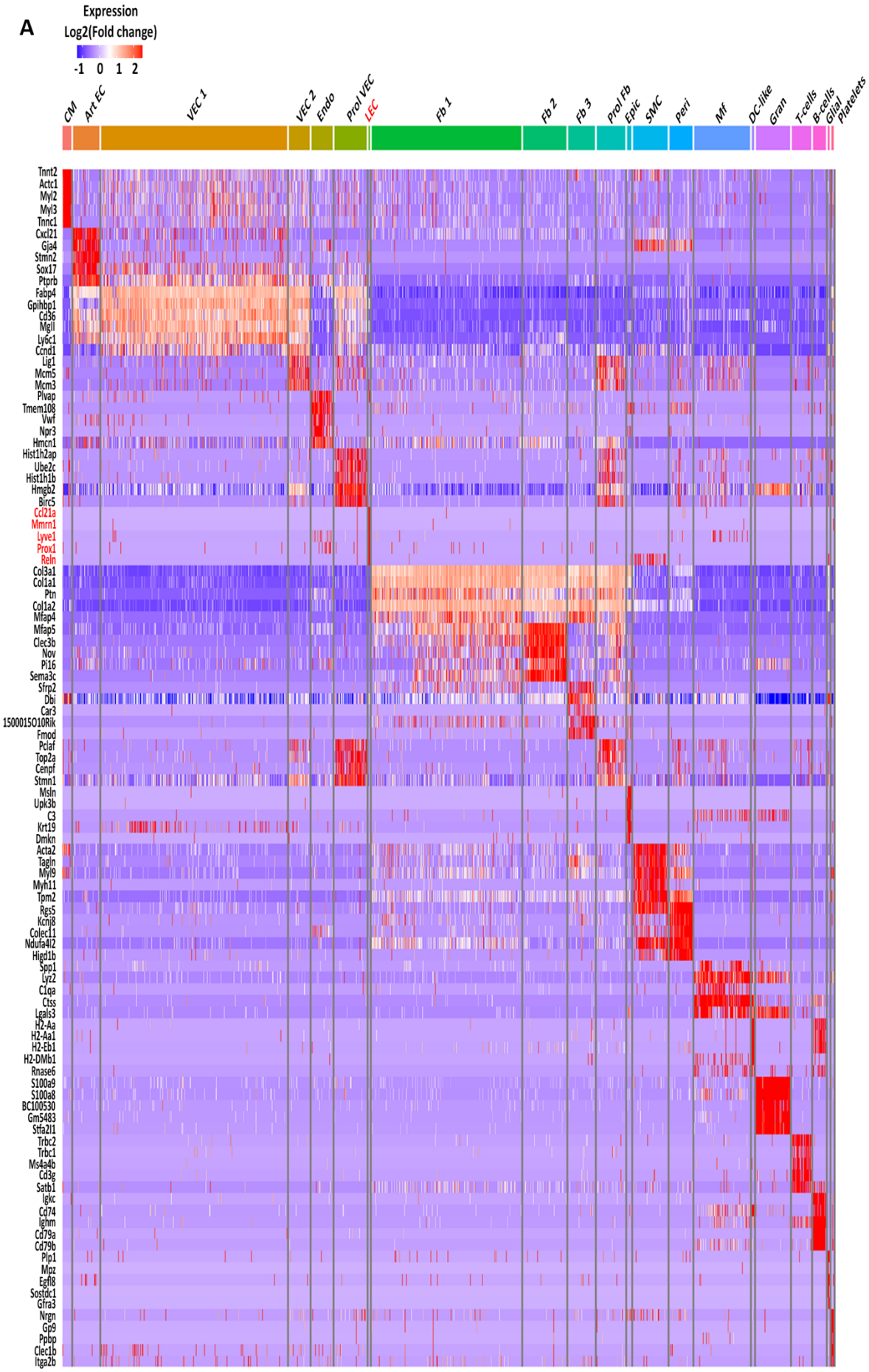
A
Expression
Log2(Fold change)
-1 0 1 2
CM
Art EC
VEC 1
VEC 2
Endo
Prol VEC
LEC
Fb 1
Fb 2
Fb 3
Prol Fb
Epic
SMC
Peri
Mf
DC-like
Gran
T-cells
B-cells
Glial
Platelets
Tnnt2
Actc1
Myl2
Myl3
Tnnc1
Cxcl21
Gja4
Stmn2
Sox17
Ptprb
Fabp4
Gpihbp1
Cd36
Mgll
Ly6c1
Ccnd1
Lig1
Mcm5
Mcm3
Plvap
Tmem108
Vwf
Npr3
Hmcn1
Hist1h2ap
Ube2c
Hist1h1b
Hmgb2
Birc5
Ccl21a
Mmrn1
Lyve1
Prox1
Reln
Col3a1
Col1a1
Ptn
Col1a2
Mfap4
Mfap5
Clec3b
Nov
Pi16
Sema3c
Sfrp2
Dbi
Car3
1500015O10Rik
Fmod
Pclaf
Top2a
Cenpf
Stmn1
Msln
Upk3b
C3
Krt19
Dmkn
Acta2
Tagln
Myl9
Myh11
Tpm2
Rgs5
Kcnj8
Colec11
Ndufa4l2
Higd1b
Spp1
Lyz2
C1qa
Ctss
Lgals3
H2-Aa
H2-Aa1
H2-Eb1
H2-DMb1
Rnase6
S100a9
S100a8
BC100530
Gm5483
Stfa2l1
Trbc2
Trbc1
Ms4a4b
Cd3g
Satb1
Igkc
Cd74
Ighm
Cd79a
Cd79b
Plp1
Mpz
Egfl8
Sostdc1
Gfra3
Nrgn
Gp9
Ppbp
Clec1b
Itga2b

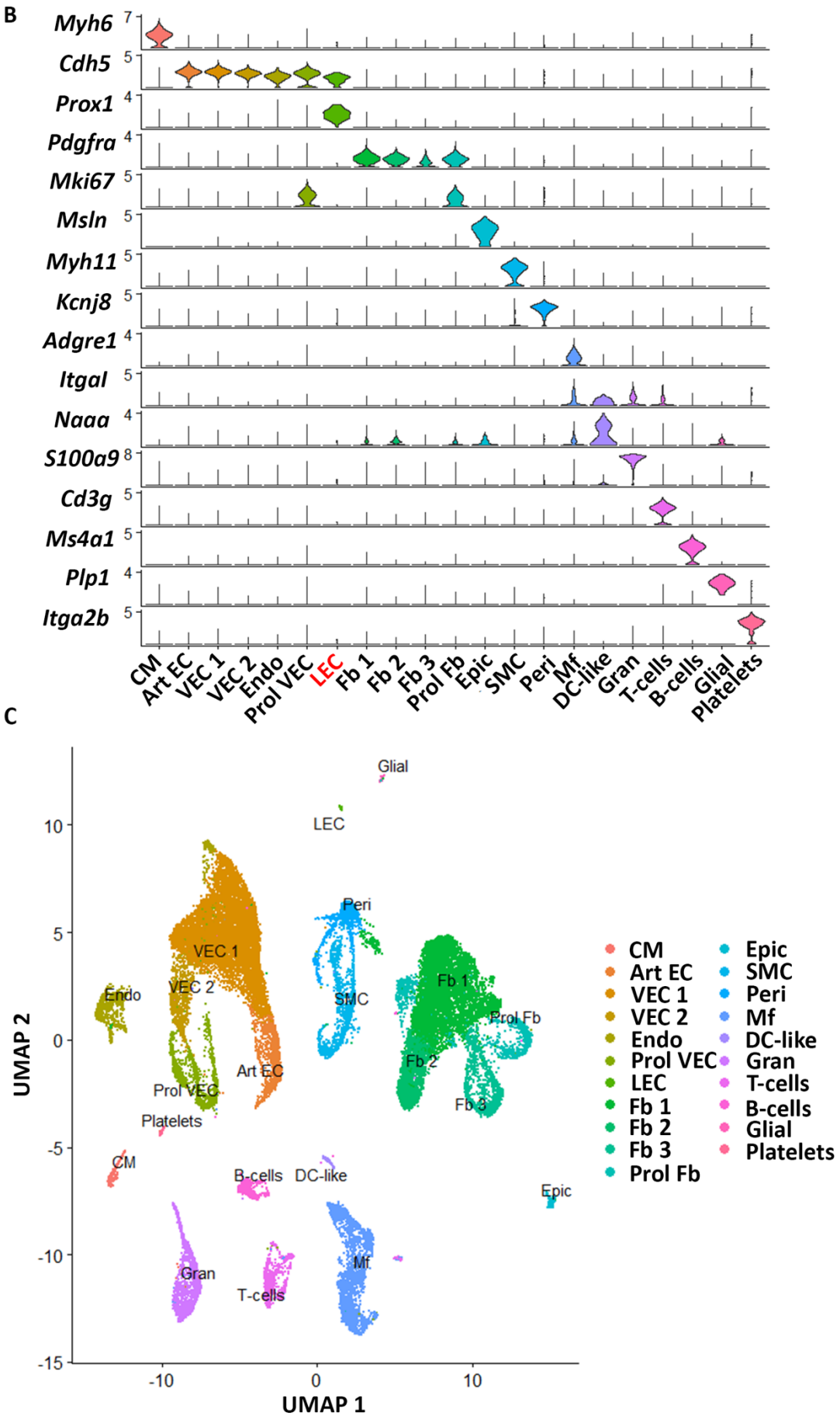
B
Myh6
Cdh5
Prox1
Pdgfra
Mki67
Msln
Myh11
Kcnj8
Adgre1
Itgal
Naaa
S100a9
Cd3g
Ms4a1
Plp1
Itga2b
CM
Art EC
VEC 1
VEC 2
Endo
Prol VEC
LEC
Fb 1
Fb 2
Fb 3
Prol Fb
Epic
SMC
Peri
Mf
DC-like
Gran
T-cells
B-cells
Glial
Platelets
C
UMAP 2
UMAP 1
CM
Art EC
VEC 1
VEC 2
Endo
Prol VEC
LEC
Fb 1
Fb 2
Fb 3
Prol Fb
Epic
SMC
Peri
Mf
DC-like
Gran
T-cells
B-cells
Glial
Platelets

Figure 6.11 Expression of gene markers for each of the cardiac populations.

The unbiased differential expression analysis identified genes that were enriched in each cluster by comparing it to all the other clusters (A). For LECs the top 5 differentially expressed genes were *Ccl21*, *Mmrn1*, *Lyve1*, *Prox1* and *Reln*. Stacked violin plots showing expression of marker genes for each cluster (B). Gene expression analysis of a selection of known cell markers (B), in combination with unbiased analysis of differentially expressed genes (A) enabled the characterisation of each cluster. UMAP plot showing the different major clusters in 2D (C). For each time point one library was generated using pooled tissues dissected from 3 individual animals to control the differences among individual animals, surgery, and tissue dissociation variations. CM = cardiomyocytes, Art EC = arterial endothelial cells, VEC = venous endothelial cells, Endo = endocardium, Prol VEC = proliferating VEC, LEC = lymphatic endothelial cells, Fb = fibroblasts, Prol Fb = proliferating Fb, Epic = epicardium, SMC = smooth muscle cells, Peri = pericytes, Mf = macrophages, DC-like = dendritic cell-like, Gran = granulocytes.

In the intact postnatal heart, endothelial (P1 38 % and P7 41 %) and fibroblast (P1 40 % and P7 39 %) populations appeared to be the dominant cell types (Figure 6.12). Moreover, the percentage of immune cells changed from P1 to P7 hearts. At P1 the percentage of myeloid cells (Mf 4.9 %, Gran 4.3 %, and DC-like 0.2 %) was substantially larger compared to the percentage of lymphoid cells (T-cell 0.3 % and B-cells 0.7 %) (Figure 6.12). In contrast, at P7 the percentage of myeloid cells decreased (Mf 3.0 %, Gran 0.9 %, and DC-like 0.1 %) with the lymphoid cells now being the main immune cell population residing in the heart (T-cell 3.2 % and B-cells 1.3 %) (Figure 6.12). Notably, cardiomyocytes (P1 1.9 % and P7 0.4 %) were underrepresented in this dataset due to technical limitations of the 10X Genomics platform related to the large cardiomyocyte size[22,23]. In chapter 7 the immune cell populations will be further analysed.

A

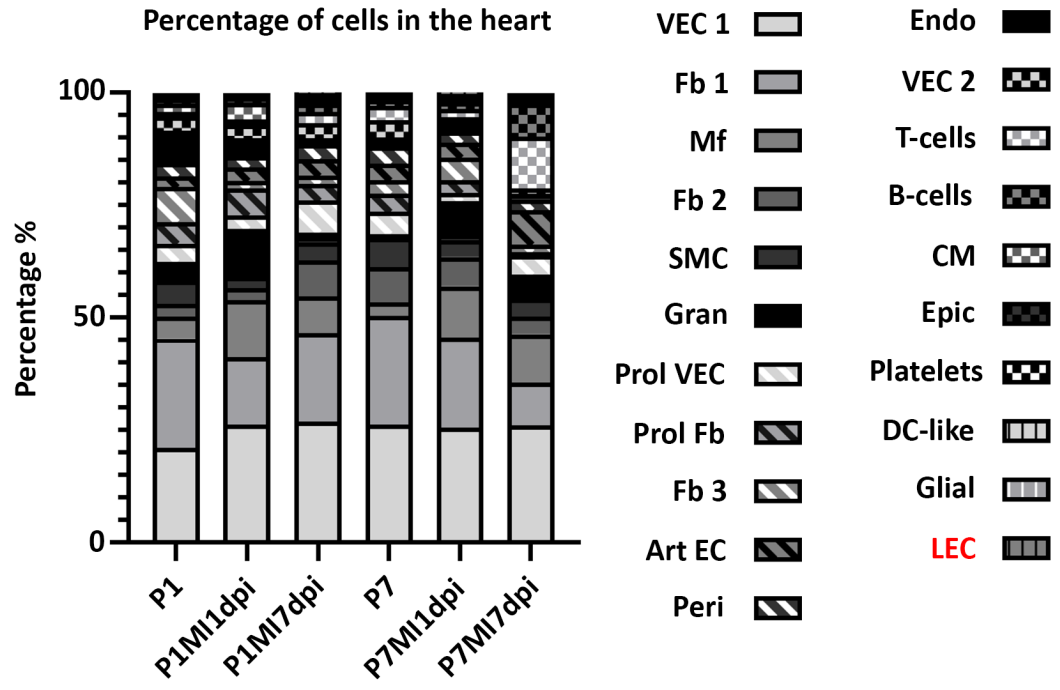

B

Percentage	P1	P1MI1dpi	P1MI7dpi	P7	P7MI1dpi	P7MI7dpi
VEC 1	20.97%	26.15%	26.88%	26.14%	25.42%	25.96%
Fb 1	24.31%	14.98%	19.63%	24.24%	20.12%	9.55%
Mf	4.92%	12.71%	8.17%	3.01%	11.44%	10.82%
Fb 2	2.83%	2.71%	8.02%	7.83%	6.48%	3.84%
SMC	5.15%	2.46%	4.11%	6.50%	3.85%	4.06%
Gran	4.26%	10.68%	2.12%	0.92%	8.60%	5.32%
Prol VEC	3.98%	3.04%	7.14%	4.91%	1.77%	4.32%
Prol Fb	4.88%	5.94%	3.68%	3.95%	2.92%	0.74%
Fb 3	7.73%	1.75%	1.81%	3.07%	5.02%	1.70%
Art EC	2.34%	2.93%	3.71%	3.61%	3.24%	7.59%
Peri	3.02%	2.52%	3.39%	3.91%	2.63%	2.36%
Endo	7.22%	3.97%	1.23%	1.91%	2.14%	1.35%
VEC 2	3.11%	3.09%	3.37%	3.90%	0.92%	1.22%
T-cells	0.34%	0.49%	2.41%	3.17%	1.93%	11.47%
B-cells	0.68%	0.58%	1.92%	1.29%	1.49%	7.29%
CM	1.89%	3.70%	0.83%	0.38%	0.44%	0.79%
Epic	1.13%	1.31%	0.24%	0.40%	0.11%	0.74%
Platelets	0.40%	0.19%	0.91%	0.19%	0.06%	0.44%
DC-like	0.19%	0.36%	0.18%	0.10%	0.84%	0.39%
Glial	0.30%	0.38%	0.20%	0.30%	0.29%	0.00%
LEC	0.34%	0.05%	0.05%	0.27%	0.31%	0.04%
Total cells	4697	3652	5521	8072	5244	2292

Figure 6.12 Percentage of each cell cluster in the heart per condition.

Although the percentage of CM is normally 50 % of all cardiac cell populations, in these samples the percentage was substantially lower (0.38 % to 3.70 %) due to technical limitation of the 10x Genomics platform. With this experimental design of limited CM, 50 % of the heart was made up by three clusters (VEC 1, Fb1 and Mf) at all conditions, while the representation of LECs was found to be the smallest overall. The percentage of Mf and Gran increased 1 day after MI, while that of T-cells and B-cells increased only 7 days after MI at both P1 and P7. CM = cardiomyocytes, Art EC = arterial endothelial cells, VEC = venous endothelial cells, Endo = endocardium, Prol VEC = proliferating VEC, LEC = lymphatic endothelial cells, Fb = fibroblasts, Prol Fb = proliferating Fb, Epic = epicardium, SMC = smooth muscle cells, Peri = pericytes, Mf = macrophages, DC-like = dendritic cell-like, Gran = granulocytes.

During the first week of postnatal heart development, the percentage of ECs increased from 38 % to 41 %, with the percentage of proliferating ECs at P1 and P7 being 4 % and 5 %, respectively (Figure 6.13). This increase during development is in line with previous observation of EC proliferation in the postnatal heart[24–26]. The endocardial cells were the only sub-population of ECs whose percentage was found to be reduced, from 7.2 % at P1 to 1.9 % at P7, potentially due to their contribution to coronary vasculature[24]. Finally, the percentage of LECs remained constant at around 0.3 % supporting the lack of lymphatic sprouting during this period (Figures 6.2-6.4).

There was an overall increase in the percentage of ECs 7 days after MI at P1, with proliferating ECs constituting 7.1 % of all ECs as compared to 4 % in the P1 control (Figure 6.13). This suggests that there is an angiogenic response to MI at the P1 stage. During this angiogenic response, the percentage of both venous and arterial ECs (30 % and 3.7 %, respectively) increased as compared to the P1 control (24 % and 2.3 %, respectively). However, the percentage of proliferating ECs showed a decrease 1 day after MI at P7 (1.8 %) as compared to the P7 control (4.9 %), potentially due to the damage caused by the injury. After 7 days of healing, the percentage of proliferating ECs increased again to that

seen in the P7 control (4.3 % and 4.9 %, respectively). In contrast to the P1 response, the percentage of venous ECs dropped after MI at P7 (27 %) as compared to the P7 control (30 %), while the percentage of arterial ECs doubled after MI at P7 (7.6 %) as compared to the P7 control (3.6 %). Unfortunately, the number of LECs identified through this experimental setup was too low to compare between conditions. Nevertheless, the specificity of LEC markers was tested after integrating all conditions (Figure 6.14). Interestingly, *Vegfr3* appeared to be highly expressed in venous and arterial ECs, albeit at a lower level than in LECs (Figure 6.14 A). The predominant site of *Vegfc* expression was the arterial endothelium, with the venous endothelium also expressing it at lower levels (Figure 6.14 B). Fibroblasts were the main cell population expressing the ligand *Vegfd* and contributing also to *Vegfc* expression (Figure 6.14 B-C). As expected, expression levels of *Pdpn* were high in LECs and epicardial cells, relative to fibroblasts (Figure 6.14 D). All EC populations expressed *Nrp2,* which was also found in macrophages and glial cells (Figure 6.14 E). Besides LECs, *Lyve1* was expressed by macrophages and endocardial cells (Figure 6.14 F). The presence of *Lyve1* in the endocardium will be discussed further in chapter 8. Finally, *Prox1* and the chemokine *Ccl21* were found to be expressed specifically by LECs (Figure 6.14 G-H).

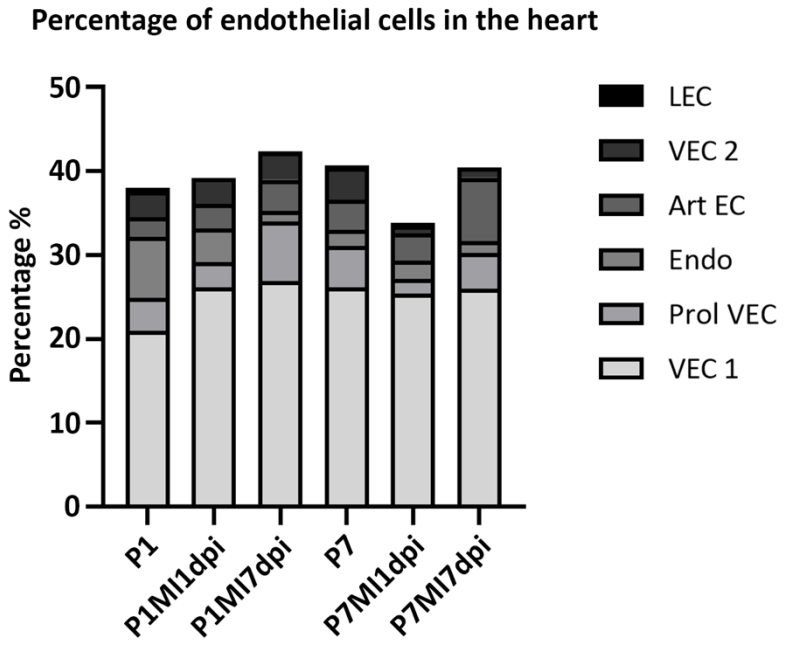

Percentage	VEC 1	Prol VEC	Endo	Art EC	VEC 2	LEC
P1	20.97%	3.98%	7.22%	2.34%	3.11%	0.34%
P1MI1dpi	26.15%	3.04%	3.97%	2.93%	3.09%	0.05%
P1MI7dpi	26.88%	7.14%	1.23%	3.71%	3.37%	0.05%
P7	26.14%	4.91%	1.91%	3.61%	3.90%	0.27%
P7MI1dpi	25.42%	1.77%	2.14%	3.24%	0.92%	0.31%
P7MI7dpi	25.96%	4.32%	1.35%	7.59%	1.22%	0.04%

Figure 6.13 Percentage of each endothelial cluster in the heart per condition.

The percentage Prol VEC, VEC 1 and Art EC was increased 7 days after MI at P1. The Endo and LEC populations were reduced after MI at P1, while the representation of VEC 2 remained stable. The percentage of Prol VEC was substantially reduced 1 day after P7 MI, before returning to pre-injury levels 7 days after MI. The representation of Art EC doubled 7 days after P7 MI, while Endo, VEC 2 and LEC populations were reduced at the same timepoint. Art EC = arterial endothelial cells, VEC = venous endothelial cells, Endo = endocardium, Prol VEC = proliferating VEC, LEC = lymphatic endothelial cells.

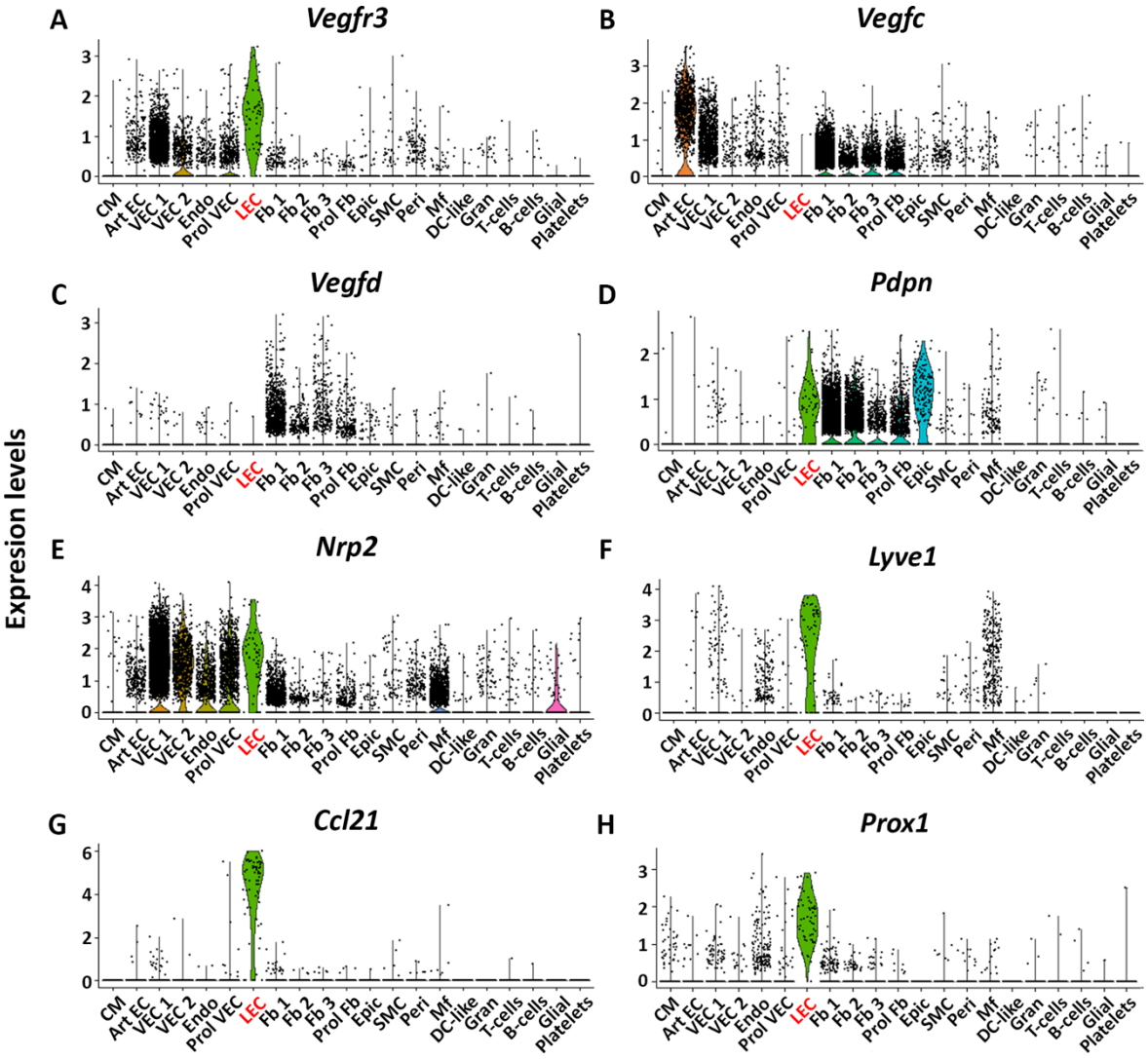

Figure 6.14 Stacked violin plots showing expression of lymphatic related genes across all populations.

The specificity of known lymphatic associated genes was examined using the integrated scRNA-seq dataset. *Vegfr3* was found to be expressed by all EC populations (A). Both ligands, *Vegfc* and *Vegfd*, were expressed by Fb populations (B and C), while *Vegfc* was predominantly expressed by Art EC and in lower levels by VEC 1 (B). *Pdpn* was highly expressed by the epicardium, as well as by Fb populations and LECs (D). *Nrp2* was expressed by all EC populations, as well as by Mf and Glial (E). High levels of *Lyve1* were found in LECs, with Mf having low levels *Lyve1* (F). *Ccl21* (G) and *Prox1* (H) appeared to be specifically expressed by LECs. CM = cardiomyocytes, Art EC = arterial endothelial cells, VEC = venous endothelial cells, Endo = endocardium, Prol VEC = proliferating VEC, LEC = lymphatic endothelial cells, Fb = fibroblasts, Prol Fb = proliferating Fb, Epic = epicardium, SMC = smooth muscle cells, Peri = pericytes, Mf = macrophages, DC-like = dendritic cell-like, Gran = granulocytes.

6.3.6. *Lyve1 knock-out affects heart healing after postnatal MI*

Lyve1 is expressed by cardiac lymphatics, macrophages, and the endocardium during postnatal stages, as shown by the scRNA-seq data. Knock-out of *Lyve1* leads to disruption

of macrophage clearance by cardiac lymphatics after MI in adult mice, with detrimental effect to cardiac function, with no other defect have been reported in this mouse line[76,78]. However, macrophages are essential for cardiac regeneration after MI at P1[210] and here we have shown that macrophages are cleared less efficiently after MI at P1 compared to P7. Consequently, it was hypothesised that deletion of *Lyve1* would not affect cardiac regeneration after MI at P1,as macrophages are required in the heart for regeneration at this stage[210], while it would negatively affect healing after MI at P7, as there is a requirement to reduce the immune cell/macrophage load for improved repair at P7 (similar to adults[76]). To investigate this hypothesis and determine the effect on cardiac function, a longitudinal cine MRI study was performed with *Lyve1*$^{+/-}$ and *Lyve1*$^{-/-}$ mice scanned on day 28 after MI at P1 or P7 (P1MI;28dpi and P7MI;28dpi, respectively). Intact *Lyve1*$^{+/-}$ and *Lyve1*$^{-/-}$ mice were also scanned at day 29 or 35 as controls for P1MI;28dpi and P7MI;28dpi, respectively. The left-ventricular function was assessed by measuring the ejection fraction (EF), cardiac output (CO), end systolic lumen (ESL), end diastolic lumen (EDL), and stroke volume (StV) (Figure 6.15 A-E and J). Other cardiac values were also calculated, such as end systolic mass (ESM), end diastolic mass (EDM), heart weight (hwt) and heart rate (Figure 6.15 F-J). Overall there was large variability observed in all conditions and time points, suggesting that a larger cohort of mice might need to be used to obtain a full statistical assessment of all measured parameters. Nevertheless, there was a trend for impaired cardiac function in *Lyve1*$^{+/-}$ and *Lyve1*$^{-/-}$ mice after MI at P1, compared to their respective intact controls (Figure 6.15 A-J). Specifically, EF was significantly decreased 28 days after MI at P1 in *Lyve1*$^{+/-}$ mice, compared to intact *Lyve1*$^{+/-}$ P29 (mean ± SEM: 61.3 ± 1.3 vs 69.1 ± 1.6; p = 0.026, Figure 6.15 A left). CO was significantly reduced 28 days after MI at P1 in *Lyve1*$^{-/-}$ mice, compared to intact *Lyve1*$^{-/-}$ P29 (mean ± SEM: 9.7 ± 1.1 vs 13.2 ±

0.7; p = 0.034, Figure 6.15 B left). Also, SV was significantly lower 28 days after MI at P1 in *Lyve1*$^{-/-}$ mice, compared to the same condition in *Lyve1*$^{+/-}$ (mean ± SEM: 20.9 ± 2.1 vs 29.3 ± 1.8; p = 0.045, Figure 6.15 E left). In contrast, no statistically significant differences were observed in EF, CO, ESL, EDL or StV between the different conditions and timepoints in the P7 experimental setup (Figure 6.15 A-E right). The values of ESM, EDM and hwt were found to be statistically significant after MI at P1 in *Lyve1*$^{+/-}$ mice compared to the other P1 conditions, as well as after MI at P7 in *Lyve1*$^{-/-}$ mice compared to *Lyve1*$^{+/-}$ mice (Figure 6.15 F-H right). The heart rate was similar in all conditions examined (Figure 6.15 I). Interestingly, a trend for larger relative infarct size was detected 28 days after MI at P7 in *Lyve1*$^{-/-}$ mice compared to the other conditions; however, this was not statistically significant (Figure 6.15 K). Overall, the MRI study highlighted potential functional impairment via reduced EF, CO SV at P1 in *Lyve-1*$^{-/-}$ hearts, thus refuting the original hypothesis that deletion of *Lyve1* would not affect cardiac regeneration after MI at P1 and would negatively affect healing after MI at P7.

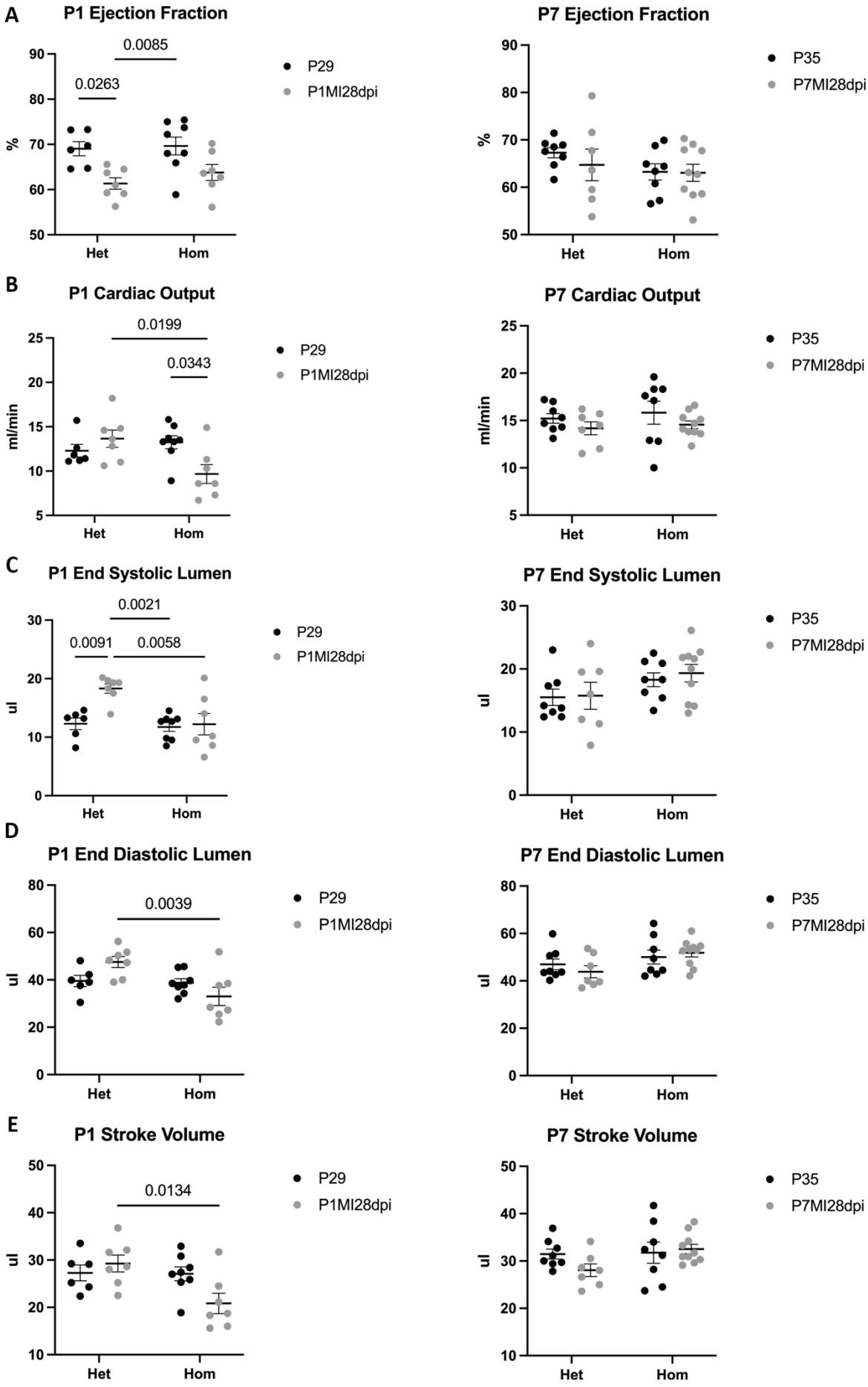
A
P1 Ejection Fraction
0.0085
0.0263
%
Het
Hom
P29
P1MI28dpi
P7 Ejection Fraction
P35
P7MI28dpi
B
P1 Cardiac Output
0.0199
0.0343
ml/min
P7 Cardiac Output
C
P1 End Systolic Lumen
0.0021
0.0091
0.0058
ul
P7 End Systolic Lumen
D
P1 End Diastolic Lumen
0.0039
P7 End Diastolic Lumen
E
P1 Stroke Volume
0.0134
P7 Stroke Volume

F

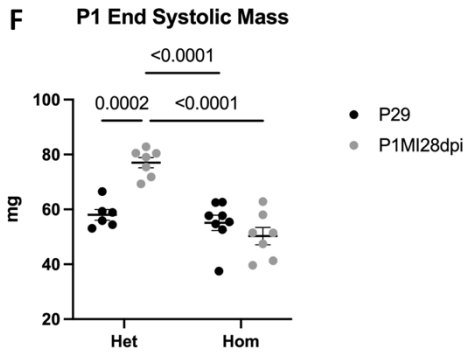

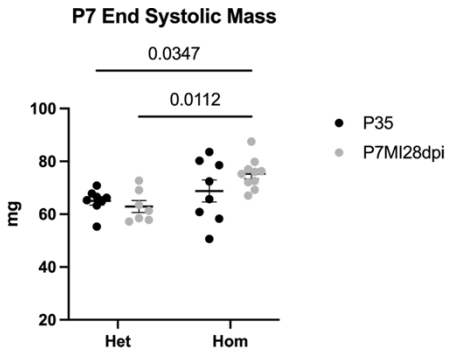

G

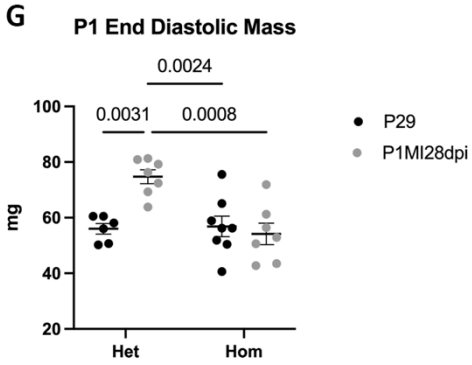

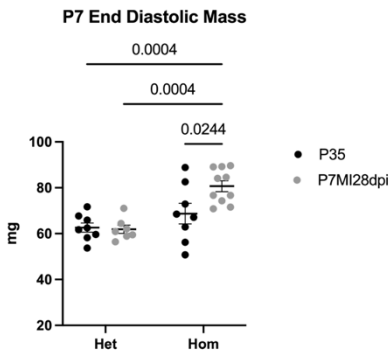

H

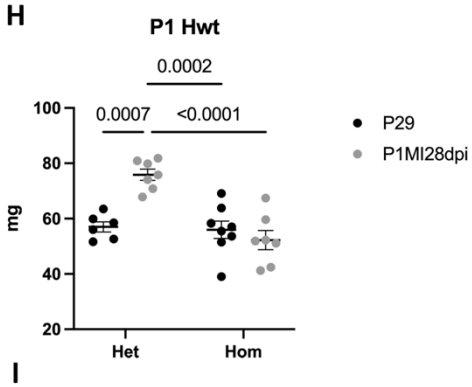

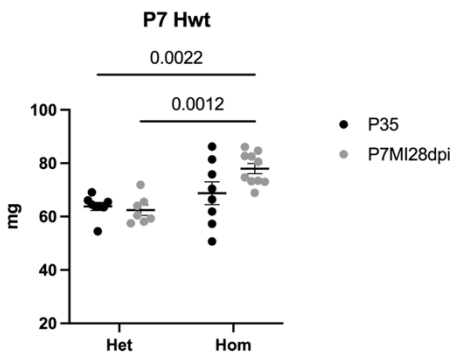

I

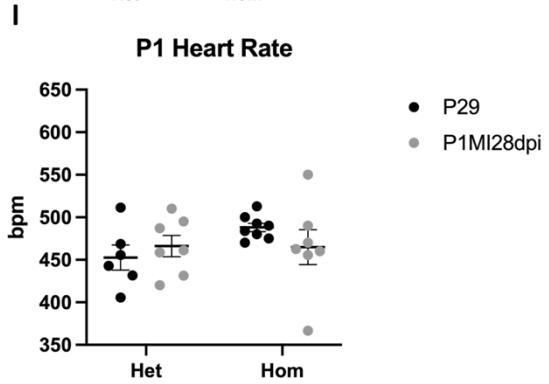

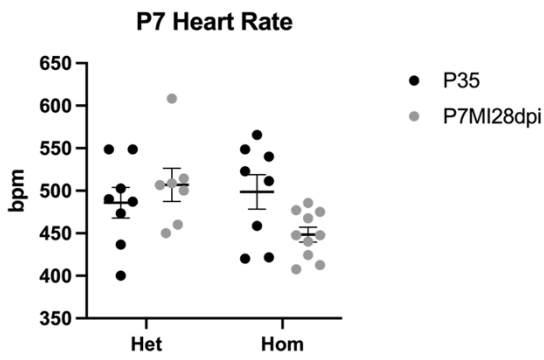

J

		HET		HOM		HET		HOM	
		P29	P1MI28dpi	P29	P1MI28dpi	P35	P7MI28dpi	P35	P7MI28dpi
	n	6	7	8	7	8	7	8	10
End Diastolic Mass	mg	56 ± 2	75 ± 3	57 ± 4	54 ± 4	63 ± 2	62 ± 2	68 ± 4	80 ± 2
End Systolic Mass	mg	58 ± 2	77 ± 2	55 ± 3	50 ± 3	65 ± 2	63 ± 2	69 ± 4	75 ± 2
End Diastolic Lumen	ul	40 ± 2	48 ± 2	39 ± 2	33 ± 4	47 ± 2	44 ± 3	50 ± 3	52 ± 2
End Systolic Lumen	ul	12 ± 1	18 ± 2	12 ± 1	12 ± 2	16 ± 1	16 ± 2	18 ± 1	19 ± 1
Stroke Volume	ul	27 ± 2	29 ± 2	27 ± 1	21 ± 2	31 ± 1	31 ± 1	32 ± 2	33 ± 1
Ejection Fraction	%	69 ± 2	61 ± 1	70 ± 2	64 ± 2	67 ± 1	65 ± 3	63 ± 2	63 ± 2
Heart Rate	bpm	453 ± 15	466 ± 13	488 ± 5	465 ± 21	486 ± 18	507 ± 19	499 ± 20	448 ± 9
Cardiac Output	ml/min	12 ± 1	14 ± 1	13 ± 1	10 ± 1	15 ± 1	14 ± 1	16 ± 1	15 ± 1
Hwt	mg	57 ± 2	76 ± 2	56 ± 3	52 ± 3	64 ± 1	62 ± 2	69 ± 4	78 ± 2
Relative infarct size	%		4 ± 1		4 ± 1		5 ± 1		6 ± 1

K

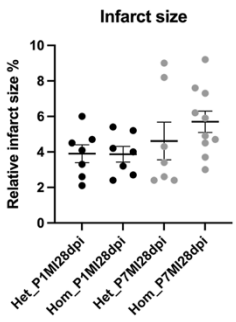

Figure 6.15 Functional cardiac parameters from MRI analyses of Lyve1 knock-out animals 28 days after MI at P1 and P7.

Plots from longitudinal cine MRI performed in *Lyve1*$^{+/-}$ and *Lyve1*$^{-/-}$ mice 28 days after MI at P1 and P7, as well as in intact P29 and P35. The MRI provided values for the left-ventricular ejection fraction (A), cardiac output (B), end systolic lumen (C), end diastolic lumen (D), stroke volume (E), end systolic mass (F), end diastolic mass (G), heart weight (H) and heart rate (I). A table with the average values and SEM for each parameter and condition is included (J). The relative infarct size (%) was calculated for all MI conditions (K). The results were inconclusive due to large variability within each condition. Data are presented as mean ± SEM; n = 5-10 for each time point. Significant differences were calculated using 2-way ANOVA.

6.4. Discussion

In this chapter, the response and function of cardiac lymphatics was investigated 7 days after MI by LAD artery ligation in regenerative P1 and non-regenerative/fibrotic P7 hearts. Previous studies have proven that cardiac lymphatics respond to the site of injury by lymphangiogenesis, reducing oedema and clearing macrophages to MLNs after MI in adult mice[38,39,76,152]. This endogenous response is important for the repair of the damaged heart. However, the cardiac lymphatic vasculature in regenerative neonatal hearts had not been investigated before.

In this study, it was shown that the response of lymphatic vessels after MI at P1 differs depending on genetic background. Specifically, there is a limited lymphatic response after MI at P1 compared to MI at P7 in C57BL/6J mice, while the lymphangiogenic response to the site of injury is evident 7 days after MI at P1 in CD1 mice. This result is supported by the data presented in chapter 5 of this thesis, showing that the lymphatic vasculature grows faster and to a greater extend during normal postnatal development in CD1 mice compared to C57BL/6J mice. Notably, a study looking into healing of the heart after adult MI in 32 different mouse strains found significant variation in function, morphology and scar formation[204]. It is therefore expected that there will be a gradient of lymphangiogenic

responses to MI depending on genetic backgrounds, as well as different degrees of cardiac regenerative capacity in postnatal mice. Interestingly, the mentioned study found that the heart of adult C57BL/6J mice had one of the worst recoveries after MI[204]. However, that study did not test CD1 adult mice[204]. Also, there has not been any research on the variable regenerative capacity of P1 hearts from various mouse strains to-date. Nevertheless, the original publication and numerous subsequent studies on postnatal heart regeneration have been conducted in CD1 mice, suggesting that they have good regenerative capacity[195,199,201,210].

Surprisingly, the lymphangiogenic response did not lead to improved macrophages clearance from the heart to the MLNs in either the CD1 or C57BL/6J mice 7 days after MI at P1. Two experiments were conducted to assess macrophage clearance after MI at P1 and P7. MLNs of CD1 pups, which had undergone adoptive transfer of adult splenic GFP^+ macrophages during the time of MI surgery, and MLNs of *Cd68-GFP*$^+$ mice were imaged 7 days after MI at P1 and P7. This showed reduced macrophage clearance after MI at P1 compared to P7. Macrophages were found to be located mainly in the medullary sinus of the MLNs, which corresponds to the area where macrophages with high phagocytic activity are found[45,257]. Together, these data indicate that macrophages were cleared from the heart to MLNs by lymphatic vessels less efficiently after MI at P1 than at P7, which supports the hypothesis that the lymphatics function differently during the regenerative window i.e. they do not clear pro-regenerative macrophages at P1 but function to clear pro-inflammatory and pro-fibrotic macrophages at P7.

The reduced macrophage clearance from the heart could potentially be explained by differences in the permeability of lymphatic cell-cell junctions. As discussed in chapter 5, the cardiac LEC junctions appear to be impermeable zippers during the early stages of postnatal development, and progressively transform to more permeable button junctions. As a result, it is possible that macrophages cannot transmigrate to cardiac lymphatic vessels during early postnatal development, such as after MI at P1. Another factor that could impact migration of macrophages to draining lymph nodes is the expression level of chemokines by LECs. For instance, lymphatic clearance of DCs and neutrophils is facilitated by the interaction between the chemokine CCL21 and its receptor CCR7 (C-C chemokine receptor type 7)[245–247,258]. CCL21 is expressed and secreted constitutively at low levels by LECs creating a gradient near the lymphatic area. DCs and neutrophils have been shown to bind CCL21 and navigate through the chemokine gradient in a CCR7-dependent manner[247]. Furthermore, the interaction between CCL21 and CCR7 is important for the docking and transmigration of DCs and neutrophils to lymphatic vessels[245,246]. In this chapter, whole-heart qPCR data showed that levels of *Ccl21* decrease significantly following MI at P1 compared to P8 intact hearts, while they remain the same after MI at P7 as in P14 intact hearts. Also, scRNA-seq found that *Ccl21* is specifically expressed by cardiac LECs, suggesting that the qPCR *Ccl21* expression data were specific to the cardiac LEC population. Macrophages have been reported to also express CCR7[259], which raises the question whether they use the CCL21 gradient to locate lymphatics. However, this potential mechanism has not yet been investigated. Following this consideration, the low levels of the chemokine CCL21 after MI at P1 could affect the macrophage clearance from the heart to MLNs. Apart from the potential macrophage chemotaxis through CCL21-CCR7 binding, there may be other molecular differences between P1 and P7 macrophages that could lead

their variable interaction with cardiac lymphatic vessels after MI. For instance, the interaction between macrophage-expressed HA and the LEC-expressed LYVE1 has been proposed to be important for the clearance of macrophages by cardiac lymphatics after adult MI[76]. Deletion of *Lyve1* leads to reduced macrophage clearance and reduced cardiac function after MI in adult mice[76]. Here, it was hypothesised that reduced macrophage clearance due to *Lyve1* knock-out would not affect cardiac regeneration after MI at P1, as macrophages are important for complete regeneration at this timepoint[210], while the effects after MI at P7 would be similar to the ones observed in the adult stages[76]. However, results from longitudinal cine MRI refuted this hypothesis, as the cardiac function appeared significantly reduced 28 days after MI at P1 in *Lyve1*$^{+/-}$ and *Lyve1*$^{-/-}$ compared to the respective intact controls. These results reflect a potential unappreciated role of LYVE1 in cardiac regeneration in non-LEC cell types, such as tissue resident macrophages. In contrast, no significant differences were observed in the cardiac function 28 days after MI at P7 compared to intact controls. The lack of effect that *Lyve1* knock-out appears to have after MI at P7 cannot be readily explained, as it was expected to lead to a reduced macrophage clearance and impaired cardiac function, similar to the adult setting[76]. It is possible that LYVE1 is not required for macrophage clearance until after postnatal development. Moreover, several trends were observed that need to be further validated with a larger cohort of animals, as the trends often contradicted each other (e.g., no functional cardiac defect detected after MI at P7 in *Lyve1*$^{-/-}$, yet these hearts had larger relative infarct size compared to the other MI conditions). The interaction of cardiac LECs with macrophages will be investigated in more detail in chapter 7.

The scRNA-seq data provided valuable information regarding the postnatal development of cardiac ECs, as well as their response to MI. The percentage of ECs, specifically proliferating ECs, was found to be increased at P7 as compared to P1, confirming the angiogenesis and proliferation of ECs during postnatal development[208,260,261]. Interestingly, the percentage of endocardial cells decreased from 7.2 % at P1 to 1.9 % at P7. This drop of endocardial cells could be explained by their contribution to the coronary endothelium[208,262]. Here, endocardial cells undergo lineage conversion and generate a distinct coronary vascular population inside the ventricular wall during the early postnatal stages[208]. A week after MI at P1, the percentage of proliferating ECs in the heart almost doubled compared to the P1 control, with the blood vasculature showing a similar increase. These results are in line with the angiogenic response described after MI at P1[210,261]. In contrast, there was a substantial decrease in the percentage of proliferating ECs 1 day after MI at P7 compared to the P14 control. In combination with the finding that the percentage of VECs remained stable, this suggests limited angiogenesis after MI at P7. Previously published scRNA-seq datasets from intact and MI hearts have failed to identify LECs due to their low cell count[141,231]. It has been suggested that the total number of ECs constitute approximately 60 % of the non-myocytes, with LECs corresponding to 5 % of the total ECs in the adult heart[139]. Consequently, it is expected that sequencing 5,000 cells from an adult heart should allow for the identification of approximately 150 LECs under optimal conditions. However, analysis of LECs proved challenging due to technical limitations and the small number of LECs found in neonatal hearts as compared to adults. Specifically, LECs were found to correspond to only 0.9 % of the total ECs in the P1 and P7 heart. As a result, a meaningful analysis could not be conducted.

6.5. Summary

The work presented in this chapter characterises the response and function of cardiac lymphatic vessels after MI in the regenerative P1 and fibrotic P7 stages. The data demonstrate that cardiac lymphatics respond differently to cardiac injury depending on genetic background. The lymphangiogenic response after MI at P1 was limited in C57BL/6J mice in comparison with the extensive response seen in CD1 mice. However, this response did not translate into increased macrophage clearance, as the number of macrophages detected in the draining lymph nodes 7 days after MI at P1 was substantially lower compared to that seen after MI at P7. Differences in the maturation and permeability of the cardiac LEC junctions between the P1 and P7 stage could be affecting the macrophage clearance efficiency. Moreover, different levels of chemokine production and secretion from the cardiac LECs could affect the ability of macrophages to locate and dock on lymphatics, subsequently leading to reduced ability to transmigrate from the interstitial space to the vessel. Surprisingly, deletion of *Lyve1* led to reduced cardiac function only after MI at P1, suggesting a currently unknown role of LYVE1 in cardiac regeneration. Finally, macrophages could have different properties at P1 versus P7 stages that affect their ability to locate, dock and transmigrate to lymphatic vessels. Overall, the cardiac lymphatic vasculature appears to be responding to MI through lymphangiogenesis but has limited functional ability to clear macrophages from the site of injury to the MLNs at the regenerative P1 stage.

7. Results III: Investigating the interaction of macrophages with cardiac lymphatics after myocardial infarction in the regenerative P1 and fibrotic P7 neonatal stages

7.1. Background

Tissue resident macrophages represent approximately 7 % of the non-cardiomyocyte population in the adult heart during homeostasis and originate from the yolk sac, foetal liver and bone marrow[138,139]. Cardiac macrophages express different gene markers depending on their origin and the animal's age[138,142,263]. Early after birth, cardiac macrophages are derived predominately from the yolk sac and foetal liver, and are CX3CR1^{+} (C-X3-C Motif Chemokine Receptor 1) and MHC-II^{-} [138,142,165,194]. These embryonic-derived macrophages are long-lived and maintained through local proliferation[138,142,165]. Functionally, embryonic-derived macrophages display anti-inflammatory and regenerative properties after MI, such as stimulating angiogenesis[138,140,143,165]. However, with age their self-renewal properties decline leading to a gradual loss of embryonic-derived macrophages, which are replaced by circulating LY6C^{+} monocytes[138,142,165]. The circulating monocytes infiltrate the heart and differentiate into various macrophage subpopulations, with preferential contribution to MHC-II^{+} macrophages[138,142,143,165]. These monocytes and monocyte-derived macrophages are mainly pro-inflammatory and contribute to cardiac remodelling by facilitating fibrotic scar formation after MI[138,140,143,165,166]. Consequently, there is a dynamic change of the cardiac macrophage landscape during the first weeks of postnatal life[138,142].

Shortly after the induction of MI, the embryonic-derived macrophages of adult mice die and are replaced by circulating monocytes and monocyte-derived macrophages that

infiltrate the myocardium to clear debris and dead cells[138,140,143,164,165]. The monocyte response is completed in a biphasic manner[163]: The first phase (1-4dpi) is characterised as pro-inflammatory with an increase in the number of $LY6C^+$ monocyte-derived macrophages that clear debris and dead cells, while the second phase (≥5dpi) is pro-reparative with an increase in the number of $LY6C^-$ monocyte-derived macrophages that contribute to angiogenesis and scar formation[140,156,165,264].

The macrophage response to MI is different in neonatal mice, as their immune system is still developing[142,209]. During the early postnatal stages the heart is populated by embryonic-derived MHC-II^- macrophages only, while there is limited infiltration of monocytes after MI[138,140,142]. These cardiac-resident macrophages promote angiogenesis and are essential for complete regeneration after MI at P1[210]. Although the interaction of macrophages with the coronary blood vasculature has been investigated in embryonic development and after MI[144,145,210], their interaction with lymphatic vasculature has only been studied in embryonic development[145]. As a result, it remains unclear whether macrophages interact with lymphatics after MI at postnatal stages.

7.2. Aims

The aim of this chapter is to identify potential molecular interactions between macrophages and cardiac LECs that could influence the lymphangiogenic response and clearing efficiency of lymphatics after MI in regenerative P1 and fibrotic P7 mice.

7.3. Results

7.3.1. *Gene expression of macrophage markers increases during postnatal development and after myocardial infarction*

To detect the molecular changes that take place in cardiac macrophage populations during postnatal development their gene expression profile was examined by performing qPCR using whole-heart extracts (Figure 7.1). The genes analysed were known pan-macrophage markers (*Cd68* and *F4/80* [Adhesion G Protein-Coupled Receptor E1]), pro-inflammatory macrophage markers (*Cd80*, *Cd86* and *Ccr2*), pro-reparative macrophage markers (*Cd206* and *Cx3cr1*) and the chemokine receptor *Ccr7*. However, cycle threshold (CT) values obtained for the pro-inflammatory macrophage markers and the chemokine receptor were greater than 30, indicating that these genes are only expressed at very low levels, preventing quantification by qPCR. Expression levels of the pan-macrophage markers and the pro-reparative macrophage markers followed a common trend (Figure 7.1). Specifically, there was a significant increase in the gene expression levels of *Cd68*, *F4/80* and *Cx3cr1* at P1 compared to the P0 baseline (LogFC ± SEM: 1.11 ± 0.17 vs 0 ± 0.18; p = 0.003, 1.15 ± 0.11 vs 0.05 ± 0.22; p = 0.02 and 1.69 ± 0.27 vs 0.01 ± 0.08; $p < 0.001$, respectively) (Figure 7.1 A-C). Although expression of *Cd206* also increased, this was not found to be statistically significant (Figure 7.1 D). From P1 until P6 the expression levels of these genes either remained stable (*Cx3cr1*) or gradually returned to the P0 baseline (*Cd68*, *F4/80* and *Cd206*). At P7, expression of all analysed genes increased significantly to more than double the levels of the P0 baseline, and either continued rising (*Cd68*, *F4/80* and *Cd206*) or remained stable (*Cx3cr1*) into adulthood. This increase in macrophage gene expression levels could reflect the replenishment of tissue-resident macrophages by circulating monocytes at later stages of the postnatal cardiac development. Alternatively, it could be linked to an increase in the embryonic-derived macrophage proliferation.

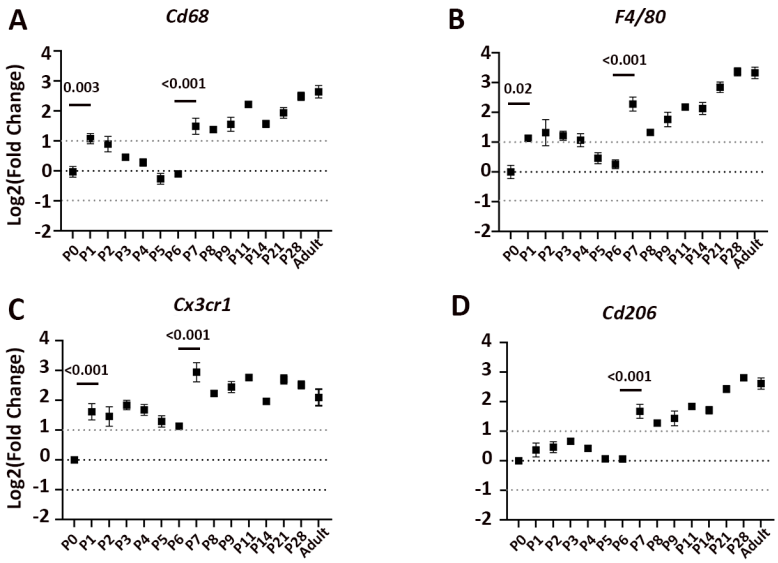

Figure 7.1 Gene expression of macrophage markers increases during postnatal development.

Genes expression levels for pan-macrophage markers *Cd68* (A) and *F4/80* (B), as well as the pro-reparative macrophage markers *Cx3cr1* (C) and *Cd206* (D) displayed similar pattern during postnatal development. After a significant increase in gene expression at P1 compared to P0, the levels gradually returned to baseline by P5. At P7 the gene expression levels increased significantly for a second time compared to P0, and from there on continued rising to adulthood. The samples were generated from whole-heart extracts. Data are presented as mean ± SEM; n = 4-5 for each time point. Significant differences were calculated using 1-way ANOVA followed by Tukey's multiple comparisons test.

Next, the gene expression levels of the aforementioned markers were assessed by qPCR using whole-heart extracts from 7 days post-MI P1 and P7 mice (Figure 7.2). Similar to what was previously observed, the Ct values for the pro-inflammatory macrophage markers and the chemokine receptor were greater than 30 indicating very low expression levels. Expression of *Cd68* and *Cx3cr1* was at the same levels 7 days after MI at P1 as the P8 age-matched control (Figure 7.2 A and C), while expression of F4/80 was significantly increased (LogFC ± SEM: 0.41 ± 0.04 vs 0 ± 0.05; p = 0.001) (Figure 7.2 B). *Cd206* was found to be expressed at slightly, yet statistically significant, lower levels after MI at P1 than the P8 control (Figure 7.2 D) (LogFC ± SEM: -0.15 ± 0.04 vs 0 ± 0.02; p = 0.011). The expression

levels of *Cd68*, *F4/80* and *Cd206* were found to be increased 7 days after MI at P7 compared to the P14 age-matched control (LogFC ± SEM: 0.72 ± 0.2 vs 0.01 ± 0.12; $p = 0.002$, 0.73 ± 0.16 vs 0.04 ± 0.2; $p = 0.029$ and 0.42 ± 0.07 vs 0.01 ± 0.13; $p = 0.02$, respectively) (Figure 7.2 E, F and H). Expression of *Cx3cr1* was also increased, but this was found not to be statistically significant (LogFC ± SEM: 0.82 ± 0.37 vs 0 ± 0.07; $p = 0.168$) (Figure 7.2 G). The increase of macrophage gene expression levels after MI at P1 and P7 could reflect the response of macrophages to cardiac injury. Notably, although these markers are known to be expressed by macrophages, these data were generated using whole-heart extracts.

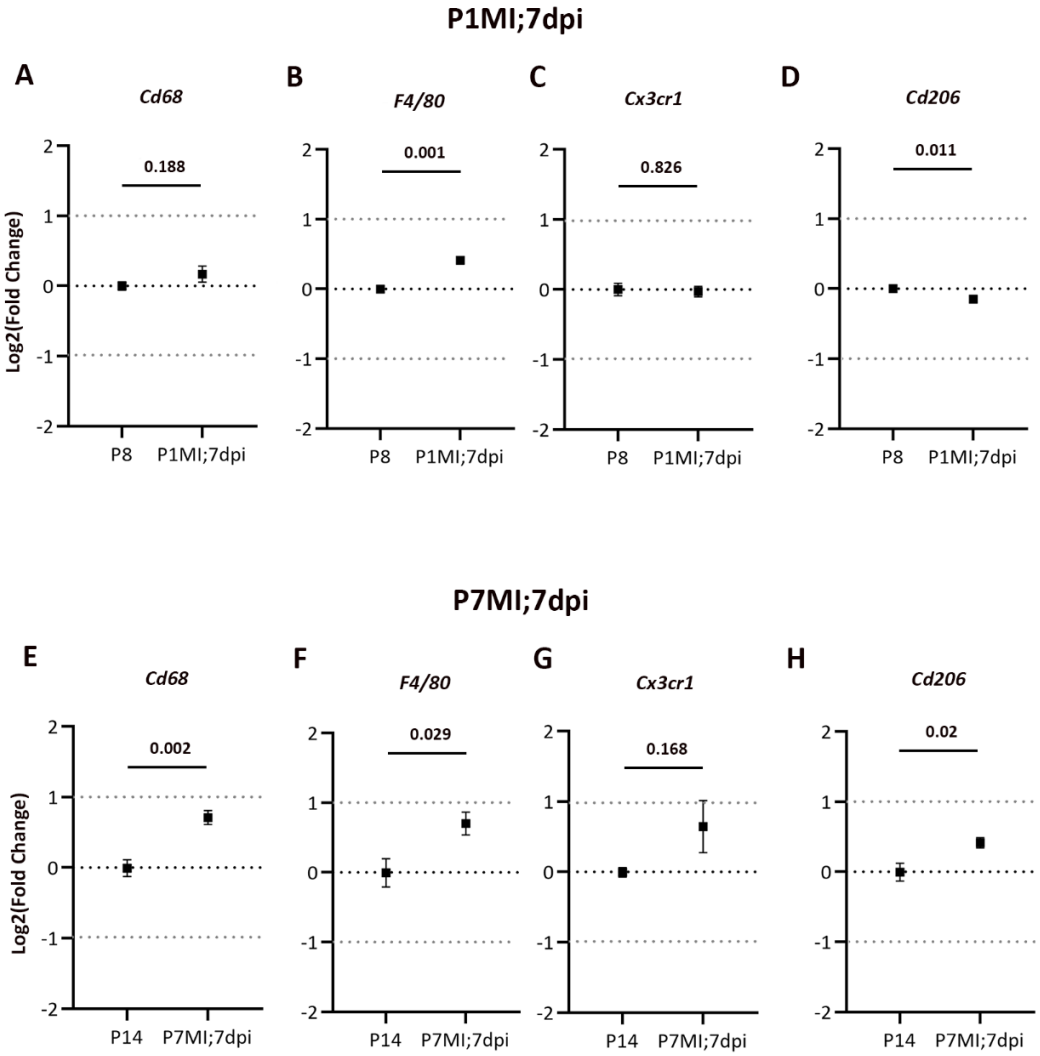

Figure 7.2 Gene expression of macrophage markers increases after MI in postnatal stages.

Gene expression levels of *Cd68* (A) and *Cx3cr1* (C) were the same after MI at P1 compared to P8, while the levels of *F4/80* (B) increased and of *Cd206* (D) decreased significantly after MI at P1 compared to P8. Gene expression levels of *Cd68* (E), *F4/80* (F) and *Cd206* (H) increased significantly after MI at P7 compared to P14, while *Cx3cr1* (G) had a non statistical significant increase. The samples were generated from whole-heart extracts. Data are presented as mean ± SEM; n = 3-4 for each time point. Significant differences were calculated using an unpaired, 2-tailed Student's t test.

7.3.2. ***Concentration of tissue-resident macrophage increases with limited infiltration of monocytes after postnatal MI***

The scRNA-seq data presented in chapter 6 were further analysed with a focus on the macrophage (Mf) population for an in-depth assessment of macrophage and monocyte

heterogeneity, as well as their response after MI at the regenerative P1 and fibrotic P7 stages (Figure 7.3 A). Note that the scRNA-seq experiment was conducted with samples from CD1 mice.

Using automated cluster annotation and manual consolidation of published gene markers for monocyte and macrophage sub-populations[231], eight clusters with defined gene expression signatures were identified (Figure 7.3 B). The following clusters with respective signature gene markers were determined: five macrophage clusters (Mf1 – *C1qa*; Mf2 – *Spp1*; Mono/Mf1 – *Ly6c2*; Mono/Mf2 – *Sox18* and Mono/Mf3 – *Gpc6*) and one monocyte cluster (Mono – *Treml4*) (Figure 7.3 F). Also, a cluster of proliferating macrophages (Prol Mf) was characterised, which was found to express high levels of cell cycle markers (Figure 7.3 C and F). Finally, a cluster of apoptotic cells (Apopt) was identified, which was found to express a high percentage of mitochondrial RNA (Figure 7.3 D and F) and contain low numbers of RNA molecules within each cell (Figure 7.3 E). Two-dimensional visualisation using UMAP revealed close association of Mono and Mono/Mf1, Mf1 and Prol Mf, as well as Mono/Mf2 and Mono/Mf3 (Figure 7.3 B). This suggests comparable gene expression features within these myeloid cell populations. In the literature, adult macrophages have been traditionally characterised as either M1 pro-inflammatory or M2 pro-reparative[265,266]. However, it has been proven that macrophages are highly heterogeneous and have a spectrum of functions, with the M1/M2 classification at the extreme ends of this spectrum[265,266]. As a result the M1/M2 nomenclature will not be used to describe macrophage clusters in this thesis.

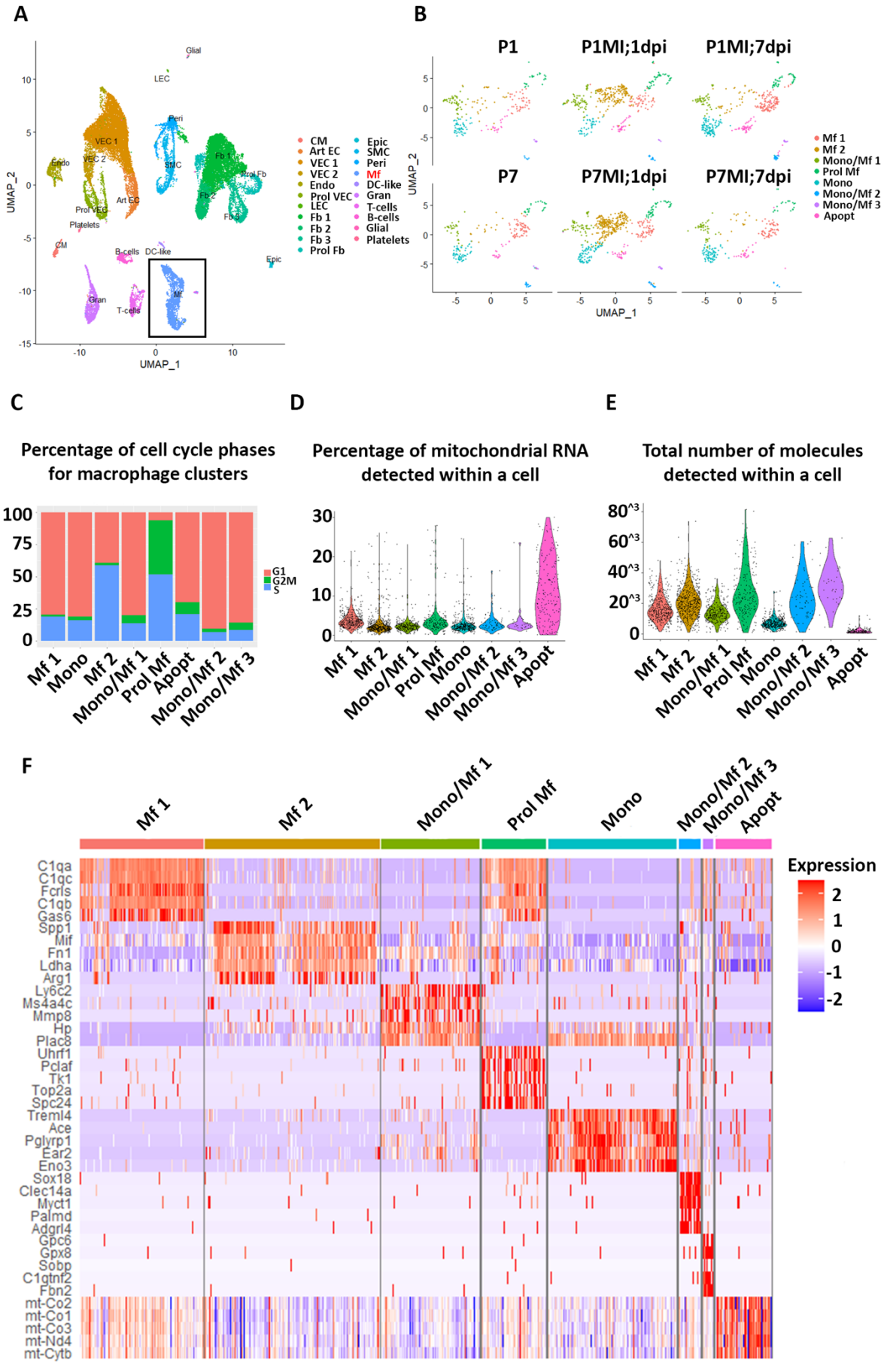
A
B
C
D
E
F
UMAP_1
UMAP_2
P1
P1MI;1dpi
P1MI;7dpi
P7
P7MI;1dpi
P7MI;7dpi
Percentage of cell cycle phases for macrophage clusters
Percentage of mitochondrial RNA detected within a cell
Total number of molecules detected within a cell
Expression

Figure 7.3 Six macrophage and monocyte populations detected in the postnatal heart after MI.

UMAP showing all the cell populations detected from scRNA-seq, the box highlights the macrophage cluster specifically (A). UMAP of the macrophage and monocyte clusters separeted based on timepoint and condition (P1 intact, P1MI;1dpi, P1MI;7dpi, P7 intact, P7MI;1dpi and P7MI;7dpi) (B). The percentage of cell cycle phages for each macrophage and monocyte cluster confirms the existans of a proliferating population (C). Also, approximately half of the cluster Mf2 is at phase S of cell division (C). The percentage of mitochondial RNA (D) and the number of molecules (E) detected within cells confirmes the existans of an apoptotic population. The unbiased differential expression analysis identified genes that were enriched in each cluster by comparing it to all the other clusters (F). Mf1 = macrophage 1; Mf2 = macrophage 2; Mono/Mf1 = Monocyte-derived macrophage 1; Prol Mf = proliferating macrophage; Mono = monocyte; Mono/Mf2 = Monocyte-derived macrophage 2; Mono/Mf3 = Monocyte-derived macrophage 3; Apopt = apoptotic macrophage.

The gene expression levels of known macrophage and monocyte genes were examined to characterise the macrophage clusters in more detail (Figure 7.4 A). All clusters exhibited high expression levels of the pan-macrophage markers *Cd68* and *F4/80*, confirming their myeloid identity (Figure 7.4 A). In agreement with previous observations, macrophages generally did not express *Mhc-II* in the postnatal heart[138,140,142]. The Mf1 cluster expressed high levels of embryonic-derived genes (*Cx3cr1*, *Cd206* and *Lyve1*) and was negative for *Ccr2*, suggesting it consists largely of embryonic-derived cardiac-resident macrophages (Figure 7.4 A). In contrast, the Mf2 cluster expressed low levels of embryonic-derived markers and high levels of *Ccr2* and *Arg1* (Arginase 1), suggesting that it contains tissue-resident macrophages originating from the bone marrow (Figure 7.4 A). Interestingly, *Arg1* and *Cd206* are considered to be classical M2 macrophage markers[265,267], yet this analysis found them to be expressed in two different clusters (Mf1 and Mf2) in a mutually-excluded manner (Figure 7.4 A). This further supports the heterogeneity of macrophages beyond the M1/M2 classification. Moreover, *Ear2* (Nuclear Receptor Subfamily 2 Group F Member 6) was found to be expressed by Mono, Mono/Mf1, Mono/Mf2 and Mono/Mf3 cells, suggesting that Mono/Mf1, Mono/Mf2 and Mono/Mf3 originate from monocytes (Figure

7.4 A). This was further supported by the expression of *Ly6c2* by Mono/Mf3 cells (Figure 7.4 A).

Next, the representation of macrophage populations in the postnatal heart was analysed (Figure 7.4 B). In intact P1 and P7 hearts, macrophages and monocytes made up a combined 3-4 % of non-myocytes. There was a rapid expansion of Mf2 macrophages from 0.65 % in the P1 control to 5.69 % 1 day after P1 MI. A similar increase of Mf2 macrophages was observed from 0.22 % in the P14 control to 5.27 % 1 day after P7 MI. After this initial expansion, the percentage of Mf2 macrophages returned to baseline levels 7 days after MI at P1 and P7. A more gradual increase was observed in the percentage of Mf1 macrophages. In the P1 control, the percentage of Mf1 macrophages was 0.91 % and increased to 1.51 % at 1dpi, finally reaching 2.26 % at 7dpi. Similarly, the percentage of Mf1 macrophages was 0.77 % in the P7 control, rising to 1.24 % at 1dpi and 2.59 % at 7dpi. The percentage of Mono/Mf2 and Mono/Mf3 macrophages remained stable at 0.5 % at all conditions and timepoints. As expected, the percentage of monocytes (Mono) remained fairly constant with 1.04 % in the P1 control and 1.90 % 7 days after MI at P1. However, the percentage increased from 0.7 % in the P7 control to 3.39 % 7 days after MI at P7. This suggests limited contribution of monocytes after MI at P1, in contrast to increased infiltration after MI at P7. Finally, there was an increase in the percentage of Mono/Mf1 macrophages from 1.24 % in the P1 control to 2.05 % 1dpi, before it dropped to 0.99 % 7dpi. The increase observed in the percentage of Mono/Mf1 macrophages in P7 hearts after MI was more gradual, rising from 0.41 % in the P7 control to 1.93 % 7dpi.

To confirm that the increase in the percentage of Mf1 and Mf2 macrophages observed after MI at P1 and P7 was due to self-proliferation, rather than monocyte differentiation, the gene expression levels of the top-5 markers for Mf1, Mf2, Mono/Mf and Mono clusters were investigated in the Prol Mf cluster (Figure 7.4 C). Prol Mf macrophages appeared to be expressing high levels of Mf1 markers in all conditions and timepoints. Interestingly, Prol Mf macrophages expressed Mf2 markers mainly 1 day after MI at both P1 and P7. In contrast, there was little to no expression of Mono and Mono/Mf1 markers by Prol Mf macrophages. These results suggest that Mf1 macrophages proliferate throughout postnatal development and after MI, while Mf2 macrophages proliferate mainly after MI. Also, the close association of Mf1 and Prol Mf clusters seen in UMAP (Figure 7.3 B) and the high levels of cell-cycle markers found to be expressed by Mf2 macrophages (Figure 7.3 C) further support the proliferation hypothesis.

Overall, the postnatal heart appears to be populated mainly by two tissue-resident macrophage populations, the Mf1 population that is *Lyve1*$^{+}$*;Ccr2*$^{-}$*;Arg1*$^{-}$ and the Mf2 population that is *Lyve1*$^{-}$*;Ccr2*$^{+}$*;Arg1*$^{+}$. These tissue-resident macrophage populations have a different temporal response after MI at P1 and P7. Mf1 macrophages proliferate during postnatal development and expand gradually during the first 7 days after MI at P1 and P7. In contrast, Mf2 macrophages expand rapidly through proliferation 1 day after MI at P1 and P7 and subsequently decrease.

A

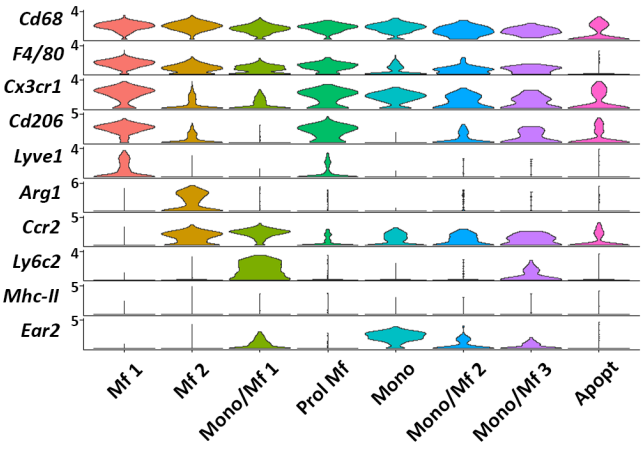

B

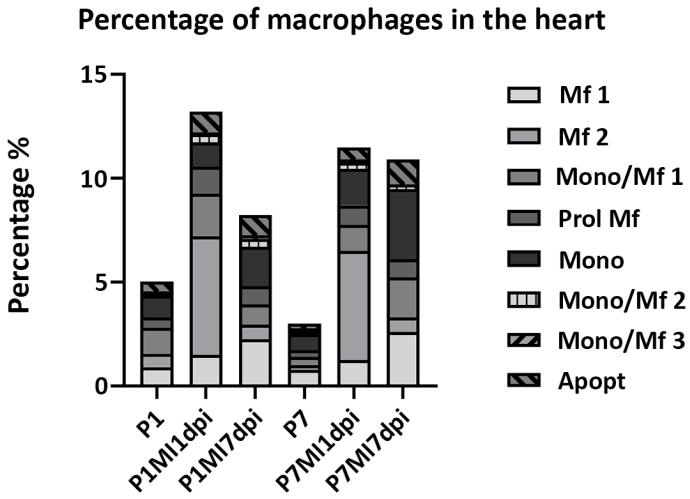

Percentage	Mf 1	Mf 2	Mono/Mf 1	Prol Mf	Mono	Mono/Mf 2	Mono/Mf 3	Apopt
P1	0.91%	0.65%	1.24%	0.50%	1.04%	0.11%	0.11%	0.46%
P1MI1dpi	1.51%	5.69%	2.05%	1.31%	1.17%	0.40%	0.09%	1.00%
P1MI7dpi	2.26%	0.68%	0.99%	0.88%	1.90%	0.37%	0.18%	0.99%
P7	0.77%	0.22%	0.41%	0.32%	0.77%	0.17%	0.11%	0.24%
P7MI1dpi	1.24%	5.27%	1.24%	0.94%	1.78%	0.29%	0.15%	0.57%
P7MI7dpi	2.59%	0.70%	1.93%	0.88%	3.39%	0.22%	0.00%	1.19%

C

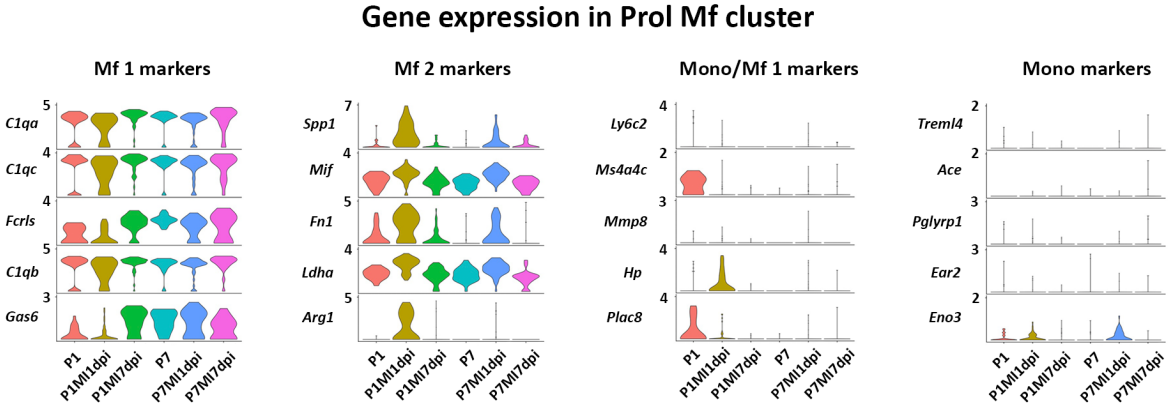

Figure 7.4 Tissue-resident macrophages proliferate with different dynamic after MI.

Stacked violin plots showing expression of gene markers for each cluster suggests two tissue-resident macrophage populations Mf1 (*Lyve1*$^{+}$*;Ccr2*$^{-}$*;Arg1*$^{-}$) and Mf2 (*Lyve1*$^{-}$*;Ccr2*$^{+}$*;Arg1*$^{+}$) (A). Percentage of each cell population at different timepoints and conditions (B). Mf1 cells respond to MI with a gradual increase, while Mf2 cells respond through a rapid increase at 1dpi (B). Percentage of Mono and Mono/Mf1 cells increase mainly 7 days after MI at P7 (B). Prol Mf express genes that are specific for Mf1 and Mf2 populations, suggesting that these two populations proliferate (C). In contrast, Prol Mf do not express monocyte specific genes (C).

7.3.3. *Potential interactions between macrophages and cardiac LECs*

Macrophages have been described to interact with several cell populations in intact hearts and after injury[231,268]. Here, the macrophage interactome was analysed to identify potential cross-talk between macrophages and LECs that could lead to lymphangiogenesis and/or macrophage clearance in the postnatal heart (Figure 7.5). For the ligand-receptor analysis the scTalk pipeline in R was used on the integrated scRNA-seq dataset, as described in the Materials & Methods[268].

After examining the expression of known ligands and receptors in all clusters of the postnatal heart, it was found that fibroblasts exhibited the largest number of outbound connections (ligands), while ECs exhibited the largest number of inbound connections (receptors) (Figure 7.5 A-B). Similarly to the general EC trend, LECs showed substantially more inbound connections than outbound (Figure 7.5 A-B). In contrast, macrophages (Mfs) were found to have approximately half the inbound compared to outbound connections (Figure 7.5 A-B). This suggests that Mfs secrete a large number of extracellular ligands that can induce paracrine or autocrine signalling. Indeed, while Mfs appeared to receive signals only from Fb1 and Gran cells, they communicated with ECs, Platelets, Peri and all immune cells by paracrine signalling, and also showed autocrine signalling (Figure 7.5 B). In contrast, LECs appeared to communicate only with Fb, Gran and Platelet cells (Figure B). Regardless

of the small number of interactions of LECs with other cell populations, the ligands secreted by LECs and Mfs were further examined (Figure 7.5 C-D). Interestingly, *Reln, Angpt2* (Angiopoietin 2), *Efnb2* (Ephrin-B2), as well as *Sema3a* (Semaphorin-3A), *Tnc* (Tenascin C) and *Ntn1* (Netrin 1) were amongst the top LEC outbound ligands (Figure 7.5 C). *Reln* has been described to have a cardioprotective role after MI[269], while *Angpt2* and *Efnb2* have angio- and lymphangio-genic functions, respectively[270–274]. Furthermore, *Sema3a*, *Tnc* and *Ntn1* have been found to regulate axon guidance during neuronal development[275–277]. The ligands found to be expressed by Mfs had mainly immune response related functions. For instance, *Ccl7 (*C-C Motif Chemokine Ligand 7) has anti-inflammatory functions and *Ccl2* (Chemokine C-C motif ligand 2) is involved in the migration of monocytes and macrophages (Figure 7.5 D). Finally, potential interactions between ligands and receptors expressed by LECs and Mfs were examined (Figure 7.5 E-F). The scTalk analysis found one potential interaction between the LEC ligand RELN and the Mf receptor ITGB1 (Integrin Subunit Beta 1), which has not previously been described in these cell populations. When screening for potential interactions between Mf secreted factors and LECs, the ligand SPP1 (Secreted Phosphoprotein 1) was found. Specifically, it was suggested to interact with LEC receptors that are known to be involved in the regulation of angio- and lymphangio-genesis (*Itgav*, *Itga5*, *Itgb1* and *Itga9*)[278–282], making SPP1 an interesting ligand for future lymphangiogenesis related studies.

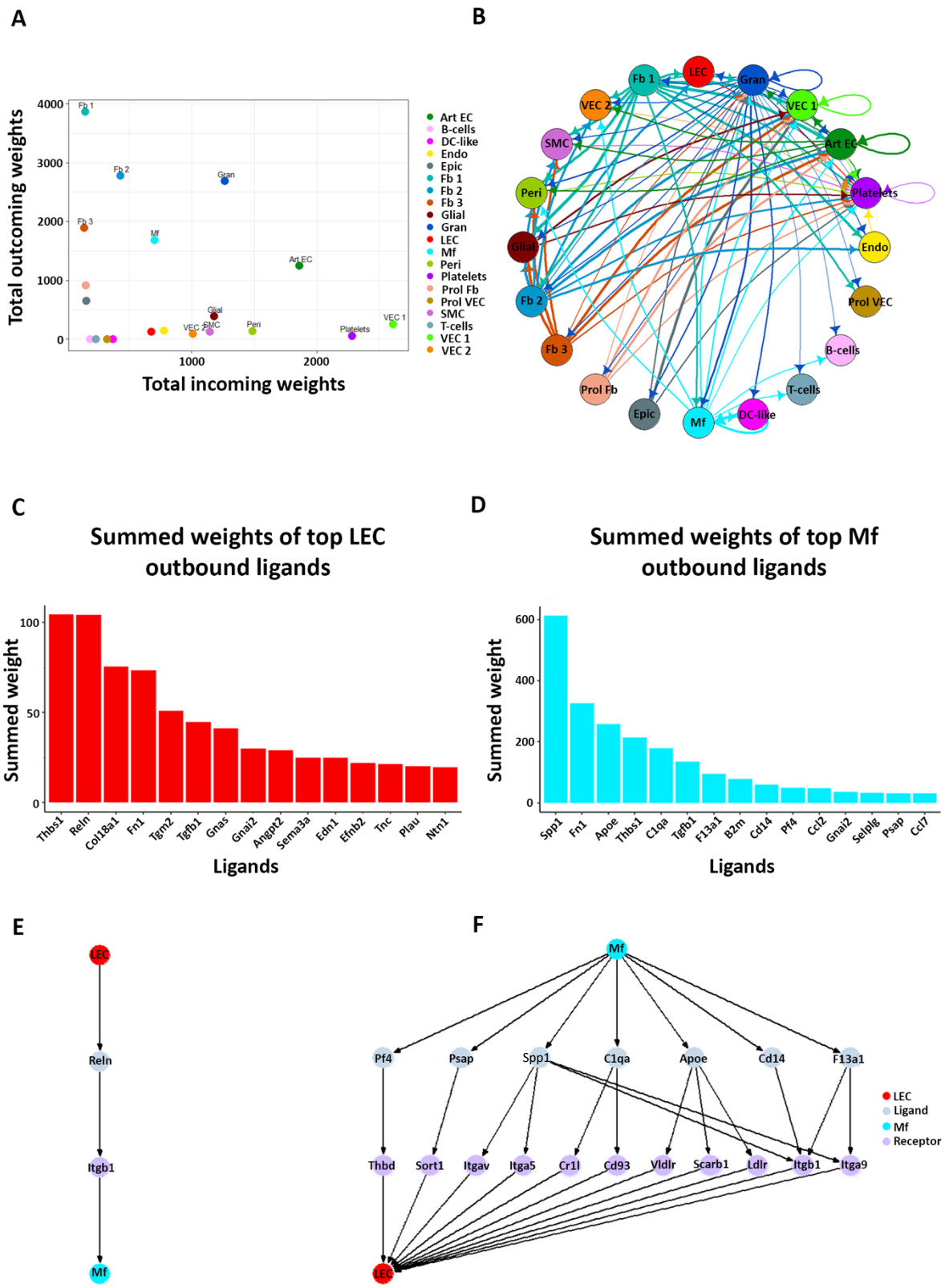

Figure 7.5 Macrophages could interact with cardiac LECs in postnatal stages.

Comparison of total incoming path weights and total outgoing path weights across populations (A). Fibroblasts appear to have the mosth outcoming, while ECs the mosth incoming (A). Hierarchical network diagram of significant cell-cell interaction pathways, with arrows and edge color indicating direction (ligand:receptor) (B). Summed ligand weights across ligand and receptor target paths for

top ligands in LEC (C) and Mf (D). Tree plot showing outgoing connections from the LECs to Mf (E) and from Mf to LECs (F). Top node refers to source population, second layer to ligands, third layer to receptors and bottom node represent the target population (E-F).

Since no ligands or receptors known to interact with LECs were identified by the previous unbiased analysis, their gene expression levels were determined in postnatal cardiac macrophages (Figure 7.6 A). Unexpectedly, macrophages were found not to express *Vegfc*, *Vegfd* or *Ccr7* (Figure 7.6 A). Also, *Has1*, *Has2* and *Has3* (Hyaluronan synthase 1, 2 and 3) were not expressed by macrophages in the postnatal heart, albeit they have been shown to mediate the interaction between DCs and LECs *in vivo*[174,283], as well as between macrophages and LECs *in vitro*[145] (Figure 7.6 A). However, all macrophage and monocyte populations were found to ubiquitously express *Itgb1* in intact and injured P1 and P7 hearts (Figure 7.6 A and C). This suggests potential cross-talk between RELN and ITGB1 in macrophages may lead to the same signalling pathway in both intact and injured postnatal hearts. Interestingly, *Spp1* was found to be specifically expressed by Mf2 macrophages, and was highly upregulated after MI at P1 and P7 (Figure 7.3 F and Figure 7.6 B). This suggests that macrophages could regulate lymphangiogenesis through the secretion of SPP1 after MI at postnatal stages. Another interesting finding was the expression of *Pdpn* by Mono/Mf3 macrophages, although at low levels (Figure 7.6 A). Monocyte-derived macrophages have been found to express *Pdpn* in response to inflammation and cancers, with macrophage-expressed PDPN playing an important role in the regulation of lymphangiogenesis[284,285]. To verify potential expression of *Pdpn*, previously published bulk RNA-seq data of macrophages isolated from CD1 P1, P7 and adult hearts by FACS in intact and at days 1, 4 and 7 after MI were re-analysed[166]. Interestingly, macrophages were found to significantly over-express *Pdpn* 1 day after MI in adult mice compared to intact adult hearts ($p < 0.001$; top 30 over-expressed genes) (Figure 7.6 D). Subsequently, the

expression levels dropped significantly 4 days after MI (p = 0.001) and even further 7 days after MI (Figure 7.6 D). This indicates a rapid response of *Pdpn*-expressing macrophages to MI in adults. In the P1 and P7 setting, expression of *Pdpn* did not change either 4 or 7 days after MI compared to the respective intact stages (Figure 7.6 D). Unfortunately, there were no data available for 1 day after MI in postnatal mice, but it is tempting to speculate that it would have reflected the same trend seen in adult mice[166]. Of note, *Spp1* was found to be significantly upregulated by FACS sorted macrophages[166] 1 day after MI in adults and 4 days after MI in neonates (p < 0.001; 1 dpi data not available; Figure 7.6 E).

Overall, the scTalk analysis of the scRNA-seq data suggests that cardiac LECs could interact with macrophages through the RELN-ITGB1 signalling pathway in postnatal mice, which identifies a putative functional pathway for future studies to validate. Also, macrophages potentially interteract with cardiac LECs by several paracrine signalling pathways, such as those involving SPP1, as well as directly through the expression of PDPN. However, macrophages appear not to express other well-characterised lymphatic associated genes, such as *Vegfc*, *Vegfd*, *Has1/2/3* and *Ccr7*. These results require further validation in the future using more targeted and sensitive methods, such as functional gene targeting studies.

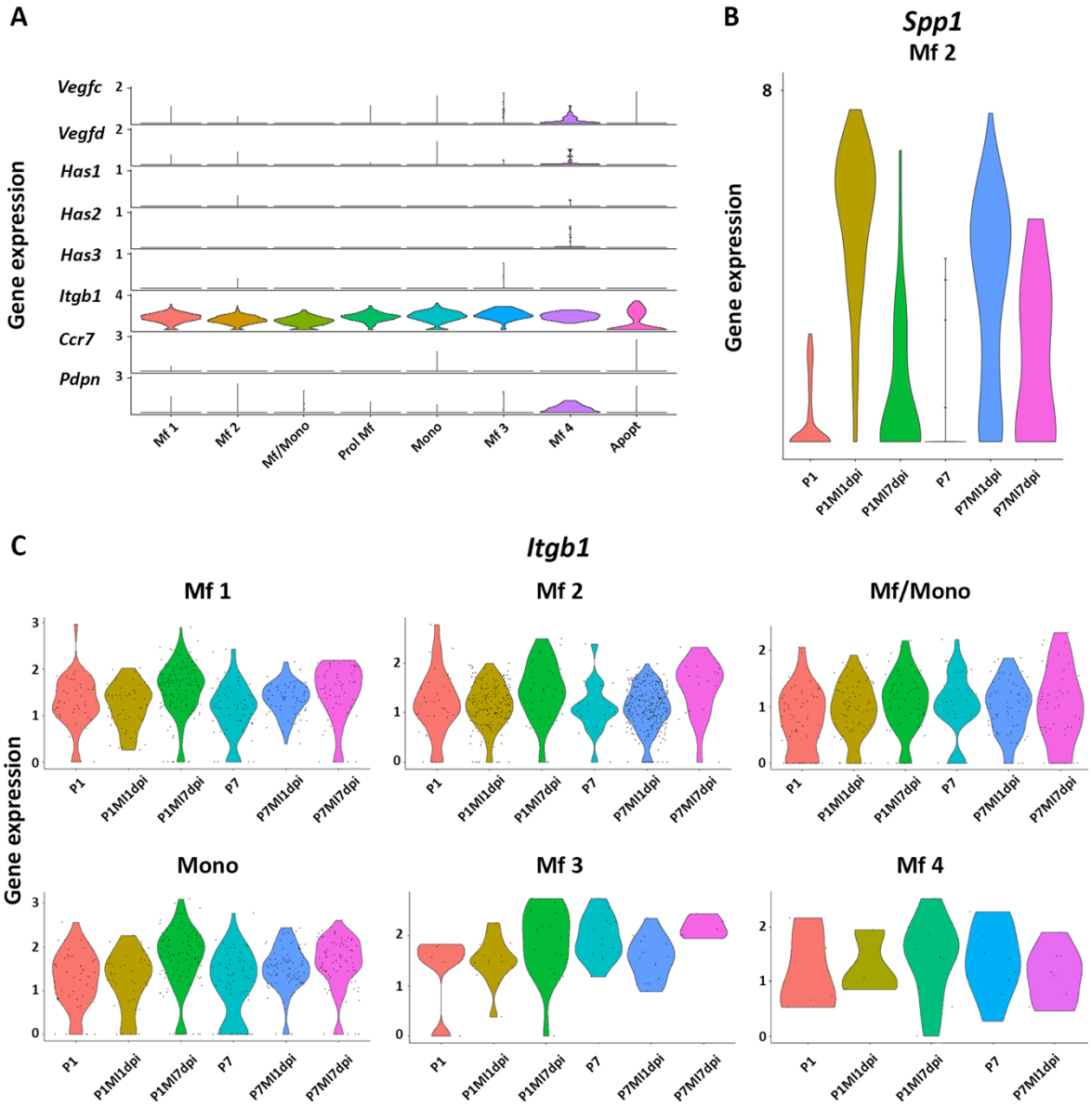
A
Vegfc
Vegfd
Has1
Has2
Has3
Itgb1
Ccr7
Pdpn
Gene expression
Mf 1
Mf 2
Mf/Mono
Prol Mf
Mono
Mf 3
Mf 4
Apopt
B
Spp1
Mf 2
Gene expression
P1
P1Ml1dpi
P1Ml7dpi
P7
P7Ml1dpi
P7Ml7dpi
C
Itgb1
Mf 1
Mf 2
Mf/Mono
Mono
Mf 3
Mf 4
Gene expression
D
Pdpn
<0.001
0.001
Gene expression
P1
P7
Adult
Baseline
1dpi
4dpi
7dpi
E
Spp1
<0.001
<0.001
<0.001 (P1)
Gene expression
P1
P7
Adult
Baseline
1dpi
4dpi
7dpi

Figure 7.6 Postnatal gene expression of potential macrophage ligands and receptors.

Stacked violin plots showing gene expression for each macrophage cluster of ligands that are known to interact with LECs (A). Expression levels of *Spp1* ligand in cluster Mf2 (B). Violin plots showing gene expression of *Itgb1* for all timepoints and conditions in every macrophage cluster (C). Previously published data from FACS macrophages[166] re-analysed to examine gene expression levels of *Pdpn* (D) and *Spp1* (E).

7.3.4. *Podoplanin-expressing macrophages do not enhance lymphatic sprouting in vitro*

To explore the possibility that inflammatory macrophages express *Pdpn* and promote lymphangiogenesis, the LEC-macrophage interaction was modelled using an *in vitro* assay of lymphatic capillary sprouting as described in Materials & Methods. Briefly, human primary LECs were co-cultured with human induced pluripotent stem cell (hiPSC)-derived macrophages and the number of lymphatic sprouting events was assessed by quantitative microscopy[145,286–288]. The hiPSC-derived macrophages used here have been previously characterised and exhibit foetal-like properties, mimicking the expression profile of tissue-resident macrophages, while upon activation they produce proinflammatory cytokines similar to monocyte-derived macrophages[145,286–288]. All cell culture experiments were performed by Dr Christophe Ravaud.

First, hiPSC-derived macrophages were classified in four groups depending on their activation state: resting, alternative activated, activated and classically activated (Figure 7.7 A). To induce the different states of activation, resting macrophages were treated with IL4 (Interleukin 4, alternative activated), with IFNγ (Interferon gamma, activated) and with a combination of IFNγ and LPS (Lipopolysaccharides, classically activated) (Figure 7.7 A). To verify the activation state of each *in vitro* macrophage group, qPCR was performed using known genes[265] (Figure 7.7 B). The gene expression level of the pan-macrophage marker *Cd18* did not change after treatment with IL4 or IFNγ (Figure 7.7 B). *Cd68*, another pan-

macrophage marker, was slightly but significantly downregulated in alternative activated and activated macrophages compared to resting macrophages (LogFC ± SEM: -0.61 ± 0.14 vs -0.02 ± 0.2 ; p = 0.046 and -0.66 ± 0.07 vs -0.02 ± 0.2; p = 0.03, respectively). However, both *Cd18* and *Cd68* were significantly downregulated in classically activated macrophages compared to resting macrophages (LogFC ± SEM: -0.96 ± 0.07 vs -0.02 ± 0.27; p = 0.049 and -2.14 ± 0.1 vs -0.02 ± 0.2; p < 0.001, respectively). As expected, macrophages treated with IL4 up-regulated alternative activated macrophage markers, such as *Ccl13*, *Ccl18*, and Cd206, compared to resting macrophages (LogFC ± SEM: 3.44 ± 0.14 vs -0.02 ± 0.22; p < 0.001, 4.7 ± 0.49 vs -0.02 ± 0.25; p < 0.001 and 1.2 ± 0.07 vs -0.02 ± 0.3; p = 0.006 , respectively). They also down-regulated classically activated macrophage markers, such as *Cxcl11* and *Tnfa* (LogFC ± SEM: -2.5 ± 0.52 vs -0.02 ± 0.72; p = 0.014 and -1.54 ± 0.27 vs -0.02 ± 0.28; p = 0.045, respectively). Macrophages treated only with IFNγ upregulated the classically activated macrophage markers *Cxcl9* and *Cxcl11* compared to resting macrophages (LogFC ± SEM: 7.37 ± 0.51 vs -0.02 ± 0.95; p < 0.001 and 2.41 ± 0.29 vs -0.02 ± 0.72; p = 0.016, respectively), while no changes were found in the expression levels of any other genes examined. Contrasting this observation, macrophages treated with both IFNγ and LPS significantly downregulated the alternative activated markers *Ccl13* and *Cd206* (LogFC ± SEM: -2.95 ± 0.45 vs -0.02 ± 0.22 and -4.48 ± 0.18 vs -0.02 ± 0.3, respectively; p < 0.001) and upregulated the classically activated markers (*Ccr7*, *Cxcl9*, *Cxcl11* and *Tnfa;* LogFC ± SEM: 6.82 ± 0.39 vs -0.02 ± 0.31; p < 0.001, 10.71 ± 0.36 vs -0.02 ± 0.95; p <0.001, 2.28 ± 0.15 vs -0.02 ± 0.72; p = 0.022 and 2.38 ± 0.58 vs -0.02 ± 0.28; p = 0.002, respectively). These expression profiles suggest that macrophage activation and classification was successful and in line with previously published data[265]. Subsequently, the expression of *Pdpn* was examined through qPCR (Figure 7.7 C). It was found that only

classically activated macrophages significantly upregulated *Pdpn* compared to resting macrophages (LogFC ± SEM: 2.83 ± 0.32 vs -0.02 ± 0.3; $p < 0.001$) (Figure 7.7 C). The Ct value for *Pdpn* was greater than 30 in resting, alternative activated and activated macrophages indicating very low expression levels.

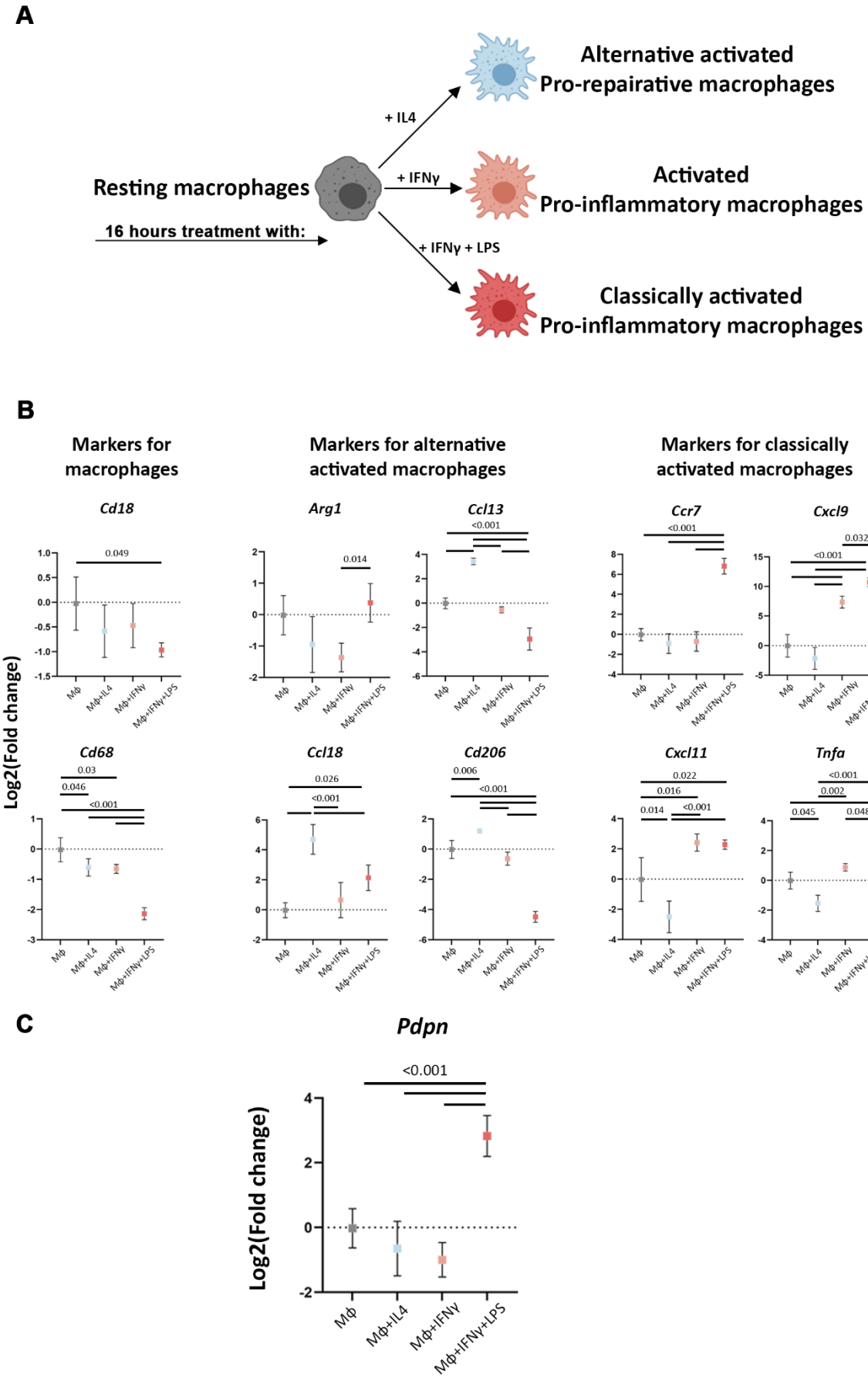
A
Alternative activated
Pro-repairative macrophages
+ IL4
Resting macrophages
+ IFNγ
Activated
Pro-inflammatory macrophages
16 hours treatment with:
+ IFNγ + LPS
Classically activated
Pro-inflammatory macrophages
B
Markers for macrophages
Markers for alternative activated macrophages
Markers for classically activated macrophages
Cd18
Arg1
Ccl13
Ccr7
Cxcl9
Cd68
Ccl18
Cd206
Cxcl11
Tnfa
Log2(Fold change)
Mϕ
Mϕ+IL4
Mϕ+IFNγ
Mϕ+IFNγ+LPS
C
Pdpn
Log2(Fold change)

Figure 7.7 Classically activated macrophages express high levels of Pdpn in vitro.

Illustration of the hiPSC-derived macrophage activation strategy (A). Gene expression of pan-macrophage, alternative activated and classically activated markers using qPCR (B). Macrophages activated with IL4 expressed higher levels of alternative activated markers, while macrophages with IFNγ alone or with LPS expressed higher levels of classically activated markers (B). Expression levels of *Pdpn* in resting and activated hiPSC-derived macrophages using qPCR (C). Classically activated macrophages expressed significantly higher levels of *Pdpn* compared to the other macrophages (C). Data are presented as mean ± SEM; n = 4 biological replicates. Significant differences were calculated using 1-way ANOVA followed by Tukey's multiple comparisons test. The data was kindly generated by Dr Christophe Ravaud.

Following the results described above, the ability of classically activated macrophages to promote lymphangiogenesis was tested in an *in vitro* co-culture macrophage and lymphatic sprouting assay (Figure 7.8). To account for the effect of macrophage secreted paracrine factors, a treatment control with macrophage media only was introduced (see also Materials & Methods). Co-culture of resting hiPSC-derived macrophages with human dermal LECs enhanced lymphatic sprouting compared the macrophage media control (Figure 7.8). This supports previously published data showing that macrophages regulate lymphangiogenesis through physical interaction, rather than paracrine factors[145]. However, similar levels of increased lymphatic sprouting were observed in all activated macrophages compared to the macrophage media control, with classically activated macrophages not displaying any further improvement in lymphatic sprouting (Figure 7.8). These data suggest that, while hiPSC-derived macrophages can enhance lymphatic sprouting *in vitro*, the mechanism involved is PDPN-independent.

While there are simillarities in the gene expression profiles of *in vitro* alternative activated and *in vivo* pro-regenerative macrophages, as well as of *in vitro* classically activated and *in vivo* pro-fibrotic macrophages, many more genes are regulated in opposite or unrelated ways[265]. Thus, the *in vitro* macrophages cannot be considered equivalent to the *in vivo*

macrophages. Consequently, *Pdpn* expression by macrophages might still contribute to lymphatic sprouting in the mouse model, even though it seems to be redundant for the enhancement of lymphatic sprouting *in vitro*.

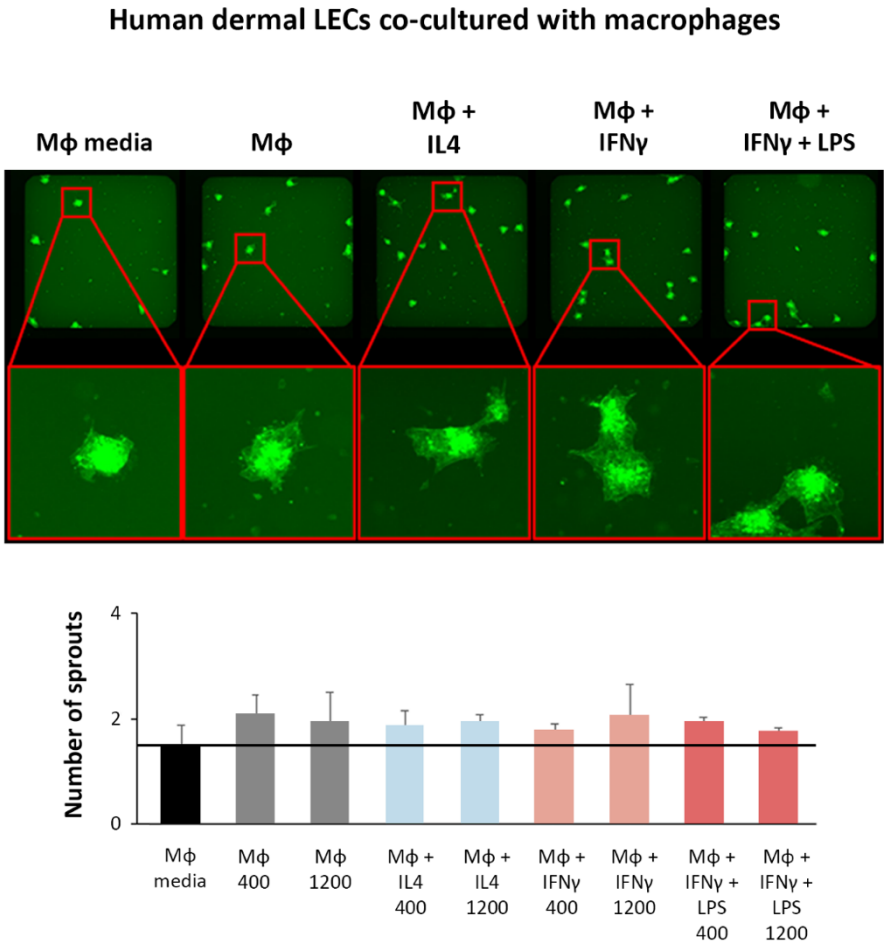

Figure 7.8 hiPSC-derived macrophages enhance lymphatic sprouting independently of Pdpn expression.

In vitro lymphatic sprouting assay, where human dermal LECs are co-culture with hiPSC-derived macrophage or macrophage media as control. Representative images of LEC sprouts in different conditions. Images were quantified for the number of lymphatic sprouts detected in each condition. The number of sprouts increased when LECs were co-culture with macrophages compared to macrophage media alone, but did not further increase with activated macrophages compared to resting macrophages. Data are presented as mean ± SEM; n = 2 biological replicates. The data was kindly generated by Dr Christophe Ravaud.

7.4. Discussion

In this chapter, the macrophage response and their interaction with cardiac lymphatics was investigated 1 and 7 days after MI in regenerative P1 and non-regenerative/fibrotic P7 hearts. Previous studies have found that macrophages are essential for the regeneration of the infarcted P1 heart by regulating processes like angiogenesis and cardiomyocyte proliferation[140,165,205,210,231]. Also, macrophages have been shown to interact with cardiac lymphatic vessels and regulate their development during embryonic stages[145,146]. However, the interaction of macrophages with cardiac lymphatics in regenerative P1 hearts had not been investigated before.

In this study, scRNA-seq analysis showed that the postnatal heart contains two molecularly distinct tissue-resident macrophage populations (mf1: *Lyve1*$^{+}$*;Ccr2*$^{-}$*;Arg1*$^{-}$ and mf2: *Lyve1*$^{-}$*;Ccr2*$^{+}$*;Arg1*$^{+}$). Previously published studies have also identified at least two macrophage populations that have different origins based on the expression of *Cx3cr1* and *Ccr2*[138,140,142,165,264]. After comparison of the expression profiles of the two macrophage populations identified here to previously published data it became evident that *Lyve1*$^{+}$*;Ccr2*$^{-}$*;Arg1*$^{-}$ macrophages correspond to embryonic-derived tissue-resident macrophages, while *Lyve1*$^{-}$*;Ccr2*$^{+}$*;Arg1*$^{+}$ match bone marrow-derived tissue resident macrophages. These tissue-resident macrophage populations responded differently after postnatal MI. *Lyve1*$^{-}$*;Ccr2*$^{+}$*;Arg1*$^{+}$ cells proliferated rapidly 1 day after MI at P1 and P7, and their representation in the heart was subsequently reduced 7 days after MI. Moreover, *Lyve1*$^{-}$*;Ccr2*$^{+}$*;Arg1*$^{+}$ macrophages did not appear to proliferate during postnatal development. In contrast, the percentage of embryonic-derived *Lyve1*$^{+}$*;Ccr2*$^{-}$*;Arg1*$^{-}$ macrophages in the heart increased gradually by local proliferation from intact to 7 days

after MI at both P1 and P7. *Lyve1*$^{+}$*;Ccr2*$^{-}$*;Arg1*$^{-}$ macrophages were also found to be proliferating throught postnatal development. These findings are in line with previously published data showing that embryonic-derived macrophages are maintained through local proliferation[138,140,142,165,264]. Besides the aforementioned tissue-resident populations, three additional macrophage populations were present in the postnatal heart. The latter were found to express the monocyte markers *Ear2* and *Ly6c2,* indicating that they are monocyte-derived macrophages. The fraction of these three monocyte-derived macrophage clusters remained low throughout development, and only one of them increased after MI at postnatal stages. Only one monocyte population was present in the heart and its fraction increased 7 days after MI at P7. Overall, these data indicate that the response of tissue-resident macrophages through proliferation is similar after MI at P1 and P7, while there are more monocytes infiltrating the heart after MI at P7 compared to MI at P1. This adds further evidence to what is already known regarding the heterogeneity of macrophages that respond to MI during postnatal and adult stages.

After MI in neonatal and adult mice, macrophages secrete ligands, which contribute to wound healing by interacting with the coronary endothelium and cardiomyocytes to promote angiogenesis and cardiomyocyte proliferation, respectively[140,165,205,210,231]. Here, an unbiased approach was used to identify potential cross-talk between the two cell populations, and a biased search was conducted for previously suggested interactions[39,76,145,284]. The unbiased approach identified a potential interaction between the LEC-expressed ligand *Reln* and the macrophage-expressed receptor *Itgb1*. RELN is specifically expressed by cardiac LECs (see also chapter 6), and its interaction with ITGB1 is required for neonatal heart regeneration, as it promotes cardiomyocyte proliferation and

survival[269]. The RELN-ITGB1 interaction has not been described previously in macrophages, and ubiquitous ITGB1 expression could provide a mechanism for cardiac macrophage proliferation. Screening for macrophage-expressed ligands that could interact with LEC-expressed receptors led to the identification of several potential interactions. The ligand *Spp1* was the most differentially expressed gene in the *Lyve1*$^{-}$*;Ccr2*$^{+}$*;Arg1*$^{+}$ tissue-resident macrophages. This was of particular interest, as its expression was highly upregulated after MI at P1 and P7, and it was suggested to interact with several cardiac LEC-expressed integrins that have been connected to angio- and lymphangio-genesis. Consequently, this raises the question whether SPP1 and its potential interaction with LEC-expressed integrins might play a role in regulating lymphangiogenesis after MI in the postnatal mouse heart. These analyses generated hypotheses regarding potential interactions between cardiac LECs and macrophages that need to be functionally validated in future studies.

When searching for previously published interactions between macrophages and LECs, the following proteins were examined: VEGFC, VEGFD, HA, CCR7 and PDPN. VEGFC is secreted by macrophages and epicardial cells after MI in adult mice[39,76]. Subsequently, VEGFC interacts with the VEGFR3 receptor and promotes lymphangiogenesis[39,76]. Here, neither *Vegfc* nor *Vegfd* were found to be expressed by macrophages in the postnatal heart. HA is a known ligand for LYVE1, and *in vitro* experiments have suggested that macrophages induce lymphatic sprouting by physically interacting with LECs in a HA-dependent mechanism[145]. Also, DCs have been found to use the HA-LYVE1 interaction to dock and transmigrate inside lymphatic vessels[174,283]. As a result, the expression of *Has1*, *Has2* and *Has3*, which are responsible for HA synthesis, was examined in macrophages. However, none of the three genes were found to be expressed by macrophages in the postnatal

heart, indicating that macrophages do not interact with cardiac LECs through the HA-LYVE1 mechanism at these stages. As discussed in chapter 6, DCs and neutrophils express the receptor CCR7 which interacts with the LEC-secreted chemokine CCL21[245–247,258]. As CCL21 creates a chemokine gradient, DCs and neutrophils use the CCL21-CCR7 interaction to locate and dock to lymphatics[245–247,258]. In chapter 6, it was found that LECs express high levels of *Ccl21* during postnatal development and after MI at P7, but the levels were significantly reduced after MI at P1. Here, the expression levels of *Ccr7* by macrophages were examined. However, *Ccr7* was found not to be expressed by macrophages in the postnatal heart, indicating that macrophages do not use the CCL21-CCR7 interaction to locate and bind LECs. Finally, a population of macrophages has been shown to interact with lymphatics and promote lymphangiogenesis in a *Pdpn*-depend mechanism in a mouse breast cancer model[284]. By re-analysing previously published bulk RNA-seq data from FACS isolated macrophages, it was determined that *Pdpn* is significantly upregulated after MI in adult mice[166,289]. Here, low levels of *Pdpn* expression were detected in one of the monocyte-derived populations, suggesting that infiltrating macrophages could induce lymphangiogenesis after MI in a PDPN-mediated way.

An *in vitro* model of lymphatic sprouting was used to further investigate the hypothesis that inflammatory macrophages express *Pdpn* and interact with lymphatics to induce lymphangiogenesis. It was found that hiPSC-derived macrophages activated with IFNγ and LPS expressed significantly higher levels of *Pdpn* compared to resting, IL4 activated and IFNγ activated macrophages. While co-culture of hiPSC-derived macrophages with human dermal LECs increased the number of lymphatic sprouts compared to the macrophage media control, no differences in sprouting were observed in the differentially activated

macrophages. This suggests that *Pdpn*-expressing macrophages do not improve lymphangiogenesis *in vitro*. However, the mechanism may be different in vivo and specifically in the neonatal and adult mouse heart.

7.5. Summary

The work presented in this chapter investigated the transcriptional response of macrophages, as well as their interaction with cardiac lymphatic vessels, after MI in the regenerative P1 and fibrotic P7 stages. The data demonstrated that the postnatal heart contains two distinct tissue resident macrophage populations (*Lyve1^{+};Ccr2^{-};Arg1^{-}* and *Lyve1^{-};Ccr2^{+};Arg1^{+}*) that show different proliferation dynamics after cardiac injury. Moreover, infiltrating monocytes and monocyte-derived macrophages were found to represent a small percentage of the non-myocyte population in the postnatal heart, with their fraction increasing only after MI at P7. Unbiased analysis of the cardiac interactome suggested that the ligand SPP1, which was significantly upregulated by *Lyve1^{-};Ccr2^{+};Arg1^{+}* macrophages after MI at P1 and P7, could potentially interact with several LEC-expressed integrins to regulate lymphangiogenesis in the infarcted postnatal heart. Also, a potential interaction between RELN and ITGB1, which are expressed ubiquitously by LECs and macrophages respectively, could have a role in macrophage proliferation. Other lymphatic-related ligands and receptors, such as VEGFC, VEGFD, HAS1, HAS2, HAS3 and CCR7 were found not to be expressed by macrophages at postnatal stages. Interestingly, PDPN was found to be expressed at relatively low levels by monocyte-derived macrophages *in vivo*, as well as by classically activated hiPSC-derived macrophages *in vitro*. However, upon co-culture with human dermal LECs, the *Pdpn*-expressing macrophages failed to increase the number of lymphatic sprouts more than the resting and alternative activated macrophages

did. Overall, macrophages appear to be highly heterogeneous in the postnatal heart, and differential expression of ligands (*Spp1*) and receptors (*Pdpn*) could potentially influence lymphangiogenesis after MI at P1 and P7.

8. Results IV: Characterisation of the Lyve1^{Cre} line as a tool to investigate cardiac lymphatics

8.1. Background

The fate of LECs in mice is hard-wired early on during embryogenesis at the level of the mesoderm. Around E9.5, paraxial mesoderm-derived endothelial cells selectively differentiate from the dorsolateral part of the anterior CV to form the first precursor LECs, characterised by the expression of the transcription factor PROX1. These LECs subsequently give rise to most of the lymphatic endothelium, including cardiac lymphatics which form after E12.5. Other non-venous sources, such as the haemogenic endothelium, second heart field and potentially dermomyotome contribute directly to LECs[38,61,62,126,127]. Expression of *Prox1* is necessary and sufficient for LEC specification, making *Prox1* deletion an attractive approach to study the development and function of lymphatics. Previous studies have relied on *Cre*-drivers to conditionally knock-out *Prox1*[38,126], as constitutive *Prox1* knock-out mice do not survive past E14.5[290]. For instance, loss-of-function studies crossing *Prox1^{Flox}* with the transgenic lines *Tie2-Cre*, *Vav1-Cre* and *Islet1-Cre* have shown that venous endothelium-derived[38], haemogenic endothelium-derived[38] and SHF-derived LECs[126], respectively, are required for cardiac lymphatic development. However, conditional knock-out strategies based on transgenic *Cre* gene reporters have caveats, as unexpected changes in *Cre* expression patterns can occur from integration site-mediated alterations, differences in copy number or epigenetic alterations of the transgene[291,292]. Knock-in *Cre* lines should circumvent this issue, as *Cre* expression is driven by endogenous enhancers and the promoter of the gene-of-interest[291,292].

Here, the *Lyve1^{Cre}* mouse line was used to conditionally delete *Prox1* to disrupt cardiac lymphatics and study its effect in neonatal heart regeneration. This is a knock-in line with

the expression of the Cre recombinase being driven by the endogenous *Lyve1* promoter, as previously described[216]. *Lyve1^{Cre}* has been shown to label the yolk sac haemogenic endothelium[293,294], yolk sac and embryo-derived haematopoietic precursors[293,294], as well as LECs and BECs[216]. However, this line has not been used to study cardiac lymphatics before, and thus this chapter will cover the detailed characterisation of the *Lyve1^{Cre}* line and assess its suitability for studies of cardiac lymphatics (e.g., cross with *Prox1^{Flox}*).

8.2. Aims

The aims of this chapter are to describe the activity of *Lyve1^{Cre}* in the mouse heart during embryogenesis and characterise the cardiac phenotype of *Lyve1$^{+/Cre}$;Prox1$^{flox/flox}$* mutant mice.

8.3. Results

8.3.1. *Lyve1^{Cre} marks cardiac lymphatics and coronary vessels during embryogenesis*

In chapter 5 it was shown that *Lyve1^{Cre}* labelled the coronary blood endothelium, supporting previous studies that identified widespread LYVE1 expression in the embryonic blood vasculature[239]. However, the *Lyve1^{+}* lineage has not been studied in detail to date in the heart. To address this shortfall, male *Lyve1$^{+/Cre}$* mice were crossed with *R26R-tdTomato* reporter females, and the hearts of the resulting embryos harvested at E14.5 and E16.5 (Figure 8.1). Transmission of *Cre* through males only was selected to avoid complications arising from germline Cre-recombinase activation[295,296].

Immunostaining of *Lyve1$^{+/Cre}$;R26R-tdTomato* hearts using antibodies against the pan-endothelial marker PECAM1 (Platelet endothelial cell adhesion molecule-1), LYVE1 and PROX1 revealed *Cre* activity in both blood and lymphatic vasculature at E14.5 (Figure 8.1

A-L). Specifically, there was signal from tdTomato and PECAM1 co-localising in both large blood vessels and capillaries throughout the ventral side of the heart (Figure 8.1 D). On the dorsal side of the heart, tdTomato was detected in PECAM1^{+} blood vessels proximal to the SV (or inflow tract), as well as in the left and right ventricular wall (Figure 8.1 G and J). The lack of anti-LYVE1 antibody immunoreactivity in blood vessels of both sides of the heart at E14.5 suggests that the blood endothelium expresses *Lyve1* transiently at an earlier stage of heart development. On the ventral side of the heart, developing PROX1^{+} lymphatic vessels were either LYVE1^{-} near the outflow tract or LYVE1^{+} towards the apex (Figure 8.1 B and E-F). Interestingly, both PROX1^{+}LYVE1^{-} and PROX1^{+}LYVE1^{+} LECs appeared to express tdTomato (Figure 8.1 B and E-F). On the dorsal side of the heart, however, PROX1^{+} LECs located in the vicinity of the SV were found to be negative for both LYVE1 and tdTomato, with *Lyve1* labelling only becoming obvious in lymphatic vessels extending into the base of the developing heart (Figure 8.1 H and K-L).

At E16.5, staining of *Lyve1$^{+/Cre}$;R26R-tdTomato* hearts with the venous marker EMCN confirmed the widespread expression of tdTomato by coronary veins and capillaries, from the SV to ventricular wall and apex (Figure 8.2 A-C and F). By this timepoint all cardiac LECs co-expressed LYVE1 and tdTomato (Figure 8.2 A, D-E and G-H).

Overall, these results suggest that *Lyve1* is transiently expressed by the coronary vasculature before E14.5. Also, not all cardiac LECs are marked by *Lyve1^{Cre}*, particularly in the vicinity of the SV.

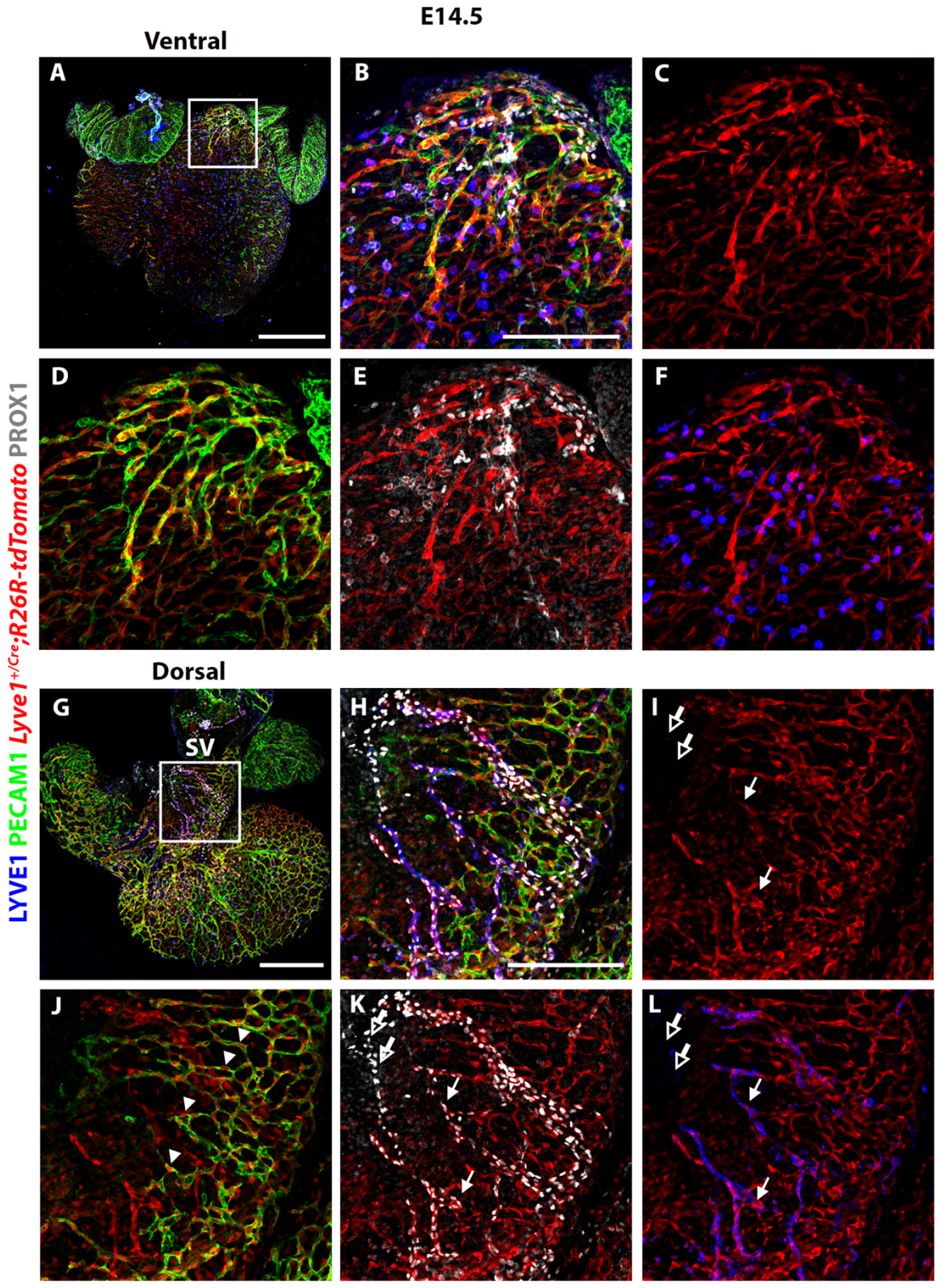

Figure 8.1 Confocal microscopy of Lyve1$^{+/Cre}$;R26R-tdTomato hearts at E14.5 shows Cre activation in coronary blood and lymphatic vessels.

(A-F) Visualisation of the ventral side of the heart at E14.5. (B-C and E-F) PECAM^{-};PROX1^{+};LYVE1^{+};tdTomato^{+} precursor LECs start forming lymphatic vessels. (B-D) tdTomato is also visible in PECAM^{+};PROX1^{-};LYVE1^{-} coronary vessels. (G-L) Visualisation of the dorsal side of the heart

at E14.5. (H-I and K-L) Near the SV, PROX1^{+} LECs appear to be negative for LYVE1 and tdTomato (hollow arrows), in contrast to LECs near the tips of the vessels which are LYVE1 and tdTomato positive (white arrows). (I-J) Coronary vessels in the SV are also positive for tdTomato (arrowheads). B-F magnified view of A box; H-L magnified view of G box; O-Q and R-T magnified views of M boxes. n = 2-4. Scale bars: 0.5 mm for A and G; 0.2 mm for B-F and H-L.

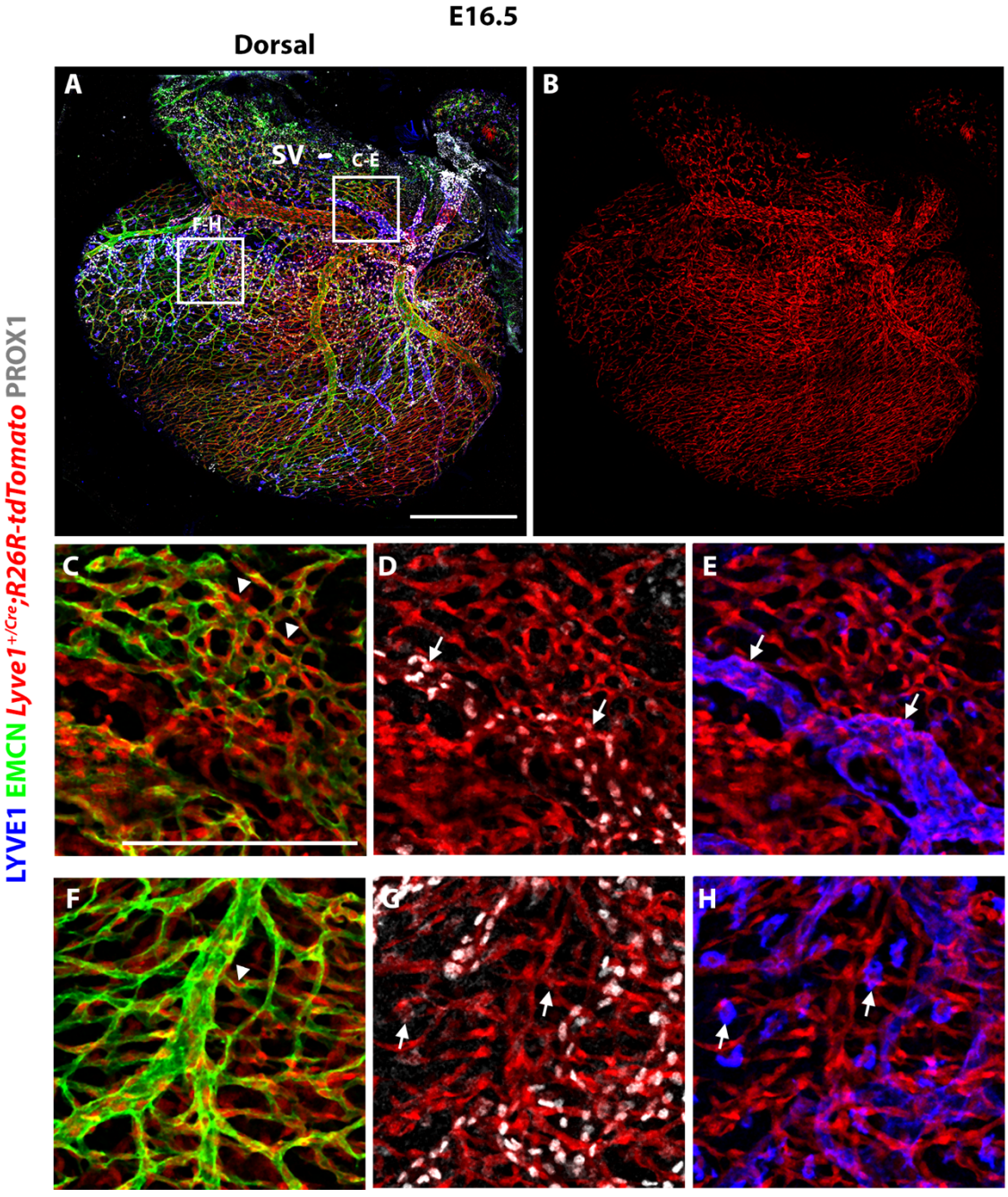

Figure 8.2 Confocal microscopy of Lyve1$^{+/Cre}$;R26R-tdTomato hearts at E16.5 shows Cre activation in coronary blood and lymphatic vessels.

Visualisation of the dorsal side of the heart at E16.5. (A-B, D-E and G-H) At this timepoint all LECs appear to be marked by *Lyve1^{Cre}*, both near the SV and towards the apex (white arrows). (A-B, C and F) tdTomato signal is detectable in both large coronary veins and capillaries stained with EMCN, although they are LYVE1 negative (arrowheads). C-E and F-H magnified views of A boxes. n = 2-4. Scale bars: 0.5 mm for A-B; 0.2 mm for C-H.

8.3.2. *Lyve1^{Cre} marks the common cardinal vein and intersomitic vessels*

During embryogenesis, coronary vessels develop from two progenitor cell populations that invest in complementary sites of the heart[208,297–299]. The venous endothelium of the SV contributes to blood vessels in the dorsal and lateral outer myocardial wall, while the endocardium contributes to vessels in the inner myocardial wall, interventricular septum, and middle of the ventral side of the heart[208,297–299]. To confirm that *Lyve1^{Cre}* is activated in the venous endothelium during embryogenesis, *Lyve1$^{+/Cre}$;R26R-tdTomato* whole-embryos were stained against PROX1 and EMCN at E10.5 (Figure 8.3). tdTomato was found to be expressed together with EMCN in capillaries of the heart (Figure 8.3 A-E) and intersomitic vessels (ISVs) (Figure 8.3 A and J-M). In the CV and ISVs, precursor LECs were found to be either PROX1^{+};EMCN^{+};tdTomato^{-} or PROX1^{+};EMCN^{+};tdTomato^{+} (Figure 8.3 F-M), supporting the hypothesis that *Lyve1^{Cre}* does not mark all cardiac precursor LECs or *Lyve1* is expressed at later stages of LEC specification (Figure 8.1 B and H). The spatiotemporal location pattern of these CV and ISV precursor LECs was found to support the hypothesis of active precursor migration towards the SV and outflow tract of the developing heart to form the first cardiac lymphatics at E12.5, as previously described (Figure 8.3 I)[38]. Also, *Prox1* expression was identified in the heart, in line with previous data of myocardial *Prox1* expression[300]. Finally, individual PROX1^{-};EMCN^{-};tdTomato^{+} cells were identified throughout the embryonic body, most likely representing yolk-sac derived macrophages (Figure 8.3 A).

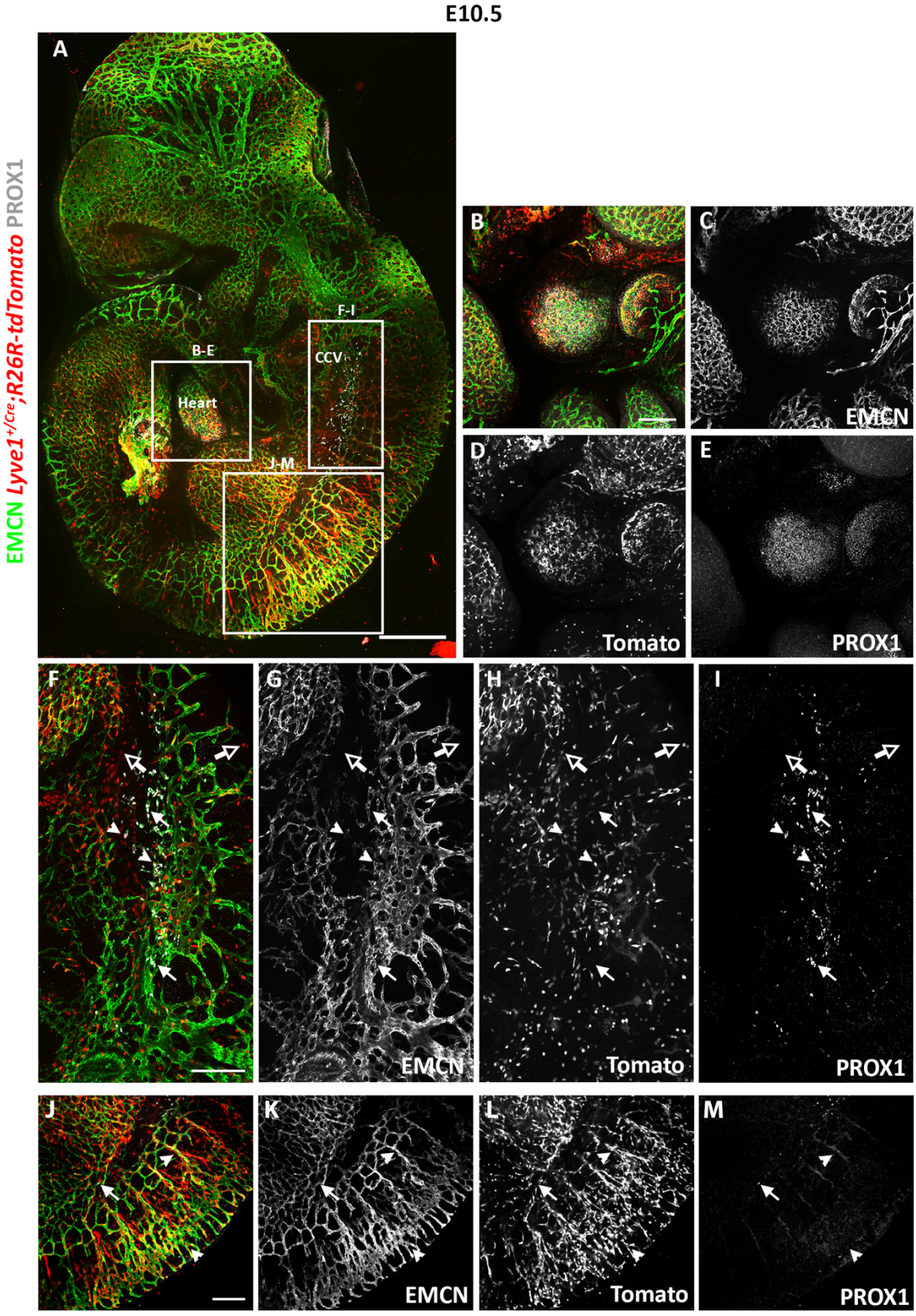

Figure 8.3 Lyve1^{Cre} is activated in intersomitic vessels, heart capillaries and partially by precursor LECs of the common cardinal vein.

(A) Representative E10.5 *Lyve1*$^{+/Cre}$*;R26R-tdTomato* embryo stained with anti-EMCN and anti-PROX1 antibodies. (B-E) High magnification shows EMCN, PROX1 and tdTomato signal in the embryonic heart. (F-I) High magnification of the CV reveals tdTomato signal in EMCN^{+} vessels, while individual PROX1^{+} precursor LECs are either EMCN^{+};tdTomato^{+} (arrowheads) or EMCN^{+};tdTomato^{-} (white arrows). Macrophages are also visible (hollow arrows). (J-M) High magnification of the ISVs displayed colocalisation of EMCN and tdTomato signal in the vessels (arrowheads), as well as PROX1^{+};EMCN^{+};tdTomato^{-} precursor LECs (white arrows). B-E, F-I and J-K magnified views of A boxes. n = 3. Scale bars: 0.5 mm for A; 0.2 mm for B-M.

To investigate the contribution of the *Lyve1*$^{+}$ lineage to the blood and lymphatic vasculature further, *Lyve1*$^{+/Cre}$*;R26R-tdTomato* embryos were harvested at E12.5, sectioned transversally to reveal the jugular veins (JVs) and jugular lymph sacs (JLSs), and stained against EMCN and PROX1 (Figure 8.4). Immunofluorescence staining demonstrated that tdTomato-expressing cells are present in both the JV (PROX1^{-};EMCN^{+}) and JLS (PROX1^{+};EMCN^{-}), thus confirming the contribution of *Lyve1*^{Cre}-labelled cells to the blood endothelium (JV) and systemic lymphatic endothelium (JLS; Figure 8.4 C, E-G, I, K-M and Figure 8.4 D, E-G, J, K-M, respectively).

Taken together, these results suggest that *Lyve1* is expressed during early embryogenesis in the venous endothelium of the heart that will contribute SV-derived coronary blood vasculature, as well as systemically in the CV (a source of cardiac lymphatic ECs) and developing ISVs.

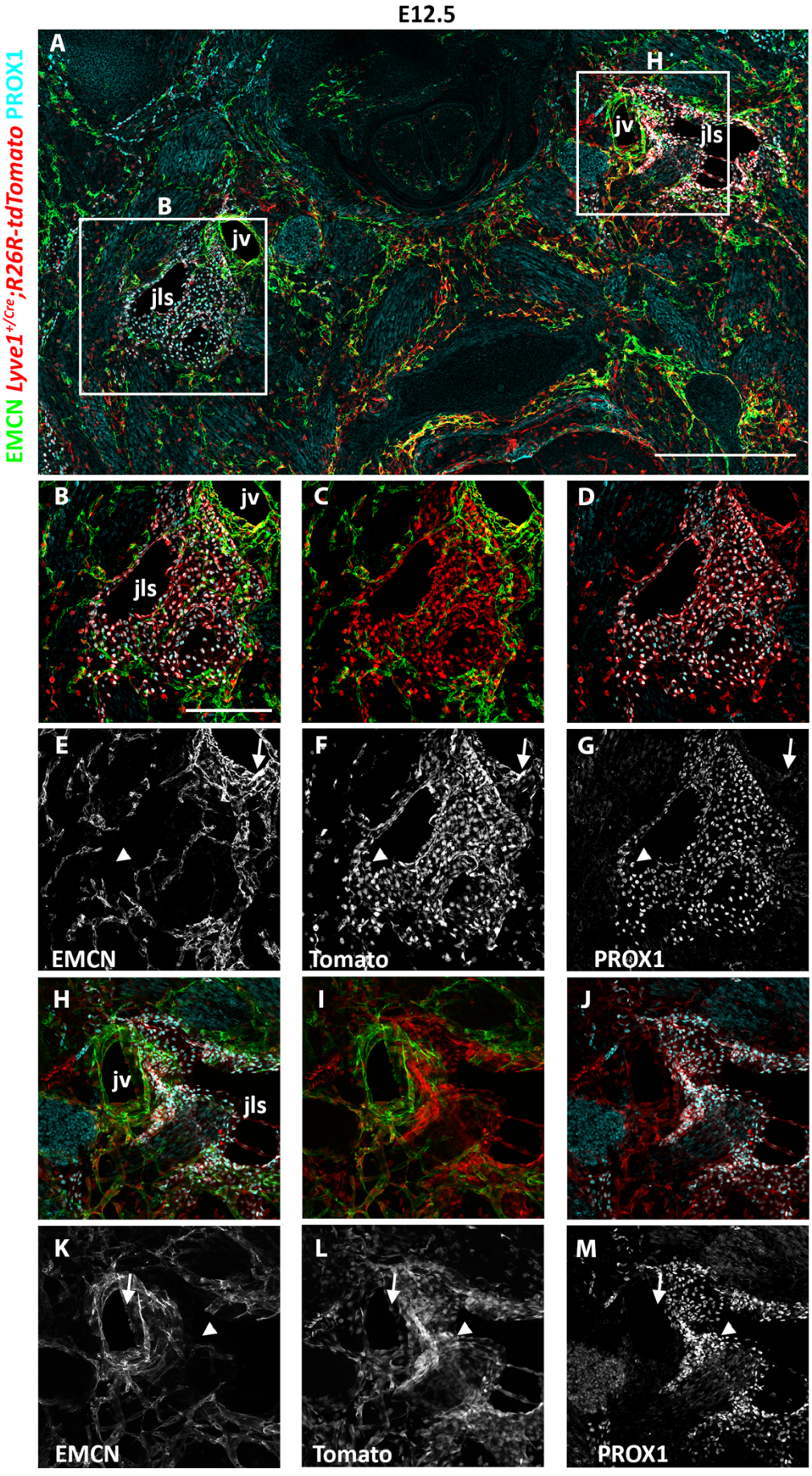
E12.5
EMCN Lyve1+/Cre;R26R-tdTomato PROX1
A
H
jv
jls
B
jv
jls
B
jv
jls
C
D
E
EMCN
F
Tomato
G
PROX1
H
jv
jls
I
J
K
EMCN
L
Tomato
M
PROX1

Figure 8.4 Lyve1^{Cre} is activated in both the jugular vein and jugular lymph sacs at E12.5.

(A) Transverse sections of *Lyve1$^{+/Cre}$;R26R-tdTomato* embryos and immunostaining with antibodies against EMCN and PROX1 at E12.5. (B-M) High magnification of the JLSs and JVs shows high levels of tdTomato expression in both EMCN^{-};PROX1^{+} (JLSs; arrowheads) and EMCN^{+};PROX1^{-} (JVs; white arrows). B-G and H-M magnified views of A boxes. n = 3. Scale bars: 0.5 mm for A; 0.2 mm for B-M.

8.3.3. *Lyve1^{Cre} marks the endocardium during embryogenesis*

Coronary vessels of the interventricular septum and mid-portion of the ventral side of the heart arise from endocardial-derived sprouts[208,297–299]. Consequently, the activity of *Lyve1^{Cre}* in the developing endocardium was investigated. Hearts from *Lyve1$^{+/Cre}$;R26R-tdTomato* embryos were harvested at E14.5 and E16.5, sectioned transversally and stained with antibodies against PECAM1 and PDPN (Figure 8.5). At both E14.5 (Figure 8.5 A-F) and E16.5 (Figure 8.5 G-L) tdTomato was found to be expressed in the epicardial layer, either by macrophages (PECAM1^{-}, Figure 8.5 C) or by endothelial cells (PECAM1^{+}, Figure 8.5 I). Also, tdTomato was detected in the developing cardiac valves (Figure 8.5 D and J), as well as in the interventricular septum (Figure 8.5 E and K). Interestingly, cells that were positive for tdTomato in the cardiac valves appeared to be negative for PECAM1, suggesting that these were not endothelial cells (Figure 8.5 D and J). These tdTomato^{+};PECAM1^{-} could be the previously described endocardium-derived tissue-resident macrophages, with functions essential for cardiac valve remodelling[301]. Finally, tdTomato was abundantly expressed in the endocardial trabeculae together with PECAM1 (Figure 8.5 F and L), supporting the hypothesis that *Lyve1^{Cre}* is also active in the developing endocardium and endocardial-derived coronary vessels.

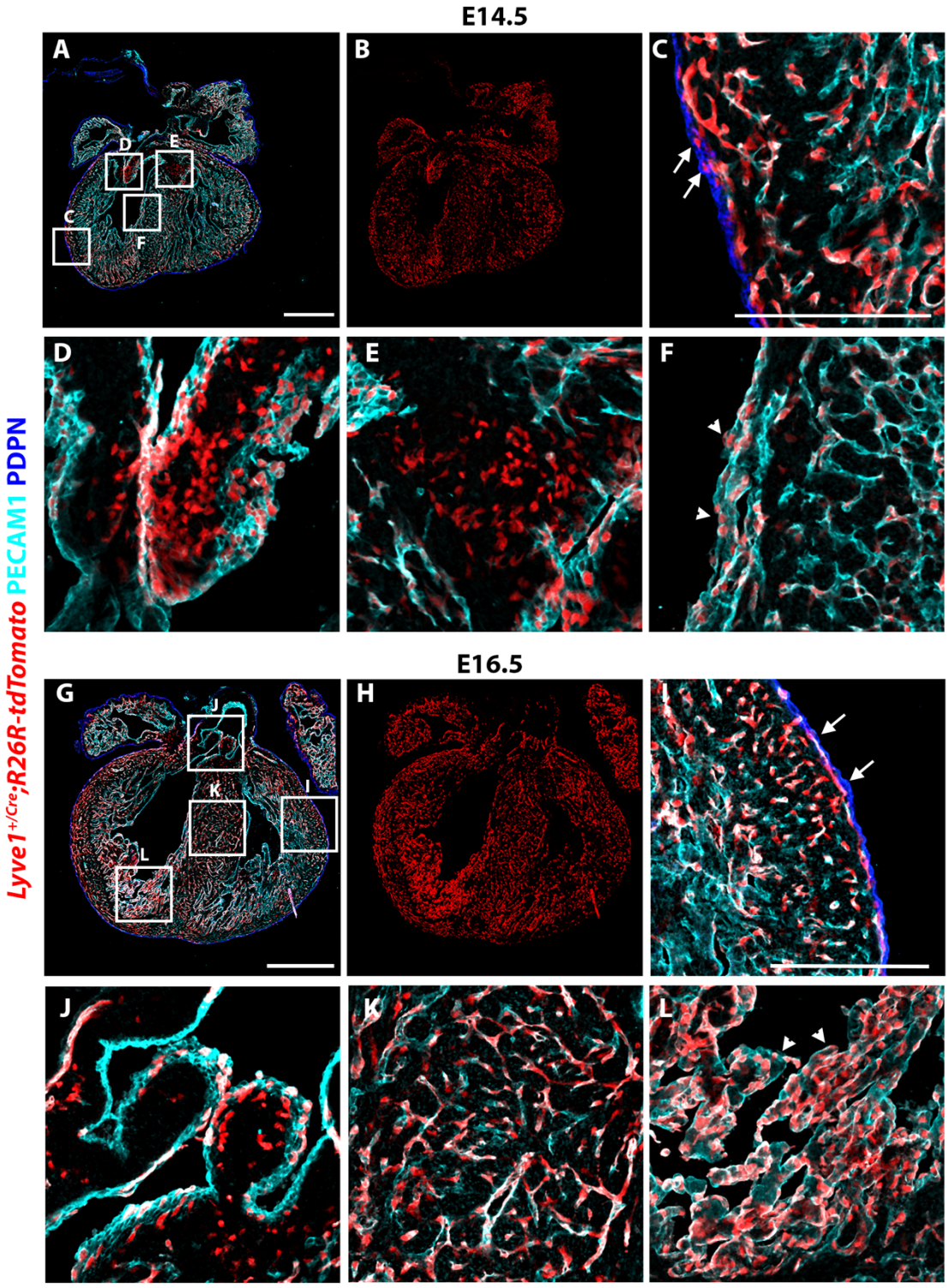

Figure 8.5 Lyve1^{Cre} is activated in the developing endocardium and cardiac valves.

(A-B) Cryosection of *Lyve1$^{+/Cre}$;R26R-tdTomato* heart at E14.5 shows expression of tdTomato throughout the embryonic heart. (C-F) High magnification images from different areas of the E14.5 heart. (C) tdTomato is detected in PECAM1 stained vessels in the myocardium, as well as in PECAM1 negative cells, possibly macrophages (white arrows), in the PDPN-expressing epicardium. (D-E) Macrophages residing in cardiac valves appear to express tdTomato. (F) The endocardial layer clearly co-expressed tdTomato and PECAM1 (arrowheads). (G-H) Cryosection of *Lyve1$^{+/Cre}$;R26R-*

tdTomato heart at E16.5. (I) Vessels expressing tdTomato are detectable in the sub-epicardial layer at this timepoint (white arrows). (J) Macrophages expressing tdTomato near the cardiac valves. (K-L) In both the interventricular septum and the endocardium PECAM1 is found only in cell that co-express tdTomato, representing coronary vessels and trabeculae (arrowheads). C-F magnified views of A boxes; I-L magnified views of G boxes. n = 2. Scale bars: 0.5 mm for A-B, G-H; 0.2 mm for C-F and I-L.

8.3.4. *Activation of Notch1 using Lyve1^{Cre} disrupts embryonic vascular development*

As proof-of-principle that the *Lyve1^{Cre}* driver targets the developing endothelium and endocardium, *Notch1* was ectopically activated (gain-of-function) by crossing *Lyve1$^{+/Cre}$* males with *Gt(ROSA)26Sor$^{tm1(Notch1)Dam}$* (*N1ICD*) female mice. The conditional *N1ICD* transgenic line expresses the Notch1 intracellular domain upon Cre activation. Previous studies have crossed *N1ICD* mice with the *Tie2-Cre* driver line[302,303]. In these studies, significant vascular defects due to *Cre* activity in the Tie2-expressing endothelium have been described, such as disorganized vessels with low density and reduced vascular complexity in the head[302,303]. Also, disruption of cardiac morphogenesis was evident due to *Cre* activity in the endocardium, atrioventricular cushions, and myocardium[302,303]. As *Tie2-Cre;N1ICD* embryos do not survive past E10.5[302,303], this timepoint was selected to investigate embryonic blood vessel and cardiac development in *Lyve1$^{+/Cre}$;N1ICD* mice.

Whole-mount staining against EMCN and confocal imaging revealed that mutant embryos had lower vascular density, with the vessels being thicker and disorganized at E10.5 (Figure 8.6 D-F) compared to control embryos (Figure 8.6 A-C). The phenotype was most evident in the head capillaries and ISVs (compare Figure 8.6 B with 6.6 E and Figure 8.6 C with F, respectively). These results are similar to the ones observed in *Tie2-Cre;N1ICD* embryos at E9.5[302,303]. In contrast to the *Tie2-Cre;N1ICD* embryos, no gross defects where detectable in the heart morphology of *Lyve1$^{+/Cre}$;N1ICD* mutant embryos compared to the control. This

could be due to technical limitations in whole-mount imaging, or due to differences between *Tie2-Cre* and *Lyve1*^{Cre} in terms of spatial and temporal activity in the developing heart. Overall, the vascular phenotype observed in the *Lyve1*^{Cre}*;N1ICD* gain-of-function experiment supports *Lyve1* expression in the blood endothelium during early embryogenesis.

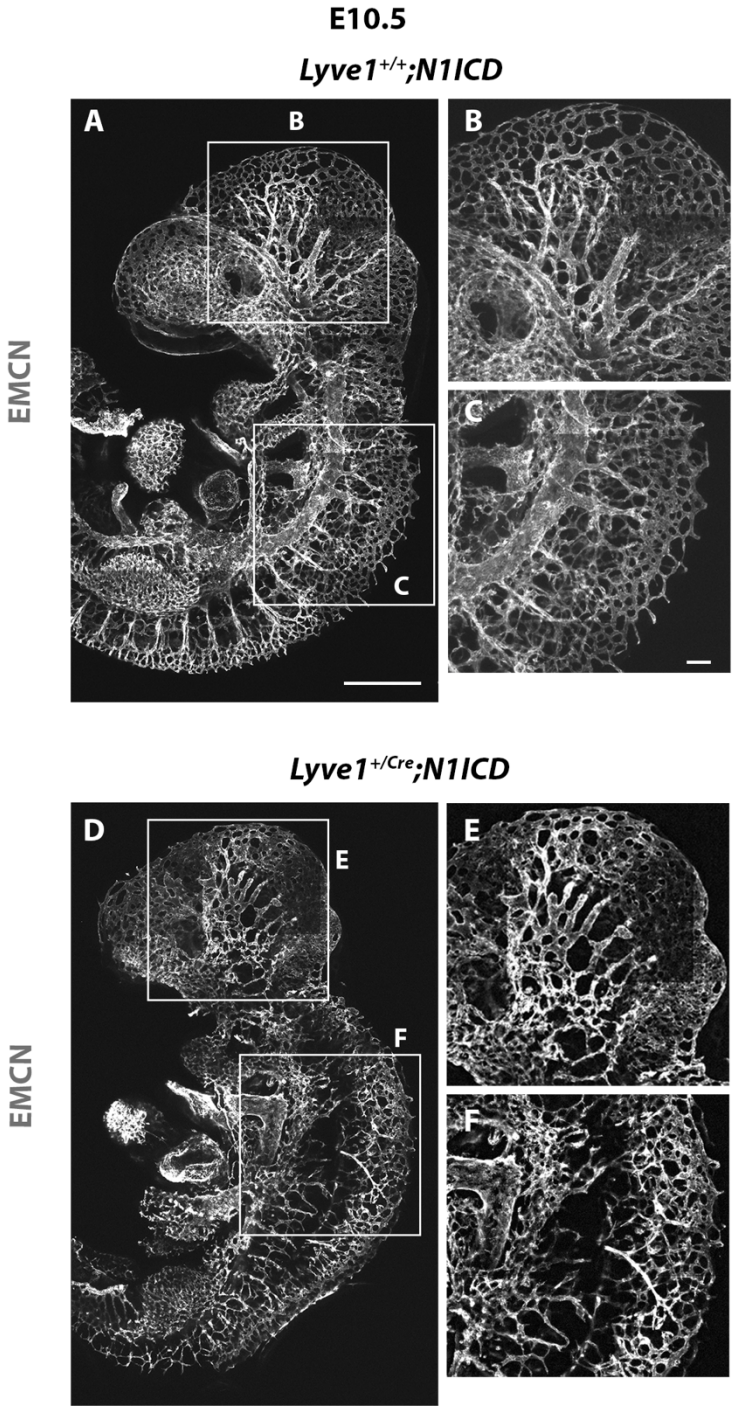

Figure 8.6 Notch1 gain-of-function in Lyve1 expressing cells leads to vascular defects in the developing embryo.

(A-F) Confocal imaging of control *Lyve1$^{+/+}$;N1ICD* and mutant *Lyve1$^{+/Cre}$;N1ICD* embryos stained against EMCN at E10.5. (A) The blood vasculature appeared morphologically normal with branches and sprouts coming from larger vessels to thinner capillaries in the control embryos. (B-C) Details of the well developing blood vasculature can be observed with high magnification in the ISVs and head of control embryos. (D) Major defects were detected in the development of the blood vasculature in mutant embryos, particularly in the head and ISVs. (E) In the head, the blood vessels had lower density, were thicker and showed reduced level of remodelling of the vascular plexus, compared to the control. (F) The ISVs were disorganized and often failed to connect to the CV. B-C

magnified views of A boxes; E-F magnified views of D boxes. n = 3-5. Scale bars: 0.5 mm for A and D; 0.2 mm for B-C and E-F.

8.3.5. *Lyve1^{Cre} marks tissue resident cardiac macrophages during embryogenesis*

Macrophages first appear in the heart at approximately E10.5, migrating from the yolk sac and residing in the epicardium/subepicardium compartment[145]. *Lyve1* is a known tissue-resident macrophage marker. However, the percentage of LYVE1^{+} cardiac macrophages, as well as the activity of the *Lyve1^{Cre}* in cardiac macrophages has not been studied before. Here, *Lyve1$^{+/Cre}$;R26R-tdTomato* embryos were harvested at E14.5 and their hearts stained for CD68 (pan-macrophage marker), CD206 (tissue resident marker) and LYVE1, and imaged using confocal microscopy (Figure 8.7 A-L). Interestingly, tdTomato and CD206 signals were detected in virtually all CD68^{+} cardiac macrophages, while both LYVE1^{+} and LYVE1^{-} macrophages were identified only on the ventral and dorsal side of the heart (Figure 8.7 B-F and H-L). Quantification of the cardiac macrophage population confirmed that approximately half of all macrophages were CD68^{+};CD206^{+};tdTomato^{+};LYVE1^{+} (54 %) and half were CD68^{+};CD206^{+};tdTomato^{+};LYVE1^{-} (44 %). The finding that 98 % of all cardiac macrophages expressed tdTomato, while only 44 % expressed LYVE1, suggests that *Lyve1* is active during the early stages of haematopoiesis and subsequently downregulated in macrophage subsets. Also, a very small percentage of CD68^{+};CD206^{-};tdTomato^{-};LYVE1^{-} macrophages (2 %) was found in the heart, potentially resembling foetal liver monocyte-derived macrophages.

In conclusion, *Lyve1^{Cre}* drives Cre activity in the cardiac lymphatic vasculature during embryogenesis. In addition, this *Cre* driver marked the SV and endocardium, which give rise to the coronary blood vasculature, as well as tissue resident macrophages.

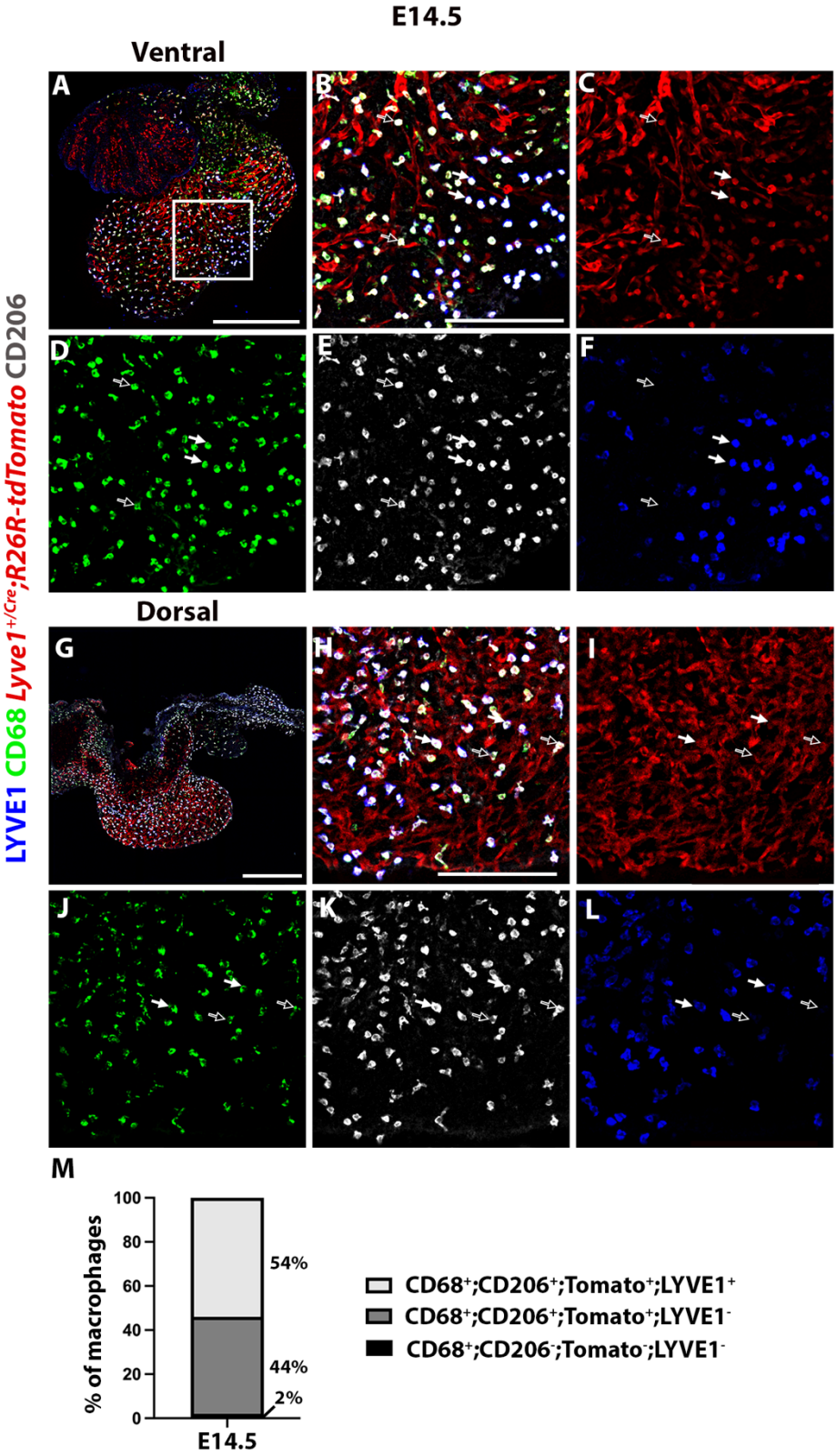

Figure 8.7 Lyve1^{Cre} is activated in cardiac resident macrophages at E14.5.

(A) Macrophages visualised on the ventral aspect of the heart of *Lyve1$^{+/Cre}$;R26R-tdTomato* embryos. (B) tdTomato was found to be expressed not only in coronary blood and lymphatic

vessels, but also in tissue resident macrophages. (C-F) $CD68^+$ cardiac resident macrophages appear to co-express CD206 and tdTomato, while they were found to be either LYVE1 positive (white arrows) or LYVE1 negative (hollow arrows) at E14.5. (G) Macrophages on the dorsal side of the heart. (H-L) Similar to the ventral side of the heart, macrophages were $CD68^+$;$CD206^+$;$tdTomato^+$ and either $LYVE1^+$ (white arrows) or $LYVE1^-$ (hollow arrows). (M) Quantification of the cardiac macrophage population found that 54 % were positive for LYVE1 and 44 % were negative for LYVE1. A small population of $CD68^+$;$CD206^-$;$tdTomato^-$ macrophages was found to contribute 2 % to the heart at E14.5. B-F magnified view of A box; H-L magnified view of G box. n = 1. Scale bars: 0.5 mm for A and G; 0.2 mm for B-F.

8.3.6. ***Conditional deletion of Prox1 in Lyve1$^+$ cells leads to impaired development and blood-filled cardiac lymphatics***

After detailed characterisation of the *Lyve1^{Cre}* line, the *Prox1^{Flox}* mouse line was used to conditionally delete *Prox1*, aiming to produce animals with defective cardiac lymphatics and assess their potential use in studies of neonatal cardiac regeneration. In a previous study, *Lyve1$^{+/Cre}$;Prox1$^{+/Flox}$* embryos were described to have oedema, with most of the pups dying shortly after birth with peritoneal chylous ascites, and around 80 % dying suddenly during the first 3 months of life[304]. In our study *Lyve1$^{+/Cre}$;Prox1$^{+/Flox}$* did not have obvious developmental defects, were viable and fertile as adults. The differences observed in the development of the *Lyve1$^{+/Cre}$;Prox1$^{+/Flox}$* mice used in this project and the ones used in the aforementioned study could be the result of the different *Prox1^{Flox}* lines used on distinct genetic backgrounds[215,304,305]. For this project, activation of Cre deletes the complete coding sequence of *Prox1* and replaces it with a GFP gene[215]. However, in the previous study Cre activation deleted only the Homeodomain, leaving the Nuclear Localisation Signal, Nuclear Receptor Boxes and Prospero Domain 1 intact[305,306]. Another explanation for the reduced postnatal viability of *Lyve1$^{+/Cre}$;Prox1$^{+/Flox}$* mice, provided by the authors of the said study, is that the *Lyve1^{Cre}* strain was not in the pure NMRI background necessary for the survival of their *Prox1^{Flox}* mice[304]. As *Lyve1$^{+/Cre}$;Prox1$^{+/Flox}$* adult mice were viable, here males were crossed with *Prox1$^{Flox/Flox}$* females to conditionally

delete both *Prox1* alleles in *Lyve1* expressing cells. Embryos generated from this cross were harvested at E16.5 (Figure 8.8 A-S) and E18.5 (Figure 8.11 A-M) and examined for their genotype and phenotype.

Genotypes were recorded to determine whether mutants survive at normal Mendelian ratios (Table 6.1). The expected percentage for each genotype was 25 % *Lyve1*$^{+/+}$*;Prox1*$^{Flox/Flox}$, 25 % *Lyve1*$^{+/+}$*;Prox1*$^{+/Flox}$, , 25 % *Lyve1*$^{+/Cre}$*;Prox1*$^{+/Flox}$ (combined control 75 %) and 25 % *Lyve1*$^{+/Cre}$*;Prox1*$^{Flox/Flox}$ (mutant 25 %). At E16.5, embryos from four independent litters were genotyped. The incidence of control samples was 62 % (22 out of 35 embryos), while the proportion of mutants was 38 % (13 out of 35 embryos) (Table 6.1), suggesting that the *Lyve1*$^{+/Cre}$*;Prox1*$^{Flox/Flox}$ genotype is not lethal at E16.5. At E18.5, embryos harvested from three independent litters were genotyped with 74 % (17 out of 23) of the samples being controls and 26 % (6 out of 23) *Lyve1*$^{+/Cre}$*;Prox1*$^{Flox/Flox}$ mutants (Table 6.1), in agreement with the laws of Mendelian inheritance. Although these results suggest that *Lyve1*$^{+/Cre}$*;Prox1*$^{Flox/Flox}$ embryos are viable, no mutant mice were recovered at birth from 4 independent litters (0 %; 0 out of 20) (Table 6.1).

Table 8 Genotypes of animals derived from the cross of males Lyve1$^{+/Cre}$;Prox1$^{+/Flox}$ with females Lyve1$^{+/+}$;Prox1$^{Flox/Flox}$.

Male *Lyve1*$^{+/Cre}$;*Prox1*$^{+/Flox}$ x Female *Lyve1*$^{+/+}$;*Prox1*$^{Flox/Flox}$

16.5	Control	Mutant
Litter 1	9	6
Litter 2	5	3
Litter 3	2	2
Litter 4	6	2
Observed	22	13
Expected	26.25	8.75

18.5	Control	Mutant
Litter 1	5	4
Litter 2	6	1
Litter 3	6	1
Observed	17	6
Expected	17.25	5.75

Born	Control	Mutant
Litter 1	5	0
Litter 2	5	0
Litter 3	4	0
Litter 4	6	0
Observed	20	0
Expected	15	5

Next, the phenotype of *Lyve1*$^{+/Cre}$;*Prox1*$^{Flox/Flox}$ embryos was assessed using bright-field microscopy. At E16.5, subcutaneous oedema and blood-filled lymphatic vessels were found in the head, tail and heart of *Lyve1*$^{+/Cre}$;*Prox1*$^{Flox/Flox}$ embryos, but not of *Lyve1*$^{+/Cre}$;*Prox1*$^{+/Flox}$ (compare Figure 8.8 A-L to M-R). This suggests that lymphatic vessels are present in the heart of *Lyve1*$^{+/Cre}$;*Prox1*$^{Flox/Flox}$ embryos, however, they are not functioning properly and are not separated from the blood vasculature. Also, in general the hearts were paler in *Lyve1*$^{+/Cre}$;*Prox1*$^{Flox/Flox}$ embryos compared to the *Lyve1*$^{+/Cre}$;*Prox1*$^{+/Flox}$ controls (compare Figure 8.8 C-F and I-L to O-R). No gross difference in body or heart size was detected

between *Lyve1*$^{+/Cre}$;*Prox1*$^{Flox/Flox}$ and *Lyve1*$^{+/Cre}$;*Prox1*$^{+/Flox}$ embryos (compare Figure 8.8 A-l to M-R).

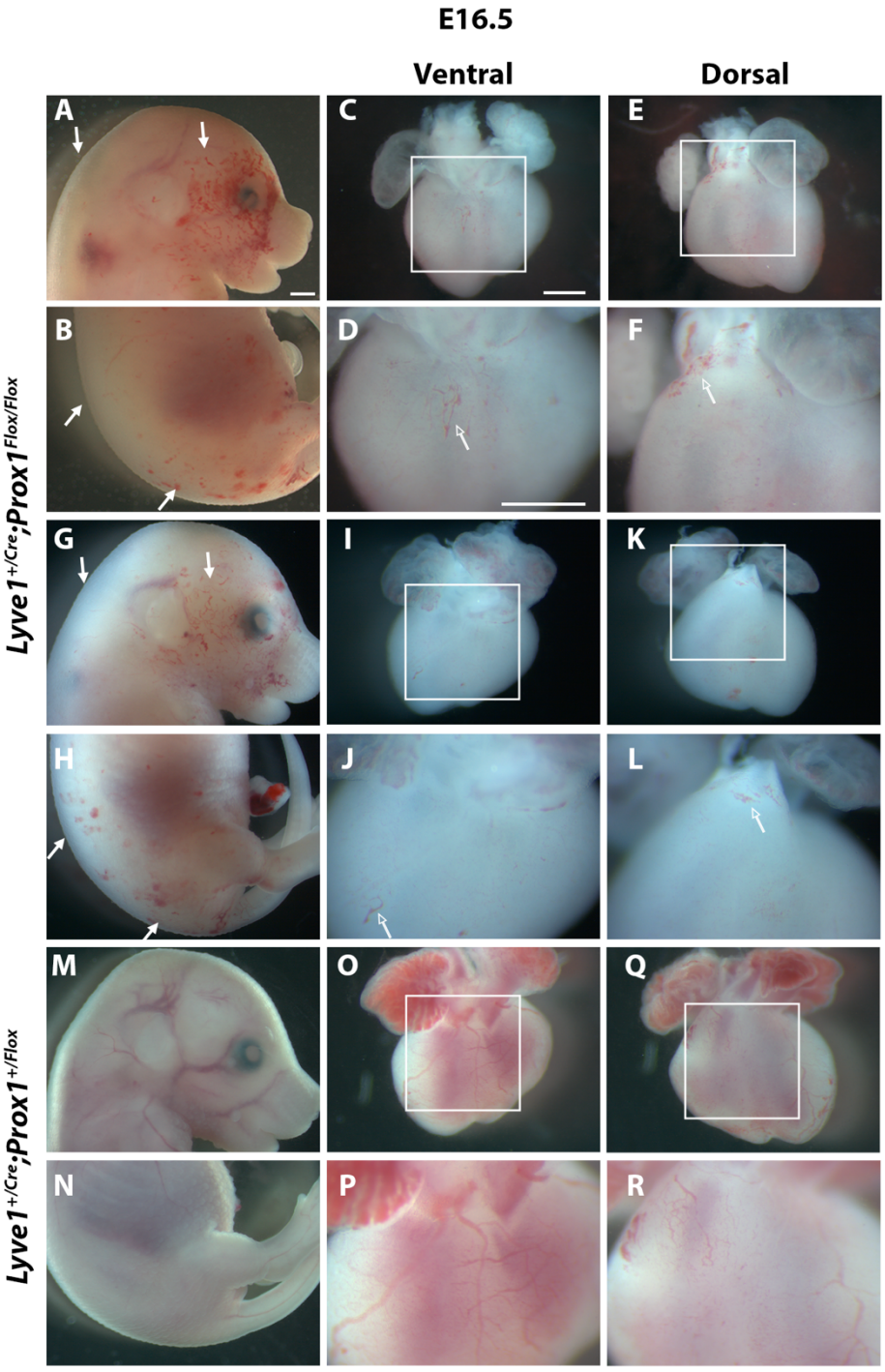

Figure 8.8 Lyve1$^{+/Cre}$;Prox1$^{Flox/Flox}$ embryos display gross developmental defects at E16.5.

(A-L) Two representative mutant embryos and corresponding hearts. (A-B and G-H) Both embryos have severe oedema and blood-filled lymphatic vessels in the head, back and tail (white arrows). (C-F and I-L) High magnification clearly shows that the heart of mutant embryos has blood-filled lymphatics near the base on the ventral and dorsal side (hollow arrows). (M-R) Control embryos do

not have oedema, nor blood-filled lymphatics in the body or the heart. D and F magnified views of C and E boxes; J and L magnified views of I and K boxes; P and R magnified views of O and Q boxes. n = 13-22. Scale bars: 0.5 mm.

To further characterise the vascular phenotype of *Lyve1*$^{+/Cre}$*;Prox1*$^{Flox/Flox}$ mutant hearts, in particular coronary and cardiac lymphatic development, immunostaining against EMCN and LYVE1 and light-sheet microscopy was used (Figure 8.9 A-L). At E16.5, cardiac lymphatics appeared normal and extended from base-to-apex on both the dorsal and ventral side of the heart in *Lyve1*$^{+/Cre}$*;Prox1*$^{+/Flox}$ control embryos (Figure 8.9 B and E). Strikingly, no lymphatics were present on the ventral aspect of *Lyve1*$^{+/Cre}$*;Prox1*$^{Flox/Flox}$ mutant hearts (Figure 8.9 K), and few LYVE1^{+} vessels were observed on the dorsal side proximal to the SV (Figure 8.9 H). No gross differences were observed in the EMCN staining pattern of *Lyve1*$^{+/Cre}$*;Prox1*$^{+/Flox}$ and *Lyve1*$^{+/Cre}$*;Prox1*$^{Flox/Flox}$ hearts (compare Figure 8.9 C-F to I-L), indicating that only cardiac lymphatics and not coronary veins are affected by the conditional deletion of *Prox1*.

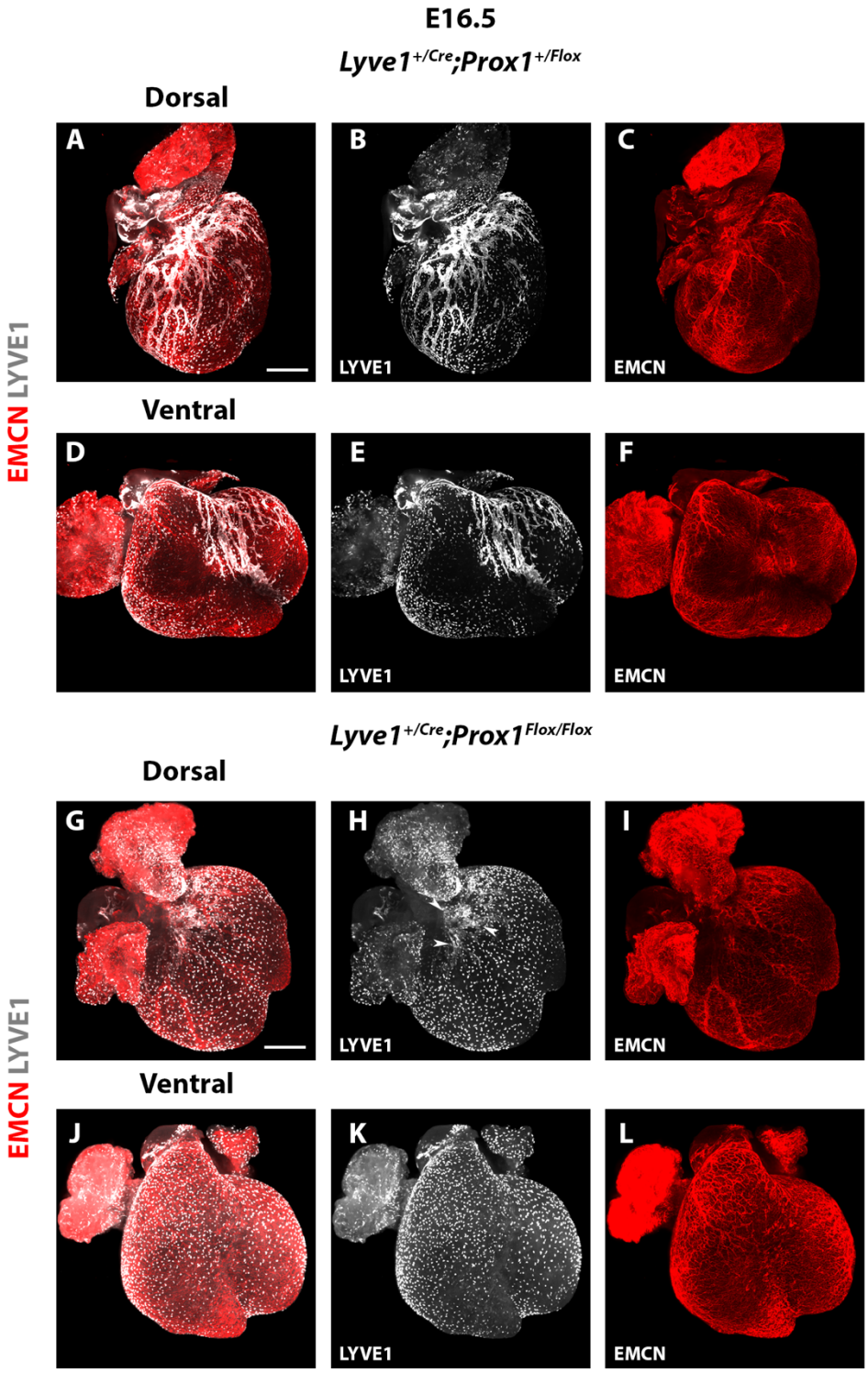

Figure 8.9 Lyve1$^{+/Cre}$;Prox1$^{Flox/Flox}$ embryos have underdeveloped cardiac lymphatics at E16.5.

(A-C) Dorsal side of a control *Lyve1*$^{+/Cre}$*;Prox1*$^{+/Flox}$ heart stained against EMCN (venous and capillary endothelium) and LYVE1 (lymphatic endothelium and macrophages). (B) Lymphatic vessels extend from the SV towards the apex, while covering a large area of the ventricular surface. Also, individual LYVE1-expressing macrophages are visible. (C) Blood vessels are covering the entire heart. (D-F) Ventral side of the control heart, shows extended and well developed lymphatic and blood vessels. (G-I) In the dorsal side of a representative *Lyve1*$^{+/Cre}$*;Prox1*$^{Flox/Flox}$ mutant heart, lymphatic vessels

are underdeveloped and retained in the SV (arrowheads in panel H), while the blood vasculature appears grossly normal. (J-L) In the ventral side of the heart, no lymphatics have formed, with LYVE1 signal being restricted to macrophages. (L) The blood vasculature has no obvious defects. n = 2-3. Scale bar: 0.5 mm.

To confirm that blood had leaked into cardiac lymphatics of *Lyve1*$^{+/Cre}$*;Prox1*$^{Flox/Flox}$ embryos at E16.5, light-sheet microscopy was used to image hearts stained for VEGFR3 and TER119, a marker of erythroid cells (Figure 8.10 A-L). Hearts from *Lyve1*$^{+/Cre}$*;Prox1*$^{+/Flox}$ embryos had a well-developed lymphatic vasculature expressing VEGFR3 at E16.5 (Figure 8.10 C-F). TER119 signal was located throughout the dorsal and ventral sides of *Lyve1*$^{+/Cre}$*;Prox1*$^{+/Flox}$ hearts (Figure 8.10 B and E) proximal to lymphatics, but never colocalising with them (Figure 8.10 A and D). The close distance between VEGFR3 and TER119 in the control hearts was expected, as cardiac lymphatics develop parallel to major coronary veins. In contrast, cardiac lymphatics were underdeveloped and found only at the base of *Lyve1*$^{+/Cre}$*;Prox1*$^{Flox/Flox}$ hearts (Figure 8.10 I and L), with the TER119 signal enriched in areas co-stained with VEGFR3 (Figure 8.10 G and J), thus confirming that mutant cardiac lymphatics were blood-filled at E16.5.

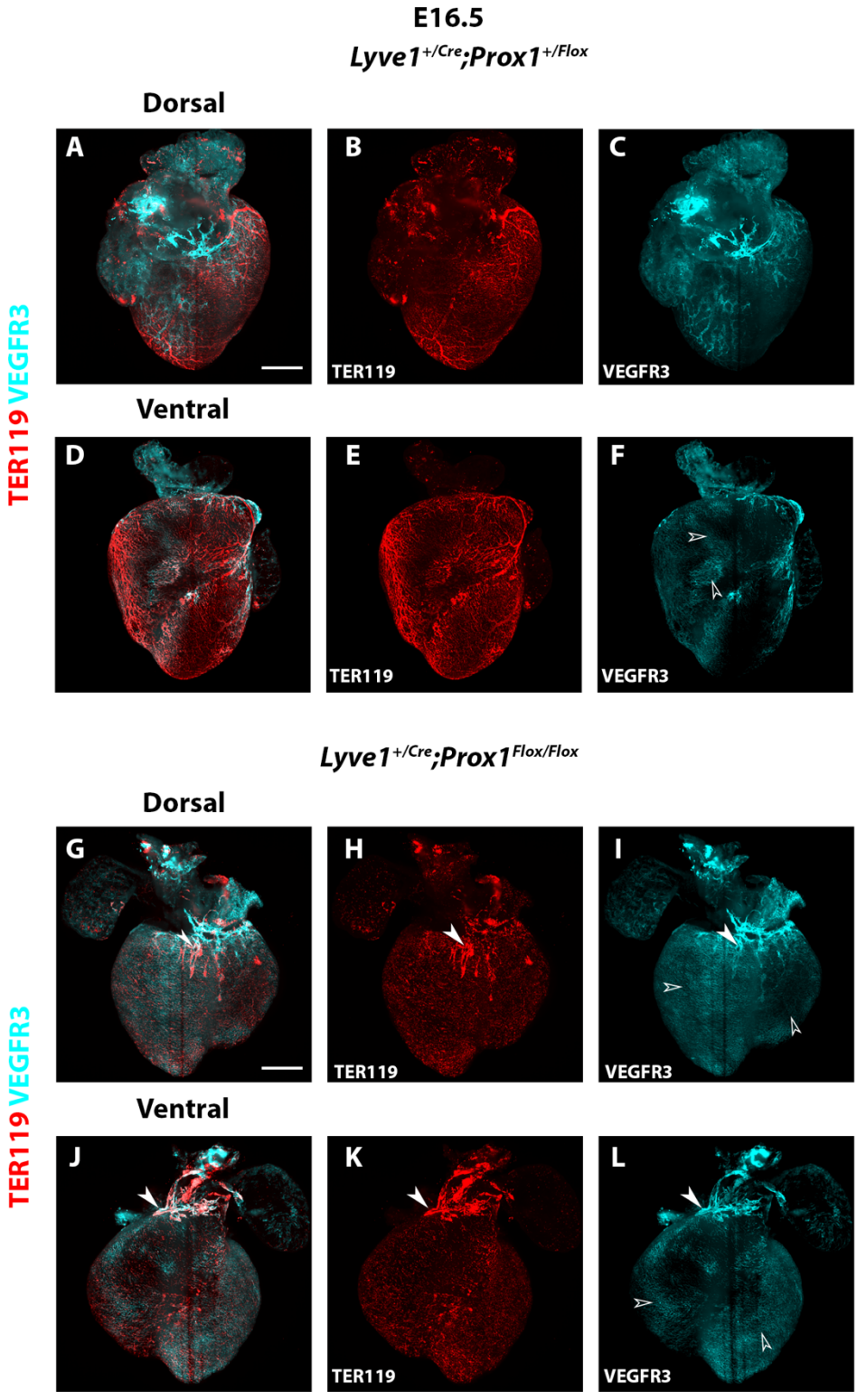

Figure 8.10 Cardiac lymphatics of Lyve1$^{+/Cre}$;Prox1$^{Flox/Flox}$ embryos contain blood at E16.5.

(A-C) Dorsal aspect of a control *Lyve1*$^{+/Cre}$*;Prox1*$^{+/Flox}$ heart stained with TER119 (erythrocytes) and VEGFR3 (lymphatics). (A-B) TER119 staining pattern represents erythrocyte-enriched blood vessels distributed throughout the heart alongside lymphatics. (C) Lymphatics sprout from the SV and cover a large area of the ventricular surface. (D-F) Ventral aspect of a control heart showing normal distribution of erythrocytes in blood vessels that do not mix with lymphatics. Note that at this timepoint VEGFR3 is still visible in blood capillaries (hollow arrowheads in panels F,I and L). (G-I) On

the dorsal side of a representative mutant *Lyve1*$^{+/Cre}$*;Prox1*$^{Flox/Flox}$ heart, TER119 is clearly seen inside the few lymphatics located near the SV (white arrowheads). (J-L) Similarly, TER119 signal colocalised with VEGFR3 signal found in underdeveloped lymphatics in the outflow track (white arrowheads). n = 2. Scale bar: 0.5 mm.

Surprisingly, the phenotype of *Lyve1*$^{+/Cre}$*;Prox1*$^{Flox/Flox}$ appeared to be less severe at E18.5 compared to E16.5 (Figure 8.11). No visible oedema or blood-filled lymphatics were apparent in *Lyve1*$^{+/Cre}$*;Prox1*$^{Flox/Flox}$ embryos at E18.5 (Figure 8.11 A-F). Also, the size and morphology of mutant embryos and their heart were not distinguishable from *Lyve1*$^{+/Cre}$*;Prox1*$^{+/Flox}$ controls (compare Figure 8.11 A-F to G-L).

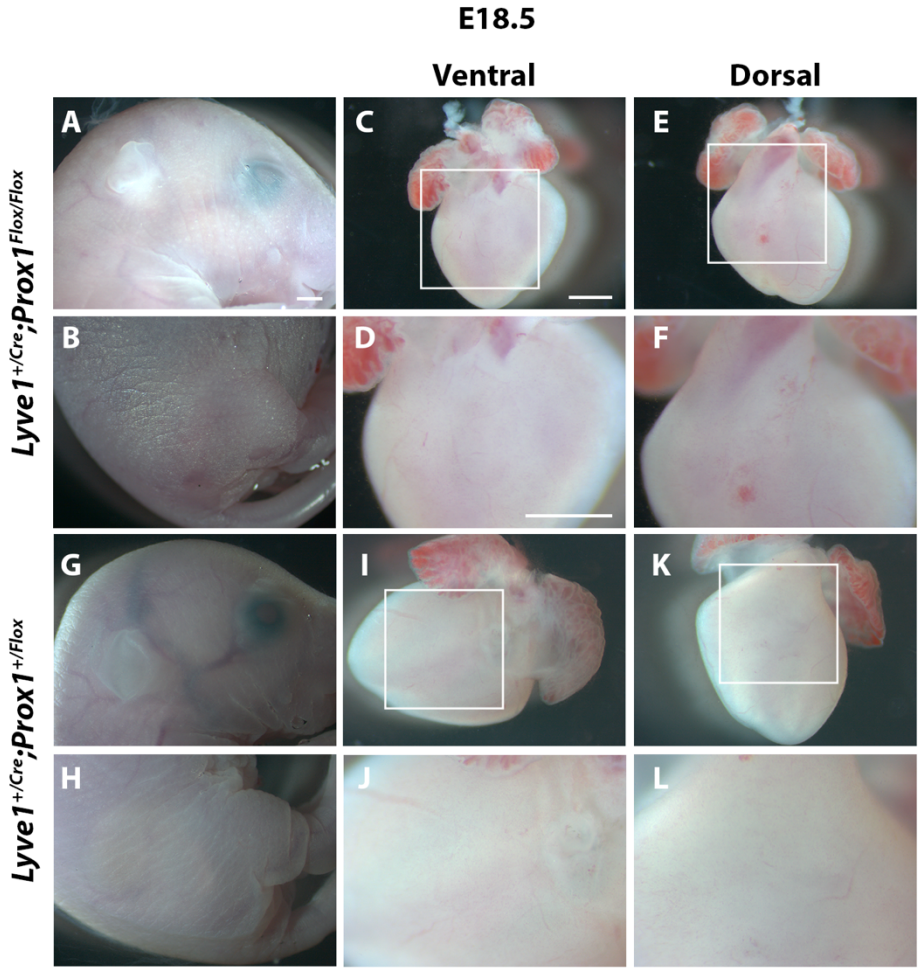

Figure 8.11 Lyve1$^{+/Cre}$;Prox1$^{Flox/Flox}$ embryos display normal development at E18.5.

(A-F) Representative mutant embryo and its heart. (A-B) At this timepoint, mutant embryos do not exhibit oedema or blood-filled lymphatics. (C-F) No obvious cardiac vessel defects are observed in mutant embryos at E18.5. (G-L) Control embryos do not exhibit oedema, nor blood-filled lymphatics in the body or heart. D and F magnified views of C and E boxes; J and L magnified views of I and K boxes. n = 6-17. Scale bars: 0.5 mm.

To understand if cardiac lymphatics were able to develop and grow further in *Lyve1$^{+/Cre}$;Prox1$^{Flox/Flox}$* embryos, light-sheet imaging was used in E18.5 hearts stained against EMCN and LYVE1 (Figure 8.12). Akin to hearts at E16.5, no cardiac lymphatics were visible in either side of the heart of *Lyve1$^{+/Cre}$;Prox1$^{Flox/Flox}$* embryos at E18.5, with LYVE1 signal originating only from cardiac macrophages (Figure 8.12 H and K). In contrast, normal expansion of cardiac lymphatics was apparent in *Lyve1$^{+/Cre}$;Prox1$^{+/Flox}$* embryos (Figure 8.12

B and E). As for the EMCN-labelled coronary veins, no apparent morphological changes were observed in *Lyve1*$^{+/Cre}$*;Prox1*$^{Flox/Flox}$ mutant hearts, compared to controls (compare Figure 8.12 C and F to I and L). These results show that the phenotype found in *Lyve1*$^{+/Cre}$*;Prox1*$^{Flox/Flox}$ embryos at E16.5 is not rescued at later stages of foetal development. Instead, it becomes lethal perinatally. Consequently, this mutant line could not be used to study the effects of defective cardiac lymphatics in neonatal heart regeneration.

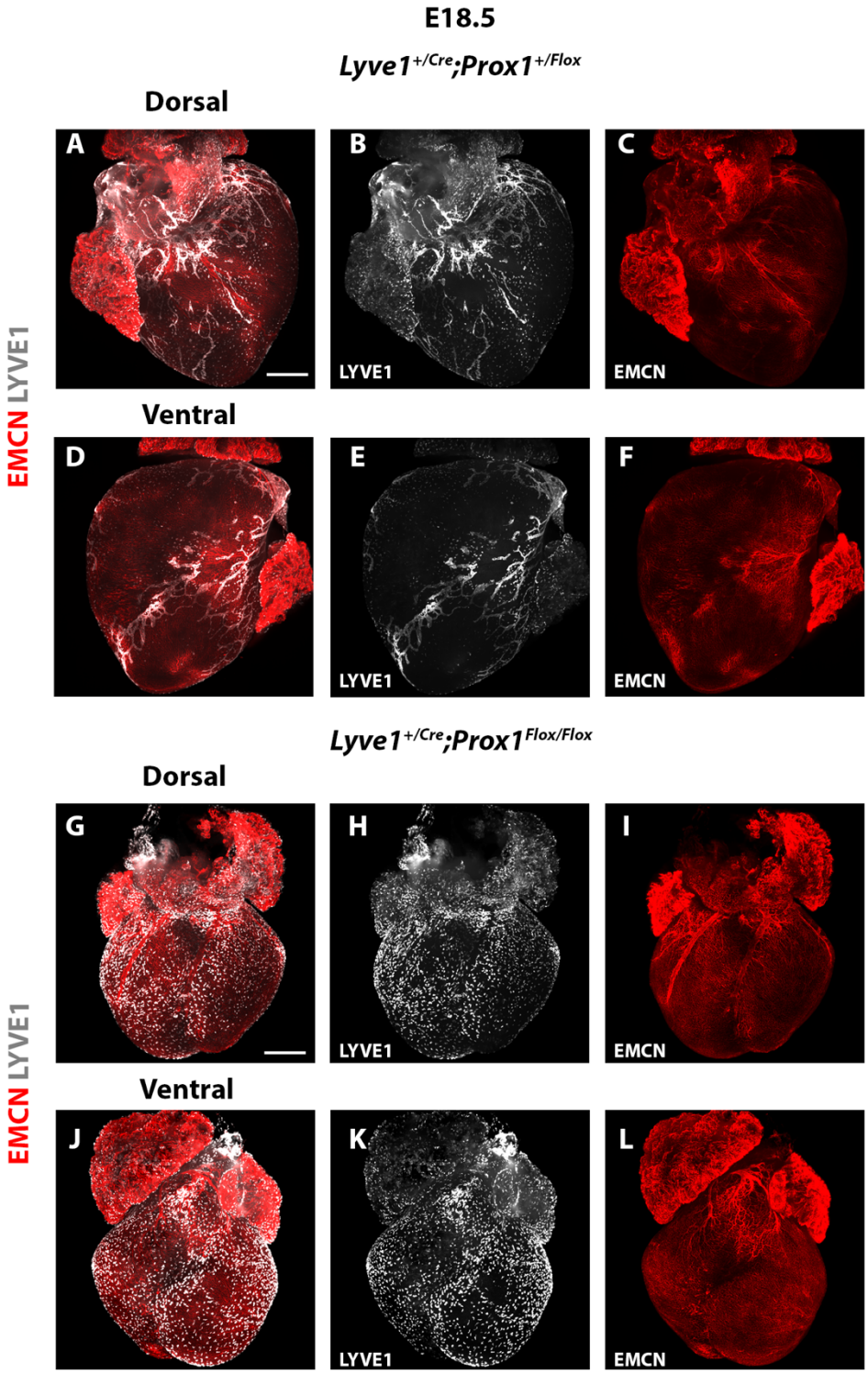

Figure 8.12 Cardiac lymphatics of Lyve1$^{+/Cre}$;Prox1$^{Flox/Flox}$ embryos remain underdeveloped at E18.5.

(A-C) Dorsal side of a control *Lyve1*$^{+/Cre}$*;Prox1*$^{+/Flox}$ heart. (B) Lymphatics have developed through lymphangiogenesis and are covering most of the areas of the heart from SV to the apex. (C) Blood vessels are covering the entire heart, with extended number of capillaries being present. (D-F) Ventral side of the control heart, shows normal lymphatic and blood vessels. (G-I) On the dorsal side of a representative mutant *Lyve1*$^{+/Cre}$*;Prox1*$^{Flox/Flox}$ heart no LYVE1^{+} lymphatics are visible, while the blood vasculature remains normal. (J-L) Similarly, no lymphatics have formed on the ventral

side of the heart, with the anti-LYVE1 antibody staining macrophages only. (L) The blood vasculature has no obvious developmental defects. n = 2. Scale bar: 0.5 mm.

To investigate potential morphological and structural defects that occur in the developing heart of *Lyve1*$^{+/Cre}$*;Prox1*$^{Flox/Flox}$ mice at E15.5, high resolution episcope microscopy (HREM) was used (Figure 8.13). Morphologically, all mutant hearts and their myocardial wall appeared smaller in size compared to control (compare Figure 8.13 A to E). Three out of four mutant hearts had open tricuspid and mitral valve leaflets (compare Figure 8.13 B to F, C-D to G and H to I), suggesting cardiac valve malformation, while one mutant heart had a perimembranous ventricular septal defect (compare Figure 8.13 A to E). The different defects observed between mutants suggest that the phenotype is not fully penetrant in *Lyve1*$^{+/Cre}$*;Prox1*$^{Flox/Flox}$ mice. Quantification of the 3D HREM data confirmed that the ventricles, atria, and tricuspid valve were significantly smaller in size compared to controls (mean ± SEM: $2.2x10^7 \pm 9x10^6$ vs $1.7x10^7 \pm 3x10^6$; $p = 0.028$, $13x10^6 \pm 2x10^5$ vs $9x10^6 \pm 7x10^5$; $p = 0.004$ and $29x10^4 \pm 2x10^4$ vs $21x10^4 \pm 1x10^4$; $p = 0.018$, respectively; Figure 8.13 J-L). No statistically significant differences were detected in mitral, pulmonary or aorta valves between mutant and control embryos (Figure 8.13 M-O). These results reflect the *Lyve1*^{Cre} expression in the endocardium, as detailed in this chapter, as well as the requirement for *Prox1* in valvulogenesis[300,307–309]. The HREM imaging was performed by Dr Jackinta Kalisch-Smith and the 3D rendering by Karolina Zvonickova.

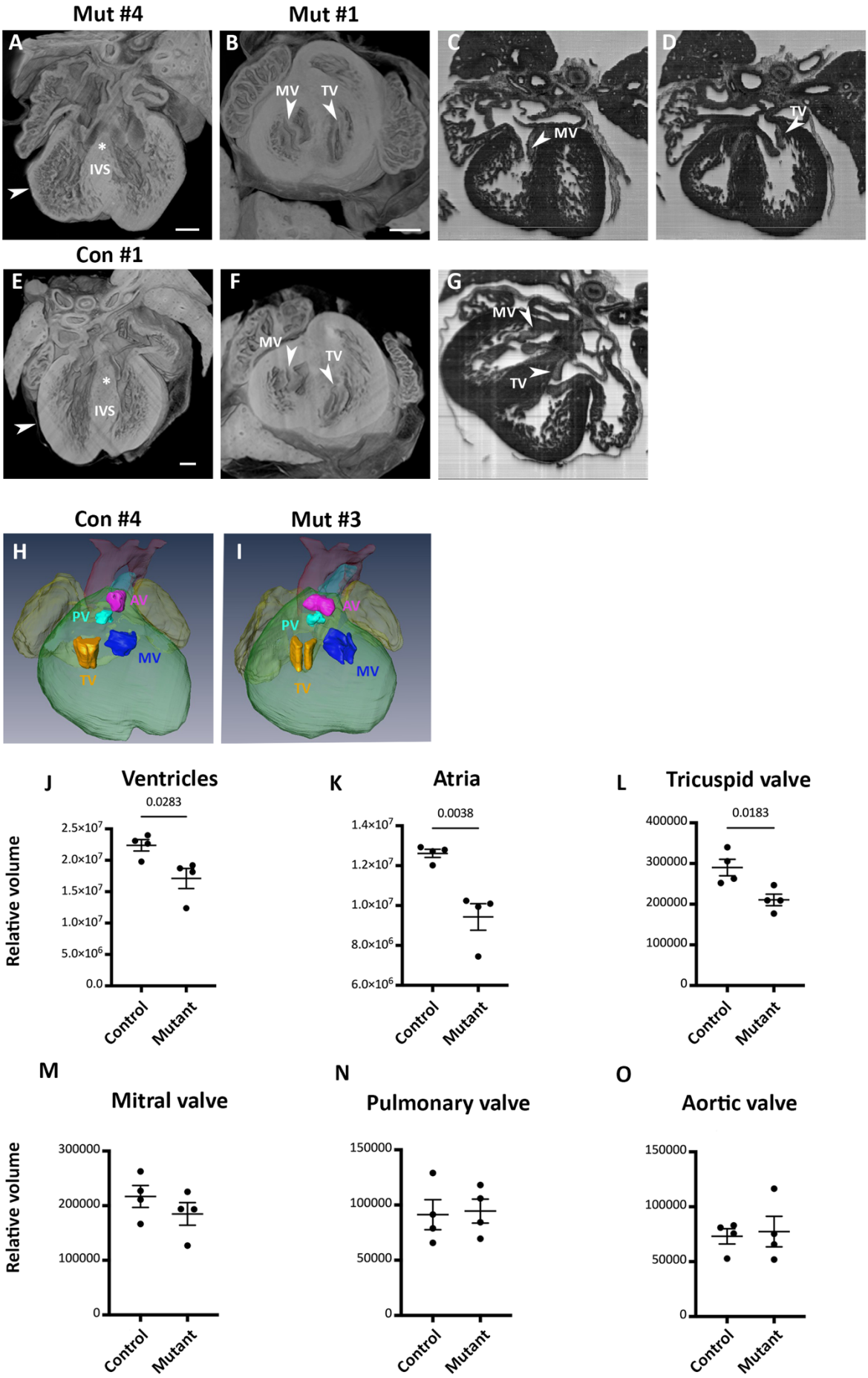
Mut #4
Mut #1
A
B
C
D
IVS
MV
TV
Con #1
E
F
G
Con #4
Mut #3
H
I
AV
PV
J
Ventricles
K
Atria
L
Tricuspid valve
0.0283
0.0038
0.0183
Relative volume
Control
Mutant
M
Mitral valve
N
Pulmonary valve
O
Aortic valve

Figure 8.13 3D HREM data from Lyve1$^{+/Cre}$;Prox1$^{Flox/Flox}$ hearts show cardiac developmental defects.

(A-D) Two mutant hearts showing developmental defects. (A) The interventricular septum (IVS) is membranous (asterisk), and the myocardial wall is thin (white arrowhead). (B-D) The mitral (MV) and tricuspid (TV) valve leaflets are open only in mutant hearts. (E-F) A representative control heart, displaying normal IVS, thick myocardial wall, and well closed MV and TV leaflets. (H-I) 3D rendering of a control and mutant heart. The leaflets of the TV are closed in the control compared to the mutant. (J-O) Quantification of the 3D rendering show significant smaller ventricles, atria, and tricuspid valve in mutant hearts compared to controls. Pulmonary valve (PV), aortic valve (AV). n = 4. Significant differences were calculated using an unpaired, 2-tailed Student's t test. Scale bar: 0.5 mm.

8.4. Discussion

In this chapter, a *Lyve1^{Cre}* mouse line was characterised in terms of specific Cre activity in the heart and further investigated by phenotypic analysis of *Lyve1$^{+/Cre}$;Prox1$^{Flox/Flox}$* mutant embryos. Previous studies have reported that *Lyve1^{Cre}* marks yolk sac haemogenic endothelium[294,310], yolk sac and embryo-derived haematopoietic precursors[294,310], as well as LECs and partially BECs[216]. Moreover, LYVE1 expression has been reported in blood vessels of the yolk sac, liver and lung, as well as in ISVs, umbilical vessels, and endocardium between E9.5 and E11.5[239,311]. Embryonic-derived tissue resident macrophages are also known to produce LYVE1[145]. Nevertheless, neither the activity of *Lyve1^{Cre}* in the embryonic heart, nor the effects of conditional knock-out of *Prox1* using this line have been investigated prior to this study.

Herein, lineage tracing experiments confirmed the labelling of coronary blood vessels earlier than E12.5 by *Lyve1^{Cre}*. Specifically, it was revealed that *Lyve1^{Cre}* marked both SV-derived and endocardium-derived coronary vessels through a series of whole-mount and section immunostaining studies, as well as genetic *Notch1* gain-of-function. During embryonic development in mice, venous endothelial cells from the SV sprout to the dorsal side of the heart, dedifferentiate, infiltrate the ventricles to form the coronary plexus, and

finally re-differentiate to form the coronary arteries and veins[299]. Here, *Lyve1*^{Cre} was found to be extensively active on the venous endothelium of SV. Hence, it would be interesting to investigate potential arterial *Lyve1* expression in future experiments.

The endocardium contributes coronary vessels to areas complementary to SV-derived vessels, mainly in the interventricular septum and the ventral side of the heart[208,297–299]. After birth the endocardium also contributes significantly to the rapidly expanding coronary vasculature[208]. Briefly, endocardial cells undergo lineage conversion during postnatal trabecular compaction forming *de novo* coronary vessels, rather than expansion of pre-existing embryonic vessels[208]. Here, *Lyve1*^{Cre}-derived progeny were found to express PECAM1 and localise in the endocardium and myocardium compartments, including the interventricular septum. Also, *Lyve1*^{Cre} labelled PECAM1^{-} cells in the cardiac valves were potentially endocardium-derived macrophages which have important roles for valve development[301]. Future experiments could explore a potential role of LYVE1 in cardiac valve development, although *Lyve1* knock-out mice have been reported to be phenotypically normal[78].

In addition to the coronary vasculature, *Lyve1*^{Cre} activity was investigated in cardiac resident macrophages during embryonic development. Virtually all CD68^{+} macrophages detected in the heart were marked by *Lyve1*^{Cre} at E14.5, as visualised by a positive tdTomato signal. Furthermore, all CD68^{+} cardiac resident macrophages co-expressed CD206 at this timepoint. However, approximately half of the CD68^{+};CD206^{+};tdTomato^{+} cardiac resident macrophages expressed LYVE1 protein, suggesting that there are at least two different but equally represented macrophage populations (LYVE1+ and LYVE1-) in the

heart at E14.5. Also, 2 % of the CD68^{+} macrophages were negative for the other markers, suggesting a potential third minor sub-population. These results are in line with previous studies showing *Lyve1^{Cre}* as marking yolk sac haemogenic endothelium, primitive and early intraembryonic definitive haematopoiesis as key sources of tissue resident macrophages[294,310].

PROX1^{+} precursor LECs were only partially labelled by *Lyve1^{Cre}* in the CV and SV at E10.5 and E14.5, respectively. By E16.5, as cardiac lymphatics grew and matured, they became positive for LYVE1. The absence of *Lyve1^{Cre}* labelling, which is found in the venous and haemogenic endothelium[294,310] as discussed, highlights the heterogeneity of precursor LECs and raises the question of whether there might be yet another source of cardiac LECs. Overall, these results confirm *Lyve1^{Cre}* as a marker of endocardium, haemogenic endothelium[294,310], and coronary and lymphatic vasculature. As a result, conditional knock-out experiments using *Lyve1^{Cre}* need to consider that *Cre* expression is not specific to LECs.

Despite *Lyve1^{Cre}* not being specific for LECs, it remains a useful tool for lineage tracing and conditional knock-out experiments. For instance, conditional deletion of *Cttnb1* in *Lyve1^{Cre}* mice has been used to show the role of β-catenin in the formation of intraluminal lymphatic valves, lymphovenous valves and venous valves[312]. In another study, *Lyve1^{Cre}* was used to suggest a potentially direct role of VEGFR2 signalling in lymphangiogenesis[311]. Here, *Lyve1^{Cre}* was crossed with *Prox1^{Flox}*, aiming to generate viable neonatal mice with disrupted lymphatics, and subsequently assess the effects in cardiac regeneration. However, the *Lyve1$^{+/Cre}$;Prox1$^{Flox/Flox}$* phenotype was perinatal lethal, with E16.5 embryos displaying severe oedema and blood-filled lymphatics in the body and heart. The few remaining

lymphatics detected in the heart of *Lyve1*$^{+/Cre}$*;Prox1*$^{Flox/Flox}$ embryos could be originating from *Lyve1*$^{-}$ sources (non-venous and non-haemogenic endothelium). For example, the SHF, which contributes lymphatics to the ventral side of the heart specifically, could contribute to the *Lyve1*$^{+/Cre}$*;Prox1*$^{Flox/Flox}$ cardiac lymphatics[126,127]. Moreover, some precursor LECs found on the dorsal side of the heart near the SV were negative for *Lyve1*^{Cre} at E14.5, as discussed previously. These might enable some cardiac lymphatic development in *Prox1* mutant hearts. However, as cardiac lymphatics matured, *Lyve1* was ubiquitously expressed by LECs leading to conditional deletion of *Prox1*, and subsequent dedifferentiation of LECs to BECs[67]. Also, LYVE1 has been described in lymphovenous valves with PROX1 being essential for their correct formation. Thus, it is possible that the blood-filled lymphatics seen in *Lyve1*$^{+/Cre}$*;Prox1*$^{Flox/Flox}$ embryos are the result of disrupted lymphovenous valve formation[51]. Surprisingly, the *Lyve1*$^{+/Cre}$*;Prox1*$^{Flox/Flox}$ phenotype appeared to be less severe at E18.5, with no oedema or blood-filled lymphatics. Immunostaining and confocal microscopy revealed that the lymphatic phenotype was not rescued, as no cardiac lymphatics were observed at E18.5 and no *Lyve1*$^{+/Cre}$*;Prox1*$^{Flox/Flox}$ mutant pups were born. As a result, the *Lyve1*$^{+/Cre}$*;Prox1*$^{Flox/Flox}$ could not be used to study the effects of disrupted lymphatics in neonatal heart regeneration. Apart from underdeveloped lymphatics, *Lyve1*$^{+/Cre}$*;Prox1*$^{Flox/Flox}$ mutant embryos had several cardiac developmental defects. Specifically, in mutant embryos the heart and myocardial wall sizes appeared smaller, with the atria, ventricles and tricuspid valve being significantly smaller compared to control. Also, the mitral and tricuspid valve leaflets were found open only in mutant hearts, suggesting potential valve malformation. The phenotype observed in the tricuspid valve, is similar to Hypoplastic Right Heart Syndrome with tricuspid valve stenosis[313]. Interestingly, *Prox1* mutations have been associated with hypoplastic left

heart[308]; however, the right side of the heart has not been investigated[308]. The development of cardiac valves is a complex and not fully understood process that starts at around E9.5. The major contributor of cardiac valves is the endocardium, while the myocardium, epicardium, neural crest and SHF also invest in the development of cardiac valves[314–317]. *Prox1* is expressed extensively throughout the myocardium and is required for the correct development of the heart and cardiac valves[300,307–309]. Hence, the defects observed in the morphology of the heart, the tricuspid valve, and the ventricular septum in *Lyve1*$^{+/Cre}$*;Prox1*$^{Flox/Flox}$ mutant embryos reflect the expression of *Lyve1*^{Cre} in the endocardium and endocardium cushions, as well as the requirement for *Prox1* in valvulogenesis and heart development[300,307–309].

Other Cre transgenic reporter lines, such as the venous *Tie2-Cre*, have been used to conditionally delete *Prox1* in the past, with some viable neonatal mice being born[38]. However, the efficiency of deleting *Prox1* progenitor LECs in the CV, as well as the phenotype observed, was variable among embryos due to varying levels of Cre activity and incomplete *Prox1* deletion[38,57]. In the future, the use of a tamoxifen driven Cre line, such as the knock-in *Prox1-Cre-ER*^{T2}, would be more appropriate for studying the effects of impaired lymphatics on neonatal heart regeneration after MI[57].

8.5. Summary

The work presented in this chapter investigated the *Lyve1* lineage in the heart, as well as the phenotype of embryos with conditional deletion of *Prox1*, using the *Lyve1*^{Cre} knock-in mouse line. The data demonstrated that *Lyve1* is expressed by the venous endothelium and endocardium, which give rise to the coronary vasculature, as well as by the lymphatic

vasculature and tissue resident macrophages. Upon crossing *Lyve1*^{Cre} with *Prox1*^{Flox} the homozygous embryos had gross developmental defects, with oedema and blood-filled lymphatics at E16.5. In the heart, the few existing lymphatics were underdeveloped and filled with blood, in contrast to the blood vasculature that appeared normal. At E18.5 the phenotype appeared less severe with no oedema or blood-filled lymphatics, although upon closer inspection the heart was depleted of lymphatics, leading to lethality of *Lyve1*$^{+/Cre}$*;Prox1*$^{Flox/Flox}$ mice during the perinatal period.

9. General discussion

9.1. Discussion

The following aims as set out in chapter 3 of this thesis have been achieved:

1) Characterise the spatiotemporal development and maturation of cardiac lymphatic vessels from birth to adulthood in two genetic backgrounds – chapter 5.

2) Characterise the lymphangiogenic response of cardiac lymphatic vessels after MI at P1 and P7 using 3D light-sheet and confocal microscopy – chapter 6.

3) Characterise the efficiency of cardiac lymphatic function after MI at P1 and P7 by performing adoptive cell transfer and MRI – chapter 6.

4) Characterise the response of LECs and macrophages after MI at P1 and P7, as well as identify potential molecular interactions between the two cell populations, by generating and analysing scRNA-seq data – chapter 7.

5) Characterise the lineage of *Lyve1*^{Cre} in the heart and assess potential applications of this line for the study of postnatal cardiac lymphatics – chapter 8.

The extent to which these aims were achieved, as well as the limitations of the findings are discussed in this chapter. Also, future experimental work derived from this thesis is outlined.

9.1.1. ***Spatiotemporal development and maturation of cardiac lymphatic vessels from birth to adulthood in two genetic backgrounds***

The cellular origin and embryonic development of the cardiac lymphatic vasculature has been studied extensively over the past decade, leading to several breakthroughs[38,61,126,127]. Briefly, cardiac LECs in mice originate from at least three sources: the paraxial mesoderm-

derived *Tie2*$^{+}$ endothelium of the CV[61,64,233]; the haemogenic endothelium of the yolk sac (*Vav1*$^{+}$, *Pdgfrb*$^{+}$, and *Csf1r*$^{+}$)[38]; and the second heart field (*Isl1*$^{+}$), which contributes LECs exclusively to the ventral aspect of the heart[126,127]. The first cardiac LECs emerge along the outflow tract on the ventral side of the heart, and from the sinus venosus on the dorsal side of the heart, at E12.5[38]. Over the next days of foetal and postnatal development, until approximately P15, cardiac lymphatics grow on both sides of the heart from base-to-apex, with the vessels on the ventral side being delayed compared to vessels on the dorsal side[36–38,234]. However, previous studies had not investigated the postnatal stages of cardiac lymphangiogenesis in detail and/or have lacked quantification analyses. In this project, the postnatal development of cardiac lymphatics was qualitatively and quantitatively assessed from birth until adulthood on two different genetic background, CD1 and C57BL/6. It was found that during postnatal development lymphatics grow with a delay on the ventral side of the heart, compared to the dorsal side. As a result, cardiac lymphatics reach full length and density by P16 on the dorsal and by P21 on the ventral side. It is possible that this temporal discrepancy in cardiac lymphatic development, which is first observed at embryonic stages, is the result of the different origins attributed to cardiac LECs. Notably, cardiac lymphatics have been described to grow not only through sprouting of pre-existing vessels (lymphangiogenesis), but also from isolated LECs (lymphvasculogenesis) in both zebrafish and mice[249]. Here, the presence of short isolated lymphatic vessels was observed, mainly in the dorsal side during the early postnatal stages. However, the origin of these isolated LECs and their contribution to the main cardiac lymphatic network were not investigated here. Previous lineage tracing experiments have shown that the local coronary vasculature and the endocardium are unlikely to contribute to the isolated LECs[249]. Overall,

it appears that part of the cardiac LECs may derive from a yet undefined non-venous source[54,61,62].

Interestingly, a recent study showed that cardiac lymphatics have sex-dependent developmental differences, with female mice having more lymphatic vessels that males[179]. While here this was not considered, it was shown that genetic background influences cardiac lymphatic development. Specifically, considerable differences were found in the rate and degree of cardiac lymphatic development between CD1 and C57BL/6 mice. Although the overall pattern of the cardiac lymphatic plexus was similar in the two genetic backgrounds, CD1 mice developed more cardiac lymphatic vessels and at earlier postnatal stages. These results highlight the importance of genetic background and add an additional factor that must be taken into consideration during experimental planning and subsequent data interpretation.

The LECs that form lymphatic vessels are held together by specialised cell-cell junctions, with previous studies describing two distinct types of junctions in the trachea and lungs: impermeable zipper-like junctions and permeable button-like junctions[30,33,235]. At early embryonic stages, initial lymphatics have only zipper-like junctions in the trachea and diaphragm. However, these junctions undergo transformation from zipper-like to button-like junctions, a process that starts approximately at E17.5 and completes after P14[84]. While cell-cell interactions in trachea and diaphragm lymphatics have been well studied, there have been no reports about a similar transformation taking place during cardiac lymphatic development. As the maturation of lymphatic junctions could potentially affect their ability to clear cells from the heart to lymph nodes, the morphology of postnatal

cardiac LEC junctions was analysed. A similar transformation was found to happen in the junctions of cardiac LECs, with zipper-like junctions found predominately during the first days of postnatal life and button-like junctions appearing during the second week after birth. Although the type of cell-cell junctions appears to be important for immune cell clearance by lymphatics from interstitial space, other factors that need to be considered and investigated in future studies, such as the extracellular matrix of LECs[17].

The results presented in chapter 5 and discussed in detail here, suggest that cardiac lymphatics are not fully developed and potentially not fully functional at P1. Consequently, it is possible that cardiac lymphatics respond and function different after MI in the P1 regenerative stage, compared to the later P7 fibrotic stage. Also, the response and function of cardiac lymphatics after MI at P1 and P7 will likely vary depending on genetic background given the developmental differences described above.

9.1.2. *Lymphangiogenic response of cardiac lymphatic vessels after MI at P1 and P7*

To generate the data presented in chapters 6 and 7 of this thesis a neonatal mouse model of permanent occlusion of the LAD artery was used[220]. Although, this model provides a useful tool for the study of cardiac injury which occurs in humans, it is important acknowledge its limitations. Surgical ligation of the LAD artery is an invasive procedure conducted in healthy mice that leads to MI, unlike in humans where coronary occlusion is the result of thrombus following atherosclerotic plaque rupture. Ideally, atherosclerotic (*ApoE*$^{-/-}$) mice could be used in all MI studies to better model the human condition, as atherosclerosis impacts the inflammatory environment and impairs healing of the infarcted heart, compared to wild type animals[318–320]. However, in practice this would be logistically

challenging as the *ApoE*$^{-/-}$ line would have to be crossed with all other lines used for surgery. Also, permanent occlusion of the LAD artery does not model the subsequent reperfusion, which occurs as soon as the patient is admitted to hospital. In the model of LAD artery occlusion, complete blockade of blood flow leads to irreversible hypoxia and major myocardial damage[321]. In ischemic reperfusion, there is a second source of cell damage that occurs as a direct result of the sudden restoration of blood flow and oxygen[321]. Induction of MI through surgical ischemic reperfusion has been described in mice and is suggested to be more clinically relevant than permanent ligation[321]. However, ischemic reperfusion comes with its own caveats, for instance there is no defined timepoint when reperfusion should take place (15 min to 2 h) and that leads to great variability in the infarct size[321]. In this study, permanent ligation was chosen as a model for the study of lymphatic response after neonatal MI, as it generates larger and more severe injury that allows clearer comparison between injured and intact animals. Nevertheless, MI induced by permanent ligation can also result in significant variability between animals, particularly as the size of the heart is significantly different at P1 and P7 stages. Variations in infarct size may have implications on some of the data presented in this thesis, as it is likely that a greater inflammatory and lymphangiogenic response takes place in animals with larger infarcts. To overcome this variability issue, it would have been preferential to use larger cohorts of animals. However, the number of mice used was limited by the number of surgery hours required and UK Home Office regulations.

As described in the introduction, adult mammals lack the ability to regenerate their heart and upon MI the lymphatic vasculature gets compromised near the infarction zone, resulting in increased oedema and reduced ability to clear immune cells. Although

lymphatics grow and sprout through lymphangiogenesis after MI in adult mice, this endogenous response is insufficient to clear infiltrated macrophages and oedema[38,39,76,152]. Several gain-of-function studies have used the ligand VEGFC to enhance lymphangiogenesis after MI in adult mice and have reported improved clearance of interstitial fluids and macrophages, consequently improving cardiac function[38,39,76,152]. Interestingly, a recent study reported that blocking endogenous lymphangiogenesis through VEGFR3 or VEGFC/D loss-of-function does not lead to worst oedema or cardiac function after MI in adult mice, compared to wild type injured mice[176]. While the study focused on the effects of depleted endogenous lymphangiogenesis[176], it did not investigate the effects of enhanced lymphangiogenesis, as previous studies have done and it did not account for additional effects of targeting VEGFC/D and VEGFR3 in other cardiovascular lineages (for example the blood vasculature)[38,39,76,152]. Taken together, these results reinforce the hypothesis that the endogenous response of cardiac lymphatics is not sufficient to influence cardiac healing, while augmented lymphatic response through the administration of exogenous factors improves cardiac healing after MI in adult mice. In contrast to adult mice, neonates can fully regenerate their heart after MI at P1, while the regenerative capacity is significantly reduced at P7[195,199]. To date, the response of cardiac lymphatics after MI in regenerative P1 and fibrotic P7 mice has not been studied.

In this thesis it was demonstrated that the response of lymphatic vessels after MI at P1 differs depending on the genetic background of the mouse. This is consistent with previous studies describing variable healing responses after MI in adult mice depending on their genetic strain[204]. An analogous study looking at the cardiac regenerative capacity of postnatal mice on different genetic backgrounds has yet to be conducted. Here, it was

found that there is limited lymphatic response 7 days after MI at P1 compared to MI at P7 in C57BL/6J mice. In contrast, there was a clear lymphangiogenic response to the site of injury 7 days after MI at P1 in CD1 mice. Interestingly, these results link with the faster development of the cardiac lymphatic vasculature observed during normal postnatal development in CD1 mice compared to C57BL/6J mice. It appears that CD1 mice have a more widespread postnatal cardiac lymphatic vasculature that develops earlier and to a larger extend. Notably, most of the genetically modified mouse lines are kept in a C57BL/6J background, which has been shown to have one of the worst recoveries after adult MI[204]. These results highlight again the importance of factoring in the genetic background during experimental planning for MI studies, as it is important to use a consistent mouse strain throughout the project.

9.1.3. *Efficiency of cardiac lymphatic function after MI at P1 and P7*

Innate immune cells are recruited to the injury site shortly after the induction of MI in adult mice. Neutrophils and monocytes are the first to infiltrate the infarcted myocardium to clear debris and dead cells by phagocytosis and efferocytosis, respectively[162]. Other leukocytes, such as T cells, also infiltrate the heart after MI in adult mice, although their effect to MI has not been well characterised[39,163]. Monocytes infiltrate the heart in a biphasic way and during these phases the embryonic-derived tissue-resident macrophages are replaced by monocyte-derived macrophages[164]. The first phase is characterised as inflammatory with an increase in the number of pro-inflammatory monocyte-derived macrophages ($CCR2^+$, $Ly\text{-}6C^+$)[140,156]. The second phase is characterised as anti-inflammatory, as tissue-resident macrophages ($CCR2^-$, $Ly\text{-}6C^-$) contribute to angiogenesis and wound healing[140,156,165]. Acute immune response to MI has been shown to be beneficial

for wound healing, while chronic inflammation can lead to excessive scar formation[39,76,186]. Thus, functional cardiac lymphatics are required to maintain an optimal immune cell load by clearing cells, as well as myocardial oedema, from the site of injury to the MLNs in adult mice following MI.

As described previously, neonatal mice have a cardiac regenerative window that lasts for a few days after birth[195,199,201]. Neonatal and adult mice have several physiological differences that could contribute to cardiac regeneration and scar formation, respectively[205]. During the first days of life cardiomyocytes are proliferating[205–207], *de novo* coronary vessels are forming[208], and the immune system is immature[209]. Several studies have focused on the response of cardiac macrophages after cardiac injury and have shown that tissue-resident macrophages increase in number without infiltration of monocytes after MI in neonatal mice[140,142,205]. Interestingly, general depletion of macrophages with the use of clodronate liposome treatment appears to inhibit cardiac regeneration and lead to reduced cardiac function after MI at P1[210]. In this thesis, it was shown through two experiments (adoptive transfer and quantification of endogenous macrophages) that the lymphangiogenic response does not translate to significantly enhanced macrophage-clearance from the heart to the MLNs in CD1 or C57BL/6J mice 7 days after MI at P1. In the adoptive transfer experiment, MLNs were imaged from CD1 pups which had undergone intramyocardial injection of adult splenic GFP^+ macrophages during the time of MI surgery at P1 or P7. GFP^+ macrophages were detected mainly in the MLNs of mice that had MI at P7, and not at P1. Also, GFP^+ macrophages were detected in the heart of recipient mice that underwent MI at P1 or P7, indicating that adoptive transfer was successful in both timepoints. These results were further supported by measuring the endogenous

macrophage content after MI at P1 and P7. While there was no significant increase in the number of macrophages detected in the MLNs at either timepoints compared to their respective control, there were significantly more macrophages after MI at P7 compared to MI at P1. Taken together, these experiments suggest cardiac lymphatics may not be competent to clear macrophages after MI at P1. However, there are some important factors that must be considered. In the adoptive transfer experiment, the neonatal heart was overloaded with adult macrophages isolated from the spleen. As described previously, adult macrophages have different properties compared to neonatal. Ideally, macrophages should be isolated from the heart, not the spleen, of donor mice that are in the same developmental stage as the recipient mice. However, the neonatal heart has very low number of macrophages and as a result a significantly large cohort of pups would have to be used making this technically challenging. In addition, it could be counter-proposed that the increased number of macrophages detected in the MLNs of mice that had MI at P7 were MLN-resident macrophages, rather than macrophages cleared from the heart by lymphatics. In the future their identity could be tested by using a myocardium reporter mouse model (such as the *Myh6-Cre/R26R-tdTomato*) for MI at P1 and P7, and subsequently imaging MLNs for macrophages that have phagocytosed labelled myocyte debris ($tdTomato^{+}$ myosin fragments) and been transported *via* afferent cardiac lymphatics[76].

Several hypotheses can be formed to explain the reduced macrophage clearance from the heart to the MLNs after MI at P1 compared to P7. An intriguing theory involves the permeability of lymphatic cell-cell junctions. As discussed above, the junctions of cardiac LECs appear to be impermeable zipper-like during the early stages of postnatal

development, and progressively transform to more permeable button-like junctions[84,322]. As a result, it is possible that macrophages cannot transmigrate to cardiac lymphatic vessels during early postnatal development, such as after MI at P1. Notably, the junctions of lymphatic capillaries in the trachea and lungs change back to impermeable zippers during sprouting and inflammation[84,322]. Consequently, in the future it would be important to assess the type of lymphatic junctions in the heart after MI at P1 and P7. Another factor that could impact migration of macrophages to draining lymph nodes is the expression level of chemokines produced by LECs. Here, it was hypothesised that macrophages could locate, dock, and transmigrate to lymphatic vessels through the CCL21-CCR7 pathway, like DCs and neutrophils do[245–247]. Gene expression profiling through scRNA-seq showed that *Ccl21* is specifically expressed by cardiac LECs in both P1 and P7 mice, intact and MI. Moreover, whole-heart qPCR data showed that expression levels of *Ccl21* decrease significantly following MI at P1 compared to P8 intact hearts, while they remain stable after MI at P7 compared P14 intact hearts. However, macrophages were found not to express *Ccr7*, the only known receptor of CCL21, at any of the conditions investigated. As a result, the CCL21-CCR7 pathway is unlikely to contribute to the lymphatic-macrophage interaction in the neonatal heart. Another molecular interaction that has been well-described is based on LEC-expressed LYVE1 and macrophage-expressed HA[145,174,283]. Importantly, LYVE1 appears to be important for the transmigration of macrophages to cardiac lymphatics after MI in adults, with *Lyve1*$^{-/-}$ infarcted hearts having low level of macrophage clearance, increased fibrotic scarring and decreased cardiac function[76]. Based on the results presented so far, it was hypothesised that decreased macrophage clearance by cardiac lymphatics due to *Lyve1* deletion would not impact cardiac regeneration after MI at P1, while it would negatively affect the healing after MI at P7, similarly to the adult. To test

this hypothesis, a large MRI study was conducted using *Lyve1*$^{-/-}$ mice. However, the results of this study were inconclusive as the values obtained for different cardiac parameters were affected by considerable variability across animals from the same experimental group. This variability is the result of different levels of cardiac injury after surgery, variable response to injury from individual animals, and technical variability caused during MRI scanning. Nevertheless, worst cardiac function was observed, with the EF, CO and SV being reduced after MI at P1 in both *Lyve1*$^{-/-}$ and *Lyve1*$^{+/-}$, compared to intact control. Surprisingly, no statistically significant differences were observed in cardiac parameters after MI at P7 in homozygous and heterozygous LYVE1 mutants, compared to controls. A larger cohort of mice would be required to ensure that the MRI study has the required statistical power, as data from animals with the same condition displayed great variability. Notably, expression of *Has1*, *Has2* and *Has3* that are required for HA synthesis was not detected in neonatal macrophages during any condition examined with scRNA-seq. As a result, it is possible that LYVE1 has an important role in tissue-resident macrophages that impacts heart regeneration at P1, while the clearance of macrophages by cardiac lymphatics is unlikely to depend on the LYVE1-HA interaction at the early postnatal stages. Hence, the mechanism for the reduced macrophage clearance by cardiac lymphatics observed after MI at P1 compared to P7 remains elusive, as the interactions of CCL21-CCR7 and LYVE1-HA have been excluded.

9.1.4. ***Response of macrophages after MI at P1 and P7, and potential molecular interaction with LECs***

Macrophages are essential for the regeneration of the heart after MI at P1, potentially by regulating angiogenesis and cardiomyocyte proliferation in the infarcted

region[140,165,205,210,231]. At this developmental stage, cardiac macrophages express *Cx3cr1*, and are yolk sac- and foetal liver-derived[138,142,165,194]. These embryonic-derived macrophages are self-maintained through local proliferation[138,142,165]. However, there is a dynamic change in the profile of cardiac macrophage during the first weeks of postnatal life, with infiltrating monocyte-derived macrophages gradually replacing the embryonic ones[138,142,165]. The infiltrating monocyte-derived macrophages express *Ly6c* and their numbers are replenished by circulating monocytes[138,142,165]. Monocyte-derived macrophages are also functionally different from embryonic-derived macrophages, as they contribute to adverse cardiac remodelling by facilitating fibrotic scar formation after MI[138,140,143,165,166].

Two molecularly distinct tissue-resident macrophage populations were identified at both P1 and P7 stages through scRNA-seq: an embryonic-derived (mf1 - *Lyve1*$^{+}$*;Ccr2*$^{-}$*;Arg1*$^{-}$) and a bone marrow-derived (mf2 - *Lyve1*$^{-}$*;Ccr2*$^{+}$*;Arg1*$^{+}$). The embryonic-derived macrophages were the only ones that appeared to proliferate during postnatal development, in line with previous reports[138,140,142,165,264]. Interestingly, there was a differential response between these two tissue-resident macrophage populations after postnatal MI. The bone marrow-derived macrophages proliferated rapidly 1 day after MI, but their representation in the heart was subsequently reduced 7 days after MI. In contrast, the percentage of embryonic-derived macrophages increased gradually by local proliferation during the 7 days after MI. Three additional macrophage populations were present in the postnatal heart and were expressing both monocyte and macrophage markers. The fraction of these monocyte-derived macrophage clusters remained low throughout development, with only one responding to MI. Both the tissue-resident and the monocyte-derived macrophages

displayed the same response to MI at P1 and P7 stages. Finally, a monocyte population was present in the heart and its representation in the heart increased specifically after MI at P7, without proliferation. This suggests that infiltration of monocytes to the infarcted heart might not take place at P1 as has been previously inferred.

Macrophages promote lymphangiogenesis and remodelling of cardiac lymphatics through physical interaction during embryonic development[145] and VEGFC secretion after MI in adult mice[39,76]. The scRNA-seq dataset was used to identify potential direct or indirect interactions between macrophages and cardiac LECs after MI in P1 and P7. Expression levels of *Vegfc* and *Vegfd* were almost undetectable in the macrophage and monocyte clusters, similar to *Has1/2/3* and *Ccr7*. *Pdpn* is expressed by a subpopulation of macrophages and promotes lymphangiogenesis in breast cancer[284]. Re-analysis of previously published bulk RNA-seq data from FACS isolated cardiac macrophages[166,289] revealed that *Pdpn* is significantly upregulated after MI in adult mice. In the scRNA-seq analysis (this study), *Pdpn* was found to be expressed in very low levels in one of the monocyte-derived populations after MI in both P1 and P7, as well as by hiPSC-derived macrophages *in vitro*. Although these results suggest that macrophages could induce lymphangiogenesis in a PDPN-mediated way after MI, *Pdpn* positive macrophages failed to significantly induce lymphangiogenesis in an *in vitro* lymphatic sprouting experiments.

Several potential molecular interactions between macrophages and LECs were identified using an unbiased computational analysis of the scRNA-seq datasets. For instance, the LEC-expressed ligand *Reln* could interact with the macrophage-expressed receptor *Itgb1*. The interaction of RELN with ITGB1 has been described before in the neonatal heart, but not

between LECs and macrophages[269]. In that study LEC-secreted RELN was found to interact with ITGB1 in cardiomyocytes, promoting proliferation, and consequently enhancing cardiac regeneration after MI at P1[269]. Hence, it is plausible that a RELN-ITGB1 interaction could promote cardiac macrophage proliferation after MI. In addition, macrophages have several candidate ligands that could interact with LEC receptors, such as PF4, PSAP, C1QA, APOE, CD14, F13A1 and SPP1. Most of these ligands have roles in regulation of inflammation (PSAP, C1QA, APOE, CD14)[323–326], wound healing (PF4 and F13A1)[327,328] and (lymph)angiogenesis (SPP1)[278–282]. The interaction of SPP1 with integrins (ITGAV, ITGA5, ITGB1 and ITGA9) has been implicated in angio- and lymphangio-genesis making SPP1 of particular interest for future studies. In the heart, bone marrow-derived tissue-resident macrophages expressed differentially *Spp1* and upregulated it after MI, although the expression levels were similar after MI at P1 and P7. The differential expression of integrins by cardiac LECs could not be tested as there was very low representation of LECs in the scRNA-seq dataset. Therefore, it cannot be excluded that SPP1-integrins mediates a differential interaction between macrophages and cardiac LECs after MI at P1 compared to P7. Overall, no molecular differences were detected in macrophages after MI at P1 compared to P7 that might explain their differential interaction and clearance by cardiac LECs. However, new hypotheses were formed that require further investigation and will be discussed below under future work.

It is important to note the scRNA-seq dataset was generated by not enriching or excluding for any specific cardiac cell population, with the aim of being unbiased. Nevertheless, each step that was used until the analysis of the data introduced an unintentional technical bias. For instance, cardiomyocytes were too large to survive FACS, which was performed to sort

for live cells before library preparation. Also, the dataset was almost depleted of under-represented cell population (such as LECs), as they were not enriching before sequencing. In the future a specific cell type enriched approach would need to be taken based on the experimental requirements for the underlying project, such as in this case FACS and sequencing specifically for LECs and macrophages.

9.1.5. *Lyve1^{Cre} lineage in the heart and assess potential applications of this line for the study of postnatal cardiac lymphatics*

Lyve1 is expressed in the yolk sac haemogenic endothelium, as well as in the primitive and early intraembryonic definitive haematopoiesis[294,310]. Also, LYVE1 is found in embryonic-derived tissue-resident macrophages, LECs and partially in BECs[145,216,239,311]. Crossing the knock-in Lyve1^{Cre} with the transgenic R26R-tdTomato mouse line enabled genetic lineage tracing of *Lyve1*$^{+}$ progeny.

Expression of tdTomato was found throughout the coronary blood endothelium at E12.5. The coronary vasculature is formed during three waves of angiogenesis in mice[329]. During embryonic development in mice, venous endothelial cells from the SV sprout to the dorsal side of the heart and form coronary arteries and veins, in a processes that involves endothelial dedifferentiation and redifferentiation[299]. The endocardium contributes coronary vessels to areas complementary to SV-derived vessels, mainly in the interventricular septum and the ventral side of the embryonic heart[208,297–299]. After birth, the endocardium makes a second contribution to the coronary vasculature[208], with trabecular compaction and endocardial cells forming *de novo* coronary vessels[208]. Through a series of experiments, tdTomato was found to be extensively expressed by the venous

endothelium of SV, as well as by PECAM1^{+} cells of the endocardium, myocardium, and interventricular septum. Also, the tdTomato signal was detected in PECAM1^{-} cells near the cardiac valves, which potentially resemble endocardium-derived macrophages of the valves[301]. Future experiments could utilise the *Lyve1^{Cre}* line to target genes in the blood endothelium from the early embryonic stages.

Lyve1^{Cre} was found to be active in both the JLS and JV at E12.5, in agreement with previous data showing LYVE1 expression[38]. However, not all PROX1^{+} precursor LECs expressed tdTomato in the CV and SV at E10.5 and E14.5, respectively. Different cell populations contribute to cardiac LECs, such as the venous endothelium[57,61], haemogenic endothelium[38], and SHF[126,127]. The absence of *Lyve1Cre* labelling of SV-derived LECs highlights the heterogeneity of precursor LECs. Although the SHF might not be expressing *Lyve1*, this source contributes lymphatics specifically to the ventral side of the heart[126,127], thus cannot explain the SV-derived LECs that are negative for *Lyve1^{Cre}*activity. By E16.5, all cardiac LECs appeared to express tdTomato and *Lyve1*, suggesting that *Lyve1* is activated in all LECs coincident with lymphatic maturation.

Virtually all CD68^{+} macrophages detected in the heart were also expressing tdTomato and *Cd206* at E14.5. However, approximately half of the cardiac resident macrophages produced LYVE1, suggesting that there are two different macrophage populations in the heart at E14.5. Also, 2 % of the CD68^{+} macrophages were negative for the other markers, proposing the existence of a third sub-population. Considering that *Lyve1^{Cre}* markers the yolk sac haemogenic endothelium, as well as yolk sac and embryo-derived haemogenic

precursors[294,310], the negative *Lyve1*^{Cre} macrophages must derive from later stages of definitive haematopoiesis, such as from the bone-marrow.

These results confirm that *Lyve1* is not specifically expressed in LECs. However, studies have focused mainly on the effects of global *Lyve1* knock-out in LECs[78,173,174]. Further research must be conducted looking into the effects of *Lyve1* knock-out in other cell populations, such as tissue-resident macrophages and blood endothelium, during embryonic and postnatal development.

Aiming to disrupt cardiac lymphatics and subsequently study the effects in postnatal cardiac regeneration, *Lyve1*$^{+/Cre}$*;Prox1*$^{Flox/Flox}$ mice were generated. To this end, *Lyve1*$^{+/Cre}$*;Prox1*$^{+/Flox}$ male mice were crossed with *Lyve1*$^{+/+}$*;Prox1*$^{Flox/Flox}$ female and the offspring were examined. Of note *Lyve1*$^{+/Cre}$*;Prox1*$^{+/Flox}$ mice were found to be viable and fertile. In a previous study, most conditional heterozygous *Prox1* knock-out (*Lyve1*$^{+/Cre}$*;Prox1*$^{+/Flox}$) mice were shown to die during embryo stages with oedema, while any surviving pup died shortly after birth[304]. The discrepancy between the two studies on the survival of *Lyve1*$^{+/Cre}$*;Prox1*$^{+/Flox}$ mice could be due to the use of different Prox1^{Flox}, as both studies used the same line for Cre driver[304]. *Lyve1*$^{+/Cre}$*;Prox1*$^{Flox/Flox}$ mice had severe oedema and blood-filled lymphatics in the body and heart at E16.5, with no surviving mutants found after birth. Interestingly, some lymphatics appeared to form on the dorsal side of the heart in *Lyve1*$^{+/Cre}$*;Prox1*$^{Flox/Flox}$ embryos. These cardiac lymphatics could be originating from a *Lyve1*$^{-}$ source, similar to the ones found to be negative for *Lyve1*$^{+/Cre}$*;R26R-tdTomato* in chapter 8. While the SHF could potentially contribute lymphatics to the ventral side of the heart[126,127], this origin does not explain the lymphatics

on the dorsal side of the heart near the SV. It is also possible that variability in Cre expression and function led to incomplete *Prox1* knock-out in some LECs, and consequently to some lymphatic formation. The oedema and blood-filled lymphatics observed in *Lyve1*$^{+/Cre}$*;Prox1*$^{Flox/Flox}$ at E16.5 could be caused by defects in lymphovenous valve formation[51]. Unexpectedly, the *Lyve1*$^{+/Cre}$*;Prox1*$^{Flox/Flox}$ phenotype appeared milder at E18.5, as no oedema or blood-filled lymphatics were observed. However, no cardiac lymphatics were observed at this timepoint. This is consistent with the ubiquitous activity of *Lyve1*^{Cre} in mature LECs and the complete deletion of *Prox1*, which leads to dedifferentiation of LECs to BECs[67]. As no *Lyve1*$^{+/Cre}$*;Prox1*$^{Flox/Flox}$ pups were born, it is possible that some resorption of the mutant embryos occurs prior to or around E18.5, potentially explaining the less severe phenotypes observed.

Apart from cardiac lymphatic phenotype, *Lyve1*$^{+/Cre}$*;Prox1*$^{Flox/Flox}$ mutants displayed similarities to Hypoplastic Right Heart Syndrome[313], with significantly smaller atria, ventricles and tricuspid valve compared to control at E15.5. Also, the IVS was defective, although this phenotype was not fully penetrated as it was found in 1 out of 4 mutants. The endocardium is the main source of cells for the developing cardiac valves, with the myocardium, epicardium, neural crest and SHF also contributing to a lesser extent[314–317]. In this thesis it was shown that *Lyve1*^{Cre} is expressed throughout the myocardium and endocardium; however, the expression of *Lyve1*^{Cre} by cardiomyocytes was not investigated. In the future, it would be interesting to stain *Lyve1*$^{+/Cre}$*;R26R-tdTomato* hearts with cardiomyocyte markers to test this possibility. The structural defects observed in the heart and the tricuspid valve in *Lyve1*$^{+/Cre}$*;Prox1*$^{Flox/Flox}$ mutant embryos confirms the expression

of *Lyve1*^{Cre} in the endocardium, and reinforces the requirement for *Prox1* in valve and heart development[300,307–309].

Overall, the *Lyve1*$^{+/Cre}$*;Prox1*$^{Flox/Flox}$ mouse cross could not be used to study lymphatic vessel malformation in the postnatal stages, and while other Cre transgenic reporter lines have been used in the past, they lack specificity and efficiency. For instance, the venous *Tie2-Cre* has generated viable neonatal mice after conditionally *Prox1* deletion[38]. However, the phenotype observed was variable among embryos, suggesting varying levels of Cre activity and incomplete *Prox1* deletion[38,57]. In the future to study the effects of impaired lymphatics in neonatal heart regeneration, the mouse lines *Prox1-Cre-ER*^{T2} [57] and *Vegfr3*^{Flox} [330] could be crossed and *Vegfr3* deletion could be induced by tamoxifen injection after postnatal MI.

10. Conclusions

The work presented in this thesis has provided novel insight into the postnatal development of cardiac lymphatic vessels and their response after MI during regenerative P1 and fibrotic P7 stages. Cardiac lymphatics grow significantly during the first three weeks of postnatal development. Simultaneously, their cell-cell junctions are transformed from impermeable zippers to permeable buttons. The developmental process of cardiac lymphatics was found to be influenced by genetic background, with CD1 mice displaying a larger vasculature compared to C57BL/6J at the same developmental stage. The genetic background also affected the response of cardiac lymphatics after MI, as the lymphangiogenic response after MI at P1 was limited in C57BL/6J compared to CD1 mice, this in turn is reflected by known differences in response to adult MI across genetic backgrounds[204]. The lymphatic response to cardiac injury was also affected by the postnatal stage of the mice, with a significantly stronger response taking place after MI at P7 compared to P1. Moreover, there was a significant increase in macrophage clearance from the heart to MLNs after MI at P7 compared to P1, regardless of genetic background. These results show that cardiac lymphatics may respond to MI through lymphangiogenesis after MI at P1, but there is limited macrophage clearance at a stage when the macrophages are deemed to be pro-regenerative and required in situ for angiogenesis and tissue-restoration at P1[210].

Investigation of the response of macrophages after postnatal MI and their interaction with cardiac LECs, revealed two tissue resident macrophage populations that displayed different dynamic after postnatal MI. Moreover, the fraction of infiltrating monocytes and monocyte-derived macrophages was found to increase only after MI at P7. Unbiased

analysis of scRNA-seq data proposed several potential interactions, such as between the macrophage-expressed SPP1 and LEC-expressed integrins. Better understanding of the molecular interaction of macrophages with cardiac lymphatics could help decipher the differential clearance of the macrophages seen after MI at P1 compared to P7 and uncover potential macrophage-driven lymphangiogenesis mechanisms for further study.

11. Future work

Following on from the findings of this thesis, future work should aim to investigate the following points:

1. Determine the morphology and type of cell-cell junctions of cardiac LECs after postnatal MI.

2. Provide further evidence of macrophage trafficking by cardiac lymphatics after MI.

3. Investigate whether cardiac lymphatics discriminate between macrophage subtypes during the clearance after MI.

4. Investigate the phenotype of *Lyve1*$^{-/-}$ animals that could affect postnatal heart regeneration.

5. Validate molecular interactions between macrophages and cardiac LECs detected by scRNA-seq.

11.1. Determine the morphology and type of cell-cell junctions of cardiac LECs after postnatal MI.

Here it was shown that cell-cell junctions in cardiac lymphatics undergo transformation during postnatal development from impermeable zipper-like junctions to permeable button-like junctions. In the trachea and lung lymphatics, where this pattern was first described, immune cells preferentially transmigrate to the lymph through button-like junctions[33,84]. This could have significant implications for this project, as it was found that macrophages did not clear as efficiently from the heart after MI at P1, when lymphatic junctions are mainly zippers, as compared to P7, when lymphatic junctions are changing to buttons. However, in the trachea and lung lymphatics new lymphatics that formed through lymphangiogenesis after infection, were described to have zipper junctions, suggesting that status of lymphatic cell-cell junctions is reversable[33,84]. Thus, it is possible that the new

lymphatics have impermeable zippers after postnatal MI in P1 and P7, although it is also possible that they remain impermeable and permeable respectively across the time course of injury response. To assess this hypothesis, high magnification (63x) confocal microscopy and staining for the junction protein VE-CADHERIN need to be used to image the junctions of forming cardiac lymphatics after MI at P1 and P7. For this study, mice with CD1 genetic background would be more optimal as they display more extensive lymphangiogenic response after MI at P1 compared to C57BL/6J, making the imaging of new injury-responsive cardiac lymphatics more accessible.

11.2. Provide further evidence of macrophage trafficking by cardiac lymphatics after postnatal MI.

The data presented in this thesis suggest that macrophages are cleared from the heart to the MLNs less efficiently after MI at P1 compared to P7. Two experiments were performed to reach this conclusion. First, adoptive transfer experiment was performed by intramyocardial injection of GFP^+ macrophages during the time of MI surgery at CD1 P1 or P7. Second, the area of endogenous macrophage in the MLNs after MI at P1 and P7 was quantified in C57BL/6J mice. Data from both experiments reached the same conclusion of differential macrophage clearance after MI at P1 and P7. However, as both experiments had caveats that were previously discussed, it will be important to expand these studies to support the conclusions. For instance, the cardiac origin of the macrophages detected in MLNs needs to be verified by using a myocardium reporter mouse model (such as the *Myh6-Cre/R26R-tdTomato*) in MI studies at P1 and P7. Subsequently, MLNs will be imaged for $CD68^+$ macrophages that have phagocytosed labelled myocyte debris ($tdTomato^+$ myosin fragments) and been transported *via* afferent cardiac lymphatics[76]. This experiment

will exclude the possibility that the increase of macrophages in the MLNs detected here after MI was due to an increase of MLN-resident macrophages. A second experiment that can be performed to measure the clearing efficiency of cardiac lymphatics after MI at P1 and P7, is intra-myocardial injection of fluorescent microspheres and quantum dots (Qdots), as has previously been described[54,131,152]. However, the clearance of artificial Qdots cannot directly translate to cell clearance, as cells have different properties such as variable size and molecular signatures as well as altered affinity for ingression into the lymphatic vessels.

11.3. Investigate whether cardiac lymphatics discriminate between macrophage subtypes during clearance after postnatal MI.

This project focused on the ability of cardiac lymphatics to clear macrophages after postnatal MI and the differences detected between P1 and P7 were mostly attributed to the LECs. However, it is important to consider the hypothesis that macrophages have different ability to transmigrate to lymphatics. This hypothesis is very attractive, especially considering the heterogeneity of cardiac macrophages. Here, scRNA-seq was used to investigate known and novel molecular interactions between macrophages and lymphatics in the postnatal heart before and after MI. Although, the same macrophage populations were identified after MI at P1 and P7, a monocyte population was elevated specifically after MI at P7. In the future it would be important to perform flow-cytometry using multiple macrophage markers not only for the heart of P1 and P7 mice after MI, but also for the MLNs. This experiment will provide a comprehensive and quantitative understanding of the macrophage landscape in the regenerative and fibrotic postnatal heart, as well as unequivocally identifying the specific macrophages that are cleared to the

MLNs after postnatal MI. This is, however, technically challenging as the lymph nodes are particularly small at the early postnatal stages, even though they swollen following MI. Thus, a considerable number of MLNs would be required to obtain a significant number of macrophages, potentially making this experiment unsustainable in terms of animal numbers. A potentially simpler approach would be to perform adoptive transfer using different GFP mouse lines. For instance, the adoptive transfer experiment presented here utilised the pan-macrophage reporter CD68-GFP to study the overall macrophage clearance after postnatal MI. Future experiments could perform a similar experiment with CX3CR1-GFP embryonic-derived macrophages or CCR2-RFP monocyte-derived macrophages. Detection of CX3CR1-GFP or CCR2-RFP macrophages in MLNs after postnatal MI would provide valuable information regarding clearance of macrophage sub-populations (for example, tissue resident versus infiltrating) by cardiac lymphatics.

11.4. Investigate the mechanism that could affect postnatal heart regeneration in *Lyve1*$^{-/-}$ animals.

Previous studies have reported normal development of *Lyve1*$^{-/-}$ mice with the only phenotype detected being reduced immune cell clearance after inflammation or cardiac injury[76,78,79]. However, *Lyve1* is not specific for LECs, being expressed from the very first stages of embryogenesis in several different cell populations. For instance, *Lyve1* is expressed by yolk sac haemogenic endothelium, yolk-sac and embryonic-derived haematopoietic precursors[294,310], and subsequently its expression is maintained in a subset of embryonic-derived cardiac-resident macrophages. Also, *Lyve1* is expressed by the venous endothelium and endocardium during the first days of embryonic development, two lineages which give rise to the coronary vasculature. Finally, *Lyve1* expression is

potentially present in endocardium-derived macrophages of cardiac valves. As a result, it is possible that *Lyve1* deletion affects one of the many non-LEC populations that it its expressed by. In this project, *Lyve1* knock-out mice were used to test the effects of reduced macrophages clearance in heart regeneration and repair after MI at P1 and P7, respectively. The hypothesis proposed in this thesis was that little to no effects in cardiac function would be detected in *Lyve1*$^{-/-}$ after MI at P1, as limited macrophage clearance was detected in normal conditions and macrophages are essential for P1 heart regeneration[210]. In contrast, decreased cardiac function was expected to be seen in *Lyve1*$^{-/-}$ after MI at P7, similarly to the results obtained from adult studies given the need to clear pro-inflammatory/pro-fibrotic macrophages at this stage for more optimal repair[76]. This hypothesis was refuted, as the cardiac function appeared impaired in *Lyve1*$^{+/-}$ and *Lyve1*$^{-/-}$ mice after MI at P1 compared to the intact heart, while limited effect was noted in *Lyve1*$^{+/-}$ and *Lyve1*$^{-/-}$ after MI at P7 compared to intact heart. This MRI study reinforces the notion that LYVE1 could have an important role for heart regeneration through either the development or function of embryonic-derived macrophages. In the future, conditional targeting of *Lyve-1* in macrophages using inducible Cre lines, such as *Cx3cr1*^{CreER} [331], would allow to investigate the function of LYVE1, as well as the effects of its deletion, in heart regeneration.

11.5. Validate molecular interactions between macrophages and cardiac LECs detected by scRNA-seq.

Understanding the underlying molecular mechanisms that determine macrophage interactions with cardiac lymphatics after postnatal MI, is one of the most important question that remains to be answered. In the past it has been suggested that macrophages

contribute to lymphangiogenesis through physical interaction[145] and secretion of lymphangiogenic factors like VEGFC[39,76]. Moreover, the interaction between LYVE1 and HA has been suggested to be important for the transmigration of macrophages by cardiac lymphatics[76,78,79]. However, these interactions have not been evaluated in the mouse model of postnatal MI. The scRNA-seq experiment conducted in this project provided candidate factors that might mediate molecular interaction of macrophages with cardiac lymphatics after MI at P1 and P7. Macrophages and monocytes were found to not express VEGFC, VEGFD, HAS1, HAS2, HAS3 and CCR7 in intact or MI conditions at P1 or P7. Although these results need to be verified with a more sensitive method, such as *in situ* hybridisation (RNAScope) and functional gene analysis, they suggest that macrophages interact with cardiac lymphatics through a yet unknown mechanism. Using an unbiased computational approach several potential interactions were uncovered, for instance between LEC-ligand RELN and macrophage-receptor ITGB1, or between the macrophage-ligand SPP1 and the LEC-expressed integrins. Future studies need to confirm these interactions firstly by *in situ* hybridisation and secondly by genetic knock-out experiments. Also, a scRNA-seq experiment enriching for macrophages and cardiac LECs could be considered, to increase the numbers of under-represented populations, such as LECs. However, while this project focused on macrophages and LECs, the scRNA-seq dataset that was generated contains information about other postnatal cardiac populations. Consequently, future studies interested in the response of other cell populations after MI at P1 and P7, such as adaptive immune cells and fibroblasts, will also benefit from the large amount of information in this dataset.

12. Appendix

12.1. Meetings attended

12.1.1. *Oral presentations*

1. Medical Science Division DPhil Research Slam, Jul 2020 (virtual meeting).
2. DPAG Development / Cell Biology Theme Research Meeting, Oct 2019, Oxford, UK.

12.1.2. *Poster presentation*

1. Annual Oxford Development Biology Symposium, Dec 2019, Oxford, UK.
2. DPAG Development / Cell Biology Theme Research Meeting, Jun 2019, Oxford, UK.
3. DPAG Student Poster Day, Nov 2019, Oxford, UK.

12.1.3. *Prizes*

1. Commendation at the DPAG Image Competition 2021

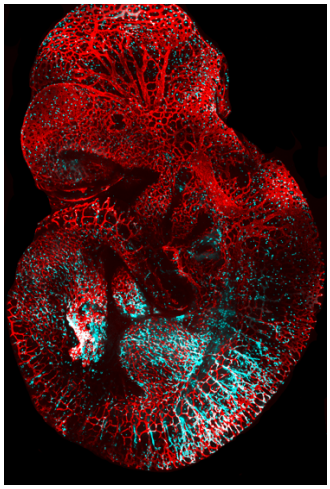

2. 2nd poster prize awarded at the DPAG Student Poster Day 2019.

(Cartoon Credit: Jackbroughamdrawing.com)

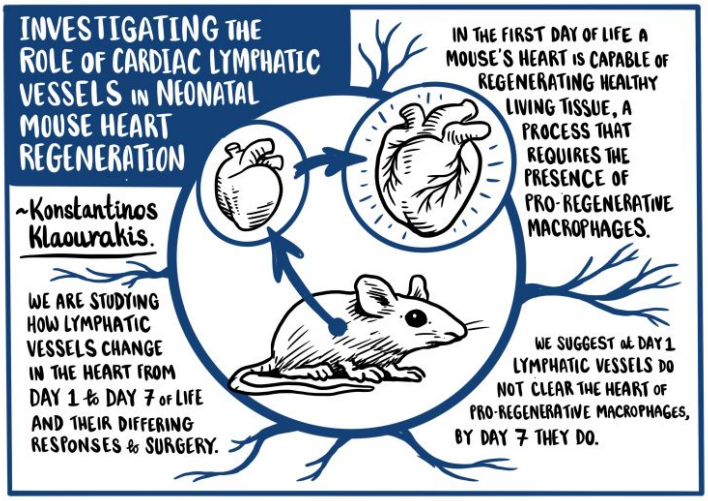

12.2. Publications

12.2.1. *Research papers and reviews*

Kalisch-Smith JI, Morris EC, Strevens MAA, Redpath AN, Klaourakis K, Szumska D, Outhwaite JE, Sun X, Vieira JM, Smart N, De Val S, Riley PR, Sparrow DB. Analysis of placental arteriovenous formation reveals new insights into embryos with congenital heart defects. Front. Genet., 2022 Jan; 10.3389/fgene.2021.806136. See appendix I for abstract.

Klaourakis K, Vieira JM, Riley PR. The evolving cardiac lymphatic vasculature in development, repair and regeneration. Nat Rev Cardiol. 2021 May;18(5):368-379. See appendix II for abstract.

Cahill TJ, Sun X, Ravaud C, Villa Del Campo C, Klaourakis K, Lupu IE, Lord AM, Browne C, Jacobsen SEW, Greaves DR, Jackson DG, Cowley SA, James W, Choudhury RP, Vieira JM, Riley PR. Tissue-resident macrophages regulate lymphatic vessel growth and patterning in the developing heart. Development. 2021 Feb 3;148(3):dev194563. See appendix III for abstract.

Sun X, Malandraki-Miller S, Kennedy T, Bassat E, Klaourakis K, Zhao J, Gamen E, Vieira JM, Tzahor E, Riley PR. The extracellular matrix protein agrin is essential for epicardial epithelial-to-mesenchymal transition during heart development. Development. 2021 May 1;148(9):dev197525. See appendix IV for abstract.

frontiers in Genetics

ORIGINAL RESEARCH
published: 19 January 2022
doi: 10.3389/fgene.2021.806136

Analysis of Placental Arteriovenous Formation Reveals New Insights Into Embryos With Congenital Heart Defects

Jacinta I. Kalisch-Smith[1], Emily C. Morris[1], Mary A. A. Strevens[1], Andia N. Redpath[1], Kostantinos Klaourakis[1], Dorota Szumska[1,2], Jennifer E. Outhwaite[3], Xin Sun[1], Joaquim Miguel Vieira[1], Nicola Smart[1], Sarah De Val[1,2], Paul R. Riley[1] and Duncan B. Sparrow[1]**

[1]BHF Centre for Research Excellence, Department of Physiology, Anatomy, and Genetics, University of Oxford, Oxford, United Kingdom, [2]Nuffield Department of Medicine, Ludvig Institute for Cancer Research Ltd., University of Oxford, Oxford, United Kingdom, [3]School of Biomedical Sciences, University of Queensland, Brisbane, QLD, Australia

OPEN ACCESS

Edited by:
Athanasia (Nancy) Stathopoulou, University College London, United Kingdom

Reviewed by:
Sandra Rugonyi, Oregon Health and Science University, United States
David Renato Christopher Natale, Queen's University, Canada

***Correspondence:**
Jacinta I. Kalisch-Smith
jacinta.kalisch-smith@dpag.ox.ac.uk
Duncan B. Sparrow
duncan.sparrow@dpag.ox.ac.uk

Specialty section:
This article was submitted to Genetics of Common and Rare Diseases, a section of the journal Frontiers in Genetics

Received: *31 October 2021*
Accepted: *15 December 2021*
Published: *19 January 2022*

Citation:
Kalisch-Smith JI, Morris EC, Strevens MAA, Redpath AN, Klaourakis K, Szumska D, Outhwaite JE, Sun X, Vieira JM, Smart N, De Val S, Riley PR and Sparrow DB (2022) Analysis of Placental Arteriovenous Formation Reveals New Insights Into Embryos With Congenital Heart Defects. Front. Genet. 12:806136. doi: 10.3389/fgene.2021.806136

The placental vasculature provides the developing embryo with a circulation to deliver nutrients and dispose of waste products. However, in the mouse, the vascular components of the chorio-allantoic placenta have been largely unexplored due to a lack of well-validated molecular markers. This is required to study how these blood vessels form in development and how they are impacted by embryonic or maternal defects. Here, we employed marker analysis to characterize the arterial/arteriole and venous/venule endothelial cells (ECs) during normal mouse placental development. We reveal that placental ECs are potentially unique compared with their embryonic counterparts. We assessed embryonic markers of arterial ECs, venous ECs, and their capillary counterparts—arteriole and venule ECs. Major findings were that the arterial tree exclusively expressed *Dll4*, and venous vascular tree could be distinguished from the arterial tree by Endomucin (EMCN) expression levels. The relationship between the placenta and developing heart is particularly interesting. These two organs form at the same stages of embryogenesis and are well known to affect each other's growth trajectories. However, although there are many mouse models of heart defects, these are not routinely assessed for placental defects. Using these new placental vascular markers, we reveal that mouse embryos from one model of heart defects, caused by maternal iron deficiency, also have defects in the formation of the placental arterial, but not the venous, vascular tree. Defects to the embryonic cardiovascular system can therefore have a significant impact on blood flow delivery and expansion of the placental arterial tree.

Keywords: placenta, endothelial, labyrinth, allantois, iron deficiency, congenital heart defects

INTRODUCTION

Delivery of oxygen and nutrients, and the disposal of waste products are both essential for an embryo to grow and develop. In mammals, these functions are provided by the placenta. In this organ, the maternal and embryonic bloodstreams are juxtaposed, providing an interface for nutrient and waste exchange. In the mouse, the chorio-allantoic labyrinth vasculature connects through the umbilical

The evolving cardiac lymphatic vasculature in development, repair and regeneration

Konstantinos Klaourakis[1,2], Joaquim M. Vieira[1,2,3]✉ and Paul R. Riley[1,2,3]✉

Abstract | The lymphatic vasculature has an essential role in maintaining normal fluid balance in tissues and modulating the inflammatory response to injury or pathogens. Disruption of normal development or function of lymphatic vessels can have severe consequences. In the heart, reduced lymphatic function can lead to myocardial oedema and persistent inflammation. Macrophages, which are phagocytic cells of the innate immune system, contribute to cardiac development and to fibrotic repair and regeneration of cardiac tissue after myocardial infarction. In this Review, we discuss the cardiac lymphatic vasculature with a focus on developments over the past 5 years arising from the study of mammalian and zebrafish model organisms. In addition, we examine the interplay between the cardiac lymphatics and macrophages during fibrotic repair and regeneration after myocardial infarction. Finally, we discuss the therapeutic potential of targeting the cardiac lymphatic network to regulate immune cell content and alleviate inflammation in patients with ischaemic heart disease.

The circulatory system of vertebrates is composed of two complementary vasculatures, the blood and lymphatic vascular systems[1]. The blood vasculature is a closed system responsible for transporting gases, fluids, nutrients, metabolites and cells to the tissues[2]. This extravasation of fluid and macromolecules results in a continuous accumulation of extracellular fluids and increased interstitial pressure[2]. Tissue fluid balance is maintained by the lymphatic vasculature, an open circulatory system that transports fluids and cells from organs back to the blood circulation[3]. In addition to regulating interstitial fluid homeostasis, lymphatic vessels have essential roles in the immune response through the uptake and transport of pathogens, antigens and immune cells from tissues to regional lymph nodes, before returning the extravasated fluid and solutes to the blood circulation.

In the heart, an extensive lymphatic network contributes to normal cardiac function in steady-state conditions and to myocardial healing after injury[4]. An increasing number of studies have determined the lineage heterogeneity of the cardiac lymphatics during development and their essential role in fibrotic repair after myocardial infarction (MI) in non-regenerative animal models, such as adult mice[5–9], and regenerative models, such as zebrafish[10–13]. These studies hold great promise for ongoing efforts to develop therapies for cardiovascular diseases, highlighting the lymphatic vessels as a potential therapeutic target to reduce myocardial oedema and modulate the immune response after MI. In this Review, we summarize the current knowledge on the development, structure and function of the cardiac lymphatic vasculature, with an emphasis on breakthroughs over the past 5 years in the study of cardiac lymphatic heterogeneity in mice and zebrafish. We also discuss emerging findings on the immunomodulatory role of the cardiac lymphatics and their functional interaction with immune cells during the fibrotic repair process after injury in the adult mammalian heart, as well as during cardiovascular tissue restoration and regeneration in neonatal mice and in adult zebrafish. Finally, we describe ongoing preclinical studies investigating the lymphatic vessels as a potential therapeutic target in acute MI.

Cardiac lymphatic structure and function

The cardiac lymphatics run alongside the blood vessel network and have many of the functional features of the systemic lymphatic vasculature (FIG. 1), specifically the maintenance of homeostasis of interstitial fluid pressure[14,15] and the modulation of the immune response[16]. Disruption of these processes can lead to severe health problems; for example, a 3.5% increase in myocardial fluids can lead to a 40% reduction in cardiac output[17,18]. Lymphatic vessels are lined by a monolayer of oak-leaf-shaped lymphatic endothelial cells (LECs) and are composed of three compartments: the initial lymphatics, the pre-collector lymphatics and the collector lymphatics[1,19]. Interestingly, the localization of the

[1]Burdon Sanderson Cardiac Science Centre, Department of Physiology, Anatomy and Genetics, University of Oxford, Oxford, UK.
[2]British Heart Foundation–Oxbridge Centre of Regenerative Medicine, CRM, University of Oxford, Oxford, UK.
[3]These authors jointly supervised this work: Joaquim M. Vieira, Paul R. Riley.
✉e-mail: joaquim.vieira@dpag.ox.ac.uk; paul.riley@dpag.ox.ac.uk
https://doi.org/10.1038/s41569-020-00489-x

© 2021. Published by The Company of Biologists Ltd | Development (2021) 148, dev194563. doi:10.1242/dev.194563

RESEARCH ARTICLE

Tissue-resident macrophages regulate lymphatic vessel growth and patterning in the developing heart

Thomas J. Cahill[1,2,‡], Xin Sun[1,2,‡], Christophe Ravaud[1,2], Cristina Villa del Campo[1,2,*], Konstantinos Klaourakis[1,2], Irina-Elena Lupu[1,2], Allegra M. Lord[3], Cathy Browne[4], Sten Eirik W. Jacobsen[3], David R. Greaves[4], David G. Jackson[5], Sally A. Cowley[4], William James[4], Robin P. Choudhury[6], Joaquim Miguel Vieira[1,2,§,¶] and Paul R. Riley[1,2,§,¶]

ABSTRACT

Macrophages are components of the innate immune system with key roles in tissue inflammation and repair. It is now evident that macrophages also support organogenesis, but few studies have characterized their identity, ontogeny and function during heart development. Here, we show that the distribution and prevalence of resident macrophages in the subepicardial compartment of the developing heart coincides with the emergence of new lymphatics, and that macrophages interact closely with the nascent lymphatic capillaries. Consequently, global macrophage deficiency led to extensive vessel disruption, with mutant hearts exhibiting shortened and mis-patterned lymphatics. The origin of cardiac macrophages was linked to the yolk sac and foetal liver. Moreover, the *Cx3cr1*$^+$ myeloid lineage was found to play essential functions in the remodelling of the lymphatic endothelium. Mechanistically, macrophage hyaluronan was required for lymphatic sprouting by mediating direct macrophage-lymphatic endothelial cell interactions. Together, these findings reveal insight into the role of macrophages as indispensable mediators of lymphatic growth during the development of the mammalian cardiac vasculature.

KEY WORDS: Macrophages, Hyaluronan, Cell adhesion, Cardiac lymphatics, Coronaries, Vessel growth and patterning

INTRODUCTION

The cardiac vasculature, composed of the coronary circulation and lymphatic vessel network, begins to develop from around mid-gestation, at approximately embryonic day (E)11.5 in the mouse. Lymphatic endothelial cells (LECs) expressing the canonical lymphatic prospero homeobox 1 transcription factor (PROX1), vascular endothelial growth factor receptor 3 (VEGFR3) and lymphatic vessel endothelial hyaluronan receptor 1 (LYVE1), first arise in the vicinity of the sinus venosus (dorsal side) and outflow tract (ventral side) of the murine heart at ~E12.5 (Klotz et al., 2015). LECs then assemble into a primitive plexus that expands and remodels prenatally in the sub-epicardial layer along the base-to-apex axis and postnatally towards the myocardium, to form an extensive lymphatic system that drains lymph from the heart to enable optimal cardiac function (Flaht-Zabost et al., 2014; Klotz et al., 2015). Defects in lymphatic drainage are associated with heart disease, where an increase in tissue fluid content by as little as 2.5% can lead to a 30-40% reduction in cardiac output (Dongaonkar et al., 2010; Laine and Allen, 1991). Conversely, cardiac lymphatics respond to myocardial infarction by re-activating a lymphangiogenic gene expression programme; therapeutic stimulation of this process enhances resolution of macrophage-driven inflammation, promoting tissue repair (Klotz et al., 2015; Vieira et al., 2018). Together, these findings emphasize the importance of the cardiac lymphatic system and the need for a better understanding of the cellular and molecular mechanisms underlying its development.

The ontogeny of LECs integrating within the heart and other organ-based lymphatics has been the focus of a paradigm shift in recent times, with non-venous endothelial precursors now accepted as an additional source of the lineage (Eng et al., 2019; Ganez et al., 2019; Klotz et al., 2015; Martinez-Corral et al., 2015; Stanczuk et al., 2015; Stone and Stainier, 2019; Ulvmar and Mäkinen, 2016). The precise identity and origin of these non-venous LEC precursors remains somewhat elusive, although genetic lineage-tracing experiments have implicated the Tie2/PDGFB-negative transient embryonic haemogenic endothelium of the yolk sac and, more recently, second heart field-derived progenitors as contributing to cardiac lymphangiogenesis (Klotz et al., 2015; Lioux et al., 2020; Maruyama et al., 2019).

Macrophages are myeloid immune cells strategically dispersed throughout the tissues of the body. They have a vast functional repertoire and emerging plasticity that converges on normal homeostasis and responses to pathology, through mediating inflammation and repair. Macrophages were initially described in sites of physiological cell death within the bulbus cordis of embryonic chick and rat hearts, using light and electron microscopy (Manasek, 1969; Pexieder, 1975; Sorokin et al., 1994). Subsequently, *in vitro* experiments confirmed macrophages as phagocytic cells and, therefore, it was hypothesized that their primary role was to remove debris arising from cell death (Sorokin et al., 1994). Indeed, macrophages are specialized phagocytes with a

[1]Burdon-Sanderson Cardiac Science Centre, Department of Physiology, Anatomy and Genetics, University of Oxford, Oxford OX1 3PT, UK. [2]British Heart Foundation - Oxbridge Centre of Regenerative Medicine, CRM, University of Oxford, Oxford OX1 3PT, UK. [3]Department of Medicine Huddinge, Center for Hematology and Regenerative Medicine and Department of Cell and Molecular Biology, Karolinska Institutet, Stockholm SE-14186, Sweden. [4]Sir William Dunn School of Pathology, University of Oxford, Oxford OX1 3RE, UK. [5]MRC Human Immunology Unit, Weatherall Institute of Molecular Medicine, John Radcliffe Hospital, University of Oxford, Oxford OX3 9DS, UK. [6]Division of Cardiovascular Medicine, Radcliffe Department of Medicine, University of Oxford, Oxford OX3 9DU, UK.
*Present address: Cardiovascular Development Program, Centro Nacional de Investigaciones Cardiovasculares, CNIC, 28029 Madrid, Spain.
‡These authors contributed equally to this work
§These authors contributed equally to this work

¶Authors for correspondence (joaquim.vieira@dpag.ox.ac.uk; paul.riley@dpag.ox.ac.uk)

D.G.J., 0000-0002-4133-9364; J.M.V., 0000-0003-2023-6304; P.R.R., 0000-0002-9862-7332

Handling Editor: Benoit Bruneau
Received 30 June 2020; Accepted 26 December 2020

© 2021. Published by The Company of Biologists Ltd | Development (2021) 148, dev197525. doi:10.1242/dev.197525

RESEARCH ARTICLE

The extracellular matrix protein agrin is essential for epicardial epithelial-to-mesenchymal transition during heart development

Xin Sun[1,2], Sophia Malandraki-Miller[1,2], Tahnee Kennedy[1,2], Elad Bassat[3,*], Konstantinos Klaourakis[1,2], Jia Zhao[1,2,‡], Elisabetta Gamen[1,2], Joaquim Miguel Vieira[1,2], Eldad Tzahor[3] and Paul R. Riley[1,2,§]

ABSTRACT

During heart development, epicardial cells residing within the outer layer undergo epithelial-mesenchymal transition (EMT) and migrate into the underlying myocardium to support organ growth and morphogenesis. Disruption of epicardial EMT results in embryonic lethality, yet its regulation is poorly understood. Here, we report epicardial EMT within the mesothelial layer of the mouse embryonic heart at ultra-high resolution using scanning electron microscopy combined with immunofluorescence analyses. We identified morphologically active EMT regions that associated with key components of the extracellular matrix, including the basement membrane-associated proteoglycan agrin. Deletion of agrin resulted in impaired EMT and compromised development of the epicardium, accompanied by downregulation of Wilms' tumor 1. Agrin enhanced EMT in human embryonic stem cell-derived epicardial-like cells by decreasing β-catenin and promoting pFAK localization at focal adhesions, and promoted the aggregation of dystroglycan within the Golgi apparatus in murine epicardial cells. Loss of agrin resulted in dispersal of dystroglycan *in vivo*, disrupting basement membrane integrity and impairing EMT. Our results provide new insights into the role of the extracellular matrix in heart development and implicate agrin as a crucial regulator of epicardial EMT.

KEY WORDS: Epicardium, EMT, ECM, Agrin, Dystroglycan, Golgi apparatus, WT1, Mouse

INTRODUCTION

The formation and growth of the mouse embryonic heart is a highly dynamic process that includes heart tube elongation and looping, chamber septation and growth. Early specified cardiac progenitors in the linear heart tube rapidly proliferate and differentiate, followed by the incorporation of distinct progenitors from the second heart field to support the structure and function of the mature four-chambered heart (reviewed by Meilhac and Buckingham, 2018; Günthel et al., 2018). Other cell lineages, such as the epicardium, endocardium and neural crest, also contribute fibroblasts, endothelium and vascular smooth muscle to the developing heart (reviewed by von Gise and Pu, 2012; Meilhac and Buckingham, 2018). In addition, proper deposition and modification of the extracellular matrix (ECM) is required for effective attachment, migration and differentiation of the various cardiovascular cell types. However, the ECM has received comparatively less research-focus and, as a consequence, the molecular determinants regulating the interactions between distinct cell compartments and matrix in the embryonic heart remain poorly understood.

ECM is the protein scaffold that not only supports cell attachment but also acts as a reservoir for signaling molecules (reviewed by Hynes, 2009, 2014). The ECM dynamically interacts with cells to regulate their behavior and in turn cells feedback by modifying the matrix to adapt to their changing cell fate and condition the local environment. ECM mainly comprises extensive networks of collagen and laminin, with basement membrane attachments mediated by proteoglycans and glycoproteins (reviewed by Rozario and DeSimone, 2010; Bonnans et al., 2014; Hynes, 2014; Walma and Yamada, 2020). The importance of ECM in various physiological processes has been the focus of a number of previous studies (reviewed by Larsen et al., 2006; Neill et al., 2015). During heart development, the ECM has been implicated in several processes, such as mesendoderm cell fate decisions, trabeculation and valve formation (Cheng et al., 2013; del Monte-Nieto et al., 2018; Gunawan et al., 2019). Within the epicardium, the layer of mesothelial cells covering the outer surface of the myocardium, which is essential for heart development, ECM components have been reported to contribute to tertiary structures within the mesothelium and establish a stem cell-like niche (Balmer et al., 2014); however, besides maintaining structural integrity, regulatory roles for the ECM within the epicardium and more generally during heart development have not been studied to date.

In mouse, the epicardium is derived from the proepicardium (PE), which is a transient embryonic structure attached at the base of the venous inflow tract. At embryonic day (E) 9.5, PE cells migrate to cover the surface of the myocardium forming an outer cell layer by E11.5. A subset of epicardial cells undergo epithelial-to-mesenchymal transition (EMT) and invade the underlying myocardium, with epicardium-derived cells (EPDCs) then differentiating into multiple cardiovascular cell types, including fibroblasts and vascular smooth muscle cells, to support coronary vessel development and growth of the embryonic heart (reviewed by Riley, 2012; Simões and Riley, 2018; Cao and Poss, 2018). Disruption of epicardial development leads to mid-gestation lethality, with mutant mice exhibiting underdeveloped hearts (Yang et al., 1995; Kwee et al., 1995). For instance, loss of the

[1]Burdon-Sanderson Cardiac Science Centre, Department of Physiology, Anatomy and Genetics, University of Oxford, Oxford OX1 3PT, UK. [2]British Heart Foundation - Oxbridge Centre of Regenerative Medicine, CRM, University of Oxford, Oxford OX1 3PT, UK. [3]Department of Molecular Cell Biology, Weizmann Institute of Science, Rehovot 76100, Israel.
*Present address: Research Institute of Molecular Pathology, Vienna Biocenter, Campus-Vienna-Biocenter 1, 1030 Vienna, Austria. ‡Present address: Department of Cellular and Physiological Sciences, Life Science Institute, The University of British Columbia, 2350 Health Sciences Mall, RM.5320, Vancouver, BC, Canada, V6T 1Z3.

§Author for correspondence (paul.riley@dpag.ox.ac.uk)

P.R.R., 0000-0002-9862-7332

Handling Editor: Benoit Bruneau
Received 2 October 2020; Accepted 3 April 2021

Bibliography

1. Morfoisse, F. & Noel, A. Lymphatic and blood systems: Identical or fraternal twins? *International Journal of Biochemistry and Cell Biology* **114**, 1–10 (2019).

2. Potente, M. & Mäkinen, T. Vascular heterogeneity and specialization in development and disease. *Nature Reviews Molecular Cell Biology* **18**, 477–494 (2017).

3. Petrova, T. V. & Koh, G. Y. Organ-specific lymphatic vasculature: From development to pathophysiology. *Journal of Experimental Medicine* **215**, 35–49 (2018).

4. Zhang, F. *et al.* Lacteal junction zippering protects against diet-induced obesity. *Science (80-.).* **361**, 599–603 (2018).

5. Choe, K. *et al.* Intravital imaging of intestinal lacteals unveils lipid drainage through contractility. *J. Clin. Invest.* **125**, 4042–4052 (2015).

6. Gur-Cohen, S. *et al.* Stem cell-driven lymphatic remodeling coordinates tissue regeneration. *Science (80-.).* **366**, 1218–1225 (2019).

7. Peña-Jimenez, D. *et al.* Lymphatic vessels interact dynamically with the hair follicle stem cell niche during skin regeneration in vivo . *EMBO J.* **38**, (2019).

8. Rockson, S. G., Keeley, V., Kilbreath, S., Szuba, A. & Towers, A. Cancer-associated secondary lymphoedema. *Nature Reviews Disease Primers* **5**, (2019).

9. Jones, G. E. & Mansour, S. An approach to familial lymphoedema. *Clin. Med. J. R. Coll. Physicians London* **17**, 552–557 (2017).

10. Brouillard, P., Boon, L. & Vikkula, M. Genetics of lymphatic anomalies. *Journal of Clinical Investigation* **124**, 898–904 (2014).

11. Kalyanasundaram, R., Khatri, V. & Chauhan, N. Advances in Vaccine Development for Human Lymphatic Filariasis. *Trends in Parasitology* **36**, 195–205 (2020).

12. Oliver, G., Kipnis, J., Randolph, G. J. & Harvey, N. L. The Lymphatic Vasculature in the 21st Century: Novel Functional Roles in Homeostasis and Disease. *Cell* **182**, 270–296 (2020).

13. Petrova, T. V. & Koh, G. Y. *Biological functions of lymphatic vessels*. *Science* **369**, eaax4063 (American Association for the Advancement of Science, 2020).

14. Zhang, F., Zarkada, G., Yi, S. & Eichmann, A. Lymphatic Endothelial Cell Junctions: Molecular Regulation in Physiology and Diseases. *Front. Physiol.* **11**, 1–17 (2020).

15. Ducoli, L. & Detmar, M. Beyond PROX1: transcriptional, epigenetic, and noncoding RNA regulation of lymphatic identity and function. *Developmental Cell* **56**, 406–426 (2021).

16. Feng, X., Travisano, S., Pearson, C. A., Lien, C. L. & Harrison, M. R. M. The lymphatic system in zebrafish heart development, regeneration and disease modeling. *Journal of Cardiovascular Development and Disease* **8**, 1–14 (2021).

17. Jackson, D. G. Leucocyte trafficking via the lymphatic vasculature-mechanisms and consequences. *Frontiers in Immunology* **10**, 1–19 (2019).

18. Adamo, L., Rocha-Resende, C., Prabhu, S. D. & Mann, D. L. Reappraising the role of inflammation in heart failure. *Nature Reviews Cardiology* **17**, 269–285 (2020).

19. Klaourakis, K., Vieira, J. M. & Riley, P. R. The evolving cardiac lymphatic vasculature in development, repair and regeneration. *Nat. Rev. Cardiol.* doi:10.1038/s41569-020-00489-x

20. Moore, J. E. & Bertram, C. D. Lymphatic System Flows. *Annu. Rev. Fluid Mech.* **50**, 459–482 (2018).

21. Scallan, J. P., Zawieja, S. D., Castorena-Gonzalez, J. A. & Davis, M. J. Lymphatic pumping: mechanics, mechanisms and malfunction. *Journal of Physiology* **594**, 5749–5768 (2016).

22. Dongaonkar, R. M., Stewart, R. H., Geissler, H. J. & Laine, G. A. Myocardial microvascular permeability, interstitial oedema, and compromised cardiac function. *Cardiovascular*

Research **87**, 331–339 (2010).

23. Laine, G. A. & Allen, S. J. Left ventricular myocardial edema. Lymph flow, interstitial fibrosis, and cardiac function. *Circ. Res.* **68**, 1713–1721 (1991).

24. Ryan, T. J. Structure and function of lymphatics. *J. Invest. Dermatol.* **93**, 18S-24S (1989).

25. Ratajska, A. *et al.* Comparative and developmental anatomy of cardiac lymphatics. *The Scientific World Journal* **2014**, 1–9 (2014).

26. Johnson, R. A. & Blake, T. M. Lymphatics of the heart. *Circulation* **33**, 137–142 (1966).

27. Sacchi, G., Weber, E., Aglianò, M., Cavina, N. & Comparini, L. Lymphatic vessels of the human heart: Precollectors and collecting vessels. A morpho-structural study. *J. Submicrosc. Cytol. Pathol.* **31**, 515–525 (1999).

28. Böger, A. & Hort, W. Qualitative und quantitative Untersuchungen am Lymphgefäßsystem des Mäuseherzens. *Basic Res. Cardiol.* **72**, 510–529 (1977).

29. Marchetti, C., Poggi, P., Calligaro, A. & Casasco, A. Lymph vessels of the rabbit heart: Distribution and fine structure in atria. *Lymphology* **19**, 33–37 (1986).

30. Schmid-Schönbein, G. W. The second valve system in lymphatics. *Lymphatic research and biology* **1**, 25–31 (2003).

31. Bazigou, E., Wilson, J. T. & Moore, J. E. Primary and secondary lymphatic valve development: Molecular, functional and mechanical insights. *Microvascular Research* **96**, 38–45 (2014).

32. Trzewik, J. & Schmid-Schönbein, G. W. Evidence for a second valve system in lymphatics: Endothelial microvalves. in *American Society of Mechanical Engineers, Bioengineering Division (Publication) BED* **15**, 1711–1717 (2001).

33. Baluk, P. *et al.* Functionally specialized junctions between endothelial cells of lymphatic vessels. *J. Exp. Med.* **204**, 2349–2362 (2007).

34. Leak, L. V. & Burke, J. F. Ultrastructural studies on the lymphatic anchoring filaments. *J. Cell Biol.* **36**, 129–149 (1968).

35. Sacchi, G., Weber, E., Aglianò, M., Raffaelli, N. & Comparini, L. The structure of superficial lymphatics in the human thigh: Precollectors. *Anat. Rec.* **247**, 53–62 (1997).

36. Juszyński, M., Ciszek, B., Stachurska, E., Jabłońska, A. & Ratajska, A. Development of lymphatic vessels in mouse embryonic and early postnatal hearts. *Dev. Dyn.* **237**, 2973–2986 (2008).

37. Flaht-Zabost, A. *et al.* Cardiac Mouse Lymphatics: Developmental and Anatomical Update. *Anat. Rec.* **297**, 1115–1130 (2014).

38. Klotz, L. *et al.* Cardiac lymphatics are heterogeneous in origin and respond to injury. *Nature* **522**, 62–67 (2015).

39. Houssari, M. *et al.* Lymphatic and Immune Cell Cross-Talk Regulates Cardiac Recovery after Experimental Myocardial Infarction. *Arterioscler. Thromb. Vasc. Biol.* **40**, 1722–1737 (2020).

40. Eliska, O., Eliskova, M. & Miller, A. J. The absence of lymphatics in normal and atherosclerotic coronary arteries in man: A morphologic study. *Lymphology* **39**, 76–83 (2006).

41. Shimada, T., Morita, T., Oya, M. & Kitamura, H. Morphological Studies of the Cardiac Lymphatic System. *Arch. Histol. Cytol.* **53**, 115–126 (1990).

42. Schineis, P., Runge, P. & Halin, C. Cellular traffic through afferent lymphatic vessels. *Vascular Pharmacology* **112**, 31–41 (2019).

43. Jalkanen, S. & Salmi, M. Lymphatic endothelial cells of the lymph node. *Nature Reviews Immunology* **20**, 566–578 (2020).

44. Liao, S. & von der Weid, P. Y. Lymphatic system: An active pathway for immune protection.

Seminars in Cell and Developmental Biology **38**, 83–89 (2015).

45. Gray, E. E. & Cyster, J. G. *Lymph node macrophages*. *Journal of Innate Immunity* **4**, 424–436 (Karger Publishers, 2012).

46. Hunter, M. C., Teijeira, A. & Halin, C. T cell trafficking through lymphatic vessels. *Frontiers in Immunology* **7**, 1–14 (2016).

47. Mandl, J. N. *et al.* Quantification of lymph node transit times reveals differences in antigen surveillance strategies of naïve CD4+ and CD8+ T cells. *Proc. Natl. Acad. Sci. U. S. A.* **109**, 18036–18041 (2012).

48. Sathish Srinivasan, R. & Oliver, G. Prox1 dosage controls the number of lymphatic endothelial cell progenitors and the formation of the lymphovenous valves. *Genes Dev.* **25**, 2187–2197 (2011).

49. Hess, P. R. *et al.* Platelets mediate lymphovenous hemostasis to maintain blood-lymphatic separation throughout life. *J. Clin. Invest.* **124**, 273–284 (2014).

50. Turner, C. J., Badu-Nkansah, K., Crowley, D., van der Flier, A. & Hynes, R. O. Integrin-α5β1 is not required for mural cell functions during development of blood vessels but is required for lymphatic-blood vessel separation and lymphovenous valve formation. *Dev. Biol.* **392**, 381–392 (2014).

51. Geng, X. *et al.* Multiple mouse models of primary lymphedema exhibit distinct defects in lymphovenous valve development. *Dev. Biol.* **409**, 218–233 (2016).

52. Martinez-Corral, I. *et al.* Nonvenous origin of dermal lymphatic vasculature. *Circ. Res.* **116**, 1649–1654 (2015).

53. Stanczuk, L. *et al.* CKit lineage hemogenic endothelium-derived cells contribute to mesenteric lymphatic vessels. *Cell Rep.* **10**, 1708–1721 (2015).

54. Gancz, D. *et al.* Distinct origins and molecular mechanisms contribute to lymphatic formation during cardiac growth and regeneration. *Elife* **8**, 1–30 (2019).

55. Veikkola, T. *et al.* Signalling via vascular endothelial growth factor receptor-3 is sufficient for lymphangiogenesis in transgenic mice. *EMBO J.* **20**, 1223–1231 (2001).

56. Karkkainen, M. J. *et al.* Vascular endothelial growth factor C is required for sprouting of the first lymphatic vessels from embryonic veins. *Nat. Immunol.* **5**, 74–80 (2004).

57. Srinivasan, R. S. *et al.* Lineage tracing demonstrates the venous origin of the mammalian lymphatic vasculature. *Genes Dev.* **21**, 2422–2432 (2007).

58. Rutkowski, J. M., Boardman, K. C. & Swartz, M. A. Characterization of lymphangiogenesis in a model of adult skin regeneration. *Am. J. Physiol. - Hear. Circ. Physiol.* **291**, H1402–H1410 (2006).

59. Sabin, F. R. On the origin of the lymphatic system from the veins and the development of the lymph hearts and thoracic duct in the pig. *Am. J. Anat.* **1**, 367–389 (1902).

60. Huntington, G. S. & McClure, C. F. W. The anatomy and development of the jugular lymph sacs in the domestic cat (Felis domestica). *Am. J. Anat.* **10**, 177–312 (1910).

61. Stone, O. A. & Stainier, D. Y. R. Paraxial Mesoderm Is the Major Source of Lymphatic Endothelium. *Dev. Cell* **50**, 247-255.e3 (2019).

62. Stone, O. A., Zhou, B., Red-Horse, K. & Stainier, D. Y. R. Endothelial ontogeny and the establishment of vascular heterogeneity. *BioEssays* **43**, 2100036 (2021).

63. Hong, Y. K. & Detmar, M. Prox1, master regulator of the lymphatic vasculature phenotype. *Cell and Tissue Research* **314**, 85–92 (2003).

64. Wigle, J. T. *et al.* An essential role for Prox1 in the induction of the lymphatic endothelial cell phenotype. *EMBO J.* **21**, 1505–1513 (2002).

65. François, M. *et al.* Sox18 induces development of the lymphatic vasculature in mice. *Nature* **456**, 643–647 (2008).

66. Srinivasan, R. S. *et al.* The nuclear hormone receptor Coup-TFII is required for the initiation and early maintenance of Prox1 expression in lymphatic endothelial cells. *Genes Dev.* **24**, 696–707 (2010).

67. Johnson, N. C. *et al.* Lymphatic endothelial cell identity is reversible and its maintenance requires Prox1 activity. *Genes Dev.* **22**, 3282–3291 (2008).

68. Murtomaki, A. *et al.* Notch1 functions as a negative regulator of lymphatic endothelial cell differentiation in the venous endothelium. *Dev.* **140**, 2365–2376 (2012).

69. Irrthum, A. *et al.* Mutations in the transcription factor gene SOX18 underlie recessive and dominant forms of hypotrichosis-lymphedema-telangiectasia. *Am. J. Hum. Genet.* **72**, 1470–1478 (2003).

70. Tai-Nagara, I. *et al.* Blood and lymphatic systems are segregated by the FLCN tumor suppressor. *Nat. Commun.* **11**, 1–12 (2020).

71. Srinivasan, R. S. *et al.* The Prox1–Vegfr3 feedback loop maintains the identity and the number of lymphatic endothelial cell progenitors. *Genes Dev.* **28**, 2175–2187 (2014).

72. Wong, B. W. *et al.* The role of fatty acid β-oxidation in lymphangiogenesis. *Nature* **542**, 49–54 (2017).

73. Yu, P. *et al.* FGF-dependent metabolic control of vascular development. *Nature* **545**, 224–241 (2017).

74. Ma, W. *et al.* Mitochondrial respiration controls the Prox1-Vegfr3 feedback loop during lymphatic endothelial cell fate specification and maintenance. *Sci. Adv.* **7**, eabe7359 (2021).

75. Karkkainen, M. J. *et al.* Missense mutations interfere with VEGFR-3 signalling in primary

lymphoedema. *Nat. Genet.* **25**, 153–159 (2000).

76. Vieira, J. M. *et al.* The cardiac lymphatic system stimulates resolution of inflammation following myocardial infarction. *J. Clin. Invest.* **128**, 3402–3412 (2018).

77. Banerji, S. *et al.* LYVE-1, a new homologue of the CD44 glycoprotein, is a lymph-specific receptor for hyaluronan. *J. Cell Biol.* **144**, 789–801 (1999).

78. Gale, N. W. *et al.* Normal Lymphatic Development and Function in Mice Deficient for the Lymphatic Hyaluronan Receptor LYVE-1. *Mol. Cell. Biol.* **27**, 595–604 (2007).

79. Luong, M. X. *et al.* Lack of lymphatic vessel phenotype in LYVE-1/CD44 double knockout mice. *J. Cell. Physiol.* **219**, 430–437 (2009).

80. François, M. *et al.* Segmental territories along the cardinal veins generate lymph sacs via a ballooning mechanism during embryonic lymphangiogenesis in mice. *Dev. Biol.* **364**, 89–98 (2012).

81. Xu, Y. *et al.* Neuropilin-2 mediates VEGF-C-induced lymphatic sprouting together with VEGFR3. *J. Cell Biol.* **188**, 115–130 (2010).

82. Karpanen, T. *et al.* Functional interaction of VEGF-C and VEGF-D with neuropilin receptors. *FASEB J.* **20**, 1462–1472 (2006).

83. Yang, Y. *et al.* Lymphatic endothelial progenitors bud from the cardinal vein and intersomitic vessels in mammalian embryos. *Blood* **120**, 2340–2348 (2012).

84. Yao, L. C., Baluk, P., Srinivasan, R. S., Oliver, G. & McDonald, D. M. Plasticity of button-like junctions in the endothelium of airway lymphatics in development and inflammation. *Am. J. Pathol.* **180**, 2561–2575 (2012).

85. Janardhan, H. P. & Trivedi, C. M. Establishment and maintenance of blood–lymph separation. *Cellular and Molecular Life Sciences* **76**, 1865–1876 (2019).

86. Welsh, J. D., Kahn, M. L. & Sweet, D. T. Lymphovenous hemostasis and the role of platelets in regulating lymphatic flow and lymphatic vessel maturation. *Blood* **128**, 1169–1173 (2016).

87. Cha, B. *et al.* Complementary Wnt Sources Regulate Lymphatic Vascular Development via PROX1-Dependent Wnt/β-Catenin Signaling. *Cell Rep.* **25**, 571-584.e5 (2018).

88. Frye, M. *et al.* Matrix stiffness controls lymphatic vessel formation through regulation of a GATA2-dependent transcriptional program. *Nat. Commun.* **9**, (2018).

89. Riaj Mahamud, M. *et al.* GATA2 controls lymphatic endothelial cell junctional integrity and lymphovenous valve morphogenesis through MIR-126. *Dev.* **146**, (2019).

90. Kazenwadel, J. *et al.* GATA2 is required for lymphatic vessel valve development and maintenance. *J. Clin. Invest.* **125**, 2879–2994 (2015).

91. Petrova, T. V. *et al.* Defective valves and abnormal mural cell recruitment underlie lymphatic vascular failure in lymphedema distichiasis. *Nat. Med.* **10**, 974–981 (2004).

92. Sabine, A. *et al.* Mechanotransduction, PROX1, and FOXC2 Cooperate to Control Connexin37 and Calcineurin during Lymphatic-Valve Formation. *Dev. Cell* **22**, 430–445 (2012).

93. Sweet, D. T. *et al.* Lymph flow regulates collecting lymphatic vessel maturation in vivo. *J. Clin. Invest.* **125**, 2995–3007 (2015).

94. Sabine, A. *et al.* FOXC2 and fluid shear stress stabilize postnatal lymphatic vasculature. *J. Clin. Invest.* **125**, 3861–3877 (2015).

95. Hernández Vásquez, M. N. *et al.* Transcription factor FOXP2 is a flow-induced regulator of collecting lymphatic vessels. *EMBO J.* e107192 (2021). doi:10.15252/embj.2020107192

96. Yang, Y., Cha, B., Motawe, Z. Y., Srinivasan, R. S. & Scallan, J. P. VE-Cadherin Is Required for Lymphatic Valve Formation and Maintenance. *Cell Rep.* **28**, 2397-2412.e4 (2019).

97. Bazigou, E. *et al.* Integrin-α9 Is Required for Fibronectin Matrix Assembly during Lymphatic

Valve Morphogenesis. *Dev. Cell* **17**, 175–186 (2009).

98. Kanady, J. D., Dellinger, M. T., Munger, S. J., Witte, M. H. & Simon, A. M. Connexin37 and Connexin43 deficiencies in mice disrupt lymphatic valve development and result in lymphatic disorders including lymphedema and chylothorax. *Dev. Biol.* **354**, 253–266 (2011).

99. Pujol, F. *et al.* Dachsous1-Fat4 Signaling Controls Endothelial Cell Polarization during Lymphatic Valve Morphogenesis - Brief Report. *Arterioscler. Thromb. Vasc. Biol.* **37**, 1732–1735 (2017).

100. Betterman, K. L. *et al.* Atypical cadherin FAT4 orchestrates lymphatic endothelial cell polarity in response to flow. *J. Clin. Invest.* **130**, 3315–3328 (2020).

101. Finegold, D. N. *et al.* Truncating mutations in FOXC2 cause multiple lymphedema syndromes. *Hum. Mol. Genet.* **10**, 1185–1189 (2001).

102. Ostergaard, P. *et al.* Mutations in GATA2 cause primary lymphedema associated with a predisposition to acute myeloid leukemia (Emberger syndrome). *Nat. Genet.* **43**, 929–931 (2011).

103. Alders, M. *et al.* Hennekam syndrome can be caused by FAT4 mutations and be allelic to Van Maldergem syndrome. *Hum. Genet.* **133**, 1161–1167 (2014).

104. Yaniv, K. *et al.* Live imaging of lymphatic development in the zebrafish. *Nat. Med.* **12**, 711–716 (2006).

105. Bussmann, J. *et al.* Arteries provide essential guidance cues for lymphatic endothelial cells in the zebrafish trunk. *Development* **137**, 2653–2657 (2010).

106. Nicenboim, J. *et al.* Lymphatic vessels arise from specialized angioblasts within a venous niche. *Nature* **522**, 56–61 (2015).

107. Hogan, B. M. *et al.* Ccbe1 is required for embryonic lymphangiogenesis and venous

sprouting. *Nat. Genet.* **41**, 396–398 (2009).

108. Geudens, I. *et al.* Role of delta-like-4/notch in the formation and wiring of the lymphatic network in zebrafish. *Arterioscler. Thromb. Vasc. Biol.* **30**, 1695–1702 (2010).

109. Aranguren, X. L. *et al.* Transcription factor COUP-TFII is indispensable for venous and lymphatic development in zebrafish and Xenopus laevis. *Biochem. Biophys. Res. Commun.* **410**, 121–126 (2011).

110. van Impel, A. *et al.* Divergence of zebrafish and mouse lymphatic cell fate specification pathways. *Dev.* **141**, 1228–1238 (2014).

111. Cermenati, S. *et al.* Sox 18 and Sox7 play redundant roles in vascular development. *Blood* **111**, 2657–2666 (2008).

112. Herpers, R., Van De Kamp, E., Duckers, H. J. & Schulte-Merker, S. Redundant roles for sox7 and sox18 in arteriovenous specification in Zebrafish. *Circ. Res.* **102**, 12–15 (2008).

113. Pendeville, H. *et al.* Zebrafish Sox7 and Sox18 function together to control arterial-venous identity. *Dev. Biol.* **317**, 405–416 (2008).

114. Koltowska, K. *et al.* Vegfc Regulates Bipotential Precursor Division and Prox1 Expression to Promote Lymphatic Identity in Zebrafish. *Cell Rep.* **13**, 1828–1841 (2015).

115. Le Guen, L. *et al.* Ccbe1 regulates Vegfc-mediated induction of Vegfr3 signaling during embryonic lymphangiogenesis. *Dev.* **141**, 1239–1249 (2014).

116. Villefranc, J. A. *et al.* A truncation allele in vascular endothelial growth factor c reveals distinct modes of signaling during lymphatic and vascular development. *Dev.* **140**, 1497–1506 (2013).

117. Joukov, V. *et al.* Proteolytic processing regulates receptor specificity and activity of VEGF-C. *EMBO J.* **16**, 3898–3911 (1997).

118. Jeltsch, M. *et al.* CCBE1 enhances lymphangiogenesis via a disintegrin and metalloprotease with thrombospondin motifs-3-mediated vascular endothelial growth factor-C activation. *Circulation* **129**, 1962–1971 (2014).

119. Wang, G. *et al.* Specific fibroblast subpopulations and neuronal structures provide local sources of Vegfc-processing components during zebrafish lymphangiogenesis. *Nat. Commun.* **11**, 1–21 (2020).

120. Janssen, L. *et al.* ADAMTS3 activity is mandatory for embryonic lymphangiogenesis and regulates placental angiogenesis. *Angiogenesis* **19**, 53–65 (2016).

121. Brouillard, P. *et al.* Loss of ADAMTS3 activity causes Hennekam lymphangiectasia-lymphedema syndrome 3. *Hum. Mol. Genet.* **26**, 4095–4104 (2017).

122. Alders, M. *et al.* Mutations in CCBE1 cause generalized lymph vessel dysplasia in humans. *Nat. Genet.* **41**, 1272–1274 (2009).

123. Scheuerle, A. E. *et al.* An additional case of Hennekam lymphangiectasia–lymphedema syndrome caused by loss-of-function mutation in ADAMTS3. *Am. J. Med. Genet. Part A* **176**, 2858–2861 (2018).

124. Ducoli, L. *et al.* LETR1 is a lymphatic endothelial-specific lncRNA governing cell proliferation and migration through KLF4 and SEMA3C. *Nat. Commun.* **12**, 1–22 (2021).

125. Jung, H. M. *et al.* MicroRNA-mediated control of developmental lymphangiogenesis. *Elife* **8**, (2019).

126. Lioux, G. *et al.* A Second Heart Field-Derived Vasculogenic Niche Contributes to Cardiac Lymphatics. *Dev. Cell* **52**, 350-363.e6 (2020).

127. Maruyama, K., Miyagawa-Tomita, S., Mizukami, K., Matsuzaki, F. & Kurihara, H. Isl1-expressing non-venous cell lineage contributes to cardiac lymphatic vessel development.

Dev. Biol. **452**, 134–143 (2019).

128. Ulvmar, M. H., Martinez-Corral, I., Stanczuk, L. & Mäkinen, T. Pdgfrb-Cre targets lymphatic endothelial cells of both venous and non-venous origins. *Genesis* **54**, 350–358 (2016).

129. Eng, T. C. *et al.* Zebrafish facial lymphatics develop through sequential addition of venous and non-venous progenitors. *EMBO Rep.* **20**, 1–17 (2019).

130. Okuda, K. S. *et al.* Lyve1 expression reveals novel lymphatic vessels and new mechanisms for lymphatic vessel development in zebrafish. *Dev.* **139**, 2381–2391 (2012).

131. Harrison, M. R. *et al.* Late developing cardiac lymphatic vasculature supports adult zebrafish heart function and regeneration. *Elife* **8**, 1–21 (2019).

132. Vivien, C. J. *et al.* Vegfc/d-dependent regulation of the lymphatic vasculature during cardiac regeneration is influenced by injury context. *npj Regen. Med.* **4**, 1–18 (2019).

133. Williams, J. W., Giannarelli, C., Rahman, A., Randolph, G. J. & Kovacic, J. C. Macrophage Biology, Classification, and Phenotype in Cardiovascular Disease: JACC Macrophage in CVD Series (Part 1). *Journal of the American College of Cardiology* **72**, 2166–2180 (2018).

134. Palis, J., Robertson, S., Kennedy, M., Wall, C. & Keller, G. Development of erythroid and myeloid progenitors in the yolk sac and embryo proper of the mouse. *Development* **126**, 5073–5084 (1999).

135. Samokhvalov, I. M., Samokhvalova, N. I. & Nishikawa, S. I. Cell tracing shows the contribution of the yolk sac to adult haematopoiesis. *Nature* **446**, 1056–1061 (2007).

136. Mass, E. *et al.* Specification of tissue-resident macrophages during organogenesis. *Science (80-.).* **353**, (2016).

137. Stremmel, C. *et al.* Yolk sac macrophage progenitors traffic to the embryo during defined stages of development. *Nat. Commun.* **9**, (2018).

138. Epelman, S. *et al.* Embryonic and adult-derived resident cardiac macrophages are maintained through distinct mechanisms at steady state and during inflammation. *Immunity* **40**, 91–104 (2014).

139. Pinto, A. R. *et al.* Revisiting cardiac cellular composition. *Circ. Res.* **118**, 400–409 (2016).

140. Lavine, K. J. *et al.* Distinct macrophage lineages contribute to disparate patterns of cardiac recovery and remodeling in the neonatal and adult heart. *Proc. Natl. Acad. Sci. U. S. A.* **111**, 16029–16034 (2014).

141. Skelly, D. A. *et al.* Single-Cell Transcriptional Profiling Reveals Cellular Diversity and Intercommunication in the Mouse Heart. *Cell Rep.* **22**, 600–610 (2018).

142. Molawi, K. *et al.* Progressive replacement of embryo-derived cardiac macrophages with age. *J. Exp. Med.* **211**, 2151–2158 (2014).

143. Heidt, T. *et al.* Differential contribution of monocytes to heart macrophages in steady-state and after myocardial infarction. *Circ. Res.* **115**, 284–295 (2014).

144. Leid, J. *et al.* Primitive Embryonic Macrophages are Required for Coronary Development and Maturation. *Circ. Res.* **118**, 1498–1511 (2016).

145. Cahill, T. J. *et al.* Tissue-resident macrophages regulate lymphatic vessel growth and patterning in the developing heart. *Development* **148**, (2021).

146. Gula, G. *et al.* Potential functions of embryonic cardiac macrophages in angiogenesis, lymphangiogenesis and extracellular matrix remodeling. *Histochem. Cell Biol.* **155**, 117–132 (2021).

147. Hulsmans, M. *et al.* Macrophages Facilitate Electrical Conduction in the Heart. *Cell* **169**, 510-522.e20 (2017).

148. Frangogiannis, N. G. Pathophysiology of myocardial infarction. *Compr. Physiol.* **5**, 1841–

1875 (2015).

149. Price, E. L., Vieira, J. M. & Riley, P. R. Model organisms at the heart of regeneration. *DMM Disease Models and Mechanisms* **12**, 1–11 (2019).

150. Sam, F. *et al.* Progressive left ventricular remodeling and apoptosis late after myocardial infarction in mouse heart. *Am. J. Physiol. - Hear. Circ. Physiol.* **279**, H422–H428 (2000).

151. Weis, S. *et al.* Src blockade stabilizes a Flk/cadherin complex, reducing edema and tissue injury following myocardial infarction. *J. Clin. Invest.* **113**, 885–894 (2004).

152. Henri, O. *et al.* Selective Stimulation of Cardiac Lymphangiogenesis Reduces Myocardial Edema and Fibrosis Leading to Improved Cardiac Function Following Myocardial Infarction. *Circulation* **133**, 1484–1497 (2016).

153. Weber, K. T. *et al.* Fibrillar collagen and remodeling of dilated canine left ventricle. *Circulation* **82**, 1387–1401 (1990).

154. Van Amerongen, M. J., Harmsen, M. C., Van Rooijen, N., Petersen, A. H. & Van Luyn, M. J. A. Macrophage depletion impairs wound healing and increases left ventricular remodeling after myocardial injury in mice. *Am. J. Pathol.* **170**, 818–829 (2007).

155. Frantz, S. *et al.* Monocytes/macrophages prevent healing defects and left ventricular thrombus formation after myocardial infarction. *FASEB J.* **27**, 871–881 (2013).

156. Nahrendorf, M. *et al.* The healing myocardium sequentially mobilizes two monocyte subsets with divergent and complementary functions. *J. Exp. Med.* **204**, 3037–3047 (2007).

157. Taira, A. *et al.* Flow Velocity of Cardiac Lymph and Contractility of the Heart: An Experimental Study. *Ann. Thorac. Surg.* **23**, 230–234 (1977).

158. Mehlhorn, U., Geissler, H. J., Laine, G. A. & Allen, S. J. Myocardial fluid balance. *European Journal of Cardio-thoracic Surgery* **20**, 1220–1230 (2001).

159. Allen, S. J. *et al.* Augmenting cardiac contractility hastens myocardial edema resolution after cardiopulmonary bypass and cardioplegic arrest. *Anesth. Analg.* **85**, 987–992 (1997).

160. Geissler, H. *et al.* Impact of cardiopulmonary bypass and cardioplegic arrest on myocardial efficiency. *Crit. Care* **3**, 1–14 (1999).

161. Lugrin, J., Parapanov, R., Krueger, T. & Liaudet, L. Murine myocardial infarction model using permanent ligation of left anterior descending coronary artery. *J. Vis. Exp.* **150**, 1–7 (2019).

162. DeBerge, M. *et al.* Efferocytosis and outside-in signaling by cardiac phagocytes. Links to repair, cellular programming, and intercellular crosstalk in heart. *Frontiers in Immunology* **8**, 1–21 (2017).

163. Yan, X. *et al.* Temporal dynamics of cardiac immune cell accumulation following acute myocardial infarction. *J. Mol. Cell. Cardiol.* **62**, 24–35 (2013).

164. Bajpai, G. *et al.* Tissue Resident CCR2- and CCR2+ Cardiac Macrophages Differentially Orchestrate Monocyte Recruitment and Fate Specification Following Myocardial Injury. *Circ. Res.* **124**, 263–278 (2019).

165. Dick, S. A. *et al.* Self-renewing resident cardiac macrophages limit adverse remodeling following myocardial infarction. *Nat. Immunol.* **20**, 29–39 (2019).

166. Simões, F. C. *et al.* Macrophages directly contribute collagen to scar formation during zebrafish heart regeneration and mouse heart repair. *Nat. Commun.* **11**, 1–17 (2020).

167. Bajpai, G. *et al.* The human heart contains distinct macrophage subsets with divergent origins and functions. *Nat. Med.* **24**, 1234–1245 (2018).

168. Tang, T. T. *et al.* Regulatory T cells ameliorate cardiac remodeling after myocardial infarction. *Basic Res. Cardiol.* **107**, 1–17 (2012).

169. Matsumoto, K. *et al.* Regulatory T lymphocytes attenuate myocardial infarction-induced

ventricular remodeling in mice. *Int. Heart J.* **52**, 382–387 (2011).

170. Hofmann, U. *et al.* Activation of CD4 + T lymphocytes improves wound healing and survival after experimental myocardial infarction in mice. *Circulation* **125**, 1652–1663 (2012).

171. Tae Yu, H. *et al.* Characterization of CD8+ CD57+ T cells in patients with acute myocardial infarction. *Cell. Mol. Immunol.* **12**, 466–473 (2015).

172. Jackson, D. G. *Hyaluronan in the lymphatics: The key role of the hyaluronan receptor LYVE-1 in leucocyte trafficking*. *Matrix Biology* **78**–**79**, 219–235 (Elsevier, 2019).

173. Lawrance, W., Banerji, S., Day, A. J., Bhattacharjee, S. & Jackson, D. G. Binding of hyaluronan to the native lymphatic vessel endothelial receptor LYVE-1 is critically dependent on receptor clustering and hyaluronan organization. *J. Biol. Chem.* **291**, 8014–8030 (2016).

174. Johnson, L. A. *et al.* Dendritic cells enter lymph vessels by hyaluronan-mediated docking to the endothelial receptor LYVE-1. *Nat. Immunol.* **18**, 762–770 (2017).

175. Vuorio, T. *et al.* Downregulation of VEGFR3 signaling alters cardiac lymphatic vessel organization and leads to a higher mortality after acute myocardial infarction. *Sci. Rep.* **8**, 1–13 (2018).

176. IV, T. C. S. K. *et al.* Genetic blockade of lymphangiogenesis does not impair cardiac function after myocardial infarction. *J. Clin. Invest.* (2021). doi:10.1172/JCI147070

177. Zhao, T. *et al.* VEGF-C/VEGFR-3 pathway promotes myocyte hypertrophy and survival in the infarcted myocardium. *Am. J. Transl. Res.* **7**, 697–709 (2015).

178. Zhao, T. *et al.* Differential expression of vascular endothelial growth factor isoforms and receptor subtypes in the infarcted heart. *Int. J. Cardiol.* **167**, 2638–2645 (2013).

179. Trincot, C. E. *et al.* Adrenomedullin Induces Cardiac Lymphangiogenesis after Myocardial Infarction and Regulates Cardiac Edema Via Connexin 43. *Circ. Res.* **124**, 101–113 (2019).

180. Reddy, K. Recent advances in the diagnosis and treatment of acute myocardial infarction. *World J. Cardiol.* **7**, 243–276 (2015).

181. Orlic, D. *et al.* Bone marrow cells regenerate infarcted myocardium. *Nature* **410**, 701–705 (2001).

182. Beltrami, A. P. *et al.* Adult cardiac stem cells are multipotent and support myocardial regeneration. *Cell* **114**, 763–776 (2003).

183. Eschenhagen, T. *et al.* Cardiomyocyte regeneration: A consensus statement. *Circulation* **136**, 680–686 (2017).

184. Quyyumi, A. A. *et al.* PreSERVE-AMI: A Randomized, Double-Blind, Placebo-Controlled Clinical Trial of Intracoronary Administration of Autologous CD34+ Cells in Patients with Left Ventricular Dysfunction Post STEMI. *Circ. Res.* **120**, 324–331 (2017).

185. Tompkins, B. A. *et al.* Preclinical Studies of Stem Cell Therapy for Heart Disease. *Circ. Res.* **122**, 1006–1020 (2018).

186. Vagnozzi, R. J. *et al.* An acute immune response underlies the benefit of cardiac stem cell therapy. *Nature* **577**, 405–409 (2020).

187. Chung, E. S., Packer, M., Lo, K. H., Fasanmade, A. A. & Willerson, J. T. Randomized, double-blind, placebo-controlled, pilot trial of infliximab, a chimeric monoclonal antibody to tumor necrosis factor-α, in patients with moderate-to-severe heart failure: Results of the anti-TNF therapy against congestive heart failure (ATTACH. *Circulation* **107**, 3133–3140 (2003).

188. Roberts, R., DeMello, V. & Sobel, B. E. Deleterious effects of methylprednisolone in patients with myocardial infarction. *Circulation* **53**, I204-6 (1976).

189. Hartikainen, J. *et al.* Adenoviral intramyocardial VEGF-DDNDC gene transfer increasesmyocardial perfusion reserve in refractory angina patients: A phase I/IIa study with

1-year follow-up. *Eur. Heart J.* **38**, 2547–2555 (2017).

190. Kataoka, Y. *et al.* The first clinical pilot study of intravenous adrenomedullin administration in patients with acute myocardial infarction. *J. Cardiovasc. Pharmacol.* **56**, 413–419 (2010).

191. Tatin, F. *et al.* Apelin modulates pathological remodeling of lymphatic endothelium after myocardial infarction. *JCI insight* **2**, 1–16 (2017).

192. Poss, K. D., Wilson, L. G. & Keating, M. T. Heart regeneration in zebrafish. *Science (80-.).* **298**, 2188–2190 (2002).

193. González-Rosa, J. M., Martín, V., Peralta, M., Torres, M. & Mercader, N. Extensive scar formation and regression during heart regeneration after cryoinjury in zebrafish. *Development* **138**, 1663–1674 (2011).

194. Lam, N. T. & Sadek, H. A. Neonatal heart regeneration comprehensive literature review. *Circulation* **138**, 421–423 (2018).

195. Porrello, E. R. *et al.* Transient regenerative potential of the neonatal mouse heart. *Science (80-.).* **331**, 1078–1080 (2011).

196. Wang, H. *et al.* Natural Heart Regeneration in a Neonatal Rat Myocardial Infarction Model. *Cells* **9**, 1–20 (2020).

197. Ye, L. *et al.* Early regenerative capacity in the porcine heart. *Circulation* **138**, 2798–2808 (2018).

198. Sereti, K. I. *et al.* Analysis of cardiomyocyte clonal expansion during mouse heart development and injury. *Nat. Commun.* **9**, 1–13 (2018).

199. Gunadasa-Rohling, M. *et al.* Magnetic Resonance Imaging of the Regenerating Neonatal Mouse Heart. *Circulation* **138**, 2439–2441 (2018).

200. Porrello, E. R. *et al.* Regulation of neonatal and adult mammalian heart regeneration by the

miR-15 family. *Proc. Natl. Acad. Sci. U. S. A.* **110**, 187–192 (2013).

201. Notari, M. *et al.* The local microenvironment limits the regenerative potential of the mouse neonatal heart. *Sci. Adv.* **4**, eaao5553 (2018).

202. Saker, D. M., Walsh-Sukys, M., Spector, M. & Zahka, K. G. Cardiac recovery and survival after neonatal myocardial infarction. *Pediatr. Cardiol.* **18**, 139–142 (1997).

203. Haubner, B. J. *et al.* Functional Recovery of a Human Neonatal Heart after Severe Myocardial Infarction. *Circ. Res.* **118**, 216–221 (2016).

204. Salimova, E. *et al.* Variable outcomes of human heart attack recapitulated in genetically diverse mice. *npj Regen. Med.* **4**, (2019).

205. Wang, Z. *et al.* Mechanistic basis of neonatal heart regeneration revealed by transcriptome and histone modification profiling. *Proc. Natl. Acad. Sci. U. S. A.* **116**, 18455–18465 (2019).

206. Naqvi, N. *et al.* A proliferative burst during preadolescence establishes the final cardiomyocyte number. *Cell* **157**, 795–807 (2014).

207. Alkass, K. *et al.* No Evidence for Cardiomyocyte Number Expansion in Preadolescent Mice. *Cell* **163**, 1026–1036 (2015).

208. Tian, X. *et al.* De novo formation of a distinct coronary vascular population in neonatal heart. *Science (80-.).* **345**, 90–94 (2014).

209. Sattler, S. & Rosenthal, N. The neonate versus adult mammalian immune system in cardiac repair and regeneration. *Biochim. Biophys. Acta - Mol. Cell Res.* **1863**, 1813–1821 (2016).

210. Aurora, A. B. *et al.* Macrophages are required for neonatal heart regeneration. *J. Clin. Invest.* **124**, 1382–1392 (2014).

211. Du Cheyne, C., Tay, H. & De Spiegelaere, W. The complex TIE between macrophages and angiogenesis. in *Journal of Veterinary Medicine Series C: Anatomia Histologia Embryologia*

49, 585–596 (2020).

212. van Rooijen, N. & Hendrikx, E. Liposomes for specific depletion of macrophages from organs and tissues. *Methods Mol. Biol.* **605**, 189–203 (2010).

213. Ferenbach, D. A. *et al.* Macrophage/monocyte depletion by clodronate, but not diphtheria toxin, improves renal ischemia/reperfusion injury in mice. *Kidney Int.* **82**, 928–933 (2012).

214. Iqbal, A. J. *et al.* Human CD68 promoter GFP transgenic mice allow analysis of monocyte to macrophage differentiation in vivo. *Blood* **124**, e33–e44 (2014).

215. Iwano, T., Masuda, A., Kiyonari, H., Enomoto, H. & Matsuzaki, F. Prox1 postmitotically defines dentate gyrus cells by specifying granule cell identity over CA3 pyramidal cell fate in the hippocampus. **139**, 3051–3062 (2012).

216. Pham, T. H. M. *et al.* Lymphatic endothelial cell sphingosine kinase activity is required for lymphocyte egress and lymphatic patterning. *J. Exp. Med.* **207**, 17–27 (2010).

217. Truman, L. A. *et al.* ProxTom lymphatic vessel reporter mice reveal Prox1 expression in the adrenal medulla, megakaryocytes, and platelets. *Am. J. Pathol.* **180**, 1715–1725 (2012).

218. Miquerol, L. *et al.* Architectural and functional asymmetry of the His-Purkinje system of the murine heart. *Cardiovasc. Res.* **63**, 77–86 (2004).

219. Dumont, D. J. *et al.* Cardiovascular failure in mouse embryos deficient in VEGF receptor-3. *Science (80-.).* **282**, 946–949 (1998).

220. De Villiers, C. & Riley, P. R. A Refined Protocol for Coronary Artery Ligation in the Neonatal Mouse. *Curr. Protoc.* **1**, e66 (2021).

221. Livak, K. J. & Schmittgen, T. D. Analysis of relative gene expression data using real-time quantitative PCR and the 2-ΔΔCT method. *Methods* **25**, 402–408 (2001).

222. Ruiz-Villalba, A. *et al.* Reference genes for gene expression studies in the mouse heart. *Sci.*

Rep. **7**, 1–9 (2017).

223. Zudaire, E., Gambardella, L., Kurcz, C. & Vermeren, S. A Computational Tool for Quantitative Analysis of Vascular Networks. *PLoS One* **6**, e27385 (2011).

224. Schindelin, J. *et al.* Fiji: An open-source platform for biological-image analysis. *Nature Methods* **9**, 676–682 (2012).

225. Rueden, C. T. *et al.* ImageJ2: ImageJ for the next generation of scientific image data. *BMC Bioinformatics* **18**, 529 (2017).

226. Pinto, A. R., Chandran, A., Rosenthal, N. A. & Godwin, J. W. Isolation and analysis of single cells from the mouse heart. *J. Immunol. Methods* **393**, 74–80 (2013).

227. Liu, X. & Quan, N. Immune Cell Isolation from Mouse Femur Bone Marrow. *BIO-PROTOCOL* **5**, (2015).

228. Stuckey, D. J., Carr, C. A., Tyler, D. J., Aasum, E. & Clarke, K. Novel MRI method to detect altered left ventricular ejection and filling patterns in rodent models of disease. *Magn. Reson. Med.* **60**, 582–587 (2008).

229. Hao, Y. *et al.* Integrated analysis of multimodal single-cell data Graphical abstract. (2021). doi:10.1016/j.cell.2021.04.048

230. Stuart, T. *et al.* Comprehensive Integration of Single-Cell Data Resource Comprehensive Integration of Single-Cell Data. *Cell* **177**, 1888-1902.e21 (2019).

231. Wang, Z. *et al.* Cell-Type-Specific Gene Regulatory Networks Underlying Murine Neonatal Heart Regeneration at Single-Cell Resolution. *Cell Rep.* **33**, 108472 (2020).

232. Bradham, R. R. & Parker, E. F. *COLLECTIVE REVIEW The Cardiac Lymphatics THE ANNALS OF THORACIC SURGERY*. **15**,

233. Wigle, J. T. & Oliver, G. Prox1 function is required for the development of the murine

lymphatic system. *Cell* **98**, 769–778 (1999).

234. Flaht, A. *et al.* Cellular phenotypes and spatio-temporal patterns of lymphatic vessel development in embryonic mouse hearts. *Dev. Dyn.* **241**, 1473–1486 (2012).

235. Pflicke, H. & Sixt, M. Preformed portals facilitate dendritic cell entry into afferent lymphatic vessels. *J. Exp. Med.* **206**, 2925–2935 (2009).

236. Li, F., Wang, X., Capasso, J. M. & Gerdes, A. M. Rapid transition of cardiac myocytes from hyperplasia to hypertrophy during postnatal development. *J. Mol. Cell. Cardiol.* **28**, 1737–1746 (1996).

237. Soonpaa, M. H., Kim, K. K., Pajak, L., Franklin, M. & Field, L. J. Cardiomyocyte DNA synthesis and binucleation during murine development. *Am. J. Physiol. - Hear. Circ. Physiol.* **271**, (1996).

238. Walsh, S., Pontén, A., Fleischmann, B. K. & Jovinge, S. Cardiomyocyte cell cycle control and growth estimation in vivo-An analysis based on cardiomyocyte nuclei. *Cardiovasc. Res.* **86**, 365–373 (2010).

239. Gordon, E. J., Gale, N. W. & Harvey, N. L. Expression of the hyaluronan receptor LYVE-1 is not restricted to the lymphatic vasculature; LYVE-1 is also expressed on embryonic blood vessels. *Dev. Dyn.* **237**, 1901–1909 (2008).

240. Lee, H. W. *et al.* Expression of lymphatic endothelium-specific hyaluronan receptor LYVE-1 in the developing mouse kidney. *Cell Tissue Res.* **343**, 429–444 (2011).

241. Mahtab, E. A. F. *et al.* Cardiac malformations and myocardial abnormalities in Podoplanin knockout mouse embryos: Correlation with abnormal epicardial development. *Dev. Dyn.* **237**, 847–857 (2008).

242. Yuan, L. *et al. Abnormal lymphatic vessel development in neuropilin 2 mutant mice*.

Development **129**, (The Company of Biologists, 2002).

243. Maden, C. H. *et al.* NRP1 and NRP2 cooperate to regulate gangliogenesis, axon guidance and target innervation in the sympathetic nervous system. *Dev. Biol.* **369**, 277–285 (2012).

244. Kaipatnen, A. *et al. Expression of the fms-like tyrosine kinase 4 gene becomes restricted to lymphatic endothelium during development*. *Medical Sciences* **92**, (1995).

245. Russo, E. *et al.* Intralymphatic CCL21 Promotes Tissue Egress of Dendritic Cells through Afferent Lymphatic Vessels. *Cell Rep.* **14**, 1723–1734 (2016).

246. Johnson, L. A. & Jackson, D. G. Inflammation-induced secretion of CCL21 in lymphatic endothelium is a key regulator of integrinmediated dendritic cell transmigration. *Int. Immunol.* **22**, 839–849 (2010).

247. Weber, M. *et al.* Interstitial dendritic cell guidance by haptotactic chemokine gradients. *Science (80-.).* **339**, 328–332 (2013).

248. Stevens, S. M., von Gise, A., VanDusen, N., Zhou, B. & Pu, W. T. Epicardium is required for cardiac seeding by yolk sac macrophages, precursors of resident macrophages of the adult heart. *Dev. Biol.* **413**, 153–159 (2016).

249. Gancz, D., Perlmoter, G. & Yaniv, K. Formation and growth of cardiac lymphatics during embryonic development, heart regeneration, and disease. *Cold Spring Harb. Perspect. Biol.* **12**, 1–18 (2020).

250. Laube, F., Heister, M., Scholz, C., Borchardt, T. & Braun, T. Re-programming of newt cardiomyocytes is induced by tissue regeneration. *J. Cell Sci.* **119**, 4719–4729 (2006).

251. Witman, N., Murtuza, B., Davis, B., Arner, A. & Morrison, J. I. Recapitulation of developmental cardiogenesis governs the morphological and functional regeneration of adult newt hearts following injury. *Dev. Biol.* **354**, 67–76 (2011).

252. E, B. & MA, P. Ventricular enlargement and remodeling following acute myocardial infarction: mechanisms and management. *Am. J. Cardiol.* **68**, 1–6 (1991).

253. MA, P. & E, B. Ventricular remodeling after myocardial infarction. Experimental observations and clinical implications. *Circulation* **81**, 1161–1172 (1990).

254. MG, S. & N, S. Left ventricular remodeling after myocardial infarction: pathophysiology and therapy. *Circulation* **101**, 2981–2988 (2000).

255. HG, Z., AM, G., S, L. & G, M. Changes in heart function and cardiac cell size in rats with chronic myocardial infarction. *J. Mol. Cell. Cardiol.* **22**, 1231–1243 (1990).

256. Kalucka, J. *et al.* Single-Cell Transcriptome Atlas of Murine Endothelial Cells. *Cell* **180**, 764-779.e20 (2020).

257. Louie, D. A. P. & Liao, S. Lymph Node Subcapsular Sinus Macrophages as the Frontline of Lymphatic Immune Defense. *Front. Immunol.* **10**, 347 (2019).

258. Beauvillain, C. *et al.* CCR7 is involved in the migration of neutrophils to lymph nodes. *Blood* **117**, 1196–1204 (2011).

259. Xuan, W., Qu, Q., Zheng, B., Xiong, S. & Fan, G.-H. The chemotaxis of M1 and M2 macrophages is regulated by different chemokines. *J. Leukoc. Biol.* **97**, 61–69 (2015).

260. He, L., Tian, X., Zhang, H., Wythe, J. D. & Zhou, B. Fabp4-CreER lineage tracing revealstwo distinctive coronary vascular populations. *J. Cell. Mol. Med.* **18**, 2152–2156 (2014).

261. Payne, S. *et al.* Regulatory pathways governing murine coronary vessel formation are dysregulated in the injured adult heart. **10**, 1–19 (2019).

262. Wu, B. *et al.* Endocardial Cells Form the Coronary Arteries by Angiogenesis through Myocardial-Endocardial VEGF Signaling. *Cell* **151**, 1083–1096 (2012).

263. Pinto, A. R. *et al.* Age-related changes in tissue macrophages precede cardiac functional

impairment. *Aging (Albany. NY).* **6**, 399–413 (2014).

264. Hilgendorf, I. *et al.* Ly-6Chigh Monocytes Depend on Nr4a1 to Balance Both Inflammatory and Reparative Phases in the Infarcted Myocardium. *Circ. Res.* **114**, 1611–1622 (2014).

265. Orecchioni, M., Ghosheh, Y., Pramod, A. B. & Ley, K. Macrophage Polarization: Different Gene Signatures in M1(LPS+) vs. Classically and M2(LPS–) vs. Alternatively Activated Macrophages. *Front. Immunol.* **0**, 1084 (2019).

266. Nahrendorf, M. & Swirski, F. K. Abandoning M1/M2 for a Network Model of Macrophage Function. *Circ. Res.* **119**, 414 (2016).

267. Jablonski, K. A. *et al.* Novel Markers to Delineate Murine M1 and M2 Macrophages. *PLoS One* **10**, e0145342 (2015).

268. Farbehi, N. *et al.* Single-cell expression profiling reveals dynamic flux of cardiac stromal, vascular and immune cells in health and injury. *Elife* **8**, (2019).

269. Liu, X. *et al.* Lymphoangiocrine signals promote cardiac growth and repair. **588**, 705–711 (2020).

270. Wang, Y. *et al.* Ephrin-B2 controls VEGF-induced angiogenesis and lymphangiogenesis. *Nat. 2010 4657297* **465**, 483–486 (2010).

271. NW, G. *et al.* Angiopoietin-2 is required for postnatal angiogenesis and lymphatic patterning, and only the latter role is rescued by Angiopoietin-1. *Dev. Cell* **3**, 411–423 (2002).

272. PC, M. *et al.* Angiopoietin-2, a natural antagonist for Tie2 that disrupts in vivo angiogenesis. *Science* **277**, 55–60 (1997).

273. K, T.-K. *et al.* Biological action of angiopoietin-2 in a fibrin matrix model of angiogenesis is associated with activation of Tie2. *Cardiovasc. Res.* **49**, 659–670 (2001).

274. H, S. Immunohistochemical demonstration of Angiopoietin-2 in lymphatic vascular

development. *Histochem. Cell Biol.* **131**, 231–238 (2009).

275. Boyer, N. P. & Gupton, S. L. Revisiting Netrin-1: One Who Guides (Axons). *Front. Cell. Neurosci.* **12**, 221 (2018).

276. A, I., A, R., E, T., JZ, K. & M, S. Structural and functional aberrations in the cerebral cortex of tenascin-C deficient mice. *Cereb. Cortex* **15**, 950–962 (2005).

277. Koncina, E., Roth, L., Gonthier, B. & Bagnard, D. Role of semaphorins during axon growth and guidance. *Advances in Experimental Medicine and Biology* **621**, 50–64 (2007).

278. Avraamides, C. J., Garmy-Susini, B. & Varner, J. A. Integrins in angiogenesis and lymphangiogenesis. *Nat. Rev. Cancer 2008 88* **8**, 604–617 (2008).

279. Huang, X. Z. *et al.* Fatal Bilateral Chylothorax in Mice Lacking the Integrin α9β1. *Mol. Cell. Biol.* **20**, 5208 (2000).

280. BL, B., H, R., D, C. & RO, H. Extensive vasculogenesis, angiogenesis, and organogenesis precede lethality in mice lacking all alpha v integrins. *Cell* **95**, 507–519 (1998).

281. TR, C., H, H., R, B., YH, K. & RA, W. Cell-autonomous requirement for beta1 integrin in endothelial cell adhesion, migration and survival during angiogenesis in mice. *Development* **135**, 2193–2202 (2008).

282. Alghamdi, A. A. A. *et al.* NRP2 as an Emerging Angiogenic Player; Promoting Endothelial Cell Adhesion and Migration by Regulating Recycling of α5 Integrin. *Front. Cell Dev. Biol.* **8**, 395 (2020).

283. Johnson, L. A., Banerji, S., Lagerholm, B. C. & Jackson, D. G. Dendritic cell entry to lymphatic capillaries is orchestrated by CD44 and the hyaluronan glycocalyx. *Life Sci. Alliance* **4**, (2021).

284. P, B.-K. *et al.* Podoplanin-Expressing Macrophages Promote Lymphangiogenesis and Lymphoinvasion in Breast Cancer. *Cell Metab.* **30**, 917-936.e10 (2019).

285. Rayes, J. *et al.* The podoplanin-CLEC-2 axis inhibits inflammation in sepsis. *Nat. Commun. 2017 81* **8**, 1–14 (2017).

286. Haenseler, W. *et al.* A Highly Efficient Human Pluripotent Stem Cell Microglia Model Displays a Neuronal-Co-culture-Specific Expression Profile and Inflammatory Response. *Stem Cell Reports* **8**, 1727–1742 (2017).

287. Wilgenburg, B. van, Browne, C., Vowles, J. & Cowley, S. A. Efficient, Long Term Production of Monocyte-Derived Macrophages from Human Pluripotent Stem Cells under Partly-Defined and Fully-Defined Conditions. *PLoS One* **8**, e71098 (2013).

288. Buchrieser, J., James, W. & Moore, M. D. Human Induced Pluripotent Stem Cell-Derived Macrophages Share Ontogeny with MYB-Independent Tissue-Resident Macrophages. *Stem Cell Reports* **8**, 334–345 (2017).

289. Cimini, M., Cannatá, A., Pasquinelli, G., Rota, M. & Goichberg, P. Phenotypically heterogeneous podoplanin-expressing cell populations are associated with the lymphatic vessel growth and fibrogenic responses in the acutely and chronically infarcted myocardium. *PLoS One* **12**, e0173927 (2017).

290. Wigle, J. T., Chowdhury, K., Gruss, P. & Oliver, G. Prox1 function is crucial for mouse lens-fibre elongation. *Nat. Genet. 1999 213* **21**, 318–322 (1999).

291. Matthaei, K. I. Genetically manipulated mice: a powerful tool with unsuspected caveats. *J. Physiol.* **582**, 481 (2007).

292. Heffner, C. S. *et al.* Supporting conditional mouse mutagenesis with a comprehensive cre characterization resource. *Nat. Commun. 2012 31* **3**, 1–9 (2012).

293. Gomez Perdiguero, E. *et al.* Tissue-resident macrophages originate from yolk-sac-derived erythro-myeloid progenitors. *Nat. 2014 5187540* **518**, 547–551 (2014).

294. Lee, L. K. *et al.* LYVE1 Marks the Divergence of Yolk Sac Definitive Hemogenic Endothelium from the Primitive Erythroid Lineage. *Cell Rep.* **17**, 2286–2298 (2016).

295. Lange, W. J. de, Halabi, C. M., Beyer, A. M. & Sigmund, C. D. Germ line activation of the Tie2 and SMMHC promoters causes noncell-specific deletion of floxed alleles. *Physiol. Genomics* **35**, 1 (2008).

296. Song, A. J. & Palmiter, R. D. Detecting and Avoiding Problems When Using the Cre/lox System. *Trends Genet.* **34**, 333 (2018).

297. Sharma, B. *et al.* Alternative Progenitor Cells Compensate to Rebuild the Coronary Vasculature in Elabela- and Apj-Deficient Hearts. *Dev. Cell* **42**, 655-666.e3 (2017).

298. Chen, H. I. *et al.* The sinus venosus contributes to coronary vasculature through VEGFC-stimulated angiogenesis. *Dev.* **141**, 4500–4512 (2014).

299. K, R.-H. *et al.* Coronary arteries form by developmental reprogramming of venous cells. *Nature* **464**, 549–553 (2010).

300. Risebro, C. A. *et al.* Prox1 maintains muscle structure and growth in the developing heart. **136**, (2009).

301. Shigeta, A. *et al.* Endocardially Derived Macrophages Are Essential for Valvular Remodeling. (2019). doi:10.1016/j.devcel.2019.01.021

302. Venkatesh, D. A. *et al.* Cardiovascular and Hematopoietic Defects Associated With Notch1 Activation in Embryonic Tie2-Expressing Populations. *Circ. Res.* **103**, 423–431 (2008).

303. Luna-Zurita, L. *et al.* Integration of a Notch-dependent mesenchymal gene program and Bmp2-driven cell invasiveness regulates murine cardiac valve formation. *J. Clin. Invest.* **120**, 3493–3507 (2010).

304. Escobedo, N., Detmar, M. & Oliver, G. Restoration of lymphatic function rescues obesity in

Prox1-haploinsufficient mice. doi:10.1172/jci.insight.85096

305. Harvey, N. L. *et al.* Lymphatic vascular defects promoted by Prox1 haploinsufficiency cause adult-onset obesity. *Nat. Genet. 2005 3710* **37**, 1072–1081 (2005).

306. Baxter, S. A. *et al.* Regulation of the lymphatic endothelial cell cycle by the PROX1 homeodomain protein. *Biochim. Biophys. Acta - Mol. Cell Res.* **1813**, 201–212 (2011).

307. Hulin, A. *et al.* Maturation of heart valve cell populations during postnatal remodeling. *Development* **146**, (2019).

308. Gill, H. K. *et al.* Separation of the PROX1 gene from upstream conserved elements in a complex inversion/translocation patient with hypoplastic left heart. *Eur. J. Hum. Genet. 2009 1711* **17**, 1423–1431 (2009).

309. O'Donnell, A. & Yutzey, K. Prox1+ Endothelial Cells in Heart Valve Development and Homeostasis. *FASEB J.* **35**, (2021).

310. Ganuza, M. *et al.* Murine hematopoietic stem cell activity is derived from pre-circulation embryos but not yolk sacs. *Nat. Commun. 2018 91* **9**, 1–16 (2018).

311. Dellinger, M. T., Meadows, S. M., Wynne, K., Cleaver, O. & Brekken, R. A. Vascular Endothelial Growth Factor Receptor-2 Promotes the Development of the Lymphatic Vasculature. *PLoS One* **8**, 74686 (2013).

312. Cha, B. *et al.* Mechanotransduction activates canonical Wnt/β-catenin signaling to promote lymphatic vascular patterning and the development of lymphatic and lymphovenous valves. *Genes Dev.* **30**, 1454–1469 (2016).

313. Dib, C., Araoz, P. A., Davies, N. P., Dearani, J. A. & Ammash, N. M. Hypoplastic Right-Heart Syndrome Presenting as Multiple Miscarriages. *Texas Hear. Inst. J.* **39**, 249 (2012).

314. Lange, F. J. de *et al.* Lineage and Morphogenetic Analysis of the Cardiac Valves. *Circ. Res.* **95**,

645–654 (2004).

315. Lincoln, J., Alfieri, C. M. & Yutzey, K. E. Development of heart valve leaflets and supporting apparatus in chicken and mouse embryos. *Dev. Dyn.* **230**, 239–250 (2004).

316. MacGrogan, D. *et al.* How to Make a Heart Valve: From Embryonic Development to Bioengineering of Living Valve Substitutes. *Cold Spring Harb. Perspect. Med.* **4**, (2014).

317. Lamers, W. H., Virágh, S., Wessels, A., Moorman, A. F. M. & Anderson, R. H. Formation of the Tricuspid Valve in the Human Heart. *Circulation* **91**, 111–121 (1995).

318. Marino, A. *et al.* Pressure overload leads to coronary plaque formation, progression, and myocardial events in ApoE–/– mice. *JCI Insight* **4**, (2019).

319. Panizzi, P. *et al.* Impaired Infarct Healing in Atherosclerotic Mice With Ly-6ChiMonocytosis. *J. Am. Coll. Cardiol.* **55**, 1629–1638 (2010).

320. Yeo, K. P. *et al.* Efficient aortic lymphatic drainage is necessary for atherosclerosis regression induced by ezetimibe. *Sci. Adv.* **6**, 2697 (2020).

321. De Villiers, C. & Riley, P. R. Mouse models of myocardial infarction: comparing permanent ligation and ischaemia-reperfusion. *Dis. Model. Mech.* **13**, (2020).

322. McDonald, D. M., Yao, L. C. & Baluk, P. Dynamics of airway blood vessels and lymphatics: Lessons from development and inflammation. in *Proceedings of the American Thoracic Society* **8**, 504–507 (2011).

323. Fraser, D., Melzer, E., Camacho, A. & Gomez, M. Macrophage production of innate immune protein C1q is associated with M2 polarization (INM1P.434). *J. Immunol.* **194**, (2015).

324. D, B. *et al.* Apolipoprotein E induces antiinflammatory phenotype in macrophages. *Arterioscler. Thromb. Vasc. Biol.* **31**, 1160–1168 (2011).

325. Bain, C. C. *et al.* Resident and pro-inflammatory macrophages in the colon represent

alternative context-dependent fates of the same Ly6Chi monocyte precursors. *Mucosal Immunol. 2013 63* **6**, 498–510 (2012).

326. van Leent, M. M. T. *et al.* Prosaposin mediates inflammation in atherosclerosis. *Sci. Transl. Med.* **13**, (2021).

327. Dardik, R. *et al.* Novel Proangiogenic Effect of Factor XIII Associated With Suppression of Thrombospondin 1 Expression. *Arterioscler. Thromb. Vasc. Biol.* **23**, 1472–1477 (2003).

328. MS, Lord, B, C., BL, F., S, M. & JM, W. Platelet Factor 4 Binds to Vascular Proteoglycans and Controls Both Growth Factor Activities and Platelet Activation. *J. Biol. Chem.* **292**, 4054–4063 (2017).

329. Lupu, I.-E., De Val, S. & Smart, N. Coronary vessel formation in development and disease: mechanisms and insights for therapy. *Nat. Rev. Cardiol. 2020 1712* **17**, 790–806 (2020).

330. P, H. *et al.* Deletion of vascular endothelial growth factor C (VEGF-C) and VEGF-D is not equivalent to VEGF receptor 3 deletion in mouse embryos. *Mol. Cell. Biol.* **28**, 4843–4850 (2008).

331. S, Y. *et al.* Fate mapping reveals origins and dynamics of monocytes and tissue macrophages under homeostasis. *Immunity* **38**, 79–91 (2013).